Alma Mater Studiorum – Università di Bologna

DOTTORATO DI RICERCA IN

Ingegneria Civile, Chimica, Ambientale e dei Materiali

Ciclo XXXII

Settore Concorsuale: 09/D2 – SISTEMI, METODI E TECNOLOGIE DELL' INGEGNERIA CHIMICA E DI PROCESSO

Settore Scientifico Disciplinare: ING – IND/24 – PRINCIPI DI INGEGNERIA CHIMICA

INNOVATIVE CERAMIC MEMBRANES FOR SWEEPING GAS MEMBRANE DISTILLATION: MEMBRANE CHARACTERIZATION AND PROCESS DEVELOPMENT

Presentata da: Mohamed Khaled Fawzy

Coordinatore Dottorato

Prof. Luca Vittuari

Supervisore

Prof. Serena Bandini

Co-supervisori

Prof. Corinne Cabassud
Dott. Felipe Varela-Corredor

Esame finale anno 2020

Acknowledgements

I would like to thank my PhD supervisor, Prof. Serena Bandini for her guidance, support and consideration during my PhD thesis. I have learned a lot from her, both personally and technically. I wish to express my gratitude to Prof. Corinne Cabassud for her supervision during my research period in Toulouse, France. I would also like to recognize the special role played by Dr. Felipe Varela-Corredor. I really appreciate his help and advice. Besides, I am grateful to all my teachers and professors for their invaluable contributions to my development. Finally, I would like to thank my parents and sister for their unconditional love, prayers and support. I could not have reached any of my goals without them.

[This page intentionally left blank]

Abstract

The employment of tubular hydrophobic carbon-based titania membranes in sweeping gas membrane distillation (SGMD) was studied in this PhD thesis. Each membrane is composed of four layers possessing different morphological properties. The membranes were manufactured by the Fraunhofer Institute for Ceramic Technologies and Systems (IKTS, Hermsdorf, Germany).

The characterization of some of the membrane morphological properties was implemented in this thesis by coupling experimental and modeled results of single gas permeation tests. This stage was a prerequisite for modeling SGMD owing to the impact of the morphological properties on the membrane mass transfer resistance. The dusty gas model was adopted in modeling the gas permeation. Two different approaches were followed during modeling. The first approach considered the morphological properties of each single membrane layer. This allowed the prediction of the role played by each layer in the overall membrane mass transfer properties. As for the second approach which is the most commonly applied in literature, average membrane morphological properties were characterized without considering the unique contribution of each membrane layer. Results demonstrated that the second approach underestimated the mass transfer resistance during SGMD processes.

The investigation of the module performance during SGMD operations was achieved by experimental and modeling studies for NaCl (aq.) feed. The model considered the Knudsen and molecular diffusion mechanisms in the membrane. The module was capable of undergoing SGMD experiments at temperatures up to 110°C which is higher than the values applied in most of the works in literature. Experimental flux results went in agreement with the modeled values obtained on using the morphological properties of each membrane layer. On the contrary, the modeled values obtained on considering average membrane morphological properties deviated significantly from the experimental results. The SGMD model was also used to estimate the effect of the operating conditions and flow configuration on the obtainable water flux. The liquid temperature and gas pressure possessed the most significant effects on the modeled flux. Besides, the contribution of the Knudsen diffusion was found to be negligible during SGMD. Other modeling studies of the membrane modules were performed for the case belonging to SGMD of ethanol (aq.). This aimed at predicting the effect of the operating conditions on the membrane selectivity. The Maxwell-Stefan modeling approach was followed in this case. Results showed that the liquid inlet temperature and the total length of the SGMD unit vessel were the most important factors affecting the obtainable selectivity.

Eventually, a hypothetical sweater desalination process was proposed. This process incorporated SGMD (using the modules studied in this thesis) as the desalination unit. Process development and optimization procedures were carried out using preliminary design and non-rigorous cost estimation. Results showed that the SGMD inlet liquid temperature was the key parameter affecting

the choice of the operating conditions and the array of the modules inside the SGMD unit. The water production cost (WPC) could be minimized by maximizing the SGMD inlet liquid temperature and the total length of the SGMD unit vessel. However, process limitations necessitated the compromise between these factors. The optimized liquid temperature was found to be 107°C for an SGMD vessel having a total length of 5.4 m. This corresponded to a water production cost (WPC) of 20.9 $\$/m^3$ such that the feed heating requirement was the determinant cost item. This WPC could be mitigated in case of the availability of a waste heat source.

Table of Contents

[This page intentionally left blank]

Chapter One

General Introduction

1.1.Membrane Distillation Separation Concept

During the past half-century, membrane separation technologies have witnessed a tremendous breakthrough and have grown from simple lab-scale studies to important industrial applications [1,2]. The separation principle and operation mode differ from one membrane separation technology to the other according to the process nature, the required application and the driving force [2,3]. A membrane contactor (MC) utilizes a porous non-selective membrane to separate two phases preventing their uncontrolled mixing and dispersion while enabling them from being in contact with each other according to a well-defined interfacial area. The membrane morphological properties control the resulting interfacial area which is necessary for mass transfer and/or reaction. Many membrane separation systems fall into the category of membrane contactors like membrane stripping, membrane crystallization, membrane scrubbing and membrane distillation [4,5].

Membrane distillation (MD) is a non-isothermal process where the vapor pressure gradient across the membrane represents the mass transfer driving force. Therefore, the rate of mass transfer can be improved in MD by heating the liquid feed which increases the vapor pressure of the volatile components contained in the feed. Accordingly, membrane distillation can be categorized as a thermally driven separation process [1,4,6,7]. Being heated, the feed is brought into contact with a porous non-selective membrane such that transmembrane mass and heat transfer from the feed side occur simultaneously towards the permeate-side. Liquid vaporization of the volatile components in the feed takes place at the pores entrance lying at the vicinity of the feed-side (feed/membrane interface). This creates an immobilized liquid/vapor interphase. As a result, the volatile components present in the feed are transported in the form of vapor molecules by diffusion through the unwetted membrane pores towards the permeate side. This is the sequel of the created vapor pressure gradient across the membrane. Then mass transfer mechanism occurring in the permeate-side depends greatly on the configuration of the membrane distillation where the permeating species are separated and recovered [1].

The pores of the membrane should be kept unwetted by the liquid streams during membrane distillation to avoid the undesired intrusion of the liquid into the membrane pores by capillary forces. This can lead to the consequence of the total passage of the liquid through the membrane until reaching the opposite membrane-side in the liquid form. The wetting phenomenon results in inefficient separation and can risk the flooding of the permeate-side marking process failure [1,4,6,7]. As a result, the difference between the feed pressure and that inside the pores should not exceed a minimum value known as the liquid entry pressure (LEP) which is dependent on the surface energy of the material and the liquid stream properties at given operating conditions [8].

Heat and mass transfer phenomena occur simultaneously during MD processes. Generally, heat is transferred across the liquid feed boundary layer from the feed bulk towards the feed-membrane interface. Then part of this heat is used to evaporate the permeating molecules from the feed while

the remaining portion is considered as heat losses and is transferred by heat conduction across the membrane towards the permeate side. Finally, the heat energy that reached the permeate-membrane interface is transferred to the permeate bulk across the permeate boundary layer. Therefore, conduction losses decrease the thermal efficiency of the membrane distillation processes as they represent the portion of total heat transferred from the bulk to the membrane that is not used in the vaporization of the permeating molecules [1,4].

1.2.Evolution of Membrane Distillation Technology

1.2.1. Short History

Membrane distillation was first introduced in the 1960s. Its development was impeded due to two main factors. The first was the difficulty in obtaining the membrane with the desired properties at a reasonable cost. The second was the uncertainties regarding the process economics when compared to conventional separation methods due to the high energy requirement required for heating the liquid feed to the desired operating temperatures [6,7].

In 1963, the first patent on membrane distillation was filed by Bodell which introduced the separation concept of membrane distillation in the scientific society. Silicone rubber membrane was used in this patent for water desalination [1,9]. In the permeate side, ambient air was allowed to flow and carry the water vapor molecules permeating from the feed side. Then the water was condensed and collected later in an external condenser. This configuration resembled the sweeping gas membrane distillation (SGMD). In 1967, another patent on membrane distillation was filed by Weyl claiming improvements in membrane distillation technology offering fewer energy demands [10]. Weyl used hot saline water and cold demineralized water as the feed and permeate sides respectively. The two sides were separated by a PTFE membrane with air-filled pores. This configuration resembled the direct contact membrane distillation (DCMD) configuration. The maximum flux reported was 1 kg/(h m^2). Then Bodell took out his second patent in 1968 [11]. This patent was a continuation of the work presented in his first patent where it was able to obtain potable water from saline water.

Other patents followed the work by Bodell and Weyl suggesting new composite materials [12] and new configurations like the spiral-wound for membrane distillation processes [13]. It is worth mentioning that the first paper on membrane distillation was published by Findley in 1967 in the Journal of "Industrial & Engineering Chemistry Process Design and Development" where the application of (DCMD) configuration was experimentally studied [14]. Various membrane materials were used like paper, glass fiber, and diatomaceous earth-containing membranes. The coating materials used to achieve the required hydrophobicity were silicone and Teflon.

In the 1980s, membrane distillation was considered a newborn technology, so the vagueness related to its principles demanded distinct definitions and descriptions. Therefore, a committee was established in Rome in 1986 at the "Workshop on Membrane Distillation" aiming at standardizing

the membrane distillation process terminology [6,9]. The main characteristics and features of the membrane distillation process as defined by the committee were as follows:

- The membrane should be porous.
- The membrane should not be wetted by the process liquids.
- Capillary condensation should not occur inside the membrane pores.
- The membrane must not lead to alterations in the liquid/vapor equilibrium of the different components in the process liquids.
- At least one side of the membrane should be in direct contact with the process liquid.
- For each component, its partial pressure gradient in the vapor phase represents the driving force for mass transfer

1.2.2. Recent Research Directions

A significant consideration is being dedicated to membrane distillation technology from industrial and academic pursuits. This has kept up the momentum for new publications regarding this technology [15]. Accordingly, the frequency of publications concerning membrane distillation has risen exponentially since the 1980s [1]. Recently, many research works found in the literature are dedicated to the characterization of membranes' properties and the investigation of their performance for various MD applications. In fact, seawater desalination is deemed to be the most studied MD application. Several works studied other applications related to concentration of solutions for food and pharmaceutical industries [16–21], water treatment [22–27] and dehumidification of desiccants [28–32]. Given that the overall performance of the MD process is greatly dependent on the morphological and physiochemical properties of the membranes used [15], many recent works in the focus on the characterization and optimization of these properties for MD processes [19,33–39]. Such properties could include the membrane hydrophobicity (expressed by contact angle and LEP), the morphological properties and the chemical, thermal and mechanical stability [1].

Most of the LEP measurements take place at room temperature [40–43]. However, measuring the LEP at higher liquid temperatures close to the desired MD operating temperature could offer a more realistic evaluation. This approach was followed by F. Varela-Corredor et al. [8] where LEP tests took place at temperatures up to 120 °C introducing the concept of the liquid entry temperature (LET). According to the authors, at a given transmembrane pressure difference, on increasing the temperature, the LEP decreases till reaching the temperature value of the LET at which wetting occurs. Regarding the morphological properties of the membranes used in MD, typical membrane characterization techniques are applied such as the scanning electronic microscopy (SEM), bubble point test, the mercury intrusion porosimetry [26,27,44,45]. Moreover, gas permeation tests represent an effective tool in the estimation of the important membrane mass transfer and morphological properties [46–51]. Aiming at investigating the performance of the membranes in MD processes, experimental and modeling studies were coupled in several works in literature [52–

62]. In many cases, this offered further simulations and optimization of the membrane properties, module geometric parameters, operating conditions and the configurations of the MD process and the employed membrane

It is worth noting that in the majority of the works in literature dedicated to MD studies, the research works are limited to membrane characterization and module performance investigation based on laboratory-scale and pilot-scale studies. However, few works in literature focused on process development and economic evaluation of large-scale MD processes [63–71]. The absence of the detailed information required for process development and optimization is considered one of the main challenges facing the implementation of MD on a commercial scale [66].

1.3.Configurations of Membrane Distillation

1.3.1. Processes

There are four main configurations of membrane distillation (MD) processes. They differ in the nature of the permeate side stream and the method by which the permeating molecules are recovered. Consequently, the configurations differ in the corresponding transfer phenomena [1]. These configurations are the direct contact membrane distillation (DCMD), the air gap membrane distillation (AGMD), the sweeping gas membrane distillation (SGMD) and the vacuum membrane distillation (VMD) [72]. The schemes corresponding to the main four membrane distillation configurations are shown in Fig. (1.1). Each MD configuration has its own advantages and disadvantages. Therefore, the choice of the most suitable configuration greatly depends on the operating conditions, feed properties and process application. Due to its simplicity and minimum equipment required, DCMD is the most studied configuration of MD with the highest number of publications such that more than half of the publications on MD are concerned with DCMD [1,7].

In the sweeping gas membrane distillation (SGMD) configuration, an inert gas stream flows in the permeate-side and is referred to as the “sweeping gas”. The vapor molecules permeating across the membrane from the feed side join the permeate side and are carried by the sweeping gas towards the outlet of the MD module [1,7]. Then, the permeating molecules could be recovered from the sweeping gas by means of external separation methods like condensation and adsorption. The configuration of SGMD is recommended for the removal of volatile components from aqueous solutions [72,73]. Temperature polarization is an undesired phenomenon as it can negatively affect the efficiency of heat transfer and the obtained mass flux. High temperature polarization is due to high heat losses by conduction across the solid matrix of the membrane. This results in less available latent heat of vaporization which is required for the vaporization of the permeating components from the feed side. SGMD offers the advantages of low temperature polarization with respect to the other configurations in addition to the absence of the risk of wetting in the permeate side. However, SGMD suffers low fluxes and adds complexity to the system due to the need for recovering the

permeating molecules from the sweeping gas as well as pretreating the sweeping gas if required [1,15].

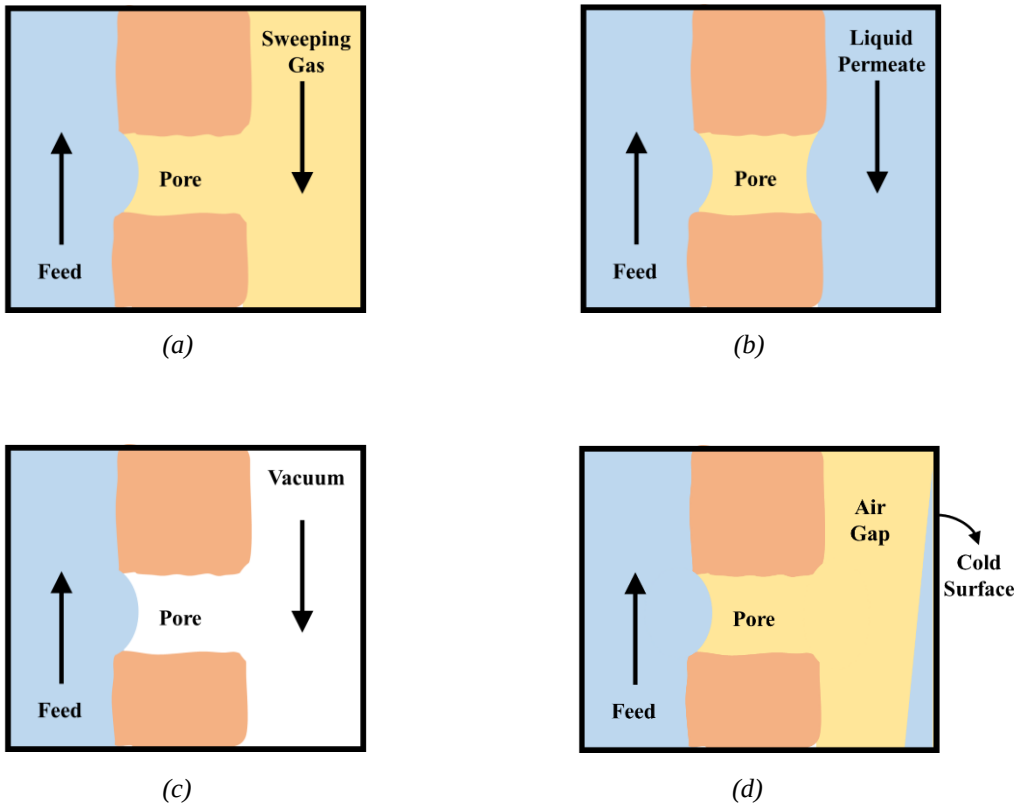

Figure (1.1) *The scheme of the main MD process configurations: (a)SGMD b)DCMD (c)VMD (d)AGMD*

In the case of direct contact membrane distillation (DCMD) configuration, the permeate side contains a flowing aqueous solution that is present at a temperature lower than that of the feed. The vapor pressure difference of the permeating component is related to the temperature difference between the two streams. Evaporation of the permeating molecules occurs at the feed/membrane interface, then diffusion in the vapor filled pores takes place across the membrane and finally, the permeating molecules condense at the permeate/membrane interface and join the permeate-side solution [1,7]. DCMD is considered as the simplest and easiest MD configuration as it needs the least equipment [9]. It is very convenient for desalination and the concentration of aqueous solutions like orange juice for example. Being compared to VMD, DCMD offers higher fluxes and can be preferred for the removal of volatile components. The simplicity of the DCMD system enables its employment in any desired membrane equipment configuration like flat sheets, spiral wound, tubular, capillaries and hollow fibers [4]. Still, DCMD configuration suffers the highest temperature polarization with respect to the other configurations and its flux is sensitive to the feed concentration [15]. Its high temperature polarization is due to the fact that it has the highest heat conduction losses among the membrane distillation configurations [6].

Air gap membrane distillation (AGMD) represents the configuration in which a stagnant air is interposed between the membrane surface and a condensation surface in the permeate side [1]. The vapor molecules from the feed side diffuse through the membrane pores and then across the stagnant air gap until reaching the cold surface where condensation occurs, and the distillate is collected at the outlet of the permeate side. The AGMD configuration has the highest energy efficiency so it can be widely employed for most membrane distillation applications [7]. The fact that there is an extra mass transfer resistance added for the vapor flow in the AGMD leads to low flux values [6,15].

As for the vacuum membrane distillation (VMD) configuration, a vacuum is applied in the permeate side. The applied vacuum pressure is less than the vapor pressure of the permeating components generating a positive driving force. Therefore, no condensation occurs in the permeate side. If necessary, the permeating molecules can be recovered by an external condenser at the exit of the downstream of the permeate side [7]. The mass transfer resistance in the permeate boundary layer is neglected and heat conduction losses across the membrane are also neglected [1,6]. VMD offers low temperature polarization and can be applied for aroma recovery. It can be also used for the removal of volatile organic compounds (VOCs) from aqueous solutions. Besides, it shows fewer heat losses by conduction than in the case of DCMD [7,74]. However, it shows a higher risk of wetting and fouling in addition to less selectivity in case of permeation of more than one volatile component [15]. The use of vacuum is considered more convenient when the operation needs to be performed at low temperatures. That's because the heat losses are negligible during VMD [9].

It is worth noting that two other hybrid variants of MD configurations were introduced aiming at increasing the flux and mitigating the energy requirements [75]. These two configurations are the thermostatic sweeping gas membrane distillation (TSGMD) and the liquid gap membrane distillation (LGMD). The latter can be also referred to as permeated gap membrane distillation. However, negligible research works studied the LGMD and the TSGMD when compared to the four main MD configurations. The TSGMD combines the configurations of the AGMD and the SGMD in order to minimize the temperature of the sweeping gas which increases significantly across the length of the membrane module in case of SGMD due to the heat transferred from the liquid feed [1,73]. In the TSGMD, part of the permeated water vapor molecules in the sweeping gas could condense inside the module according to the operating conditions while the uncondensed portion is recovered by an external condenser [1,76]. As for the LGMD, it combines the configurations of the DCMD and the AGMD such that the gap present between the membrane and the condensing surface in the permeate side of the AGMD system is filled by the distilled water that has permeated across the membrane from the feed side and has condensed on reaching the permeate side. This water acts as a stagnant cold liquid solution inside the membrane module [75].

1.3.2. Membranes

The most common and traditionally applied types of membrane geometries are the flat-sheet and hollow-fiber membranes [44]. Typically, both membrane geometries are prepared from PP, PVDF and PTFE. It is also possible to prepare flat sheet membranes from PVDF-PTFE composite materials [7]. Hollow fiber membranes can offer high compactness up to 9000 m^2/m^3 [77]. This enables them from possessing larger surface area per unit volume than flat sheet membranes. The higher packing density of hollow fiber membranes is due to the small outer diameter of fibers. Besides, they offer lower mass transfer resistance when compared to the planar membranes. This is the result of the relatively small membrane thickness in hollow fibers with respect to flat sheet membranes [78,79].

1.3.3. Modules

As for the module configurations, the most commonly used geometries in membrane distillation systems are the plate frame, hollow fiber, tubular and spiral wound [6]. The membranes are grouped and assembled or packed in a defined array in a module that represents the membrane distillation equipment [80]. The choice of the right module geometry (module configuration) for membrane distillation depends on the process nature, limitations and application. A good module configuration is the one that can offer compactness, robustness and minimum pressure drops according to the system fluid dynamics. This can result in an improvement in the mass transfer and the obtainable flux [15].

Flat membranes are used in both the plate frame and the spiral wound modules. In the plate frame modules, the membrane and a spacer are layered together between two flat sheets. This geometry has a very wide application in the lab-scale due to its simplicity and easiness of cleaning and experimental management. Their use in the common membrane distillation applications as water desalination and wastewater treatment is widely spread. In case of the spiral wound geometry, flat sheet membrane and spacer are enveloped together and are then rolled around a central collection tube that is perforated. The feed moves in an axial direction and permeates across the membrane where the permeate moves radially towards the center and exits from the central perforated collection tube [81].

Thousands of hollow fibers are grouped and then packed inside a shell tube resembling the hollow-fiber module with a fiber-side and a shell-side. The feed can either pass inside the fiber or in the shell where it permeates towards the other side and then is collected and recovered. In case wetting occurs in the hollow-fiber modules, the whole module should be replaced [81]. The high compactness of hollow-fiber modules enables them from having a small footprint for a given effective mass transfer area. This makes this geometry of membrane distillation very attractive for industrial applications [6]. Although, hollow-fiber modules offer the advantages of both high compactness and low mass transfer resistance, the complexity involved in the modeling of the

transfer phenomena in hollow fibers modules is one of the main challenges in their study and development [82]. The tubular membranes have a geometry that is very close to that of the shell and tube heat exchangers. Tubes are grouped and inserted in the shell. Due to their low tendency of fouling, easy cleaning and high mass transfer area, tubular membranes are considered to be more practical then hollow fibers. However, they suffer high operating cost and have less compactness than the hollow-fiber modules [81].

1.4.Membranes used in Membrane Distillation

1.4.1. Polymeric Membranes

The commercial polymeric membranes used in membrane distillation (MD) are porous hydrophobic membranes that are made of polypropylene (PP), polyvinylidene difluoride (PVDF) or polytetrafluoroethylene (PTFE) (Teflon) [83]. Hollow fibers of polyethylene (PE) were also employed in desalination by MD [84]. Typically, the phase inversion technique is applied in the manufacturing of PVDF membranes while the stretching and thermal phase separation techniques are employed in the manufacturing of PP membranes. PTFE is generally manufactured using the sintering or the stretching techniques [1]. SEM images of PVDF and PTFE membranes are shown in Fig (1.2).

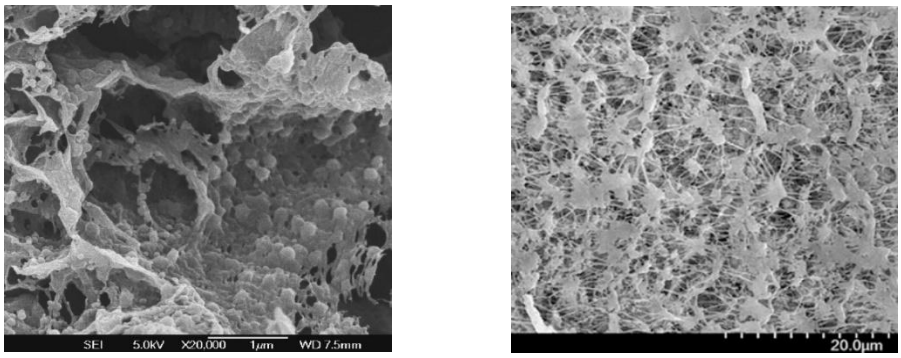

(a) *(b)*

Figure (1.2) *SEM images for: (a) PVDF membrane [85] (b) PTFE membrane [86]*

1.4.2. Ceramic Membranes

On being compared to ceramics, polymeric materials have some drawbacks as low thermal and chemical stability in addition to poor mechanical strength [78]. Higher thermal stability of ceramic materials could offer relatively high feed temperatures during MD operations. This could augment the mass transfer driving force given that MD is a thermally driven process. Moreover, ceramic membranes could offer higher lifetime than polymeric membranes since ceramics can undergo cleaning, backwashing and sterilization with harsh cleaning agents and/or at high temperatures [80]. Accordingly, the employment of ceramic membranes in MD has attracted attention in many

research works found in literature [44,87]. However, ceramic membranes lack the uncompromisable hydrophobicity necessary for avoiding pores wetting and module flooding. This is due to the presence of the hydroxyl group in ceramics giving them their hydrophilic nature. Also, ceramics suffer from high membrane thermal conductivity that may negatively affect the thermal efficiency in MD. Still, this could be mitigated by optimizing the membrane thickness [88]. Besides, ceramic membranes could be hydrophobized to prevent wetting and flooding [78]. Other drawbacks of ceramic membranes are their high capital cost on being applied on a large scale besides their lower packing factor and high fragility [80]. The ceramic membranes mainly studied in literature for MD processes are metal oxides like alumina, zirconia, titania, silica while few studies considered non-metal oxides like silicon nitride [79,89]. There are many manufacturing methods of ceramic membranes like slip casting, tape casting, pressing, extrusion [5] .

The hydrophobization of ceramic membranes can take place by surface modification techniques like grafting and hydrophobic surface coating [1,78]. In most of the works devoted to the application of ceramics in MD, direct grafting with organo-silane compounds is the most adopted surface modification technique [44,87]. Simply, silane is a molecule that contains a silicon atom having four functional groups while the organosilane is the silane that has one or more organic groups forming bonds between carbon and Si like that in alkylated silicon (R-Si-). This bond is very stable and non-polar due to the organic nature of the functional group. On grafting, the organo-silane forms hydrogen, ionic, van der Waals, or covalent bonds with the ceramic membrane surface. The most widely employed organo-silanes in the hydrophobization process are fluoroalkyl silanes (FAS) while the main approaches used are the immersion, chemical vapor deposition (CVD) and the sol-gel methods [44]. SEM images are shown in Fig (1.3) for silica-based membranes before and after being grafted by fluoroalkyl silane.

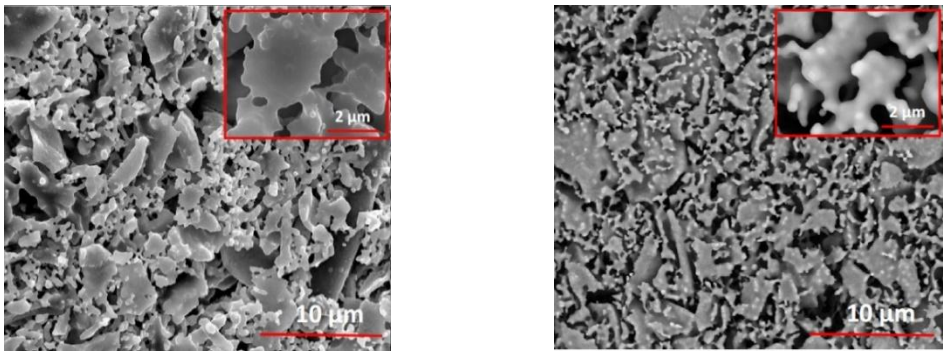

(a) *(b)*

Figure (1.3) *SEM images for silica-based membrane [90] : (a) Before being grafted (b) After being grafted*

Before grafting, the ceramic membrane surface is hydroxylated because as the concentration of the hydroxyl groups on the membrane surface increase, the reaction between the FAS molecules and the membrane surface is enhanced. FAS compounds contain both, the hydrolysable and hydrophobic end groups where the length of the hydrophobic group, grafting time and grafting

temperature affect the hydrophobization process results [34–36,91–93].The hydrolysable group combines with the hydroxyl groups on the surface of the ceramic membrane [80,94] and the free hydrophilic groups are responsible for the hydrophobic character of the grafted membranes as demonstrated by Fig (1.4). FAS are the most used due to their high performance, low water absorption, resistance to oxidation and solvents. They have characteristics similar to those of PFTE but FAS are much easier to handle. Other coating materials used in ceramic membrane hydrophobization are chloro-alkyl silanes, alcohols, PDMS [36]. The first work on hydrophobic ceramic membranes for MD was reported by Labort et al. in 2004 [95]. They used alumina and zirconia membranes that were hydrophobized by 1H 1H 2H 2H perfluorodecyltriethoxysilane. Having applied the air gap membrane distillation (AGMD) configuration, they were able to achieve fluxes up to 6.9 kg/(h m^2) at a feed temperature of 95 °C.

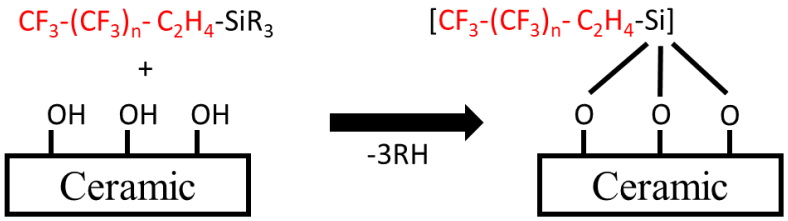

Figure (1.4) *Representation of the main reaction involved during the hydrophobization of ceramics by FAS compounds (updated from [80])*

1.4.3. Membrane Requirements

The membranes used in MD should offer high permeability and stable performance [15]. Therefore, the choice of the membrane material represents one of the main critical MD process aspects. A good membrane material should offer controlled contact between the two phases involved in the process without dispersing one into the other. This can be guaranteed by avoiding liquid intrusion into the membrane pores. Besides, high thermal and chemical stabilities and sufficient mechanical strength of the membrane are crucial for a successful MD operation. It is also utterly obvious that one of the most important requirements of the membrane is that it should be available at a low cost [1]. Accordingly, many membrane properties need to be examined, characterized and optimized prior to its employment in MD processes. The membrane properties can be morphological and physiochemical. The membrane morphological properties include the mean pore size, pores size distribution, maximum pore size, porosity, tortuosity, thickness. As for the physiochemical properties of the membrane, they dictate the interaction behavior of the membrane with the process streams. Such properties include the membrane surface hydrophobic nature, the interfacial surface tension, thermal conductivity, thermal stability, chemical stability and mechanical strength [80].

Pore wetting can lead to possible clogging of pores reducing the active area available for mass transfer. Exacerbated cases of wetting could result in module flooding and failure of the MD process. In a satisfactory MD operation where wetting and flooding are prevented, the liquid/vapor equilibrium taking place at the feed/membrane interface is the only determinant of the selectivity factor in membrane distillation [96]. Also, if the feed solutions contain dissolved salts like the case of saline water, partial pore wetting may lead to precipitation of salts inside the pores causing partial or total clogging of pores. Consequently, the active area available for mass transfer and the obtained flux are reduced. In most of the applications of membrane distillation, the liquid process stream is a hydrophilic aqueous solution which necessitates the usage of hydrophobic membranes. This prevents the wetting and flooding phenomena as long as the pressured difference between the liquid stream and the gas entrapped in the pores is kept below the liquid entry pressure (*LEP*) [1,4]. The membrane's surface energy and the feed temperature are regarded as the main factors affecting the *LEP* value [8]. It is worth noting that although the transmembrane pressure should not exceed the *LEP* value, it should not be negative. A negative transmembrane pressure corresponds to the case at which the permeate pressure is higher than that of the feed inducing a pressure-driven reverse transmembrane flow. This phenomenon is known as bubbling [80]. Obviously, the *LEP* represents a critical membrane characteristic [81]. It needs a clear investigation in order to ensure the applicability of membrane distillation experiments within the desired operating conditions. The *LEP* value can be theoretically estimated from the Laplace's equation as given by Eq. (1.1)

$$LEP = \left(P_f - P_p\right)_{\min} = \frac{-2\,\beta\,\gamma_l \cos\theta}{r_{\max}} \tag{1.1}$$

where P_f and P_p represent the feed and permeate pressure values respectively (for SGMD, AGMD and VMD) while γ_l and θ represent the surface tension of the liquid at the liquid/air interface and the liquid-solid contact angle respectively. r_{max} is the maximum pore radius and β is the pore geometric factor and it is equal to unity in case of cylindrical pores. The contact angle increases as the polarity difference between the liquid and the membrane increases [4]. High contact angle and *LEP* are desired characteristics of the membrane due to low corresponding risk of wetting and flooding. From Eq. (1.1), it can be indicated that the membranes that are more hydrophobic (have higher contact angle) and possess small pore size can offer higher *LEP* values. The commonly used pore size in the membrane distillation process lies within the range of 100 nm to 1 μm [15]. Besides, *LEP* value increases as the liquid surface energy decreases [81].

Another important membrane aspect is its mass transfer properties [97]. According to the mass transfer resistance involved in membrane distillation processes, the molar transmembrane flux increases by increasing the porosity and mean pore size and by reducing the membrane thickness and pore tortuosity [15]. As a matter of fact, both mass and heat transfer take place simultaneously in membrane distillation processes. Therefore, the effect of these morphological properties on the

permeability should be investigated form the point of view of the transmembrane mass and heat transfer phenomena together. Aiming at improving the MD process thermal efficiency, the thermal conduction losses can be minimized by maximizing the heat transfer resistance across the membrane. This can take place by increasing the membrane thickness [88,98]. However, this negatively impacts the transmembrane mass transfer. As a result, the membrane thickness should be carefully optimized [1,15]. Besides, the heat conduction losses can be reduced by choosing a membrane material possessing low thermal conductivity (high heat conduction resistivity) [1] and by increasing the porosity of the membrane since the thermal conductivity of the gas entrapped in the pores is around ten times less than that of the solid matrix of the membrane [15]. The thermal conductivity of the commercial membranes used in membrane distillation is in the range of 0.04-0.06 W/(m.K) [1].

In addition to high permeability and hydrophobicity, high chemical stability is an indispensable membrane property for sustainable MD performance. The reaction between the membrane and the processes streams can affect the properties of the membrane matrix and the surface energy of the membrane. The latter can affect the hydrophobic nature of the membrane which could risk wetting and flooding. As a result, the membrane material should be resistant to the chemical attacks of the process fluids in order to preserve its desired properties [15,40,97].

Given that MD is thermally driven [1], high feed operating temperatures are desired in MD processes. However, the membrane properties and the hydrophobic nature of the membrane surface could be affected by long-term operations at high temperatures due to thermal degradation [15]. This could result in pore wetting and flooding. Therefore, thermally stable membranes could offer a high driving force and stable flux in MD processes [97].

Generally, the operating pressure difference involved in membrane distillation is close to or below the atmospheric pressure. This is relatively low when compared to other membrane separation processes like reverse osmosis (RO). Therefore, the required membrane mechanical properties in MD are not so high [97]. However, sufficient membrane strength is required in order to avoid cracks and failures. The mechanical properties of a given membrane material can be improved by increasing its thickness and decreasing its porosity [15]. However, high membrane thickness and low porosity correspond to high mass transfer resistance. Therefore, these morphological properties need to be well examined and optimized.

Fouling in membrane distillation takes place due to the deposition and accumulation of undesired materials on the membrane surface and/or in membrane pores. This could lead to partial or total clogging of pores with the consequence of flux declination [83]. The fouling mechanism is affected by the foulant properties (like its molecular size, diffusivity, solubility, charge, hydrophobicity), the feed properties (like the flow rate, pressure, temperature and concentration)

and the membrane properties (like pore size, pore size distribution, hydrophobicity, functional groups and roughness) [99]. The interfacial interactions, the affinity of the membrane and its charge with respect to the foulant particles could determine the fouling degree. Minimum fouling tendency occurs when the membrane surface and the fouling particles carry the same charge due to the produced repulsion between them. As the surface roughness increases, the hydrophobicity increases due to more entrapment of air in the membrane pores at the surface [83].

1.5.Transmembrane Mass Transfer in Membrane Distillation

The mass transfer of vapor molecules in membranes used in MD processes has been widely studied and investigated where some theoretical models were developed based on the kinetic theory of gases [98]. The most common modeling approaches developed for the description of mass transfer across the membranes during membrane distillation include macroscale approaches like Fick's law, Maxwell-Stefan approach, or the dusty gas model (DGM). Besides, the Navier-Stokes equations could be applied and numerically solved for detailed studies of the gas behavior inside a single membrane pore. The choice of the adequate modeling approach depends on the flow nature, space and time scales and the purpose of the modeling study [100].

The main considered flow mechanisms of transmembrane mass transfer in membrane distillation can be either continuum (viscous flow and/or molecular diffusion) or non-continuum (Knudsen diffusion) or the flow can lie in the transition region between the continuum and the non-continuum flow regimes [9,96]. The flow type can be predicted according to the Knudsen number (*Kn*) which represents the ratio of the mean free path taken by the permeating molecule l^{free} to the pore diameter d_p as given by Eq (1.2) [4]. The mean free path represents the distance between two successive molecule-molecule collisions and is estimated by the kinetic theory of gases according to Eq(1.3).

$$Kn = \frac{l^{free}}{d_p} \tag{1.2}$$

$$l^{free} = \frac{K_B T}{P\pi\sigma^2\sqrt{2}} \tag{1.3}$$

where, T,P,K_B,σ represent temperature, pressure, Boltzmann's constant and the collision diameter of the molecule respectively. On one side, continuum flow tends to be prevailing in the cases at which the mean free path of the gas is much smaller than the pore size. This is due to the fact that the collisions between the molecules with each other are more predominant than the collisions between the molecules with the pore walls. In such cases, the corresponding Knudsen number is much smaller than unity (Kn<0.01) [9,81]. On the other side, the non-continuum flow becomes the

predominant mass transfer mechanism in case the collisions between the molecules with the pore walls are much more significant than the collisions between the molecules with each other. The corresponding Knudsen number in such cases is larger than unity (Kn>1) [4,81]. Apparently, the transition region lies between these two extremes at (0.01<Kn<1) [4,101]. The main difference between the MD models adopted in literature lies in the considered flow mechanisms and the arrangement of their mass transfer resistance during MD processes [9].

The dusty gas model (DGM) described by E. A. Mason and A. P. Malinauskas [102] is commonly adopted in describing the transmembrane mass transfer in MD processes [1]. The DGM combines the (Poiseuille) viscous flow, molecular (ordinary) diffusion, Knudsen diffusion and surface flow mechanisms assuming the existence of a hypothetical mixture that is composed of the gas and the porous medium. Conceptually, the porous medium is assumed to resemble giant spherical molecules (dust particles) that are motionless and are uniformly held in space by external forces. The gas motion between these dust particles can be described by the kinetic theory of gases [100,102]. Surface diffusion is always neglected in the modeling of MD processes [9]. It is worth noting that the DGM was derived for isothermal systems which are not the case of MD. F. Gao et al. introduced a polytropic equation of state to the discretized form of the DGM in order to estimate the temperature profile across the membrane pores during gas permeation tests [51]. In spite of that, a constant average value of the membrane temperature is usually applied in the DGM for MD modeling. This assumption is accepted especially in systems operating at small membrane temperature gradients [4]. The resistances of the flow mechanisms considered by the DGM can be assumed to be arranged in a manner similar to that of electric resistors. This can be demonstrated by the arrangement shown in Fig (1.5).

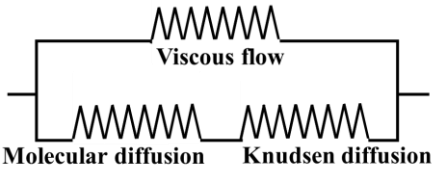

Figure (1.5) Transmembrane mass transfer resistance according to the DGM [1]

The most general form of the DGM is expressed for the transitional flow regime by the set of Equations (1.4-1.9) [4,100,101] after neglecting the surface diffusion. The inclusion or the omission of one or more of these mass transfer mechanisms depends greatly on the operating conditions, membrane morphological properties and process nature [4,9].

$$\frac{J_i^D}{D_{i,e}^K} + \sum_{h=1\neq i}^{n} \frac{P_h J_i^D - P_i J_h^D}{D_{ih,e}} = \frac{-\nabla P_i}{R_g T} \tag{1.4}$$

$$J_i^V = \left(\frac{\varepsilon r^2}{8\tau}\right) \frac{-P_i}{R_g T \mu_i} \nabla P \tag{1.5}$$

$$J^i = J_i^D + J_i^V \tag{1.6}$$

$$D_{ih,e} = \left(\frac{\varepsilon}{\tau}\right) P D_{ih} \tag{1.7}$$

$$D_{i,e}^K = \left(\frac{\varepsilon}{\tau}\right) D_i^K \tag{1.8}$$

$$D_i^K = \frac{d_p}{3} \sqrt{\frac{8 R_g T}{\pi M_i}} \tag{1.9}$$

where, J_i^D, J_i^V, J_i represent the diffusive, viscous and total fluxes of component (*i*) respectively while D_i^K, D_{ih} represent the Knudsen diffusivity and the binary diffusion coefficient of component (*i*) in a binary mixture (*i/h*) respectively. The subscript "e" refers to the effective values. The total pressure, the partial pressure of component (*i*) and that of component (*h*) are represented by P, P_i, P_h while μ_i, M_i represent the viscosity and molecular weight of component (*i*) respectively.

The porosity $\mathcal{E}$ represents the ratio between the volume of all the pores with respect to that of the membrane while the tortuosity τ represents the ratio between the pore length and the membrane thickness [47]. In the case of perfectly cylindrical pores, the tortuosity is equal to one while in case of tortuous pore paths, the tortuosity is larger than unity. From the definitions of the porosity and the tortuosity, it can be indicated that the porosity-tortuosity ratio $\mathcal{E}/\tau$ represents the ratio of the cross-sectional area of all the pores to the mass transfer area of the membrane. Therefore, the porosity-tortuosity ratio represents the ratio of the mole flux across the membrane to the mole flux across the pores.

Some simplifications can be adopted in modeling the mass transfer during MD processes according to the implemented configuration and operating conditions [4,9]. A set of simplified cases and the corresponding mass transfer expressions are given in Table (1.1).

Table (1.1) *Transmembrane mass transfer expressions for different cases of MD (updated from [4])*

Case	Mass Transfer Expression	Eq.	Comments
DCMD, SGMD (Permeation of a single component *i* across stagnant gas *h* in pores)	$\frac{J_i}{D_{i,e}^K}+\frac{P_h J_i}{D_{ih,e}}=\frac{-1}{R_g T}\nabla P_i$ Dusty Gas Model	(1.10)	• Neglected viscous flow due to constant pressure in pores
AGMD (permeation of single component *i* across stagnant gas *h* in pores)	$J_i=\frac{D_{ih,e}}{R_g T\left\lvert P_h\right\rvert_{\ln}}\nabla P_i$ $\left\lvert P_h\right\rvert_{\ln}$ is the log mean of pressures of *h* at both sides of membrane	(1.11)	• Neglected viscous flow due to constant pressure in pores. • Neglected Knudsen diffusion when compared to large molecular diffusion in membrane and air gap for AGMD
Permeation of more than one component across stagnant gas in pores)	$\sum_{h=1\neq i}^{n}\frac{P_h J_i - P_i J_h}{D_{ih,e}}=\frac{-\nabla P_i}{R_g T}$ Stefan-Maxwell Equation	(1.12)	• Neglected viscous flow due to constant pressure in pores. • In case of low Knudsen number
VMD (neglected continuum flow) (for a single component *i*)	$J_i=\frac{-D_{i,e}^K\nabla P_i}{R_g T}$ Knudsen Diffusion	(1.13)	• Predominant non-continuum flow in case of large Knudsen number at very low-pressure values.
VMD (transition region flow for a single component *i*) , Single gas *i* permeation test	$J_i=\frac{-\nabla P}{R_g T}\left[\left(\frac{\varepsilon r^2}{8\tau}\right)\frac{P}{\mu_i}+D_{i,e}^K\right]$ Dusty Gas Model	(1.14)	• Absence of molecular diffusion in case of the presence of a single gas

The integrated form of Eq (1.10) [1] expressed by Eq (1.15) can be derived as follows for ideal gas and for a flat membrane of a thickness δ .

$$\frac{J_i}{D_i^K}+\frac{y_h J_i}{D_{ih}}=\left(\frac{\varepsilon}{\tau}\right)\frac{-1}{R_g T}\nabla P_i$$

$$\because \nabla P_i=-\nabla P_h=-CR_g T\ \nabla y_h$$

$$\therefore J_i\left(\frac{1}{D_i^K}+\frac{y_h}{D_{ih}}\right)=\left(\frac{\varepsilon}{\tau}\right)C\nabla y_h$$

$$\frac{J_i}{C}\int_0^{\delta} dz=\left(\frac{\varepsilon}{\tau}\right)D_i^K D_{ih}\int_{y_{h,fm}}^{y_{h,pm}}\frac{dy_h}{D_{ih}+y_h D_i^K}$$

$$\frac{J_i}{C}\left[z\right]_0^{\delta}=\left(\frac{\varepsilon}{\tau}\right)D_i^K D_{ih}\left[\left(\frac{1}{D_i^K}\right)\ln\left(\left(y_h D_i^K\right)+D_{ih}\right)\right]_{y_{h,fm}}^{y_{h,pm}}$$

$$J_i=\left(\frac{\varepsilon}{\tau\delta}\right)CD_{ih}\ln\left(\frac{\left(y_{h,pm}D_i^K\right)+D_{ih}}{\left(y_{h,fm}D_i^K\right)+D_{ih}}\right) \qquad (1.15)$$

where C and y represent the total molar concentration and the mole fraction in the vapor state respectively while the subscripts "*fm*" and "*pm*" refer to the feed-membrane interface and the permeate-membrane interface respectively. z represents the direction of diffusion.

As a simplification of the DGM expression in Eq (1.15), the Wilke model combined with the Bosanquet formula can be proposed [103,104]. The Wilke model describes the molar flux across the membrane relative to the molar average velocity by Fick's law using an effective diffusion coefficient D_{ih}^{Eq} instead of the binary diffusion coefficient. This is given by Eq (1.16). The effective diffusion coefficient is estimated by the Bosanquet formula for equimolar diffusion as expressed by Eq (1.17) assuming that the Knudsen and molecular diffusion mass transfer resistances lie in series as it is assumed by the DGM [103,105].

$$J_i=-\left(\frac{\varepsilon}{\tau}\right)C\,D_{ih}^{Eq}\,\nabla y_i \qquad (1.16)$$

$$\frac{1}{D_{ih}^{Eq}}=\frac{1}{D_{ih}}+\frac{1}{D_i^K} \qquad (1.17)$$

Accordingly, the molar flux with respect to stationary coordinates can be expressed by Eq(1.18) which can be integrated to the form of Eq(1.19) for a flat membrane having a thickness δ.

$$J_i = -\left(\frac{\varepsilon}{\tau}\right) C\, D_{ih}^{Eq}\, \nabla y_i + y_i J_i \tag{1.18}$$

$$J_i = -\left(\frac{\varepsilon}{\tau\delta}\right) C\, D_{ih}^{Eq} \ln\left(\frac{y_{h,pm}}{y_{h,fm}}\right) \tag{1.19}$$

The application of both equations, Eq(1.17) and Eq(1.19) can be referred to as the Wilke-Bosanquet model [103–105] or generalized Fick's law with equivalent diffusion coefficient [106]. This approach is proposed in many works in literature regarding the description of transmembrane mass transfer during MD operations [1,47,82,98,106–108]. The approaches expressed by Eq(1.15) and (1.19) become almost identical in case of negligible mole fraction of the permeating species and in case of negligible Knudsen diffusion.

1.6.Comparison between Membrane Distillation and Conventional Separation Methods

Membrane distillation (MD) is considered as a hybrid between thermal distillation and membrane separation technology. However, MD can offer some important advantages over the conventional trayed or packed distillation columns [55,109]. The available interfacial area available for mass transfer is constant in MD regardless of the ratio of the flow rates of the streams in the feed and permeate sides. This ensures a stable operation that can be easily managed and controlled. MD offers a higher mass transfer area per unit volume so it can be preferred for compact systems [80]. Also, MD operations avoid the problems associated with phase mixing like entrainment and emulsification. The membrane materials used in MD can be either polymeric or hydrophobized ceramics which offer high corrosion resistance [81]. Considering the possible energy savings in MD, the liquid feed is not heated to the boiling point as in conventional distillation processes. Besides, MD operating temperatures can be below 80° which could allow the employment of low-grade waste and/or alternative energy sources such as solar, wind or geothermal energies, and waste thermal energy sources [110]. However, when compared to convention distillation processes, there is extra resistance in MD owing to the presence of the membrane [78].

Similarly, evaporation used in crystallizers is limited by the low area available for evaporation. This could result in high energy demands. The higher mass transfer area in MD allows crystallization at lower operating temperatures. This could lead to possible energy savings [111]. The low operating temperature in MD could be also beneficial in the concentration of juices. Conventionally, the concentration of juices takes place by multi-stage vacuum evaporation. However, the high operating temperature utilized in such processes could lead to the loss of important flavors due to the decomposition of some organic compounds [19].

Reverse osmosis (RO) which is a pressure-driven process is currently the most utilized technology for water desalination. On being compared to RO, MD was found to offer higher salt

rejection [23,81]. Besides, MD can offer less required feed pretreatment and better potential of energy recovery from renewable energy [112,113]. It is worth noting that although MD could be auspicious for various industrial applications, few studies are dedicated in literature to the process development of MD. Unfortunately, this has resulted in insufficient details and information about the accurate scale-up procedures, process development and cost estimation of industrial-scale desalination MD processes [1].

1.7.Main Applications of Membrane Distillation: Literature Survey

1.7.1. Seawater Desalination

The lack of enough freshwater resources in remote places or in regions of high demand was exacerbated by the growing world population and industrial breakthrough. Freshwater is needed for both, domestic and industrial use [114,115]. This has given rise to the development of desalination technologies at the present time in order to be employed in freshwater production. The most commonly used desalination technologies are reverse osmosis (RO), multi-effect distillation (MED) and multi-stage flash (MSF). The application of MD in water desalination has attracted many researchers due to their advantages over conventional methods in terms of high rejection and possible energy savings in case of the availability of low-grade waste heat sources [81,112,113].

The main works found in literature dedicated to the employment of polymeric membranes in MD for water desalination applications are listed in Table (1.2). PVDF is considered as one of the most studied polymeric membranes in MD. New material modifications to PVDF were suggested in literature to improve water fluxes for desalination purposes [116–118]. Q. F. Alsalhy et al. applied the AGMD configuration using a flat copolymer of PVDF and hexafluoropropylene (HFP) [116]. However, low fluxes were obtained. Similarly, M. R. S. Kebreia et al. employed a novel thin-film composite (TFC) membrane with ultrathin zeolitic imidazolate framework (ZIF-8)/chitosan layer coated on the polyvinylidene fluoride (PVDF) membrane [117]. The corresponding flux was 3.5 times that obtained by the unmodified PVDF.

Ceramic membranes were also investigated in literature for water desalination by MD. A list of the corresponding main works is presented in Table (1.3) such that the highest water flux (60 $L/(h.m^2)$) was reported by C-C.Ko et al. [78]. In this work, alumina hollow fiber membranes hydrophobized by 1H,1H,2H,2H-perfluorooctyltriethoxysilane were used. This corresponded to an aqueous solution feed of NaCl (3.5 wt.%) at 70°C and a permeate side pressure of 0.03 bar.

Table (1.2) *Main works in literature employing polymeric membranes in MD for water desalination*

MD Type	Geometry	Membrane	Operating Conditions	Flux (Kg/(m^{2}h))	Ref.
SGMD	Flat	PTFE d_p=199 nm δ=55μm Ɛ=69 % τ=1.59	Feed: deionized water T_f=70°C v_f=0.15 m/s T_p=20°C v_p=0.8m/s	14.4	[119]
		PTFE d_p=0.48μm δ=178 μm Ɛ=80 %	Feed: NaCl (aq.) T_f=71.6°C C_f=30 g/L v_f=0.16 m/s T_p=17.3°C v_p=2.11 m/s	10	[120]
	Hollow fibers	PVDF d_p= 0.1 μm δ= 50 μm Ɛ=55 %	Feed: NaCl(aq.) T_f=70°C C_f=5 mg/L v_f=0.02 m/s v_p=0.54 m/s	1.3	[82]
DCMD	Flat	PTFE d_p=0.22μm δ=0.11mm Ɛ=83 %	Feed: NaCl (aq.) (1 % wt.) T_f=60°C v_f=0.55m/s T_p=20°C	21	[41]
		PTFE d_p=0.27μm δ=170 μm Ɛ=77%	Feed: Red sea water T_f=70°C V_f=90 L/h T_p=20°C V_p=60 L/h	46	[121]
		PTFE d_p=0.22μm δ=39 μm Ɛ=53.4 % τ=4.02	Feed: deionized water T_f=60°C V_f=1.5L/m T_p=20°C V_p=1.5L/m	28.7	[122]
		PTFE d_p=0.2μm δ=160 μm Ɛ=88%	Feed: NaCl (aq.) T_f=65°C V_f=10L/m C_f=15 ppt T_p=19-25°C V_p=4L/m	38	[123]
		PVDF δ=27 μm	Feed: NaCl (aq.) (10 % wt.) T_f=65°C V_f=1.5 L/m T_p=20°C V_p=1.5L/m	60	[124]
		PTFE d_p=0.2μm δ=35 μm	Feed: brine from desalination T_f=70°C V_f=1.5L/m T_p=30°C V_p=1.5L/m	29.1	[55]
		PVDF d_p=0.22μm δ=125 μm Ɛ=70 %	Feed: Na2SO4(aq.) (2 Molar) T_f=60°C T_p=30°C	11	[56]
			Feed: NaCl(aq.) (4.5 Molar) T_f=60°C T_p=30°C	13	
	Hollow fibers	PP δ=0.25mm Ɛ=70 %	Feed: NaCl (aq.) (3.5 % wt.) T_f=78.6°C V_f=6L/m T_p=19°C	32.6	[52]
VMD	Flat	PP d_p=0.2μm δ=91 μm Ɛ=70 % τ=1.42	Feed: deionized water T_f=60°C v_f=0.4 m/s P_p=20 mbar	48	[125]
	Capillary	PP d_p=0.2μm δ=400 μm Ɛ=70 % τ=1.42	Feed: deionized water T_f=60°C v_f=0.8 m/s P_p=90 mbar	9	
	Flat	PTFE d_p =0.2 μm	Feed: deionized water T_f=80°C V_f=2 L/m P_p=35 kPa	17	[58]
	Hollow fibers	PE δ=0.4 mm	Feed: NaCl (aq.) T_f=60°C v_f=2.5 m/s P_p=2 kPa	33	[84]
		PTFE d_p=0.4 μm δ=0.45mm Ɛ=50 % τ=2	Feed: deionized water T_f=70°C v_f=1.6 m/s P_p=3 kPa	19	[126]
		PVDF d_p=0.28μm Ɛ/δ=22m^{-1}	Feed: deionized water T_f=80°C V_f=0.6 L/m P_p=45 kPa	1.8	[127]
AGMD	Flat	PTFE d_p=0.2μm δ=100 μm Ɛ=80 %	Feed: NaCl (aq.) (4.2 % wt.) T_f=80°C V_f=1.5L/m $V_{coolant}$=1.5L/m $T_{coolant}$=20°C Air Gap thickness=9mm	6.5	[128]

Ɛ:porosity, d_p: pore diameter, τ:tortuosity, v:velocity, T:temperature, P:pressure, V:volumetric flow rate, Subscripts (f:feed, p:permeate)

Table (1.3) *Main works in literature employing ceramic membranes in MD for water desalination*

MD type	Geometry	Membrane	Grafting Material	Operating Conditions	Flux ($Kg/(m^2h)$)	Ref
VMD	Hollow fiber	Alumina	Octyl (C6)	T_f=50°C 1 M NaCl V_f=140 ml/min P_p=3kPa	20	[33]
	Planar	Silica/ Alumina	Decyl (C8)	T_f=70°C 3.5 wt% NaCl V_f=1 l/min P_P=0.03 bar	29	[34]
	Hollow fiber	Alumina	Octyl (C6)	T_f=70°C V_f=1 l/min P_p=90kPa 10 Brix° Sucrose solution	20	[19]
				50 Brix° Sucrose solution	12	
DCMD	Nano fiber	Titania	Octyl (C6)	T_f=80°C 3.5 wt% NaCl T_p=20°C	12.2	[35]
VMD	Hollow fiber	Alumina	Octyl (C6)	T_f=70°C 3.5 wt% NaCl P_p=0.03 bar	60	[78]
	Planar	Alumina	Octyl (C6)	T_f=75°C P_p=0.09MPa 3 wt% NaCl	10.39	[91]
AGMD	Hollow fiber	Alumina	Decyl (C8)	T_f=80°C V_f=35 l/h 3 wt% NaCl T_p=20	43	[77]
DCMD		β-Sialon $Si_4Al_2O_2N_6$	Octyl (C6)	T_f =80C V_f=100 l/h 4 wt% NaCL T_p=20 in DCMD V_p=100 L/h in DCMD	6.79	[93]
VMD				P_p=0.02 bar in VMD	10.75	
DCMD	Planar	Alumina	Octyl (C6)	T_f=80°C v_f=0.03 m/s T_p=20°C v_p=0.03 m/s 4 wt% NaCl	17	[37]
SGMD		Alumina/ Graphite	Octyl (C6)	T_f=90°C V_f=240 l/h 4 wt% NaCl Gas: dry N_2 T_G=20°C V_G=337 l/h	21	[38]
AGMD	Capillary	Alumina/ Clay	Decyl (C8)	T_f=70°C V_f=0.429 l/min 0.5 M NaCl T_p=10°C	4.11	[39]
DCMD	Hollow fiber	Silicon nitride	Octyl (C6)	Tf=80°C 4 wt% NaCl V_L=100 l/h T_p=20 in DCMD V_p=100 l/h in DCMD	10.4	[79]
VMD				Pp=0.02bar in VMD	27	
AGMD	Tubular	Titania	Octyl (C6)	T_f=90°C 0.5 M NaCl T_p=5°C	3.75	[40]
			Tetradecyl (C12)		3.86	
		Phosphate/ Zirconia	Decyl (C8)	T_f=95°C T_p=5°C Water oil content 110 mg/L	6.88	[129]
DCMD	Planar	Alumina	Decyl(C8)	T_f=53°C T_p=18°C 0.1M NaCl	8	[130]
			Trichlorom-ethylsilane		7.8	
DCMD	Planar	Yttria Stabilized Zirconia	Octyl (C6)	T_f=80°C V_f=100 l/h T_p=20°C V_p=100 l/h 4 wt % NaCl	24	[110]

MD type	Geometry	Membrane	Grafting Material	Operating Conditions	Flux (Kg/(m^{2}h))	Ref
AGMD	Tubular	Zirconia	Decyl (C8)	T_f=95°C T_p=5°C 0.5 M NaCl V_f=400 l/h	4.7	[96]
		Titania			0.83	
DCMD		Zirconia		T_f=95°C T_p=35°C 0.5 M NaCl V_f=400 l/h V_p=50 l/h	3.96	
		Titania			0.8	
VMD		Zirconia		T_f=40°C V_f=210 l/h 0.5 M NaCl P_p=3 mbar T_p=room Temp	7.5	
		Titania			0.83	
AGMD	Tubular	Zirconia/ Alumina support	Decyl (C8)	T_f=99°C T_p=5°C 1 M NaCl	5.42	[42]
	Tubular	Alumina	Decyl (C8)	T_f=95°C T_p=5°C 1 M NaCl	5.4	[95]
		Zirconia			6.9	
DCMD	Hollow Fiber	Kaolin clay $Al_2Si_2O_5(OH)_4$	Decyl (C8)	T_f=70°C T_p=15°C V_f=0.7 l/m V_p=0.5 l/m AS(III) solution	28	[131]
				AS(V) solution	24	
SGMD	Planar	α-Si_3N_4	Dimethyle dichlorosilane / Dichloro methyl silane	T_f=90°C V_f=100 l/h Gas: dry N_2 V_G=100 l/min 4 wt% NaCl	11	[132]
AGMD	Tubular	MF (0.18µm) Clay	Decyl (C8)	T_f=95°C v_f=2.6 m/s 1 M NaCl T_p=5°C	6.5	[133]
		UF(15 nm) Clay			4.6	
SGMD	Planar	ɣ-$Y_2Si_2O_7$	Dimethyle dichlorosilane & Dichloro methyl silane	T_f=90°C V_f=1 l/min V_p=1 L/min dry N_2 4 wt% NaCl	14	[92]
DCMD				T_f=70°C T_p=5°C	15.55	
SGMD	Planar	SiN_2O		T_f=90°C 4 wt% NaCl	11.11	[134]
DCMD	Hollow Fiber	Amorphous Silica-based	Decyl (C8)	T_f=60°C T_p=10°C v_f=0.023 m/s v_p=0.003 m/s 6 g/l NaCl	35	[90]
		Crystalline Silica-based			33	
VMD	Tubular	Alumina	Hexadecyl trimethoxy silane	T_f=70°C v_f=160 l/h 3 wt% NaCl P_p=5 kPa	30	[135]

ε:porosity, d_p: pore diameter, τ:tortuosity, v:velocity, T:temperature, P:pressure, V:volumetric flow rate, Subscripts (f:feed, p:permeate)
Octyl (C6): 1H, 1H, 2H, 2H -perfluorooctyltriethoxysilane Decyl(C8): 1H,1H,2H,2HPerfluorodecyltriethoxysilane

1.7.2. Water Treatment

Removal of volatile organic compounds (VOCs) from aqueous solutions has a wide range of industrial and environmental applications. In the field of wastewater treatment, membrane distillation can be employed to reduce the concentration of VOCs in the wastewater to reach the allowable environmental limits [136]. Regarding the field of wastewater treatment, extensive experimental and modeling studies were undertaken by S. Bandini et al. regarding the removal of VOCs (acetone, ethanol, isopropanol, ethyl acetate, methyl acetate and methyl tertiary butyl ether (MTBE)) from water by applying VMD [24]. The membranes used were flat PTFE with PP support. The results of this work suggested that increasing the feed flowrate improved the flux of the VOCs due to the reduction in the concentration polarization. In a similar work, the removal of ethanol and acetone from water by flat PTFE membranes applying the SGMD configuration was studied by C. Boi et al. [136] such that SGMD was recommended for obtaining high selectivity of the VOCs.

Ceramic membranes were also studied in the separation of VOCs by MD [137,138]. Ethanol removal from water by VMD was investigated by W. Kujawsky et al. who used commercial tubular alumina, zirconia and titania membranes [137]. The hydrophobization of the membranes was achieved by per-fluoro-octyl-tri-ethoxy-silane (C6) and by per-fluoro-tetra-decyl -tri-ethoxy-silane (C12). The C6 coating resulted in higher ethanol selectivity than the C12 where the pore size of the hydrophobized membrane played an important role in determining the obtained selectivity.

Halogenated volatile organic compounds (HOVs) as chloroform, trichloroethylene (TCE) and tetrachloroethylene could lead to the pollution of groundwater and surface water [139]. In their work, N. Couffin et al. studied the application of vacuum membrane distillation (VMD) in the separation of TCE [140]. Flat PVDF membranes were investigated for this purpose. The removal of HOVs by VMD showed low energy demands. For a similar application, hollow fibers of polypropylene (PP) were studied by A. M. Urtiaga et al. for the removal of chloroform from water by VMD using a modeling approach [141]. The performance was compared to the pervaporation process using the PDMS membranes and applying the same module geometry for the VMD. Results showed that pervaporation could offer better chloroform selectivity.

The separation of ammonia by membrane distillation (MD) could have wide applications in the treatment of wastewater and biogas plant effluents. Besides, the recovery of ammonia by MD can be employed in the production of ammonia-based fertilizers. A.Zarebska et al. studied the separation of ammonia from pig manure by MD using PP and PTFE membranes [99]. The feed side stream was the solution of raw swine manure while the permeate side stream was an acidic strip solution. This configuration used is similar to the DCMD combining stripping and absorption such that ammonia was stripped from the feed then permeated across the membrane and then was absorbed by the permeate side stream. The study in this work focused on fouling mitigation and it was claimed that MD could be a promising method for separating ammonia from animal wastes in case the appropriate feed pretreatment requirements were met. Another work regarding ammonia

removal by MD was performed by Q .He et al who studied the removal of ammonia from the biogas slurry by VMD [142]. According to this work, the feed pH and temperature played a great role in the obtained ammonia flux and selectivity since they have a significant effect on the ammonia equilibrium in the aqueous solution.

Other works investigated the employment of MD in the removal of dyes [26], oil [129], arsenic [131,143], glycerol [23], N-methyl-2-pyrrolidone (NMP) [59], boric acid [22] and radioactive isotopes [22,144–146] from wastewater. Results showed that MD could offer very high rejection. However, membrane fouling and in some cases, low flux were considered the main process challenges. Besides, some works in literature were concerned with process development and optimization for industrial wastewater treatment applications [27,45,147].

The integration of air gap membrane distillation (AGMD) to chemical pretreatment stages for the removal of tetra methyl ammonium hydroxide (TMAH) was studied by Imtisal-e- Noor et al. [27]. Economic analysis showed that the treatment of 20,000 m^3/year of the TMAH wastewater would require a specific cost of 16 \$/m^3. AGMD was also examined by E. U. Khan et al for recycling the rejected water from biogas production [148]. The membranes used in this study were flat PTFE membranes with polypropylene (PP) supports. The assessment of the techno-economic viability of integrating membrane distillation in the treatment of water rejected from biogas production was carried out by the same research group [147]. According to the conducted process development study, the reduction of the content of TS from 4.1% to 0.05% in the recirculated water could increase the biogas production by 45-50 %. Also, the cost per permeate was estimated to be around 5.6 €/m^3 for a rejected water feed temperature of 75-80°C. Another economic analysis regarding wastewater treatment by MD was conducted by A. Carrero-Parreno et al. [45]. This represented the first work that developed a multi-stage membrane distillation systems (MDS) mathematical model coupled with heat recovery for optimizing the treatment of shale gas-produced water. The economic study presented in this work considered DCMD using PTFE membranes. Economic analysis showed that for a feed containing TDS at a concentration in the range of 150-250 g/kg, the treatment cost would be up to 23 \$/m^3. However, it is worth noting that membrane distillation alone would encounter some challenges like fouling and pore wetting by the shale gas wastewater. The application of DCMD in wastewater treatment was also investigated by C.F. Couto et al. for the removal of pharmaceutical active compounds (PhACs) [21]. In this work, the effect of the concentration of humic acid (HA) on the separation performance was studied. HA was a foulant model representing the various natural organic matter (NOM). An 8 % decline in the flux was observed due to the fouling nature of the HA. However, according to a similar study performed by D. Amaya-Vias et al., the presence of HA showed no fouling or membrane damage [149].

1.7.3. Concentration of Solutions

The concentration of various aqueous solutions offers the advantages of easy and cheap product transportation and storage. Besides, the concentration of juices and syrups elongates the storage life due to the reduced water activity [150,151]. When compared to high-temperature evaporation, membrane distillation (MD) can offer the advantage of less energy consumption and better preservation of the aroma compounds [21,152]. Owing to that, MD can be applied in the beverage industry like in the production of high-quality wine, aroma recovery and concentration of juices [153].

The first publication regarding the concentration of sucrose aqueous solutions using the sweeping gas membrane distillation (SGMD) was presented by C. Cojocaru et al. [150] where modeling and experimental studies were employed in optimizing the operating conditions. A similar approach was followed by S. Al-Asheh et al. [154] and Y.-R. Chen et al. [19]. The performance of both VMD and SGMD was analyzed and compared by R. Bagger-Jørgensen et al. for aroma recovery in black currant juice [152]. Concentration by VMD was considered sufficient unlike the case of SGMD. This was attributed to the relatively low driving force of SGMD. Regarding the VMD, S. Bandini .et al investigated its application using PP membranes in concentrating must juice [153]. According to the results of this work, it was recommended to use reverse osmosis (RO) to concentrate the must solutions from 20 to 30°Brix and then use VMD to concentrate the residual to 50°Brix. The idea of integrating MD with other separation methods was also presented in the work of C.A. Quist-Jensen [151] who studied the concentration of orange juice by integrating ultrafiltration and direct contact membrane distillation (UF/DCMD). Results confirmed the preservation of the important nutrients by MD.

It is worth mentioning the possible application of osmotic membrane distillation (OMD) in the field of solutions concentration [20,155–158]. OMD is a non-thermal membrane distillation variant and is sometimes referred to as osmotic distillation (OD). The feed and the permeate side streams are liquid solutions present at the same temperature, but they differ in concentration [159]. Osmotic membrane distillation can be applied for concentrating thermo-sensible solutions since it can work at room temperature and pressure which enables it from preserving the important nutritional characteristics. OMD has wide applications like in the concentration of milk, fruit and vegetable juices, instant tea and coffee [155].

1.7.4. Other Applications

Other applications of MD could include biofuel processing, crystallization and dehumidification of desiccants. The removal of VOCS by MD can have an important role in biofuel processing which could present an auspicious solution to the growing energy demand that is expected to rise by 48% between the years 2012 and 2040 [160]. For example, MD can be applied in the water-ethanol azeotrope separation required for the dewatering of bioethanol fuel [161,162]. M. M. A. Shirazi et

al. studied the integration of SGMD to a bioethanol plant [161]. Flat PTFE membranes were utilized in this study. According to their results, increasing the feed temperature and flow rate had the most impact on the permeation flux due to the improvements in the driving force and the reduction in the concentration polarization. The application of AGMD in the separation of bioethanol from algal-based fermentation broths was evaluated by P. Loulergue et al. [162] where AGMD was claimed to be an efficient separation technique for such a process. However, A. Kujawska et al. [163] obtained relatively low fluxes suggesting limitations of the AGMD in the removal of ethanol, butanol and acetone.

Membrane crystallization (MCr) is an extension of membrane distillation and it aims at concentrating solutions to ranges above the supersaturation. This in turn, promotes nucleation and crystallization rates [33,164]. This combination between membrane distillation and crystallization can also be referred to as membrane distillation crystallization (MDC) or membrane assisted crystallization (MAC). It can be used to recover valuable salts from the effluents of the processed brines and desalination processes [111]. The first MDC investigation using real industrial wastewater was performed by J. Kim et al. [165]. This work aimed to assess the feasibility of employing MD in the recovery of water and valuable minerals from shale gas produced water (SGPW). The minerals recovery reached 84 %. The feasibility of applying direct contact membrane distillation (DCMD) in recovering the valuable minerals from SGPW was demonstrated in this work. However, the applicability of such technology required an investigated unit with ensuring effective scale collection and control. DCMD was also studied for recovering water from sodium sulfate (Na_2SO_4) aqueous solutions [164] where stable performance and successful Na_2SO_4 crystallization were achieved. The employment of DCMD and vacuum membrane distillation (VMD) using ceramic membranes in the crystallization of lithium chloride (LiCl) and NaCl was investigated by C.-C. Ko [33] The obtained permeate flux in case of VMD was more than the double that obtained in case of DCMD due to the higher mass transfer driving force in VMD. The feasibility of applying sweeping gas membrane distillation (SGMD) in membrane assisted crystallization (MAC) was studied by F. Anisi et al. [111]. This was aimed at investigating the potential of concentrating the aqueous solution of L-ascorbic acid (vitamin C) to the degree of supersaturation to aid the crystallization process. The feed temperature and sweeping gas flow rate were the most significant factors affecting the SGMD flux.

The application of membrane contactors in CO_2 stripping can be considered an interesting topic where the operating principle is very similar to that of membrane distillation having the configuration of the SGMD process. The employment of membrane contactors in the stripping of CO_2 from monoethanolamine (MEA) was studied by S. Koonaphapdeelert et al. [166]. In their work, nitrogen was used as the stripping agent (sweeping gas). Hydrophobic surface-modified hollow fiber alumina membranes were used.

Air dehumidification has wide applications in air conditioning and natural gas processing [28]. In air dehumidification by liquid desiccants, the liquid is brought into contact with humid air in an absorber where the moisture in the air is absorbed by the liquid desiccant. Accordingly, the liquid desiccant air-conditioning system removes latent and sensible heats from the humid air. This process is more environmentally friendly than conventional air conditioning systems [29]. This is

due to the fact that liquid desiccant requires no refrigerants and fewer energy requirements. The most commonly used liquid desiccants in the industry are glycols and halide solutions like those containing lithium chloride (LiCl), lithium bromide (LiBr), calcium chloride($CaCl_2$), tri ethylene glycol and other salts. The moisture removal capacity is promoted by cooling and dehumidifying the liquid desiccant used in the absorption step [30]. Therefore, the dehumidification of the spent (humidified) liquid desiccant is necessary for its regeneration in order to be reused again in moisture absorption. Packed columns can be used for the regeneration step. However, the entrainment of the desiccant into the dehumidified conditioned air could engender detrimental consequences to human health and building structures and furniture [28]. Membrane distillation can be safely applied in the regeneration step of spent liquid desiccants to obtain freshwater and a dehumidified liquid desiccant [29,31]. R. Lefers et al. studied the application of vacuum membrane distillation (VMD) in liquid desiccant dehumidification [30]. Aqueous solutions of $CaCl_2$ and $MgCl_2$ represented the spent liquid desiccants. Results confirmed the feasibility of using VMD for regenerating the studied liquid desiccants and for obtaining fresh distilled water. J. Zhou et al. theoretically investigated the application of VMD in the regeneration of humidified liquid desiccants [31]. The model developed in this work was validated by comparing the simulated results to the corresponding experimental results from other works found in literature [30,167]. Modeled results suggested flow feed rates for high percentage removal of humidity. In another modeling study, the utilization of the air gap membrane distillation (AGMD) in regenerating the liquid desiccant $LiCl_2$ was examined by A. S. Rattner [32]. In this work, hypothetical values of membrane properties, device geometry and operating conditions were proposed based on the typical corresponding experimental works in literature. The modeled results showed less dehumidification capacity of MD than what is generally claimed in the other works in literature.

Other than water desalination objectives, details about the main studied applications of MD in literature are listed in Table (1.4).

Table (1.4) *Main works in literature for MD applications other than water desalination*

MD Type	Geometry	Membrane	Application	Operating Conditions	Total Flux (Kg/(m2.h))	Ref
DCMD	Tubular	PP d_p=0.2 µm δ=0.4 mm Ɛ=77.5 %	Concentration of black fruit currant juice	Feed: Currant juice (11°Brix) T_f=35°C V_f=100L/h T_p=15°C V_p=250L/h	1.8	[168]
SGMD	Flat	PTFE Ɛ=70 % d_p=0.22µm δ=175 µm	Concentration of glycerol	Feed: Glycerol (aq.) (1 % wt.) V_f=0.4 L/m T_f=65°C V_p=0.45 Nm^3/h	20.93	[23]
		PTFE d_p=0.45µm δ=178µm Ɛ=80 %	Concentration of sucrose solution	Feed: Sucrose (aq) C_f=223 g/L T_f=71°C v_f=0.15 m/s T_p=20°C v_p=2.1 m/s	3.88	[150]
		PTFE d_p=0.45µm δ=100µm Ɛ=70%	NH_3 separation from water	T_f=65°C V_f=250 mL/m C_f=100 mg/L of NH_3 T_p=T_{room} V_p=3L/m P_p=4 bar	10	[169]
		PTFE d_p=0.1µm δ=260µm	Recovery of volatile fruit juice aroma compounds	T_f=45°C V_f=400L/h T_p=27°C V_p=1.2 m^3/h P_p=1 atm	4.9	[152]
VMD				T_f=30°C V_f=500L/h ΔP=2500 Pa	21	
	Tubular	PP d_p=0.2µm	Butanol/water separation	Feed: Butanol (aq.) (1 wt %) T_f=T_{room} V_f=80L/h P_p=25 mbar	2.5	[170]
	Capillary				3.5	
	Flat	PTFE δ=50 µm d_p=0.22µm Ɛ=60-70 %	Ethanol/water separation	Feed: Ethanol(aq.) (5 % wt.) T_f=60°C V_f=50L/h P_p=92 kPa	24	[57]
	Hollow fibers	PP δ=0.05mm Ɛ=62%	Concentration of N-methyl-2-pyrrolidone	T_f=75°C X_f=0.02 NMP P_p=0.09 MPa	6.52	[59]
		PP d_p=0.18µm δ=0.86mm Ɛ=60%	Separation of boric acid from radioactive wastewater	C_f=100 g/L of boric acid T_f=70°C V_f=41.8 L/h P_p=0.97 atm	6	[22]
		PP Ɛ=60% d_p=0.18µm δ=0.63mm	Separation of Cs^+ from radioactive wastewater	T_f=70°C V_f=41.8 L/h C_f=10 mg/L of Cs^+ P_p=50.05 kPa	6.1	[145]
		PP Ɛ=60% d_p=0.18µm δ=0.86mm	Separation of Sr^{2+} from radioactive wastewater	T_f=70°C V_f=41.8 L/h C_f=10 mg/L of Sr^{2+} P_p=0.98 atm	6.7	[146]
		PP d_p=85 nm δ=50µm Ɛ=33%	NH_3 separation from water	Feed: Raw biogas slurry T_f=75°C V_f=60 mL/m C_f=2.5 g/L Total NH3 nitrogen P_p=10 kPa	1.45	[142]
		PP Ɛ=60% d_p=0.2 µm δ=0.125mm		T_f=50.4°C P_p=736 Pa V_f=250 mL/m C_f=218 mg/L of NH_3	1.1	[171]

1.8.Aim and Outline of This PhD Thesis

Membrane distillation (MD) is usually suggested in many works in literature as a promising technology for seawater desalination. However, most of the works and research dedicated to MD are limited to lab-scale characterization and investigation studies. In fact, this lack of details about the scale-up procedures and accurate economic analysis of MD processes has been one of the main challenges facing the implementation of this technology on an industrial scale. This has led to varying opinions about the attainable water production cost from desalination processes employing the MD technology. Therefore, the main objective of the presented PhD thesis is to investigate the employment of sweeping gas membrane distillation (SGMD) in seawater desalination on an industrial scale. The membranes used were tubular hydrophobic multi-layer titania membranes. The choice of ceramic membranes was based on the fact that they can offer a substitute to polymeric membranes which are commonly applied in MD. This is attributed to the higher chemical, thermal and mechanical stability possessed by ceramic membranes.

Indeed, the investigation of the module performance during SGMD lab-scale experiments was of vital importance before proceeding with process development and optimization procedures followed in this PhD thesis. In addition to that, the preliminary design of the desalination process necessitated the development of an adequate model that could enable the simulation of the SGMD separation unit incorporated in the overall process. Moreover, the characterization of the membrane morphological properties is deemed to be a prerequisite for SGMD modeling since the membrane morphological properties can play a significant role in the resulting membrane mass transfer coefficient. On that account, the strategy implemented in this thesis took place according to the following sequence.

- The characterization of the unknown or unconfirmed membrane morphological properties took place by gas permeation tests and modeling.
- These characterized morphological properties were used as inputs to a developed SGMD model.
- The module performance during SGMD at high liquid temperatures was investigated. This took place by the aid of lab-scale SGMD experiments of NaCl (aq.) feed coupled with the developed SGMD model.
- The developed SGMD model was used in simulating the SGMD unit in a proposed hypothetical sweater desalination process. Eventually, process development and optimization took place aiming at finding the optimum operating conditions and array of the membrane modules in the SGMD unit vessel.

The morphological characterization of the multi-layer hydrophobic ceramic membranes is discussed in Chapter (2). This was carried out by coupling experimental and modeled results of single gas permeation tests. The dusty gas model was adopted in the description of the mass transfer during the gas permeation tests due to the contributions of the Knudsen diffusion and viscous flow

mechanisms. Two modeling approaches were utilized. The first considered the morphological properties of each membrane layer. This method is referred to as the "layer-by-layer" method. The second approach was used to characterize the average membrane morphological properties regardless of the unique role played by each membrane layer in the membrane overall mass transfer resistance. The second approach is commonly applied in literature. The SGMD mass transfer resistance was modeled according to the characterized morphological properties obtained from each approach. The description of the materials used, the experimental and modeling approaches are discussed in this chapter.

The investigation of the module performance was implemented by experimental and modeling studies. This was discussed in Chapter (3). Lab-scale SGMD experiments were conducted using NaCl (aq.) feed at relatively high liquid temperatures. The transmembrane mass transfer was modeled according to the contributions of the Knudsen and molecular diffusion mechanisms. The experimental results were compared to modeled results obtained on considering the role of the morphological properties of each membrane layer and were also compared to modeled results obtained on considering average morphological properties of the membrane. The developed SGMD model was employed for further simulations to estimate the effect of the operating conditions on the flux and to predict the role played by each of the molecular and Knudsen diffusion mechanisms.

Even though the main thesis objective is related to seawater desalination, SGMD modeling of ethanol (aq.) was performed in Chapter (4). This was based on the possible application of SGMD in the removal of volatile organic compounds (VOCs) from aqueous solutions. The Maxwell-Stefan modeling approach was employed in the description of the transmembrane mass transfer of water and ethanol. The modeling results were used in estimating the effect of the operating conditions and the total SGMD unit length on the flux and selectivity.

Chapter (5) presents the main thesis objective. In this chapter, a hypothetical desalination process is proposed incorporating SGMD as the separation unit. Preliminary process design was coupled with the SGMD model in order to simulate the overall process performance. Non-rigorous cost estimation was also carried out. Process development and optimization were based on the water production cost (WPC). The main operating conditions and design parameters were optimized. In addition to that, the results attained by using the "single-pass" configuration were compared to those attained on using the "feed and bleed" configuration. The process limitations, the followed approach of process development, the optimization procedures and the obtained results are all discussed in Chapter (5).

Eventually, the main conclusions drawn from the entire thesis are presented in Chapter (6) to get an overview of the work done.

List of Symbols

Latin Letters	
C	Molar Concentration
D_i^K	Knudsen diffusion of component i
D_{ih}	Molecular diffusion of component i in a binary mixture (i/h)
d_p	Pore diameter
J	Molar flux
Kn	Knudsen number
K_B	Boltzmann's constant
LEP	Liquid entry pressure
l^{free}	Mean free path
M	Molecular weight
P	Pressure
r	Pore radius
R_g	Universal gas constant
T	Temperature
y	Molar fraction in vapor phase
z	Direction of diffusion
Greek Letters	
β	Geometric factor
γ_l	Surface tension of the liquid at the liquid/air interface
δ	Thickness
ε	Porosity
θ	Contact angle
μ	Dynamic viscosity
σ	Collision diameter
τ	Tortuosity
Subscripts and Superscripts	
e	Effective
Eq	Equivalent
D	Diffusive

f	Feed
fm	Feed/membrane interface
h	Component h
i	Component i
l	Liquid
max	Maximum
min	Minimum
p	Permeate
pm	Permeate/membrane interface
V	Viscous

[This page intentionally left blank]

Chapter Two

Morphological Characterization of Multilayer Hydrophobic Ceramic Membranes for Membrane Distillation

2.1.Introduction

Owing to the important role played by the membrane morphological properties in the overall performance of the membrane distillation (MD) process, several works in literature were dedicated to the characterization and optimization of the membrane morphological properties [19,33–39]. Besides, modeling of MD processes can represent an important tool in module investigation and performance improvement [1]. Prior to MD modeling, the main morphological properties of the membrane like the porosity, pore size, tortuosity factor and thickness should be well characterized. This is due to the fact that these properties affect the simulated transmembrane mass and heat transfer during MD processes at given operating conditions [46].

Regarding the most commonly applied characterization techniques of the membrane morphological properties, the porosity of the membrane can be simply estimated by the Archimedian method while microscopic techniques like the scanning electronic microscopy (SEM) can be used to analyze the surface microstructure and important morphological properties of the membrane [1]. The pore size distribution of the membrane can be obtained by the bubble point test, the mercury intrusion porosimetry or the liquid displacement technique [1,4]. In addition to that, gas permeation tests could be employed in the estimation of important morphological properties and mass transfer parameters [46–51].

Recently, there has been a growing interest among the scientific community in the application of ceramic membranes in MD [91,94,130,132], due to their high thermal and chemical stability; such materials might give greater morphological stability than polymeric membranes over time. As it has been mentioned in Chapter (1), fluoroalkylsilanes are usually applied in the hydrophobization of the ceramic membranes employed for MD applications [42,89,137]. Accordingly, hydrophobic titania membranes were studied in this thesis for sweeping gas membrane distillation (SGMD) applications. The studied membranes are composed of 4 layers that possess different morphological properties. The main membranes' morphological parameters like pore size, porosity, tortuosity, thickness were reported by the manufacturer except for some values that were either unconfirmed or unknown. Besides, these parameters are not adjustable, since they can be determined independently of flux measurements in MD operations.

In the current chapter, the main focus is on the characterization of the unconfirmed and unknown morphological properties of the membrane. These characterized properties were then used as inputs to the SGMD model that was applied to estimate the transmembrane mass transfer resistance during SGMD in case of the permeation of water vapor across air-filled pores. This was done by considering the morphological properties of each layer and the consequent contribution of each layer. This can be referred to as the "layer-by-layer" (LBL) method. The transmembrane mass transfer was also estimated according to the average membrane morphological properties estimated

by the conventional characterization method in literature [1,36,172] which can be termed as the "average membrane morphology" (AMM).

The morphological characterization presented in the current chapter is based on coupling experiments with modeling for single gas permeation across the membrane. The model used was the dusty gas model (DGM) discussed in Chapter (1) involving the contributions of the viscous (Poiseuille) flow and Knudsen diffusion mechanisms. The ordinary diffusion was not considered due to the presence of single gas inside the membrane pores which resulted in the absence of concentration gradient across the membrane. This characterization approach can be considered as a continuation of the characterization procedures followed by the manufacturer [46]. Typically, in symmetric polymeric membranes, the morphological properties can be estimated by elaborating gas permeation data according to the dusty gas model (DGM) equations, whereas for polymeric asymmetric membranes the same method can be used to get information about the skin morphology [1]. An improved method was developed by J. Kong et al. for asymmetric PVDF membranes [172]. This method was later applied by the same authors for the characterization of ceramic membranes as well [36,173], to estimate averaged parameters of the entire membrane. Only M. Weyd et al. [46] performed the characterization of multilayer membranes according to the "layer-by-layer" (LBL) technique, which allowed them to get morphological parameters of every single layer by the elaboration of gas permeation data according to the DGM.

2.2.Materials and Methods

2.2.1. Membranes and Modules

The studied membranes are hydrophobic carbon-based titania membranes that had been manufactured by the Fraunhofer Institute for Ceramic Technologies and Systems (IKTS, Hermsdorf, Germany). The membranes were delivered in the form of single channels and capillary bundles. The capillary bundles had the shell and tube configuration with uniformly arranged capillaries and unbaffled shell. The schemes of the single channel, capillary bundle, housing and the multi-layer membrane are shown in Fig (2.1). The uncoated samples represent the basic ceramic membranes without the hydrophobic coating. They are the same for both, the single channels and the capillary bundles. However, the only difference between the membranes used in single channels and those used in capillary bundles is the thickness of the support layer. This is based on the information provided by the manufacturer. The uncoated membrane is composed of four layers having different thicknesses and other different morphological properties.

The "support" represents the outer layer of the lumen (tube) and it possesses a pore size of 4500 nm. The top layer located at the vicinity of the lumen side is referred to as "layer 3" and its nominal pore size is 100 nm while its thickness is 10 µm. The "support" layer is followed by intermediate layers that are referred to as "layer 1" and "layer 2" having thickness values of 30 µm each and nominal pore size values of 800 nm and 250 nm respectively.

The manufacturing technique of the uncoated membranes was described by the manufacturer [174]. Besides, SEM pictures and the morphological characterization of each layer of the studied membranes were presented by M.Weyd et al. [46]. The detailed description of the manufacture of the capillaries and bundles was also provided by the manufacturer in addition to the followed procedures of the hydrophobization process [175]. Two subsequent techniques were followed such that the "uncoated "membrane is carbon-coated by the deposition and pyrolysis of a polymeric precursor. This is patented in [176] and well documented in [177,178]. After that, surface grafting of the membrane surface took place by fluoroalchylsilane (FAS, tridecafluoro-1,1,2,2 tetra-hydro-octyl-trichloro-oxysilane). This followed the procedures mentioned in the patent of I.Voigt et al. [179]. The ends of both, the coated and uncoated membranes were refined by epoxy resin endcaps in order to avoid leakage potential of liquids or gases from the lumen side towards the shell side through the inlet section annulus. The same epoxy resin was also employed to seal the capillaries on the ceramic plates of the bundle to avoid permeation across the ceramic plates. Efficient hydrophobic coating could prevent pore wetting and offer immobilized liquid-vapor interface at the pore entrance of "layer 3". The coating on "layer 3" represents the actual barrier against wetting during membrane distillation processes.

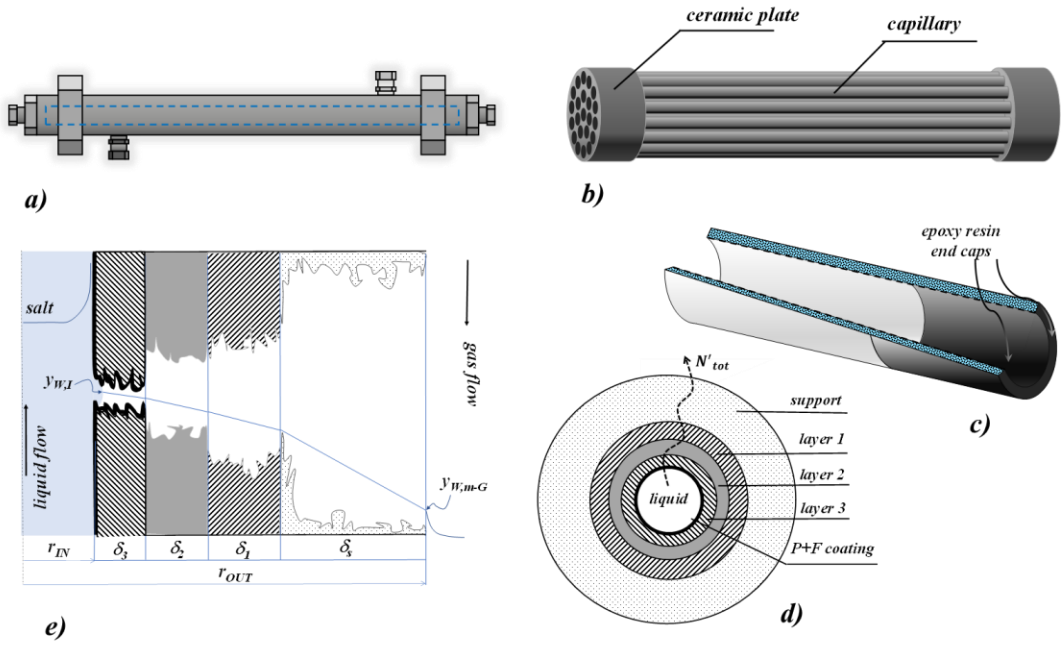

Figure(2.1) *Scheme of membrane and module.* ***(a)*** *Housing;* ***(b)*** *Capillary bundle;* ***(c)*** *Section of a cylindrical membrane;* ***(d)*** *Multilayer membrane cross-section;* ***(e)*** *Details of the radial section of the coated membrane showing the water composition profiles, with reference to SGMD of a salt-water solution.* [47]

2.2.1.1.Single Channels

The studied membranes have a cylindrical geometry and are composed of four layers indicated by *(j)* such that (*j*) can be noted as (1) or (2) or (3) or (s) when referring to "layer 1" or "layer 2" or "layer 3" or the "support" respectively. Each layer (*j*) is characterized by its corresponding pore diameter (dp_j), thickness (δ_j) and porosity-tortuosity ratio ($(\varepsilon/\tau)_j$).

The single channels that were studied possessed the following geometric characteristics. They had an inner diameter and outer diameter of 7 mm and 10 mm respectively with a total length of 250 mm. On excluding the length of the end caps, the effective length of the single channel is 224 mm and its effective inner area A_{IN} is 49.2 cm^2. The characterization involved different kinds of samples which can be referred to as follows.

- The samples representing the uncoated membrane containing only the "support" layer are referred to as "Support A" and "Support B".
- The samples representing the basic uncoated membranes composed of the four layers are referred to as "S-DA" and "S-DB".
- The samples representing the coated membranes composed of the four layers are referred to as "S2515" and "S2516".

The manufacturer provided the complete information of the morphological parameters of each layer of the uncoated single channels with the exception of "layer 3". This can be found in Table (2.1) in the form of nominal values. These values were obtained by measurement procedures described by the manufacturer [46] such that scanning electron microscope (SEM) was applied to estimate the thickness of each layer while mercury porosimeter was used to predict the corresponding volume porosity.

The combination of single gas permeation tests and modeling was implemented by the manufacturer to estimate the tortuosity factor of each membrane layer [46]. The model used was the dusty gas model (DGM) considering the transmembrane gas flow to be due to the contributions of the viscous flow and Knudsen diffusion. First, the "support" layer was solely used in the gas permeation tests. By combining experimental and modeled permeance results of the support layer, it was possible to estimate its tortuosity factor. Then the intermediate layer "layer 1" was deposited on the support. Single gas permeation experiments and modeling were performed again but this time, on the membrane composed of the "support" and "layer 1" together. This allowed the estimation of the tortuosity factor of "layer 1". The same concept was repeated in order to predict the tortuosity factors of "layer 2" and then of "layer 3". It is worth noting that this kind of characterization using the "layer-by-layer" method allowed the characterization of all the connected open pores involved in the gas transfer across the four layers of the membranes. Therefore, in order to interpret the results precisely, it is important to observe that the values of the tortuosity are not

absolute. This is because they depend on the values of volume porosity and pore diameter applied in the modeling equations of the DGM. Therefore, the porosity-tortuosity ratio (ε/τ) is the value that is given by the elaboration technique rather than the evaluation of the absolute porosity and the absolute tortuosity. This can explain the reason of reporting the data in the form of (ε/τ) in Table (2.1)

The hydrophobization ensures the immobilization of the liquid/vapor interface at the pore entrance at the liquid/membrane interface. This principle is demonstrated in Fig (2.1e) representing pores that are not flooded by the liquid feed. Despite the fact that the hydrophobic coating was distributed along the surface of all the pores, only the coating located at the inner layer ("layer 3") of the membrane is deemed to be effective. "Layer 3" is the layer that is to be at the vicinity of the liquid feed during MD processes.

Table 2.1 *Morphological parameters of single channel (Nominal values provided by the manufacturer)*

Membrane Layer	δ_j *(µm)*	dp_j *(nm)*	ε_j	$(\varepsilon/\tau)_j$
support	1500	4500	0.33	0.11
layer 1	30	800	0.34	0.20
layer 2	30	250	0.39	0.34
layer 3	10	100	---	---

2.2.1.2.Capillary Bundles

The studied capillary bundles possessed geometric characteristics that are reported in Table (2.2). It is important to note that although, the manufacturer provided the necessary morphological parameters of the "uncoated" bundles that correspond to the single-channels (see Table 2.1-case a)), the support thickness was not given by the manufacturer. Besides, both the pore diameter and the porosity-tortuosity ratio of "layer 3" in case of bundles were not provided by the manufacturer. In this PhD thesis, single gas permeation experiments and modeling were applied to estimate these morphological properties that were not provided by the manufacturer.

Table 2.2 *Characteristics of "coated" capillary bundles*

Membrane fiber			***Bundle and vessel***			
code	$\delta_{support}$ *(μm)*	*ID/OD (mm)*	N_f *(fibers)*	*L (cm)*	A_{IN} *(cm^2)*	*shell OD (cm)*
B2754	750	1.56 /3.20	37	20	363	3.60
B2755						
B2756						
B2758	580	1.90/3.20	22	20	263	2.50
B2888	750	1.90/3.54	37	20	442	3.60

N_f :number of fibers, ID:inner diameter, OD:outer diameter, L: length of module

2.2.2. Gas Permeation Experimental Tests

Following the morphological characterization concept performed by the manufacturer, traditional equipment was used in this PhD thesis during gas permeation tests [1,172] as shown in Fig (2.2). Dry air was allowed to pass across the membrane and the bundles in a dead-end mode by means of transmembrane total pressure difference. The permeation occurred in the "straight mode" for all the samples such that the air was introduced in the lumen side and then it permeated across the membrane towards the shell side. Some samples also were tested in the "reverse mode" such that the air passed from the shell side towards the lumen side. Gas permeation tests took place at room temperature (20°C-24°C). The total pressure difference across the membrane (ΔP_{tot}) during the tests was in the range of 0.1-1.2 bar. This corresponded to average pressure (P_{av}) values ranging from 1 to 7 bar. The average pressure (P_{av}) represented the arithmetic mean of the inlet and outlet gas pressure values.

Two flowmeters were available. The choice of the manometer that was to be used depended on the range of gas volumetric flowrates. Flowmeter FI-1 which was located upstream the membrane was used in the case of flow rates higher than 1200 STP m^3/h while flowmeter FI-2 was used downstream the membrane in the case of flow rates ranging from 400 to 1200 STP m^3/h. The temperatures of the inlet and outlet gas streams were also measured by temperature indicators TI-1 and TI-2 respectively.

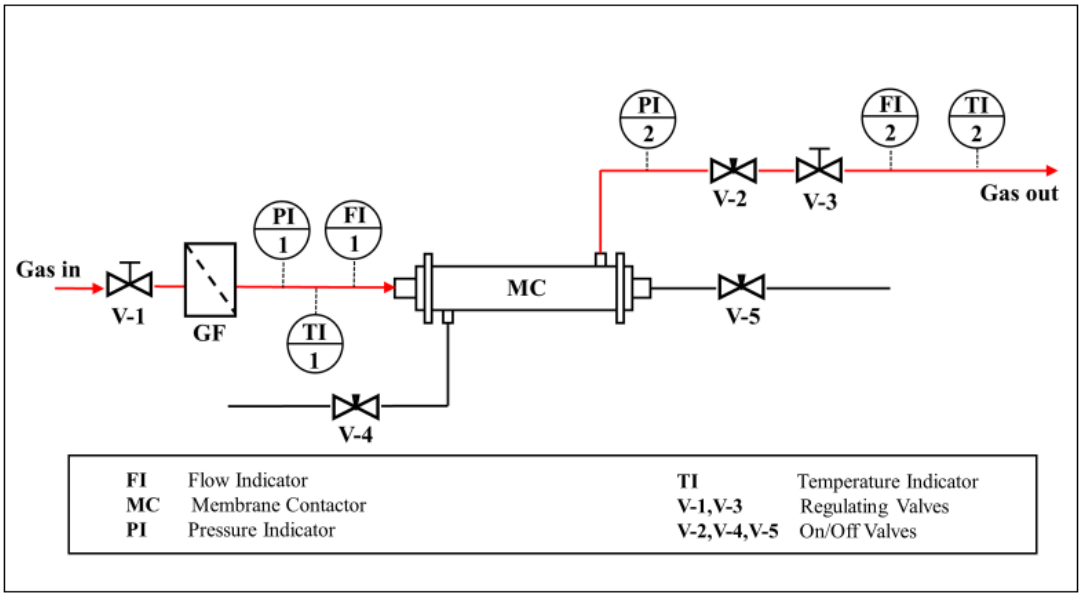

Figure (2.2) *Equipment set-up for gas permeation experimental tests in straight mode*

The protocol of measurement required a preliminary drying of the virgin sample in an oven at 60°C for 4 hours. This was followed by a stabilization step in which the sample was kept, for at least 1 hour, at a transmembrane pressure difference of 1 bar, with the atmospheric pressure downstream the membrane. The gas permeation equipment shown in Fig (2.2) was designed to measure volumetric flow rates of air across the membranes. Different mean (average) pressure values and transmembrane pressure gradients were applied during the tests. Valve V-1 was connected to a dry air line (maximum pressure available was 7 bar). Valves V-4 and V-5 were kept closed during all the trials while valve V-2 was kept open. Various combinations of pressure difference values across the membrane were obtained by regulating the openings of valves V-1 and V-3. These values were calculated according to the inlet and outlet pressure values that were measured by the manometers PI-1 and PI-2 respectively. For each value of P_{av}, a stabilization time of at least 10 minutes was required after the regulation of the setpoint. Three or more subsequent measurements of the volumetric flow rate were performed. Then the arithmetic mean of the measured values was considered as the final value.

Eventually, for air permeating across the membrane at a molar flow rate N_{air}, the experimental membrane permeance results were elaborated versus the values of the average pressure across the membrane P_{av}. The experimental membrane permeance was calculated by Eq (2.1) according to the total transmembrane pressure difference ΔP_{tot} and was based on the membrane inner interfacial area A_{IN}. Aiming at comparing the different samples that possessed different interfacial areas, the permeance was reported with reference to the inner area of each sample.

$$permeance = \frac{N_{air}}{A_{IN}\Delta P_{tot}} \tag{2.1}$$

2.3.Theoretical Premises for Discussion of Results

2.3.1. Diffusive Mass Transport in Sweeping Gas Membrane Distillation

In order to understand the "results and discussion" section, some theoretical premises are necessary. Mass transport in MD across a multilayer cylindrical membrane is considered, in which the driving force is represented by a concentration gradient across the membrane. The scheme and notation of Fig(2.1e) are used for the development of the following equations; in that case, the concentration gradient is fulfilled by using a sweeping gas in the permeate side [1,4]. The considered case refers to that of aqueous solutions containing only one volatile compound (as it is, for example, the simple case of sodium chloride-water solutions with air as the sweeping gas stream). However, the same kind of composition profile across the membrane (shown in Fig (2.1e)) can be expected in other MD operations, such as direct contact MD and/or air gap MD and/or osmotic distillation [1,4].

Mass transfer across the membrane during sweeping gas membrane distillation (SGMD) is represented by the transfer of water vapor across four cylindrical layers containing a stagnant gas phase. The case of molecular diffusion across a stagnant gas under steady-state conditions is well known in literature [180]. In the case of macroporous membranes, those equations require some modifications in order to consider the possible different contributions to the resultant diffusive mechanism, as well as of the number of pores existing in the cylindrical wall of the membrane.

Although molecular diffusion is the main mechanism, owing to the rather high pore sizes, the contribution of Knudsen diffusion can be accounted as well and included in an equivalent diffusivity D_{Weq}, according to the Bosanquet equation [181], as represented by Eq(2.2). The Knudsen diffusivity $D_{W,Kn,j}$ depends on the average pore diameter and the average temperature existing in the j-layer.

$$\frac{1}{D_{Weq,j}} = \frac{1}{D_{WG}} + \frac{1}{D_{W,Kn,j}} \;; \quad D_{W,Kn,j} = \frac{d_{pj}}{3}\sqrt{\frac{8R_gT}{\pi M_W}} \tag{2.2}$$

R_g and M_W represent the universal gas constant and the molecular weight, respectively. D_{WG} is the molecular diffusion of water in the gas phase, which should be calculated at the temperature and pressure existing in the *j*-layer.

The number of pores per unit length N'_p is included in the volume porosity for layer j (ε_j) which generally depends on the radial coordinate. It can be considered as an average value, according to the relationships (2.3), which are written referring to the case of cylindrical pores of equal diameter, assuming the logarithmic mean surface A_{LM} as average interfacial area.

$$\varepsilon_j(r) = \varepsilon_{av} = \frac{V_{void}}{V_{tot}} = \frac{N_p \pi d_{pj}^2 \times \delta_j}{4 A_{LM,j} \times \delta_j} = \frac{N_p d_{pj}^2}{8 r_{LM,j} L} = \frac{N'_p d_{pj}^2}{8 r_{LM,j}} \tag{2.3}$$

The general equation describing the total molar flow per unit length across a single membrane layer (N'_{tot}) is then represented by Eq (2.4), in which the mass transfer coefficient of water in the j-layer of the membrane k_{Wj} is defined straightforwardly, considering the volume porosity and the pore tortuosity.

$$N'_{tot} = \frac{2\pi\varepsilon_j c_j D_{Weq,j}}{\tau_j \times ln \dfrac{r_{OUT,j}}{r_{IN,j}}} ln\left(\frac{1-y_{W,r_{OUT,j}}}{1-y_{W,r_{IN,j}}}\right) = k_{Wj} c_j 2\pi r_{LM,j} ln\left(\frac{1-y_{W,r_{OUT,j}}}{1-y_{W,r_{IN,j}}}\right) \;\; ; \;\; k_{Wj} = \left(\frac{\varepsilon}{\tau}\right)_j \frac{D_{Weq,j}}{\delta_j} \tag{2.4}$$

$r_{IN,j}$ and $r_{OUT,j}$ represent the inner and outer radii of the layer (*j*), c_j is the molar concentration of the gas phase inside the layer and *(y)* is the mole fraction. In case of a multilayer membrane, under steady-state conditions, by using Eq (2.4) it is possible to combine the mass transfer coefficients of each layer to obtain the mass transfer coefficient of the membrane k_{Wm}; with reference to the scheme and notation of Fig (2.1e), Eq (2.5) can be finally derived.

$$\frac{N'_{tot}}{k_{Wm} c_m 2\pi r_{LM,m}} = ln\left(\frac{1-y_{W,m-G}}{1-y_{W,I}}\right) \;\; ; \;\; \frac{1}{k_{Wm} c_m 2\pi r_{LM,m}} = \sum_{j=1}^{3,s} \frac{1}{k_{Wj} c_j 2\pi r_{LM,j}} \tag{2.5}$$

Eq (2.5) does not contain adjustable parameters depending on the process type nor on the process fluids; the morphological parameters of each layer can be determined by independent measurements, as made in the "layer-by-layer" method by M. Weyd et al. [46], for instance. When the parameters are known, Eq (2.5) can be used to predict total flux across the membrane, to simulate module and process performances at any operative conditions of temperature, pressure and composition, once the mole fraction of water is related to the corresponding bulk conditions.

2.3.2. Pressure-Driven Gas Transport in Macro-Porous Membranes

Single gas permeation across porous solids is typically due to the contribution of three main mechanisms [182]: a viscous motion according to Poiseuille flow, the Knudsen diffusion and the so-called slip flow regime. Often, as an alternative to that model, the Dusty Gas Model (DGM) [102] is used considering only the viscous and Knudsen contributions. The DGM approach was applied in the current chapter for describing the single gas permeation across the membranes. As the work in this PhD thesis continues and completes the morphological characterization started by the manufacturer [46], it is mandatory to apply the same equations previously used, since all the morphological parameters (reported in Table (2.1) as nominal ones) are related to each other and therefore they should be used consistently. A summary of the equations used in this work is reported in the following (schemes and notation of Fig (2.1) are used). At a generic axial section of a layer j of a cylindrical membrane, the steady-state gas flow rate of component (*i*) across the layer per unit length (N_i'), under a constant pressure difference ΔP_j , can be expressed as reported in Eq (2.6a).

$$N_i' = \alpha_{ij}\, 2\pi r_{LM,j}\, \Delta P_j \tag{2.6a}$$

$$\alpha_{ij} = \left(\frac{\varepsilon}{\tau\delta}\right)_j \left[a_{ij} P_{av,j} + c_{ij}\right] = \left(\frac{\varepsilon}{\tau\delta}\right)_j \left[\frac{d_{pj}^2}{32\eta_G R_g T_j} P_{av,j} + \frac{4}{3}\frac{d_{pj}}{\sqrt{2\pi R_g T_j M_i}}\right]$$

$$P_{av,j} = \frac{P_{IN,j} + P_{OUT,j}}{2}; \quad \Delta P_j = P_{IN,j} - P_{OUT,j}$$

in which α_{ij} is the permeance of component *i* across the *j*-layer; $P_{IN,j}$ and $P_{OUT,j}$ are the inlet and outlet pressures, respectively, in the *j*-layer; a_{ij} and c_{ij} are coefficients representing the viscous and Knudsen diffusion contributions, respectively; η_G is the dynamic viscosity of the gas. In the case in which the parameters can be assumed as constant values along the membrane effective length *L* (or as average values along *L*), the total gas flow rate across the layer can be written as:

$$N_i = \alpha_{ij}\, 2\pi r_{LM,j}\, L\, \Delta P_j = \alpha_{ij}\, A_{LM,j}\, \Delta P_j \tag{2.6b}$$

Apparently, the permeance of each layer depends on the morphological parameters of that layer, the gas properties and the operative conditions. Combining the mass transfer resistances of all the layers, the overall membrane permeance (α_{im}) of the permeating component *i* can be expressed by Eq (2.7).

$$N_i = \alpha_{im}\, A_{LM,m}\, \Delta P_{tot} \Leftrightarrow N_i \left[\sum_{j=1}^{3,s} \frac{1}{\alpha_{ij} A_{LM,j}}\right] = \Delta P_{tot} \tag{2.7}$$

$$\frac{1}{\alpha_{im} A_{LM,m}} = \sum_{j=1}^{3,s} \frac{1}{\alpha_{ij} A_{LM,j}}; \quad \Delta P_{tot} = \sum_{j=1}^{3,s} \Delta P_j = P_{IN,3} - P_{OUT,s}$$

It is important to observe that the porosity parameter of each layer, appearing in Eq (2.6a), corresponds to the same volume porosity defined in Eq (2.3).In the case of a 4-layer membrane, as it is the case of this work, Eq (2.6a,2.6b) represent a set of equations which allow to calculate the gas molar flow and the pressures along each layer, if the operative conditions of temperature and of $P_{IN,3}$ and $P_{OUT,s}$ (that is of ΔP_{tot}) are given in addition to knowing the values of the morphological parameters of each layer. The permeance of each single layer, as well as the total membrane permeance, can be finally estimated straightforwardly. On the other hand, Eq (2.6-2.7) can be used also to calculate the unknown morphological parameters of a layer, by fitting the experimental results of total permeance, assuming that the morphological parameters of all the other layers are known. This procedure is exactly the one used by M. Weyd et al. [46] to calculate the tortuosity factors of the "support" and of the "layers 1 and 2" of the "uncoated" single channels, and it will be used also in this work to estimate the morphological properties of the "layer 3", both for uncoated and for coated samples.

The results can then be compared to those obtained following the usual protocols used for polymeric membranes [1,36,172], according to which average values of the porosity-tortuosity ratio $(\varepsilon/\tau)_m$ and of the average pore diameter d_{pm} are calculated by fitting the experimental results of permeance over the entire membrane. In that case, referring to the notation of this work, Eq (2.8) represents the overall membrane permeance as a function of the average pressure across the membrane, according to the DGM premises.

$$\alpha_{im} = \frac{N_i}{A_{LM,m}\ \Delta P_{tot}} = \left(\frac{\varepsilon}{\tau \delta_{tot}} \right)_m \left[a_{im} P_{av} + c_{im} \right] \tag{2.8}$$

$$a_{im} = \frac{d_{pm}^2}{32 \eta_G R_g T_{av,m}} \quad ; \quad c_{im} = \frac{4}{3} \frac{d_{pm}}{\sqrt{2 \pi R_g T_{av,m} M_i}}$$

$$\Delta P_{tot} = P_{IN} - P_{OUT} \ ; \ P_{av} = \frac{P_{IN} + P_{OUT}}{2} \ ; \ \delta_{tot} = \sum_{j=1}^{3,s} \delta_j$$

It is self-evident that Eq (2.8) predicts a linear behavior of the total membrane permeance with the average pressure existing across the overall membrane; the parameters can be estimated according to a very simple fitting procedure which accounts for the slope and the intercept of the interpolating straight line.

2.4.Results and Discussion

2.4.1. Gas Permeation

2.4.1.1.Single Channels

The Air permeance experimental data, based on the inner area of the membrane sample as defined by Eq (2.1) are shown in Fig (2.3), for different kinds of single channels, as a function of the average pressure across the membrane. The comparison between the permeance of the "uncoated support" (single layer) and the overall permeance of the "uncoated single channels" (4-layered membrane) is shown in Fig (2.3a). It can be observed that the permeance of the "support" is nearly five to ten times greater than the corresponding values for the uncoated single channels. This can be attributed to the relatively large pore size possessed by the "support layer". Fig (2.3b) compares the permeance of the "uncoated" samples with the corresponding values obtained for "coated" samples. On one side, no differences were observed between the results obtained by the "straight mode" and those obtained by the "reverse mode". This could be considered as an intrinsic confirmation that the measurement procedure was accepted for characterizing the "open pores". On the other side, there was a remarkable effect of the coating on the permeance. In fact, the coating resulted in a 50% reduction in the permeance of the "coated" samples with respect to the "uncoated" ones.

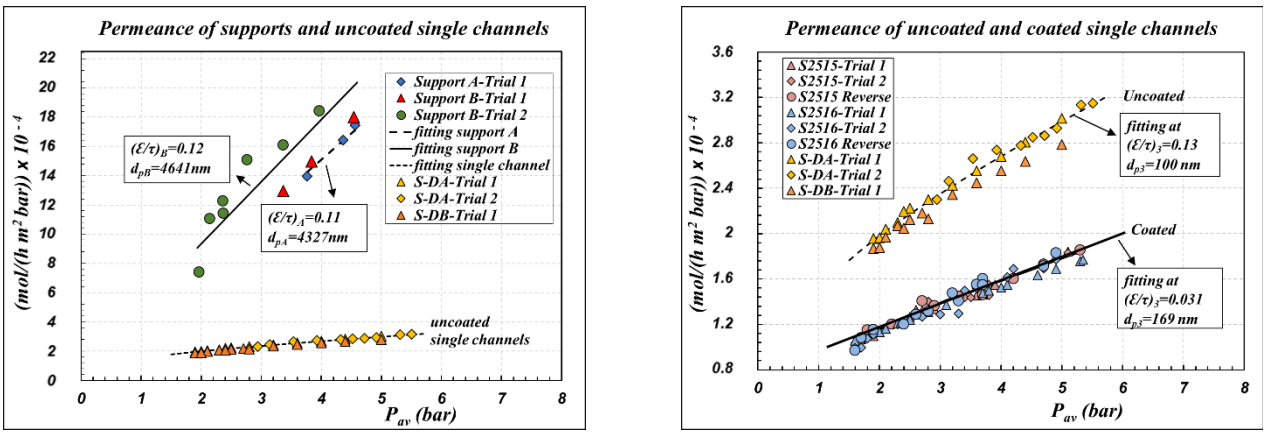

(a) *(b)*

Figure (2.3) *Gas (air) permeation experimental and modeled results at room temperature in case of: (a) Supports and uncoated single channels (b)Uncoated and coated single channels*

Both, the experimental permeance results (points) and modeled results (fitting lines) are shown in Fig (2.3). The modeled results were obtained by fitting the unknown morphological properties to the experimental results according to the layer-by-layer (LBL) method represented by the Eq(2.6-2.7). All the morphological parameters estimated are collected in Table (2.3) and compared with the corresponding nominal values given by the manufacturer; the quality of the fitting is expressed in terms of the corresponding percentage relative error (%RE) between the calculated and experimental data.

Obviously, the expected linear behavior of the DGM was obtained according to the experimental and modeled results in case of both, the uncoated and coated samples. This indicated that the model premises had been fulfilled. Modeling results showed that there was a substantial reconfirmation of the nominal values of the "support". Regarding "layer 3" of the uncoated samples, its porosity-tortuosity ratio *($\mathcal{E}/\tau$)* estimated according to experimental and modeling results showed that it was lower than the corresponding values of "layer 2" and "Layer 1" but aligned with them. Besides, results enabled the reconfirmation of the pore size of "Layer 3" that had been declared by the manufacturer.

The same characterization procedures (coupling of experimental and modeled permeance results) was followed for "Layer 3" of the "coated" samples, assuming that the morphological parameters of the other three layers ("Layer 2", "Layer 1" and "Support") were not affected by the coating procedure. This is based on their relatively pore size with respect to "Layer 3". The obtained results were rather interesting. The estimated porosity-tortuosity ratio ($\mathcal{E}/\tau$) of "Layer 3" values were found to be lower than the values of the "uncoated" case. However, the estimated pore size of "layer 3" was observed to be higher than in the case of "uncoated" samples. In other words, results showed that the coating had led to an increase in the average pore size and a reduction in the porosity-tortuosity ratio of "Layer 3" at the same time. These results can be explained by considering the very first step of the coating process. The plugging of the small pores of "Layer 3" is possible during the carbonization step. Besides, the hydrophobization step involving the grafting procedure with fluoroalkylsilanes could result in an additional pore-blocking. Consequently, the pore size distribution of "Layer 3" could be altered due to the omission of the small blocked pores which could augment the average pore diameter. Such results go in agreement with those observed by other authors with different membranes grafted by fluoroalckylsilanes [77,138,173].

The concluded morphological properties of the membrane layers corresponding to the coated and uncoated single channels are reported in Table (2.3) which can be regarded as an update of the values provided by the manufacturer shown in Table (2.1). The "average membrane morphology method" (AMM) expressed by Eq (2.8), was used to estimate the average membrane parameters according to the experimental data shown in Fig (2.3b). The corresponding results of the estimated average morphological properties are also given in Table (2.3) as "average membrane values" for both, the coated and uncoated single channels. The calculations performed according to the "AMM" method also noted the effect of coating on reducing the membrane porosity and the possibility of pore-blocking due to the carbonization and grafting steps. This went in agreement with the observations obtained using the LBL method.

Table 2.3 *Morphological parameters of single channels. Nominal values are compared with those obtained by gas permeation tests elaborated according to different procedures*

	δ_j **(μm)**	dp_j *(nm)*	ε_j	$(\varepsilon/\tau)_j$	**%RE**
uncoated single channels					
support	1500 [a]	4500 [a]	0.33 [a]	0.11 [a]	---
		4484(3) [b]	---	0.11(3) [b]	12.16
layer 1	30 [a]	800 [a]	0.34 [a]	0.20 [a]	---
layer 2	30 [a]	250 [a]	0.39 [a]	0.34 [a]	---
layer 3	10 [a]	100[a]	---	---	---
		100(3) [b]	---	0.13(3) [b]	3.52
average membrane values	1570 [a]	232(3) [c]	---	3.90(3) [c]	2.39
coated single channels					
layer 3	10 [a]	169(6) [b]	---	0.031(6) [b]	3.54
average membrane values	1570 [a]	259(6) [c]	---	1.94(6) [c]	2.98

(a): nominal values by manufacturer, (b): obtained in this thesis by Eq(2.6,2.7), (c): obtained in this thesis by Eq(2.8), %RE: average percentage error between modeled and experimental values

According to their definitions, the porosity could not be above unity while the tortuosity factor could not be below unity. This would result in a porosity-tortuosity ratio that should never be above unity. However, the morphological results estimated by the AMM method appeared to be inconsistent with their physical significance such that the estimated porosity-tortuosity ratio values were larger than unity. These values of the average porosity-tortuosity ratio are aligned with those estimated by other authors who carried out some elaborations of the same characterization approach using the AMM method. Koonaphapdeelert & Li [36] documented that for 300 μm thick alumina fibers, it was possible to attain porosity-tortuosity ratios of 1.88 and 2.24 for non-grafted and grafted membranes respectively. Therefore, it could be indicated that the average morphological properties of the entire membrane based on the AMM method might not offer an accurate estimation of the important membrane mass transport properties that are required as inputs to membrane distillation modeling.

Aiming at understanding the role played by the morphological properties of each layer in constituting the mass transfer resistance of the membrane during gas permeation, the pressure profile of air was modeled according to the layer-by-layer characterization method along the direction of the transmembrane airflow. This is presented in Fig (2.4) for coated and uncoated single channels. The negative effect of the coating on the permeance appeared in the relatively large pressure drop in the layer at the vicinity of the feed side "Layer 3" in case of the coated single channel with respect to corresponding pressure drop in the same membrane layer in case of the uncoated sample. It can be also indicated that for both, the coated and uncoated single channels, the main pressure drop occurred in "Layer 3" while the pressure gradient across the support could be relatively insignificant. This can be attributed to the fact that "Layer 3" possessed the smallest pore size while the support possessed the largest pores size and porosity-tortuosity ratio among the membrane layers.

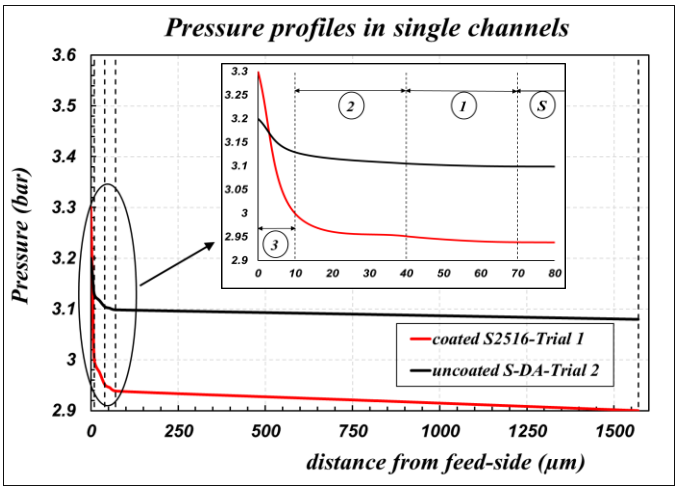

Figure (2.4) *Modeled Pressured profile during air permeation at room temperature for uncoated and coated single channel*

2.4.1.2.Capillary Bundles

The experimental results of air permeance as defined by Eq (2.1) are shown in Fig (2.5) for the capillary bundles. Besides, the modeled permeance values based on the "layer-by-layer" (LBL) method for estimating the pore diameter and porosity-tortuosity ratio of "Layer 3" are also represented by the fitting lines. Similar to what has been mentioned for the single channels, the modeled results assumed that the carbonization and hydrophobizaion procedures did not significantly alter the properties of the other three layers. The corresponding modeled morphological results are given in Table (2.4).

Bundle B2758 was chosen as a representative of the coated capillary bundles. The high degree of agreement of its experimental and modeled data estimated by the LBL method as shown in Fig (2.5b) encouraged the usage of its geometric and morphological properties as inputs for further modeling studies. This bundle was used for modeling the SGMD resistance and for modeling the pressure profile across the membrane layers during gas permeation results as it is given by Fig (2.6). Similar to what had been observed for the single channels, "Layer 3" represents the layer of the greatest pressure drop and consequently, it represents the controlling resistance during air permeation tests. By comparing the results of the single channels to those of the capillary bundles, it can be noted that the overall air permeance was not affected in a sensible manner by the different thicknesses of the "support" layer possessed by single-channel and that possessed by the capillary. The reproducibility of the results was well-attained for all the studied bundles. However, the capillary bundle B2758 seemed to be much more aligned with single channels.

Table 2.4 *Capillary bundles: elaborations of gas permeance data.*

	Parameters of layer 3			***Average membrane parameters***		
code	d_{p3} *(nm)*	$(\varepsilon/\tau)_3$	***RE%***	dp_m *(nm)*	$(\varepsilon/\tau)_m$	***RE%***
B2754	548	0.0029	3.14	468	0.27	3.36
B2755	534	0.0032	4.69	1232	0.053	7.56
B2756	435	0.0044	3.41	354	0.44	3.40
B2888	328	0.0069	3.13	337	0.38	3.25
B2758	68	0.084	3.03	87	3.414	2.89

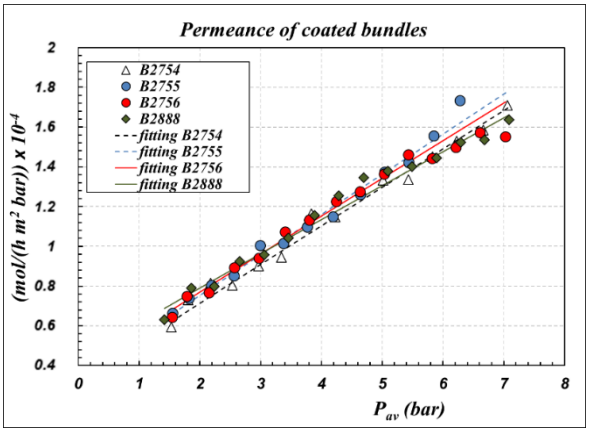

(a)

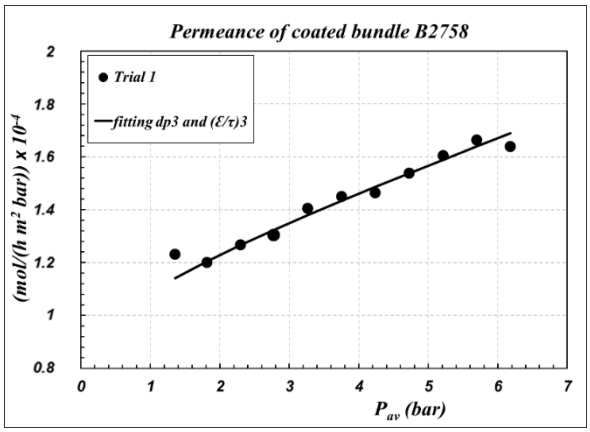

(b)

Figure (2.5) *Gas (air) permeation experimental and modeled results at room temperature in case of: (a) Coated bundles (b)Coated bundle B2758*

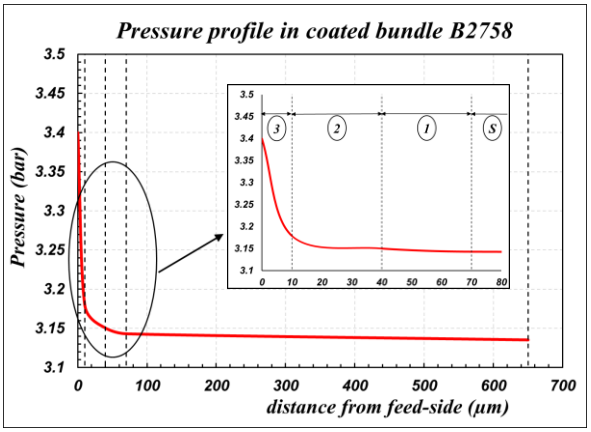

Figure (2.6) *Modeled Pressured profile during air permeation at room temperature for coated bundle B2758*

2.4.2. Membrane Mass Transfer Resistance in Sweeping Gas Membrane Distillation

The morphological characterization developed in the previous sections allowed the prediction of the parameters $(d_p)_3$ and $(\varepsilon/\tau)_3$ necessary for the determination of the overall mass transfer coefficient of the membrane, as described by Eq(2.4,2.5) to simulate/predict the transmembrane flux in MD operations. Based on those results, it was then possible to estimate the mass transfer resistances of each layer and the overall resistance across the multilayer membrane. For that purpose, the relationships reported in Eq(2.5) are re-elaborated according to Eq(2.9), to get an expression of the mass transfer resistance of water across the total membrane ($\bar{R}_{Wm}$) and across each layer j ($\bar{R}_{Wj}$).

$$\bar{R}_{Wm} = \frac{1}{k_{Wm}} = \sum_{j=1}^{3,s} \bar{R}_{Wj} = \sum_{j=1}^{3,s} \frac{r_{LM,m}}{k_{Wj}\, r_{LM,j}} \tag{2.9}$$

Vapor/liquid equilibrium was assumed to take at the pore entrance (entrance to "Layer 3") at the given operating temperature and pressure for pure water in the liquid phase and water/air in the vapor phase. Aiming at understanding the degree by which the operating conditions and support thickness affect the modeled mass transfer resistance, the following case studies were considered:

- Base case: 70°C, 1.5 bar, original support thickness such that δ(support)=1500μm
- Case A: 90°C, 1.5 bar, original support thickness such that δ(support)=1500μm
- Case B: 70°C, 2 bar, original support thickness such that δ(support)=1500μm
- Case C: 70°C, 1.5 bar, small support thickness such that δ(support)=1000μm

By comparing the results of cases, A, B and C to those of the Base case, it would be possible to identify the extent of the effect played by the liquid temperature, gas pressure and support thickness respectively on the modeled mass transfer during SGMD.

It is worth noting that even though the uncoated channels cannot be employed in MD due to their hydrophilicity, their transmembrane mass transfer resistance during SGMD was modeled in order to compare their performance to that of the coated channels. This could be beneficial in evaluating the coating effect on the transmembrane mass transfer resistance during SGMD.

The total membrane mass transfer resistance and the resistance of each layer during SGMD are shown in Fig (2.7) according to the morphological properties estimated by the LBL method. It can be demonstrated that the controlling mass transfer during SGMD is the "support" layer. This can be attributed to its relatively large thickness when compared to the other layers. On considering the original support thickness (1500µm), the support layer thickness represents around 95.5% of the overall membrane thickness. Given that the mass transfer is purely diffusive during SGMD, the thickness plays a great role in the mass transfer resistance at given operating conditions. This explains the reason why the support controlled the SGMD process. The same observation was drawn for the coated and uncoated single channels. Even though the coating significantly reduced the permeance of the membranes during air permeation, it did not significantly affect the transmembrane mass transfer resistance during SGMD. This could be demonstrated by the almost similar results obtained for the coated and uncoated single channels in Fig (2.7a) and (2.7b). There was a remarkable percentage increase in the SGMD mass transfer resistance of "Layer 3" due to the coating procedures. Despite that, the percentage increase in the overall membrane resistance was negligible due to the relatively insignificant role played by "Layer 3" in the overall SGMD membrane resistance. This is due to the fact that the effect of the pore size reduction in "Layer 3" resulting from the carbonization and hydrophobization could be significant when the viscous flow was considered. However, the negative effect of the pore size reduction in "on the purely diffusive flux during SGMD is negligible when compared to the corresponding role played by the large support thickness. This can be illustrated by Fig (2.7c) that compares the total membrane resistance resulting from the contribution of the morphology of each membrane layer to the membrane resistance resulting from a hypothetical "support equivalent" membrane. The "support equivalent membrane" is assumed to be a single membrane layer having the morphology of the support. According to the results, the SGMD modeling of the original 4-layered membrane as a "support-equivalent" membrane is accepted in case modeling simplifications are required.

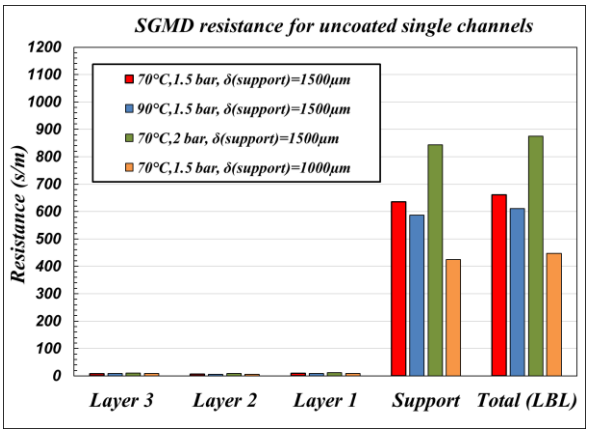

(a)

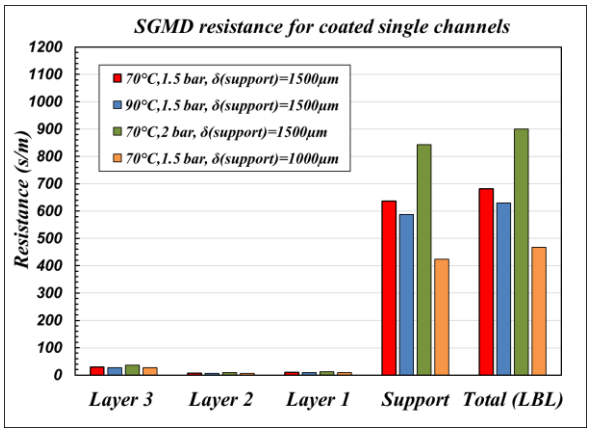

(b)

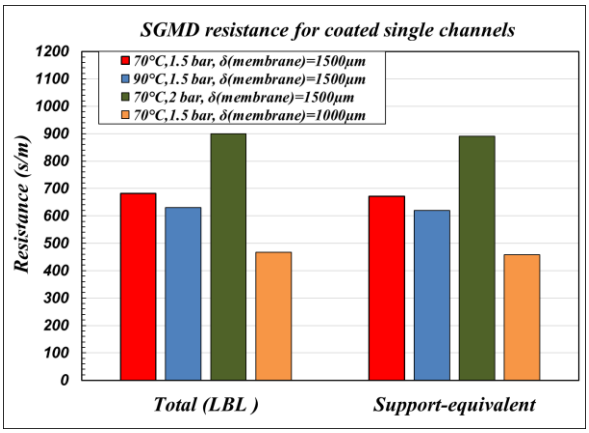

(c)

Figure (2.7) *Modeled SGMD resistance (LBL) at different operating conditions and support thickness in case of: (a) uncoated single channel (b) coated single channel (c) coated single channel and the corresponding "support equivalent" membrane*

The negative effect of the support thickness on the membrane resistance during SGMD is also explicitly identifiable in Fig (2.8a) for each given set of operating conditions. However, as the support thickness decreases, the improvement effect of its reduction on the membrane mass transfer coefficient decreases. That is because the significance of the role played by the other membrane layers increases as the support thickness decreases. The morphological properties of each layer allowed the estimation of the water vapor mole fraction gradient across the membrane layers as it is shown in Fig (2.8b). The change in water concentration across the membrane is almost due to the contribution of the support which is regarded as another confirmation of the fact that the support controls the SGMD. However, "Layer 3" experienced the largest concentration gradient during SGMD. This is attributed to its relatively small pore size and porosity-tortuosity ratio with respect to the other membrane layers.

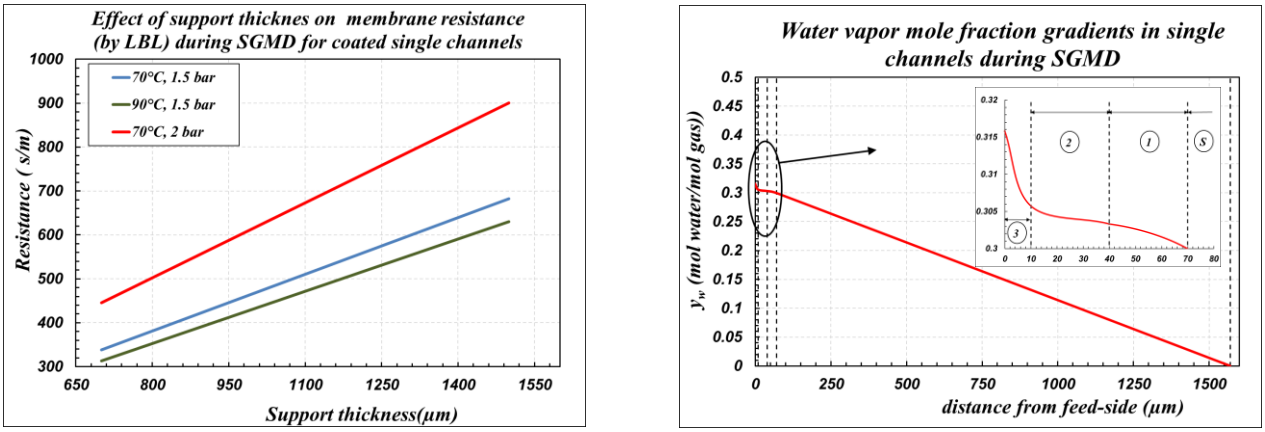

(a) *(b)*

Figure (2.8) *Modeled SGMD (LBL) for coated single channel showing: (a) effect of support thickness on membrane mass transfer resistance at different operating conditions*
(b) Water vapor mole fraction gradients in the membrane layers

Fig(2.9) represents the comparison between the SGMD transmembrane mass transfer resistance obtained according to the morphological properties estimated by the "layer-by-layer" (LBL) method and that obtained according to properties estimated by the "average membrane morphology" (AMM) method. It can be observed that the mass transfer is greatly underestimated on considering the morphological properties estimated by the AMM and that it is very close to the mass transfer resistance of "Layer 3". This could be attributed to the fact that "Layer 3" is deemed to be the controlling layer during gas permeation and the average morphological properties of the membrane estimated by the AMM were based on the gas permeation experimental results without considering the role of each membrane layer. Apparently, the extent of the positive effect of increasing the liquid temperature and/or decreasing the gas pressure on the mass transfer coefficient during SGMD can be noticed form the mass transfer resistances corresponding to different operating conditions in Fig (2.7, 2.8a, 2.9).

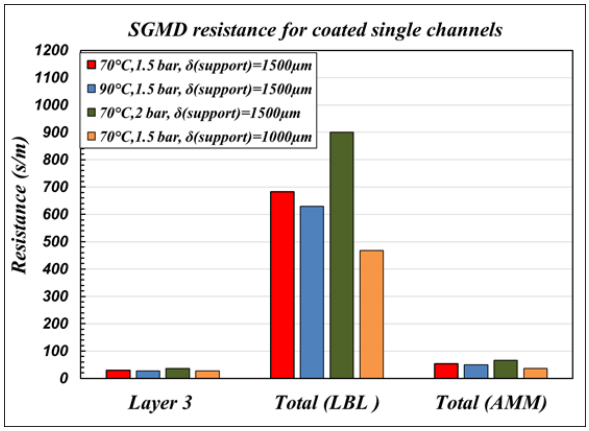

Figure (2.9) *Modeled SGMD mass transfer resistance for coated single channel showing resistance of layer 3 and the total membrane according to the morphology estimated by the (LBL) method and according to those estimated by the (AMM) method*

2.5.Conclusions

The combination of the experimental and modeling of single gas permeation was a useful tool in the reconfirmation of some morphological properties declared by the manufacturer and in the characterization of other unknown properties. The pore diameter and porosity-tortuosity ratio of the "Layer 3" were estimated for coated capillary bundles and for coated and uncoated single channels. "Layer 3" which represents the layer that is to be in the vicinity of the liquid feed during SGMD was found to be the controlling resistance during gas permeation. This was due to its relatively small pores when compared to the other membrane layers. Experimental results allowed the evaluation of the negative effect of the carbonization and hydrophobization procedure on the membrane permeance while the gas permeation modeling results allowed the attribution of this reduction in permeance to possible alteration in the morphological properties resulting from these procedures.

The estimated morphological properties were based on two approaches which were the "layer-by-layer" (LBL) method and the "average membrane morphology method" (AMM). The former considers the contribution of the morphological properties of each membrane layer on the overall membrane mass transfer properties while the latter views the membrane as a single layer and uses average morphological properties for the entire membrane.

The modeled mass transfer resistance during SGMD demonstrated that the support is the controlling mass transfer resistance due to its relatively large thickness with respect to the other membrane layers. Therefore, the exacerbated mass transfer resistance of "Layer 3" due to the hydrophilization procedures was nearly insignificant on the overall membrane mass transfer resistance during SGMD.

Results also showed that using the average membrane morphological properties (estimated by the AMM approach as inputs to the SGMD modeling equations) greatly underestimated the mass transfer resistance during SGMD with respect to the mass transfer resistance obtained on considering the morphological properties of each layer as estimated by LBL method. Possible improvements in the mass transfer coefficient could take place by increasing the temperature, decreasing the pressure and by reducing the support thickness. However, the operating conditions and the minimum support thickness are compromised according to the available thermal and mechanical stability of the membrane.

List of Symbols

Latin Letters	
a_{ij}	Viscous flow coefficient of component i in layer j
A	Area
c_{ij}	Knudsen diffusion coefficient of component i in layer j
c_j	Total molar concentration in layer j
c_m	Total molar concentration in membrane
d_p	Pore diameter
D_{Weq}	Equivalent diffusion coefficient of water
D_{WG}	Molecular diffusion coefficient of water in gas
$D_{W,Kn}$	Knudsen diffusion coefficient of water
k	Mass transfer coefficient
L	Length
M	Molecular weight
N_{air}	Molar flow rate of air
N_p	Number of pores
N'_p	Number of pores per unit length
N'_{tot}	Total molar flow rate per unit length across membrane
N_i	Molar flow rater of component i
P	Pressure
r	Radius
R_g	Universal gas constant
$\bar{R}$	Mass transfer resistance
T	Temperature
V	Volume
y	Mole fraction in the vapor phase
Greek Letters	
α	Permeance
δ	Thickness

ε	porosity
η	Dynamic Viscosity
τ	Tortuosity
Subscripts and Superscripts	
av	Average
G	Gas
i	Component i
I	Liquid/membrane interface
j	Layer j
IN	Inner or Inlet
LM	Logarithmic mean
m	membrane
$m-G$	Membrane/gas interface
OUT	Outlet
S	Support layer
tot	Total
$Void$	Void in membrane
W	Water
3	Layer 3

[This page intentionally left blank]

Chapter Three

Investigation of Membrane Module Performance during Sweeping Gas Membrane Distillation of Sodium Chloride Aqueous Solution

3.1.Introduction

The phase of membrane characterization plays a pivotal role in ensuring that the membrane distillation (MD) process requirements are met by the studied membranes. However, the practical application of the membranes in MD operations cannot be decided only according to the results of the membrane characterization techniques. In fact, the investigation of the performance of the membrane module during experimental MD operations is essential for the assessment of the applicability of the module in fulfilling the requirements of the given MD processes at the desired operating conditions. In addition to experimental studies, modeling of MD could be beneficial in the module performance investigation [82] and the overall process simulation and optimization [74,183]. Modeling studies could offer a clear vision of the important key parameters affecting the module performance. This could enable the prediction of the effect of the MD operating conditions [55,57,119,184] and main membrane properties, geometric parameters and process configurations on the overall MD performance. In addition to that, some developed models could allow the demonstration of how the driving force, the flux, and process limitations vary across the length of the module and/or the vessel containing the modules [74,82]. This could be of great importance in process design and optimization since the optimized operating conditions and process lay out are mainly dependent on the module performance. This will be discussed in more details in the part related to process development and optimization in Chapter (5). Accordingly, many recent works in literature were dedicated to module investigation for different MD configurations and for various purposes using experimental and/or modeling studies [54,60,171,185,186].

In the current chapter, sweeping gas membrane distillation (SGMD) experiments were run by means of a bench-scale SGMD set-up for the ceramic capillary bundles whose morphological properties were characterized in Chapter (2). The performance of the studied ceramic membranes during SGMD was investigated and assessed by these experimental studies. Moreover, modeling was utilized in the estimation of the water flux and the simulation of the module performance. NaCl (aq.) solution was selected as the feed stream. In fact, seawater desalination is deemed to be the main studied application of membrane distillation in literature [41,94,122,128]. During desalination by SGMD, the water permeates from the feed side containing the NaCl (aq.) solution towards the permeate side containing the sweeping gas. The permeated water vapor molecules are then carried by the sweeping gas towards the outlet of the module where those water molecules can be recovered by means of condensation [1]. It is worth noting that the computational complexity in modeling capillary membranes in SGMD has been a challenge facing the application and development of such technology [82]. As for the modeling studies performed in the current chapter, an equivalent diffusion coefficient was employed in describing the transmembrane mass transfer during SGMD considering the contributions of the Knudsen and molecular diffusion mechanisms. This equivalent diffusion coefficient was calculated according to the Bosanquet equation which is commonly applied in similar approaches in literature dedicated to modeling the transmembrane mass transfer in MD operations [1,47,82,98,106–108].

3.2.Materials and Methods

3.2.1. Capillary Bundles

The SGMD experimental and modeling studies regarded the capillary bundles that were discussed in Chapter (2). They refer to the capillary bundles of the hydrophobic carbon-based titania membranes. These membranes were manufactured by the Fraunhofer Institute for Ceramic Technologies and Systems (IKTS, Hermsdorf, Germany). The membranes are composed of four layers possessing different morphological properties. During SGMD experiments the liquid feed was introduced to the tube-side such that the membrane layer in the vicinity of the liquid is named "Layer 3". It is followed by "Layer 2", "Layer 1" and finally by the outer layer which is the "Support". Details about the manufacturing, the characterization and the hydrophobization procedures of the membranes were discussed in Chapter (2). The studied capillary bundles were coded as B2754, B2755, B2756, B2888 and B2758. The geometric parameters of the bundles including the fiber inner diameter (d_{IN}) and outlet diameter (d_{OUT}), the number of fibers (N_f), the effective module length (L_{eff}) and the shell diameter (d_S) are listed in Table (3.1). The effective module length represents the distance between the shell inlet and outlet nozzles, whereas the tube side length is equal to 20 cm for all the bundles. The LEP values for the studied bundles at room temperature are also included in the table. They were obtained by LEP tests performed by F. Varela-Corredor et al. [8,80]. The high values of the obtained LEP demonstrated the accepted hydrophobic character of the bundles.

Table (3.1) *Geometric parameters and room temperature LEP values of the capillary bundles*

Bundle	d_{IN} *(mm)*	d_{OUT} *(mm)*	N_f *(fibers)*	L_{eff} *(mm)*	d_S *(cm)*	*LEP (bar)*
B2754	1.56	3.20	37	13	3.60	4.2
B2755						4
B2756						6.2
B2888	1.9	3.54				unavailable
B2758		3.20	22	17	2.50	6.9

The morphological properties of each membrane layer of the bundles are listed in Table (3.2) where the pore size and porosity-tortuosity ratio of "Layer 3" were estimated in Chapter (2) according to the "layer-by-layer" approach. Another approach was employed in Chapter (2) for characterizing the membrane morphological properties. It followed the "average membrane morphology" (AMM) method which is commonly applied in literature [2,10,26] assuming the membrane to be composed of a single layer with average morphological properties without considering the role played by each membrane layer in the overall membrane mass transfer properties. These characterized average properties are listed in Table (3.3) for the capillary bundles.

Table (3.2) *Morphological properties of the four layers of the capillary bundles*

Bundle	Layer 3			Layer 2			Layer 1			Support Layer		
	d_p *(nm)*	(ε/τ)	δ *(µm)*	d_p *(nm)*	(ε/τ)	δ *(µm)*	d_p *(nm)*	(ε/τ)	δ *(µm)*	d_p *(nm)*	(ε/τ)	δ *(µm)*
B2754	548	0.0029	10	250	0.34	30	800	0.20	30	4500	0.11	750
B2755	534	0.0032										
B2756	435	0.0044										
B2888	328	0.0069										
B2758	68	0.084										580

Table (3.3) *Average membrane morphological properties of the capillary bundles as estimated by the AMM method*

	Average values	
Bundle	dp_m *(nm)*	$(\varepsilon/\tau)_m$
B2754	468	0.27
B2755	1232	0.053
B2756	354	0.44
B2888	337	0.38
B2758	87	3.414

3.2.2. Sweeping Gas Membrane Distillation Experiment

3.2.2.1.Experimental Set-up

The experimental performance of the capillary bundles was assessed using a bench-scale sweeping gas membrane distillation (SGMD) set up that was built by F. Varela-Corredor [80]. A representation of the SGMD set up is shown in Fig (3.1). The main equipment involved were the feed tank, feed pump, membrane contactor, thermostatic bath, gas compressor, gas condenser, set of valves, pipelines and indicators of temperature, flow, pressure and pressure difference. The elements used in the SGMD pilot plant were carefully chosen to resist high temperatures up to 150°C and pressures up to 10 barg. The feed tank is represented by a pressure vessel that is completely constructed of stainless steel AISI 316L. The capacity of the feed tank is 5 Liters while its maximum allowable operating temperature and pressure are 180 °C and 10 barg respectively. PTFE gasket is used to seal the top cover of the feed tank which is connected to indicators, relief valve, sampling pipe and the liquid feed inlet. A pressurized gas cylinder containing inert gas (N_2) is connected to the feed tank. The nitrogen gas flow into the feed tank can be allowed in a controlled manner in order to regulate the liquid feed pressure inside the feed tank. Liquid samples can be withdrawn from the feed tank to measure their conductivity which can be then used in the estimation

of the corresponding liquid salinity. The liquid feed was allowed to flow from the feed tank to the membrane contactor while the liquid outlet of the membrane contactor was recirculated back to the feed tank. The required feed temperature was attained and controlled by applying a thermostatic bath using silicone oil that could operate at temperatures up to 240 °C. Simultaneously, the thermostatic bath was used to heat the gas temperature before being introduced to the membrane contactor as it is shown in Fig (3.1). A simple condenser was used to condense the permeated water vapor carried by the sweeping gas at the outlet of the membrane contactor such that cold water was used in the condensation processes. Moreover, during some of the SGMD tests, a column of silica gel was used after the condenser in order to adsorb the uncondensed water vapor. The condenser was used to ensure the absence of salt in the distilled water to make sure that no salt passed across the membrane with the permeated water molecules during the SGMD experiments.

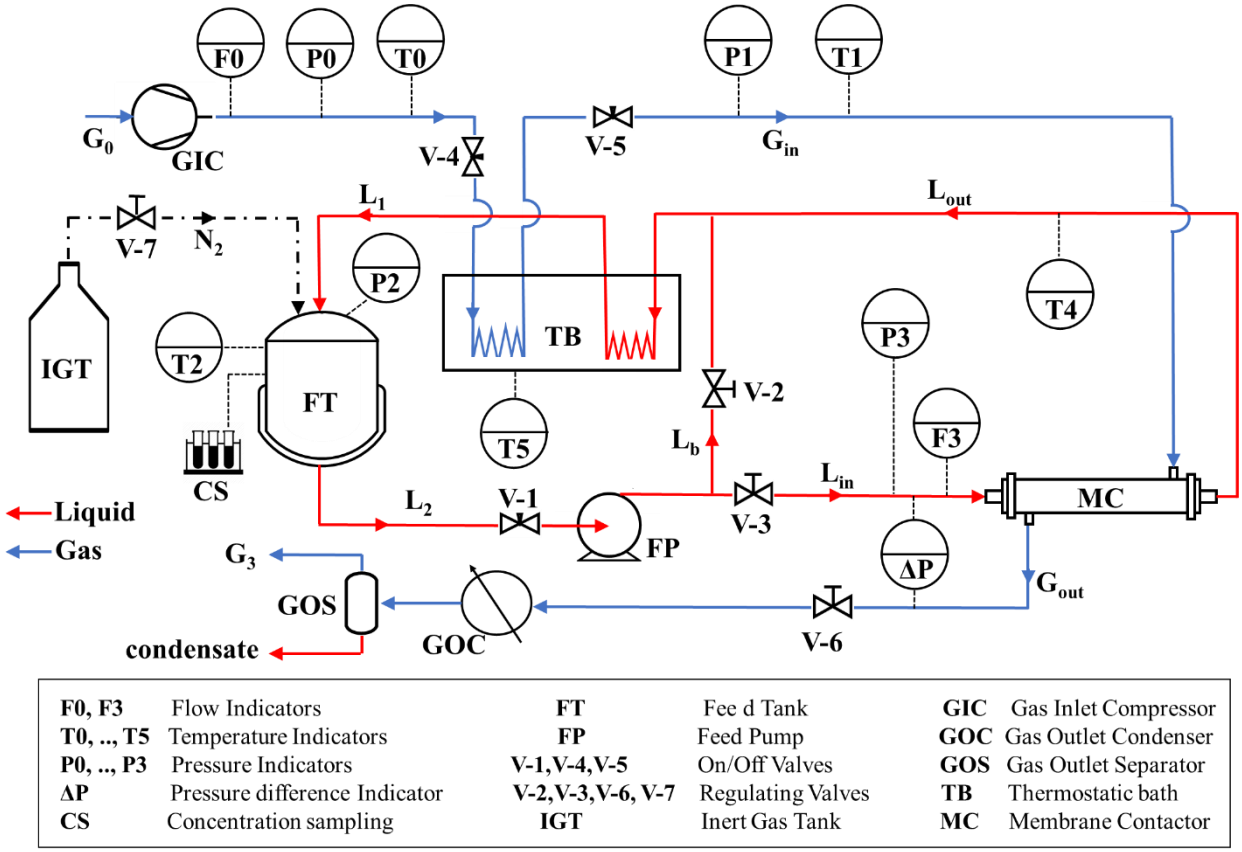

F0, F3	Flow Indicators	**FT**	Fee d Tank	**GIC**	Gas Inlet Compressor
T0, .., T5	Temperature Indicators	**FP**	Feed Pump	**GOC**	Gas Outlet Condenser
P0, .., P3	Pressure Indicators	**V-1,V-4,V-5**	On/Off Valves	**GOS**	Gas Outlet Separator
ΔP	Pressure difference Indicator	**V-2,V-3,V-6, V-7**	Regulating Valves	**TB**	Thermostatic bath
CS	Concentration sampling	**IGT**	Inert Gas Tank	**MC**	Membrane Contactor

Figure (3.1) *Representation of the bench-scale SGMD set up used during SGMD experiments for NaCl(aq.) feed*

The liquid temperature and pressure in the tank were measured by indicators T2 and P2 respectively while the volumetric flow rate and pressure of the feed at the tube-side inlet were measured by indicators F3 and P3 respectively. For each experiment, the desired initial feed concentration was attained by mixing demineralized water (maximum conductivity of 20 µS/cm at room temperature) with anhydrous NaCl salt. The salt concentration in the aqueous solution was measured by a conductometer. In a counter-current flow manner, dry air was introduced to the shell-side of the module representing the sweeping gas in the permeate-side. The gas stream (G0) was

initially at room temperature where its volumetric flow rate, pressure and temperature were measured by the indicators F0, P0 and T0 respectively. The transmembrane pressure difference monitored by the differential manometer (ΔP) (shown in Fig(3.1)) was controlled during the whole experiment ensuring it did not exceed the liquid entry pressure (LEP) value to avert membrane wetting and flooding.

3.2.2.2.Experimental Flux Measurement Procedures

The rate of change of the salt concentration in the liquid tank was used in estimating the water flux and the amount of the remaining circulating liquid. This took place assuming total salt rejection by the membrane. Accordingly, liquid samples were withdrawn periodically from the tank to measure the salt concentration of the circulating liquid using a calibrated conductometer. The time (*i*) is the time at which the sample is withdrawn from the feed tank and is indicated by (t_i). Experimental water flux at time t_i was calculated by Eq (3.1).

$$<\dot{m}_w''\Big|_{t_i}> = \frac{m_{w(t_i - \Delta t)} - m_{w(t_i)}}{A_{IN} \times \Delta t} \qquad ,i \neq 1 \tag{3.1}$$

where, $m_{w(t_i - \Delta t)}$, $m_{w(t_i)}$ represent the mass of the recirculating water (water remaining in the system) at time $(t_i - \Delta t)$ and at the time of sample withdrawal (t_i) respectively while (Δt) is the time interval taken between two successive sample withdrawals. A_{IN} is the membrane inner surface area.

3.3.Modeling of Sweeping Gas Membrane Distillation of NaCl (aq.) Solution

3.3.1. Local Model

The applied SGMD local model for NaCl (aq.) feed was based on the following set of assumptions.

- Steady state process
- The liquid feed is allocated in the tube-side while the sweeping gas is allocated in the shell-side.
- Water represented the only permeating component (100% salt rejection)
- The sweeping gas is insoluble in the liquid feed.
- The transmembrane mass transfer is diffusive where an equivalent diffusion coefficient was used to consider the contributions of the molecular and Knudsen diffusion mechanisms.
- Well-insulated module (no heat losses)
- No defects and no leakages (no mass losses)
- Ideal gas behavior of the permeate-side stream

The set of Eqs. (3.2 – 3.9) were used to calculate the local molar and heat fluxes in addition to the membrane interfacial concentrations and temperatures. The equations are represented for the cylindrical geometry of a single fiber having a unit length. Mass transfer during SGMD takes place over three main steps which are listed as follows.

1) Transfer of liquid water molecules through the liquid mass boundary layer according to the film theory [187]. This is described by Eq (3.2).
2) Transfer of water vapor across the membrane pores (See Eq (3.3)) by a purely diffusive flow due to the contributions of the molecular and Knudsen diffusion mechanisms
3) Transfer of water vapor through the gas mass boundary layer according to the film theory. This is represented by Eq (3.4).

The expected profiles of the mole fractions of water and salt during SGMD are illustrated in Fig (3.2). Mass transfer expressions (Eqs. (3.2 – 3.4)) used the same notations of the mole fractions shown in this figure such that (*x*) and (*y*) represent the mole fractions in liquid and vapor states respectively while the subscripts (*w*), (*s*), (*L*), (*G*), (*m*) refer to water, salt, liquid stream, gas stream and membrane respectively. At the liquid/membrane and gas/membrane interfaces, the subscripts (*Lm*) and (*Gm*) are used while at the liquid and gas bulks, the subscripts (*Lb*) and (*Gb*) are used respectively.

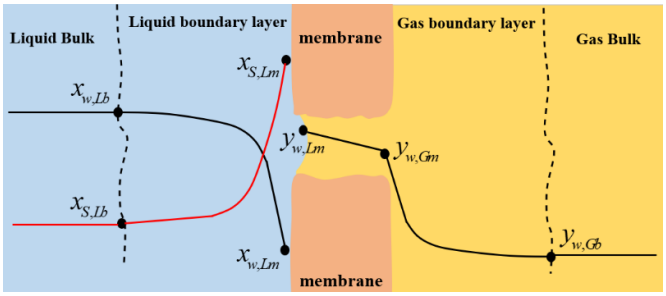

Figure (3.2) *Expected mole fraction profile of NaCl salt and water in the liquid and of water in the membrane and the gas during SGMD*

$$N'_w = \frac{k_{w,L}\,\rho_L}{M_L}\ln\left(\frac{1-x_{w,Lm}}{1-x_{w,Lb}}\right)\pi d_{IN} \tag{3.2}$$

$$N'_w = \frac{k_{w,m}\,P_G}{R_g T_m}\ln\left(\frac{1-y_{w,Gm}}{1-y_{w,Lm}}\right)\pi d_{lm} \tag{3.3}$$

$$N'_w = \frac{k_{w,G}\,P_G}{R_g T_G}\ln\left(\frac{1-y_{w,Gb}}{1-y_{w,Gm}}\right)\pi d_{OUT} \tag{3.4}$$

where, N'_w and k_w represent the molar flow rate of water in a single fiber of a unit length and the mass transfer coefficient of water respectively. ρ, M, P, T, R_g refer to density, molecular weight, pressure, absolute temperature and universal gas constant respectively. The membrane temperature T_m is the arithmetic mean of the temperature at the liquid/membrane interface T_{Lm} and that at the gas/membrane interface T_{Gm}. The membrane inner, outer and logarithmic mean diameters are represented by d_{IN}, d_{OUT}, d_{lm} respectively.

The liquid/vapor equilibrium occurring at the liquid-membrane interface can be expressed by the modified Raoult' law according to Eq (3.5).

$$y_{w,Lm}\, P_G = P^*_{w(T_{Lm})}\, \gamma_{w,Lm(T_{Lm}, x_{w,Lm})}\, x_{w,Lm} \tag{3.5}$$

where, $P^*_w, \gamma_{w,Lm}$ represent the water vapor pressure and activity coefficient respectively at the liquid/membrane interface.

Both mass and heat transfer occur simultaneously during SGMD. The expected temperature profile is qualitatively represented by Fig (3.3) such that heat transfer takes place during SGMD over the following steps.

1) Heat transfer from the liquid bulk towards the liquid/membrane interface through the liquid thermal boundary layer. The heat transfer rate per unit axial length for a single fiber across the liquid thermal boundary layer Q'_L can be estimated by Eq (3.6). At the liquid/membrane interface, a portion of the heat transferred across the liquid boundary layer is utilized in vaporizing the permeating stream while the remaining portion represents the net heat energy Q'_{net} which can be estimated by the heat balance at the liquid/membrane interface as expressed by Eq (3.7).

2) Thermal conduction across the membrane towards the gas side at neglected convective contribution. This is described by Fourier's law [188] as given by Eq (3.8).

3) Heat transfer from the gas-membrane interface towards the gas bulk through the gas thermal boundary layer as described by Eq (3.9).

$$Q'_L = h_L \left(T_{Lb} - T_{Lm}\right) \pi d_{IN} \tag{3.6}$$

$$Q'_{net} = Q'_L - \left(N'_w \ \lambda^w_{(T_{Lm})}\right) \tag{3.7}$$

$$Q'_{net} = \frac{2\pi k_m^{cond.}}{\ln\left(\frac{d_{OUT}}{d_{IN}}\right)} \left(T_{Lm} - T_{Gm}\right) \tag{3.8}$$

$$Q'_{net} = h_G \left(T_{Gm} - T_{Gb}\right) \pi d_{OUT} \tag{3.9}$$

where, λ^w, $k_m^{cond.}$, h represent the latent heat of vaporization of water, the thermal conductivity of the membrane and the convective heat transfer coefficient respectively.

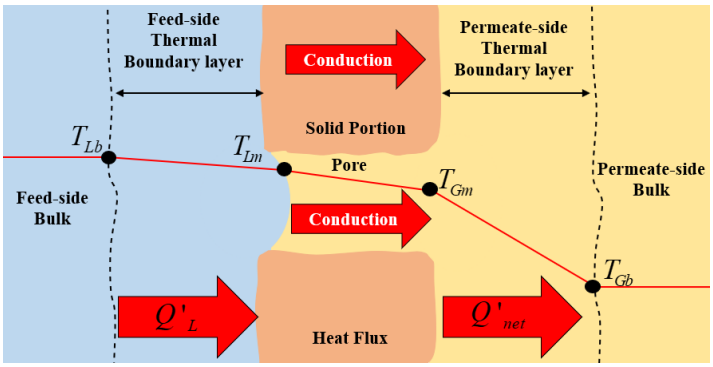

Figure (3.3) *Expected temperature profile in the liquid, membrane and gas during SGMD*

The local model solution strategy considered the following steps and can be represented by Fig(3.4).

1) The local operating conditions for the gas and liquid streams were used to estimate their corresponding physical properties as given in Appendix (A).
2) The mass and heat transfer coefficients in the liquid and gas boundary layers were predicted according to the given geometry and physical conditions.
3) The membrane mass transfer coefficient and thermal conductivity were estimated according to:
    - Morphological properties of each membrane layer characterized by the "layer-by-layer" (LBL) method that was discussed in Chapter (2).
    - Average values of the membrane morphological properties characterized by the "average membrane morphology" (AMM) that was discussed in Chapter (2).

4) The local molar and heat fluxes in addition to membrane interfacial concentrations and temperatures were evaluated from the set of Eqs. (3.2-3.9) using an iterative solution. The corresponding algorithm of the implemented iterative procedures is illustrated in Fig (3.5).

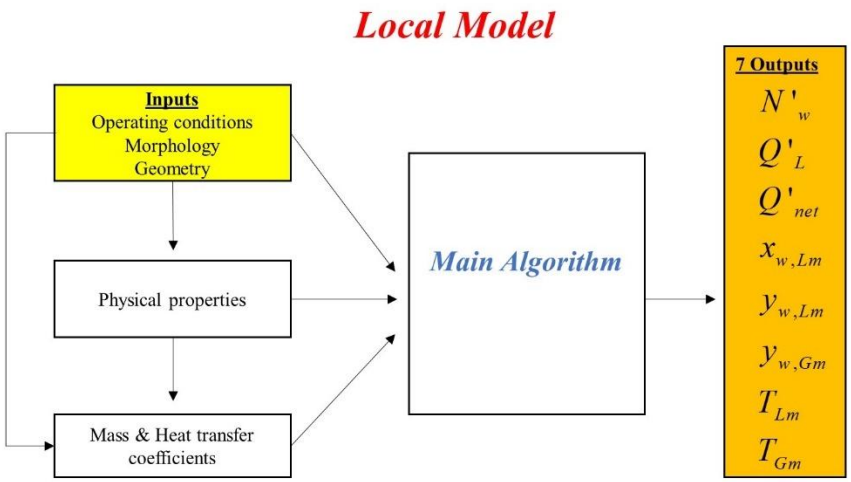

Figure (3.4) *The strategy of the solution of the SGMD local model (NaCl(aq.) feed)*

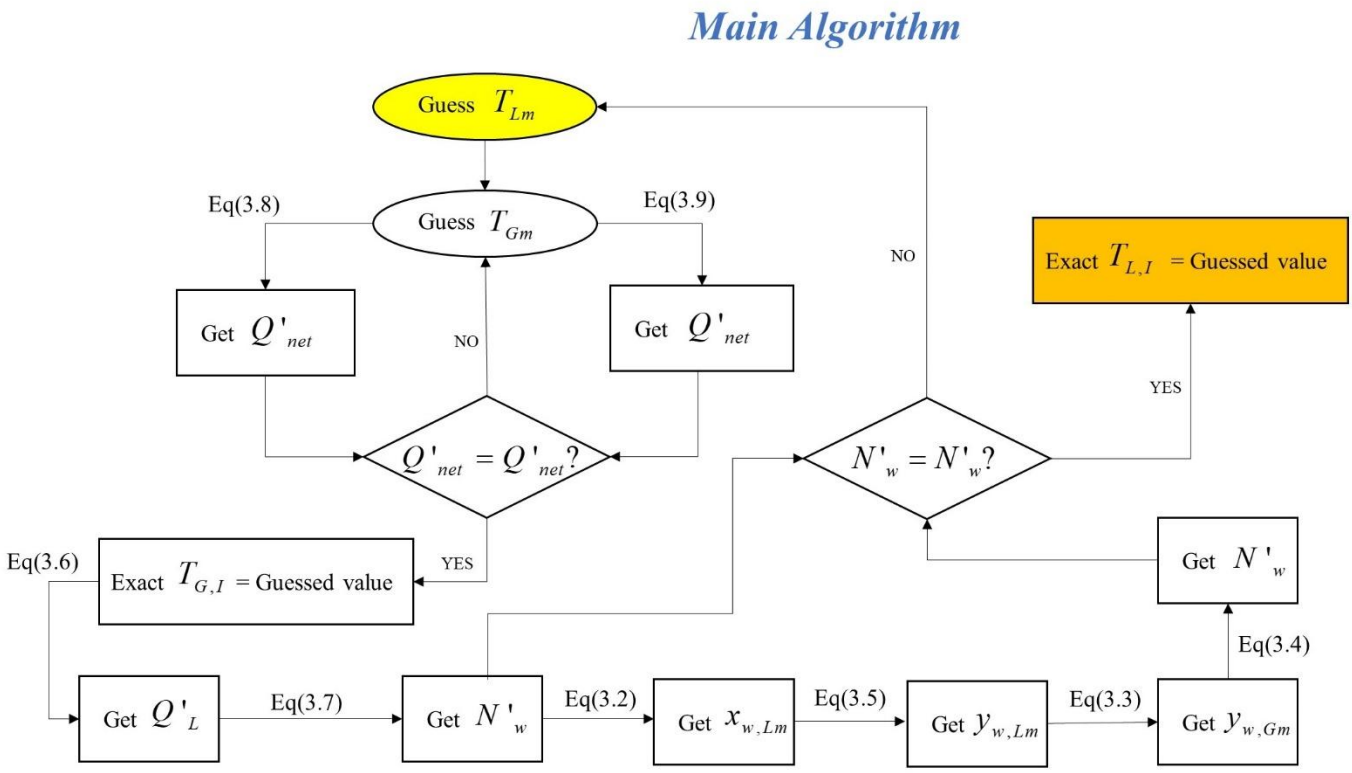

Figure (3.5) *The algorithm used in the solution of the SGMD local model (NaCl(aq.) feed)*

3.3.2. Modeling according to Plug Flow Concept

A finite-difference model was employed in the simulation of the SGMD process in the studied ceramic capillary bundles. The module was discretized in order to consider the axial gradients of the operating conditions occurring in the tube side and shell side streams and to consider the effect of these gradients on the resulting water flux. This was done along the axial direction (z-direction) of the module (according to the plug flow model concept) . A MATLAB code was developed for the required computational execution. The module was divided into n elements (units) connected in-series along the axial direction (z-direction) as it is presented in Fig(3.6). The same adopted assumptions in the local SGMD model were considered in the axially discretized model in addition to the following assumptions.

- The fibers are identical and uniformly packed in the shell ensuring uniform hydrodynamics.
- 1-D transfer phenomena in the bulks of the liquid and gas streams (z-direction)

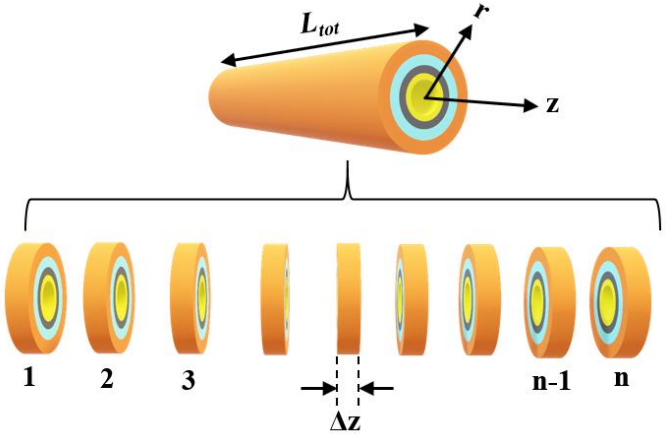

Figure (3.6) *Representation of the axial discretization of the module into (n) elements during SGMD modeling*

In the case of co-current configuration, both the liquid (tube-side stream) and the sweeping gas (shell-side stream) flow in the positive axial direction. In the case of counter-current configuration, the sweeping gas flows in the positive axial direction while the liquid flows in the negative axial direction. Each element (unit) represents a control volume of constant physical properties for each of the two streams. The discretization representations in case of co-current and countercurrent flow manners are shown Figs (3.7) and (3.8) respectively. For a *single fiber*, the governing axial differential transfer equations in the liquid (feed-side) and the sweeping gas (permeate side) are given in Tables (3.4) and (3.5) respectively.

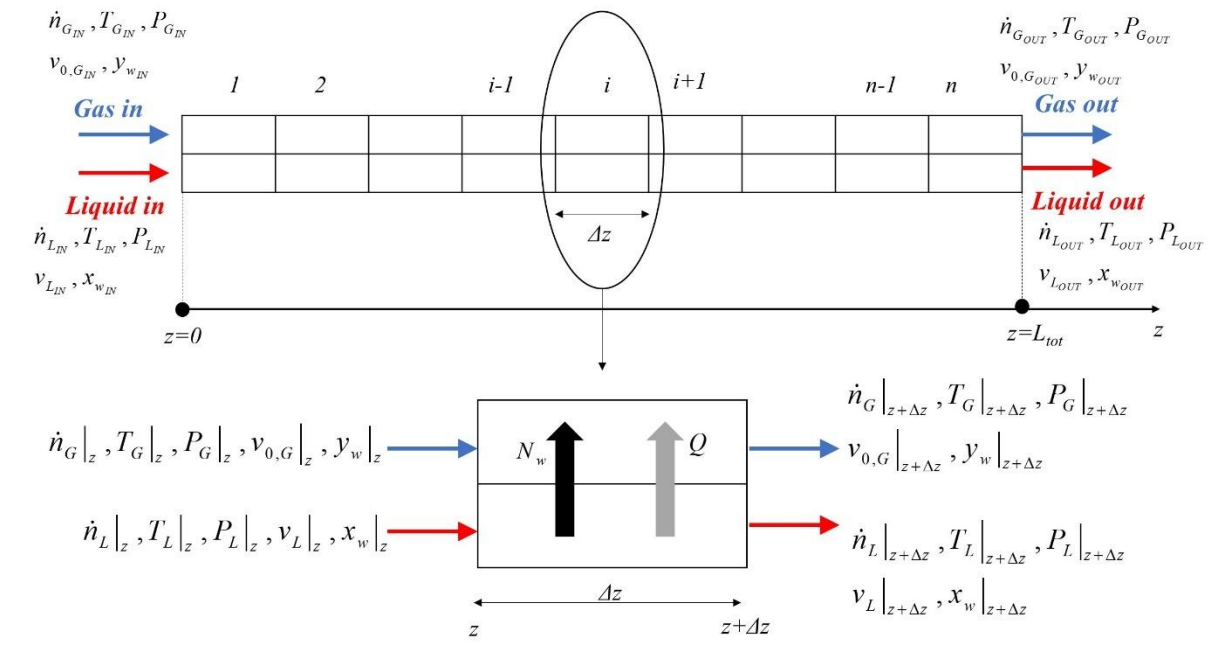

Figure (3.7) *Representation of the axial discretization of the module in case of co-current flow (NaCl(aq.) feed)*

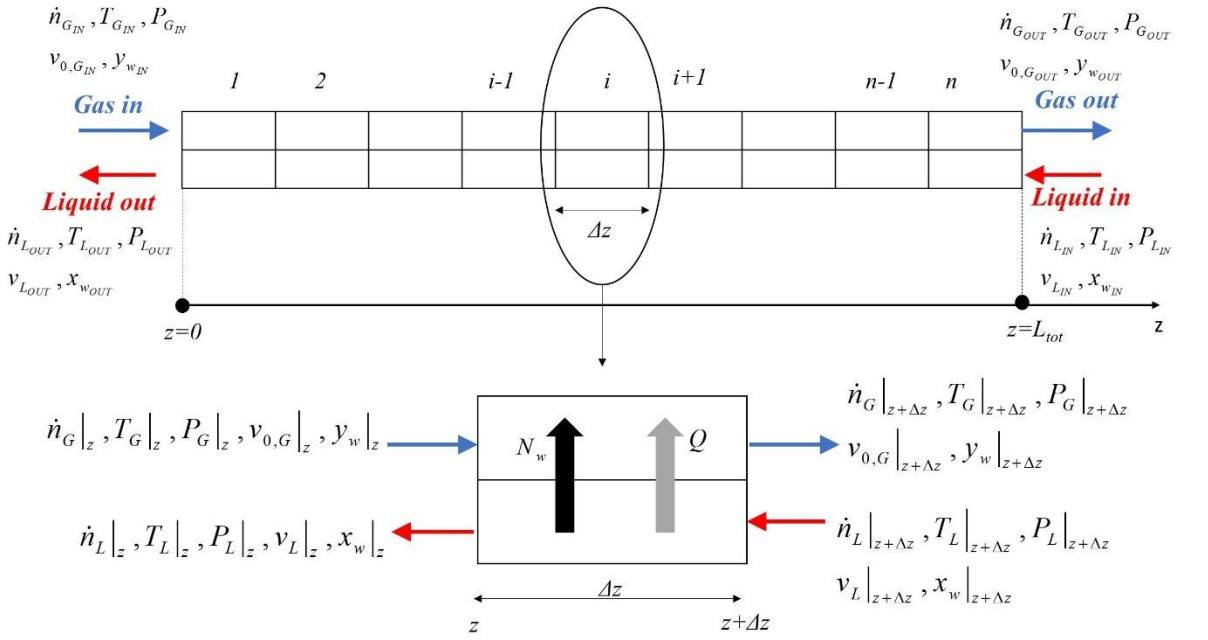

Figure (3.8) *Representation of the axial discretization of the module in case of counter-current flow (NaCl(aq.) feed)*

Table(3.4) *Governing axial differential transfer equations in the liquid feed*

Co-current	Counter-current	Comments	Eq.
$\frac{d\dot{n}_L}{dz} = -N'_w$	$\frac{d\dot{n}_L}{dz} = N'_w$	From total mass balance	(3.10)
$\frac{d\dot{n}_s}{dz} = 0$		From salt mass balance	(3.11)
$\frac{dT_L}{dz} = \frac{-Q'_L}{\dot{n}_L \tilde{C}_{p_L}}$	$\frac{dT_L}{dz} = \frac{Q'_L}{\dot{n}_L \tilde{C}_{p_L}}$	From heat balance	(3.12)
$\frac{dv_L}{dz} = \frac{-4N'_w M_w}{\pi d_{IN}^2 \rho_L}$	$\frac{dv_L}{dz} = \frac{4N'_w M_w}{\pi d_{IN}^2 \rho_L}$	From continuity equation	(3.13)
$\frac{dP_L}{dz} = -4f\rho_L \frac{v_L^2}{2d_{IN}}$	$\frac{dP_L}{dz} = 4f\rho_L \frac{v_L^2}{2d_{IN}}$	Darcy–Weisbach equation [189]	(3.14)

Table(3.5) *Governing axial differential transfer equations in the sweeping gas*

Co-current or Counter-current	Comments	Eq.
$\frac{d\dot{n}_G}{dz} = N'_w$	From total mass balance	(3.15)
$\frac{d\dot{n}_a}{dz} = 0$	From air mass balance	(3.16)
$\frac{d\,T_G}{dz} = \frac{Q'_{net}}{\dot{n}_G \tilde{C}_{P,G}}$	From heat balance	(3.17)
$\left(\frac{1}{\rho_G}\right)\frac{d\rho_G}{dz} = \left(\frac{-1}{T_G}\right)\frac{dT_G}{dz} + \left(\frac{1}{P_G}\right)\frac{dP_G}{dz} + \left(\frac{M_w - M_a}{M_G}\right)\frac{dy_w}{dz}$	From ideal gas law	(3.18)
$\rho_G\left(\frac{dv_{0,G}}{dz}\right) + v_{0,G}\left(\frac{d\rho_G}{dz}\right) = \frac{4N'_w M_w}{\pi\left(\frac{d_S^2}{N_f} - d_{OUT}^2\right)}$	From continuity equation	(3.19)
$\frac{dP_G}{dz} = \frac{8N_f \eta_G v_{0,G}}{d_S^2\left(\frac{1}{2}\left(\frac{\ln(\varepsilon_p)}{1-\varepsilon_p} + 1 + \frac{1-\varepsilon_p}{2}\right)\right)}$, $\varepsilon_p = N_{f,tot}\left(\frac{d_{OUT}}{d_S}\right)^2$	From equivalent annulus theorem [190]	(3.20)

$\dot{n}$ represents the molar flow rate per fiber while the subscript "*a*" refers to the air present in the sweeping gas. f, ε_p, η_G refer to the friction factor, the module packing factor and the gas viscosity respectively. $v_L, v_{0,G}$ represent the liquid velocity in the tube side and the gas interstitial velocity in the shell side respectively

The expression of the sweeping gas pressure gradient (Eq (3.20)) originating from the momentum balance in the shell-side was based on the equivalent annulus theorem introduced by C. Gostoli et al. [190] in case of laminar flow. This theorem is valid on condition that the fibers are not closely packed, and that the flow is uniformly distributed. In case of non-laminar flow, Eq (3.21) was used instead.

$$\frac{dP_G}{dz} = -4\frac{f}{d_{eq}}\rho_G\frac{v_{0,G}^2}{2} \tag{3.21}$$

Dirichlet boundary conditions were specified for the governing equations according to the inlet conditions of both streams.

In case of co-current flow, the following boundary conditions were used.

$$\begin{aligned}
&at\ z=0: \quad \dot{n}_G = \dot{n}_{G,IN}, \quad \dot{n}_a = \dot{n}_{a,IN}, \quad T_G = T_{G,IN} \\
&P_G = P_{G,IN} \quad , v_{0,G} = v_{0,G,IN}, \quad \rho_G = \rho_{G,IN}, \quad y_w = y_{w,IN} \\
&at\ z=0: \quad \dot{n}_L = \dot{n}_{L,IN}, \quad \dot{n}_s = x_{s,IN}\dot{n}_{L,IN}, \quad T_L = T_{L,IN}, \quad P_L = P_{L,IN}, \quad v_L = v_{L,IN}
\end{aligned}$$

In case of counter-current flow, the following boundary conditions were used.

$$\begin{aligned}
&at\ z=0: \quad \dot{n}_G = \dot{n}_{G,IN}, \quad \dot{n}_a = \dot{n}_{a,IN}, \quad T_G = T_{G,IN} \\
&P_G = P_{G,IN} \quad , v_{0,G} = v_{0,G,IN}, \quad \rho_G = \rho_{G,IN}, \quad y_w = y_{w,IN} \\
&at\ z=L_{tot}: \quad \dot{n}_L = \dot{n}_{L,IN}, \quad \dot{n}_s = x_{s,IN}\dot{n}_{L,IN}, \quad T_L = T_{L,IN}, \quad P_L = P_{L,IN}, \quad v_L = v_{L,IN}
\end{aligned}$$

Where the subscript " *IN* " refers to the conditions at the stream inlet as it is indicated in Fig (3.7) and (3.8) for the co-current and countercurrent configurations respectively.

Finally, the water mass flux J_w (based on the membrane inner area) obtained from a module having a total length L_{tot} can be calculated from the contributions of all the discretization elements according to Eq(3.22).

$$J_w = \frac{1}{L_{tot}} \int_0^{L_{tot}} J_{w,z}\, dz \tag{3.22}$$

The finite-difference numerical method was implemented to transform the governing differential equations into a system of nonlinear algebraic equations. For discretized n elements having uniform thickness Δz, Eq (3.22) can be represented in the form of Eq(3.23).

$$J_w = \frac{M_w}{n\,\pi d_{IN}} \sum_{i=1}^{n} N'_{w,i} \tag{3.23}$$

The implemented solution algorithms for the axially discretized SGMD models are illustrated in Fig (3.9) and (3.10) for the co-current and counter-current cases respectively.

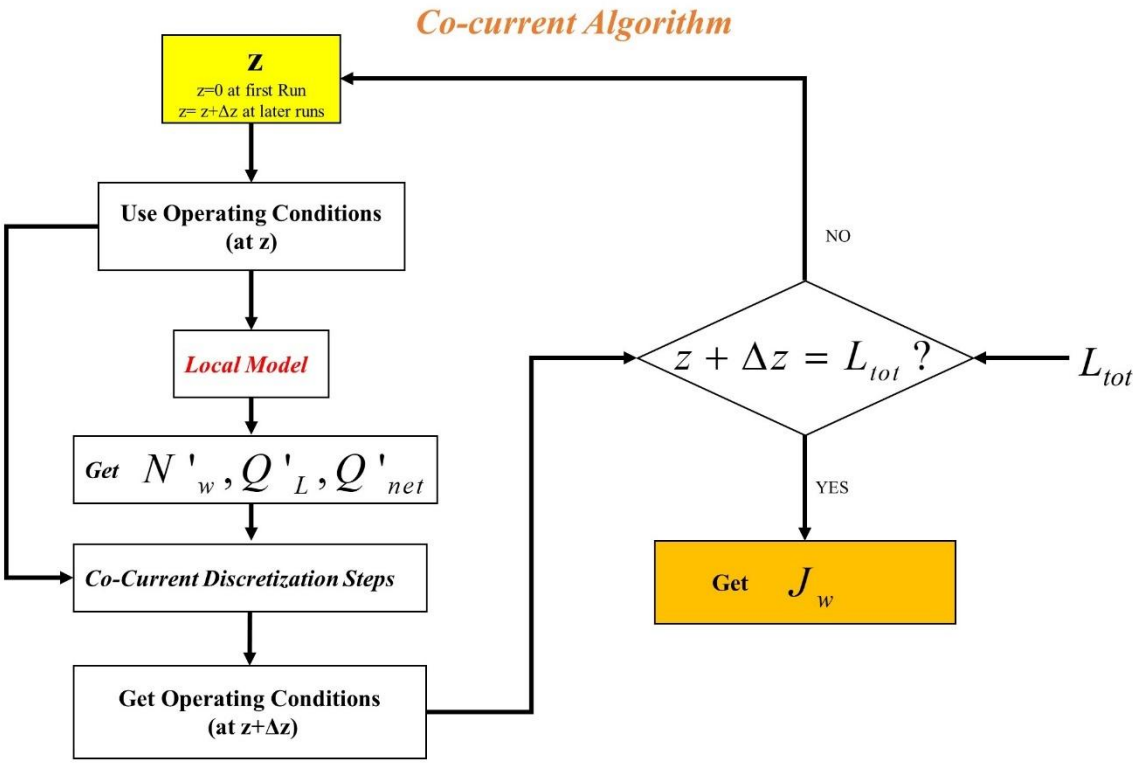

Figure (3.9) *The algorithm used in the solution of the axially discretized SGMD model in case of co-current flow (NaCl(aq.) feed)*

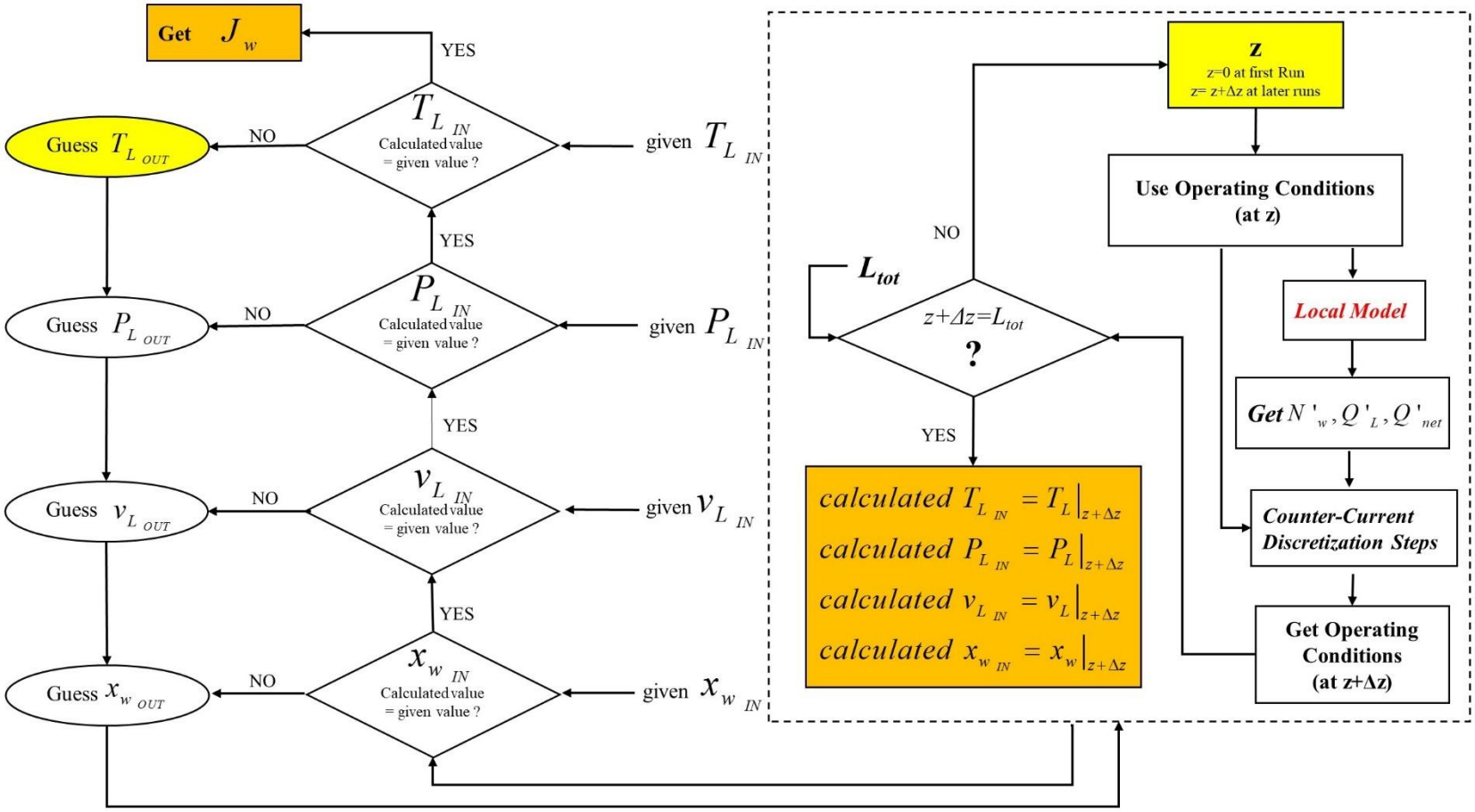

Figure (3.10) *The algorithm used in the solution of the axially discretized SGMD model in case of counter-current flow (NaCl(aq.) feed)*

3.3.3. Constitutive Equations

Solving the local model represented by the set of Eqs. (3.2–3.9) necessitated the use of the constitutive equations required for estimating the mass and heat transfer coefficients in the boundary layers in addition to the membrane mass transfer coefficient and thermal conductivity. Regarding the mass transfer coefficient of water in the membrane, its estimation took place according to an equivalent diffusion coefficient resulting from the contributions of the Knudsen diffusivity $D_{W,Kn}$ and the molecular diffusivity D_{WG} as it has been discussed in Chapter (2). The Bosanquet equation (expressed by Eq (3.24)) [82] was used to estimate the equivalent diffusion coefficient of water in layer j ($D_{Weq,j}$) assuming the mass transfer resistances of the molecular and Knudsen diffusion mechanisms to be lying in series. The Knudsen diffusion coefficient in layer j can be evaluated by Eq (3.25) [1]. In case of modeling according to morphology characterized by the layer-by layer "LBL" method, the mass transfer coefficient of water in each membrane layer was estimated by Eq (3.26) and was used in the estimation of the overall membrane mass transfer coefficient according to Eq (3.27). This was based on summing the mass transfer resistances of each layer to express the overall membrane mass transfer resistance. In case of modeling according to morphology characterized by the average membrane morphology "AMM" method, the average morphological properties of the membrane were used directly in the estimation of the overall membrane mass transfer coefficient instead of using each layer properties.

$$\frac{1}{D_{Weq,j}} = \frac{1}{D_{WG}} + \frac{1}{D_{W,Kn,j}} \tag{3.24}$$

$$D_{W,Kn,j} = \frac{d_{pj}}{3}\sqrt{\frac{8R_gT_m}{\pi M_W}} \tag{3.25}$$

$$k_{Wj} = \left(\frac{\varepsilon}{\tau}\right)_j \frac{D_{Weq,j}}{\delta_j} \tag{3.26}$$

$$\frac{1}{k_{Wm}\, c_m\, \pi\, d_{lm,m}} = \sum_{j=1}^{3,s} \frac{1}{k_{Wj}\, c_j\, \pi\, d_{lm,j}} \tag{3.27}$$

where c represents gas molar concentration. At constant pressure and constant temperature (mean membrane temperature), the gas molar concentration can be assumed to be constant across the membrane.

The thermal conduction across the membrane can be predicted according to the contributions of the membrane solid matrix and the gas entrapped inside the membrane pores. This was done according to the iso-strain approach which is commonly used in modeling the transmembrane heat

transfer in membrane distillation operations [101,191]. The thermal conductivity of membrane layer "*j*" termed by $k_j^{cond.}$ is estimated according to the thermal conductivity of the gas entrapped in the pores $k_G^{cond.}$, the thermal conductivity of the solid matrix $k_{solid}^{cond.}$ and the porosity of layer "*j*" ε_j by Eq(3.28). Apparently, the membrane thermal resistance can be calculated by summing up the thermal resistance of the membrane layers since they are lying in series. In fact, this can enable the prediction of the thermal conductivity of the membrane by Eq (3.29). The value of $k_{solid}^{cond.}$ corresponds to the thermal conductivity of titania estimated at the membrane temperature.

$$k_j^{cond.} = \varepsilon_j \, k_G^{cond.} + \left(1-\varepsilon_j\right) k_{solid}^{cond.} \tag{3.28}$$

$$k_m^{cond.} = \ln\left(\frac{d_{OUT}}{d_{IN}}\right)\left(\sum_{j=1}^{3,s}\frac{\ln\left(\frac{d_{OUT}}{d_{IN}}\right)}{k_j^{cond.}}\right)^{-1} \tag{3.29}$$

The values of Nusselt number (*Nu*) in the liquid and gas boundary layers were predicted using semi-empirical correlations that are typically used for shell-tube heat exchangers. The applied correlations are given in Table (3.6). The Chilton-Colburn analogy incorporating mass and heat transfer [192] was implemented. This aimed at estimating the corresponding values of Sherwood number (*Sh*). This analogy took place based on the same set of correlations in Table (3.6). The dimensionless numbers used in the empirical correlations are collected in Table (3.7).

Table (3.6) *The applied correlation in the estimation of the Nusselt number in the tube and shell sides*

Side	Correlation	Validity range	Eq.	Reference
Tube (liquid)	$Nu = 3.66 + \frac{0.0668\, Gz_H}{1+0.04\, Gz_H^{2/3}}$	$Re < 2100$ $Gz_H < 100$	(3.30)	[193]
	$Nu = \left(3.66^3 + 1.61^3 Gz_H\right)^{1/3}$	$Re < 2100$ $0.1 < Gz_H < 10^4$	(3.31)	[194]
	$Nu = 0.116\left(Re^{2/3} - 125\right) Pr^{1/3}\left[1+\left(\frac{d_{IN}}{L_{tube}}\right)^{2/3}\right]$	$2100 < Re < 10^4$ $60 < \frac{L_{tube}}{d_{IN}} < 250$	(3.32)	[195]
Shell (gas)	$Nu = 0.128\, d_{eq}^{0.6} Re^{0.6} Pr^{1/3}$	$80 < d_{eq} Re < 2\times10^4$	(3.33)	[196,197]

It is worth noting that *(d_{eq})* used in Eq (3.33) is the equivalent shell diameter in inch and is calculated by Eq (3.34). The correlation (Eq (3.33)) was developed by D. A. Donohue [196] to

predict the *Nu* for unbaffled shell-tube heat exchangers considering the effect of tube arrangement on the resulting flow pattern. This was based on the experimental works carried out by B. Short [198] and by R. E. Heinrich et. al [199]. Most of the correlations available in literature for shell-tube heat exchangers were developed for baffled shell configurations which account for the turbulence effects created in the shell-side. The usage of such relations for unbaffled membrane modules could lead to overestimation of the transfer coefficients. This promoted the preference for using the correlation derived by D. A. Donohue during SGMD modeling.

$$d_{eq} = \frac{\left(d_S^2 - N_f\, d_{OUT}^2\right)}{\left(d_S + N_f\, d_{OUT}\right)} \tag{3.34}$$

Table (3.7) *Dimensionless numbers used in the estimation of Nu and Sh numbers*

<table>
<tr><th>Heat transfer</th><th>Mass transfer</th><th>Comments</th></tr>
<tr><td>$Nu = \frac{h\, l^*}{k^{cond.}}$</td><td>$Sh = \frac{k\, l^*}{D_{AB}}$</td><td rowspan="4">$l^* = d_{IN}$ (for tube)
$l^* = d_{OUT}$ (for shell)
$v^* = v_L$ (for tube)
$v^* = v_{0,G}$ (for shell)</td></tr>
<tr><td colspan="2">$Re = \frac{\rho\, v^*\, l^*}{\eta}$</td></tr>
<tr><td>$Pr = \frac{\eta\, \hat{C}p}{k^{cond.}}$</td><td>$Sc = \frac{\eta}{\rho\, D_{AB}}$</td></tr>
<tr><td>$G\,z_H = Re\, Pr\, \frac{d_{IN}}{L_{tube}}$</td><td>$G\,z_M = Re\, Sc\, \frac{d_{IN}}{L_{tube}}$</td></tr>
</table>

The gas interstitial velocity in the shell side $v_{0,G}$ is affected by the module packing factor ε_p , gas total volumetric flow rate $\dot{V}_G$ and shell diameter d_S as given by Eq(3.35).

$$v_{0,G} = \frac{\dot{V}_G}{\left(1-\varepsilon_p\right)\left(\frac{\pi}{4} d_S^2\right)} \tag{3.35}$$

The friction factor *f* used in the pressure gradient estimation is a function of the Reynolds number *Re* as given in Table (3.8). It is worth noting that the characteristic length of the *Re* applied in gas pressure drop estimation is the shell equivalent diameter d_{eq}.

Table (3.8) *The effect of the Reynolds number on the friction factor*

Re	<2300	2300-5000
f	$16 / Re$	$0.079 Re^{-1/4}$

3.4.Results and Discussion

3.4.1. Investigation of Module Performance during SGMD Experiments

The experimental operating conditions of the studied bundles are listed in Table (3.9). The symbols of the measured quantities in the table refer to the same ones shown in the experimental setup representation in Fig (3.1). Given that bundle B2758 possessed the highest LEP value among the studied bundles as it has been mentioned in Table (3.1), this bundle was chosen for relatively long SGMD experimental time spans. Some of the experimental results for the capillary bundle B2758 are shown in Fig (3.11). Two SGMD experimental trials took place for this bundle. Each trial was conducted over two consecutive days. The effect of the liquid temperature on the salt concentration in the recirculating liquid is given by Fig (3.11a) and (3.11b) for trials 1 and 2 respectively. The salt concentration in the liquid is expressed by the salinity (g NaCl/kg liquid).

Table (3.9) *SGMD experimental operating conditions for different bundles and experimental points (The symbols of the measured quantities refer to those in Fig (3.1))*

	Liquid inlet to tube-side (L_{in})						**Gas inlet to shell-side (G_{in})**				
Point	**T2** (°C)	**P3** (bar)	**F3** (L/h)	**C_S** (g/kg)	**v3*** (m/s)	**ΔP** (mbar)	**T1** (°C)	**P1** (bar)	**F0** (m^3_{STP}/h)	**v1**** (m/s)	**Bundle**
B	61.5	4.95	100	18.79	0.39	-	43.0	4.10	5.15	0.56	B2755
C	88.9	2.55	100	18.92	0.39	-	49.0	2.20	2.91	0.60	
D	90.9	2.60	100	19.68	0.39	-	61.0	2.25	2.70	0.57	B2756
E	89.9	2.45	100	18.24	0.39	-	51.5	1.90	1.87	0.45	B2754
F	89.6	2.30	100	18.31	0.39	-	55.5	1.90	1.82	0.44	
H	64.6	3.34	100	19.50	0.45	170	41.7	4.05	1.71	0.58	B2758
I	89.7	3.98	100	19.67	0.45	250	56.1	3.95	0.24	0.63	
J	64.1	2.90	100	19.82	0.45	200	43.1	2.70	1.51	0.58	
K	89.5	4.84	100	20.03	0.45	212	60.8	4.86	4.12	0.90	
L	40.9	2.30	100	18.58	0.45	310	39.3	2.13	2.05	0.98	
M	72.6	2.98	100	18.74	0.45	310	52.5	2.88	2.73	1.01	
N	50.3	5.13	104	18.90	0.46	325	44.5	5.00	4.64	0.96	
O	87.1	5.08	105	19.13	0.47	308	64.5	5.10	4.66	1.00	
P	110.3	5.33	103	19.58	0.46	329	69.8	5.23	4.87	1.03	
Q	110.2	5.25	100	19.93	0.45	290	69.3	5.10	4.76	1.03	
R	70.2	5.18	150	17.97	0.40	331	57.3	5.20	4.84	0.43	B2888
S	89.3	5.13	150	18.75	0.40	296	61.5	5.25	4.87	0.44	
T	90.5	5.03	150	19.58	0.40	251	61.8	5.00	4.63	0.44	
U	91.10	5.05	150	19.95	0.40	264	62.0	5.08	4.66	0.43	

* *liquid velocity in tube-side* ** *Gas interstitial velocity in the shell-side* $\left(v_{0,G}\right)$

The transient and steady regions are both shown in Fig (3.11) to illustrate the experiment proceedings. The initial salinity was around 19.45 g/kg and 19.80 g/kg for the first and second trials respectively. Regarding the experimental points in Table (3.9), points (H, I, J, K) refer to the first trial while points (L, M, N, O, P, Q) refer to the second trial. The maximum liquid temperatures attained during the SGMD experiments were 90°C and 110°C for the first and second trials respectively. It can be demonstrated from Fig (3.11a) and (3.11b) that there was an increase in the salinity of the liquid as the experiments were progressing indicating the transmembrane permeation of water. The rate of increase in salinity was used in estimating the corresponding experimental water flux as calculated by Eq (3.1). The measured salinity and calculated flux are shown in Fig (3.11c) and (3.11d) for trials 1 and 2 respectively. It is worth mentioning that the experimental flux obtained at a given time (t_i) does not correspond to the instantaneous measured temperature and operating conditions at this exact time but corresponds to the average conditions during the time span (Δt) taken between the time at which the current sample was withdrawn (t_i) and the time at which the previous sample was withdrawn (as explained in section 3.2.2.2).

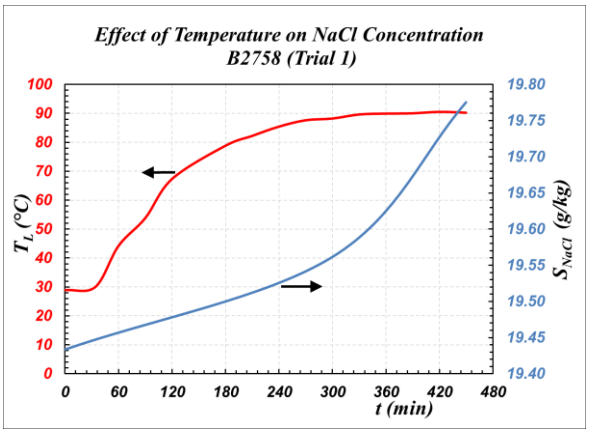

(a)

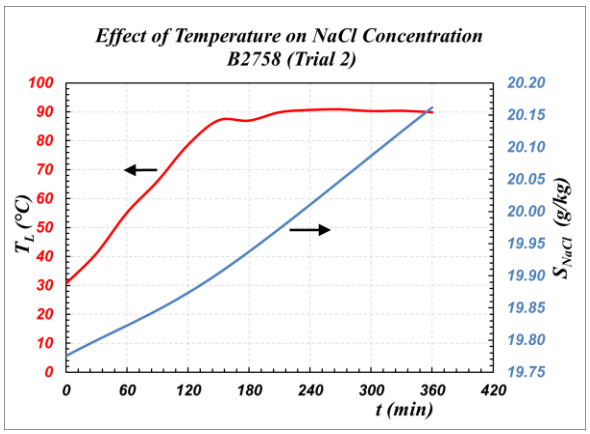

(b)

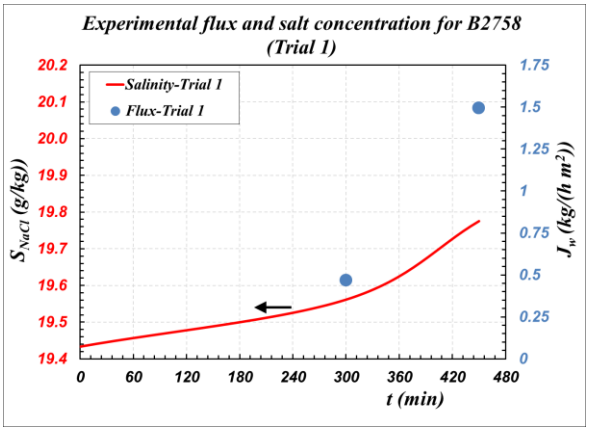

(c)

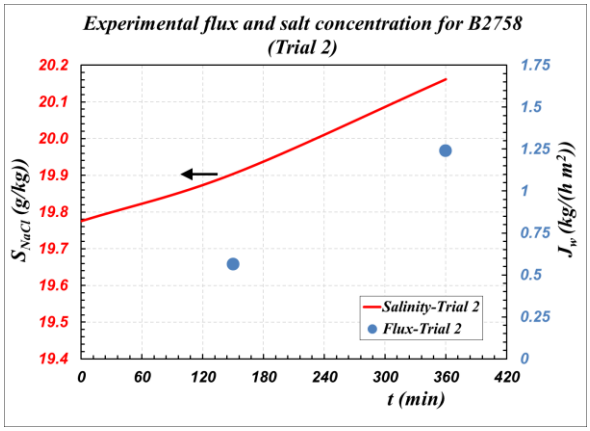

(d)

Figure (3.11) *SGMD experimental results of the bundle B2756 showing: (a) rate of change of liquid temperature and salinity for Trial 1 , (b) rate of change of liquid temperature and salinity for Trial 2, (c) average flux and rate of change of salinity for Trial 1, (d) average flux and rate of change of salinity for Trial 2*

By comparing the heating rate and the corresponding obtained flux for each trial, the enhancement effect of heating on the water flux was observed. This was expected due to the resulting improvement in the mass transfer driving force arising from the exponential dependence of the water vapor pressure on the liquid temperature. However, operating conditions other than the liquid temperature were not strictly fixed as it can be noted from the operating conditions corresponding to the bundle B2758 in Table (3.9). According to the experimental results, the ability of the capillary bundle B2758 to undergo SGMD at relatively high temperature (up to 110°C) was confirmed. Moreover, the undesired phenomena like leakage, flooding and thermal shocks were insignificant during the SGMD experiments. The obtained experimental flux reached values up to 2.5 kg/hm^2. This value could be increased by reducing the gas side pressure during the SGMD experiments.

3.4.2. SGMD Model Validation

The discretized form of the SGMD model in case of the counter-current flow configuration was employed in the estimation of the water flux for the tested capillary bundles in order to compare the experimental flux with the corresponding modeled values. The effect of the number of the axially discretized elements on the estimated flux and gas outlet temperature is given in Fig(3.12). The modeled flux and the gas outlet temperature were chosen to indicate the effect of the discretized length on the mass and heat transfer residuals. A module total length of 20 cm was considered. It can be indicated that by increasing the number of the discretized elements, the modeled values tend to reach steady values such that increasing the number of discretization elements above 10 would result in relatively slight changes in the modeled values. On comparing the results obtained by the local model (at n=1) and those on using 20 discretized elements, the percentage difference between the two approaches is around 2.25% for the modeled water flux and around 20.4 % for the estimated outlet gas. Regarding the modeled water flux, the accepted deviation between the discretized model and the local model for the studied capillary bundles was considered accepted. Therefore, in case computational savings are required, the local model could be used for flux prediction during SGMD in the studied modules.

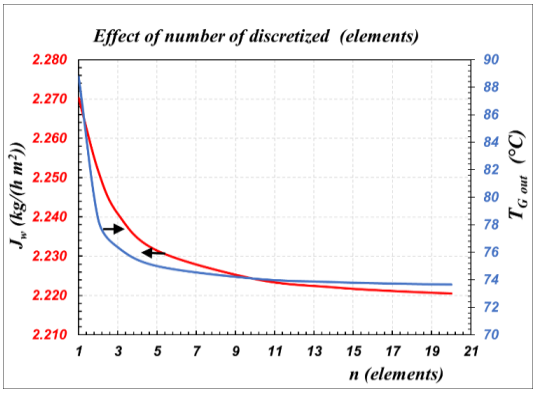

Figure (3.12) *Effect of the number of the axially discretized elements in module on the modeled flux and outlet gas temperature at T_{Lin}=90°C , S_{in}=20gNaCl/kg , v_{Lin}=0.5m/s, T_{Gin}=45°C, P_{Gin}=4.7bar, inlet gas rel.humidity=0%*

The SGMD experimental and modeled water flux results for the studied capillary bundles are given in Fig (3.13). The labeled points in Fig (3.13a) refer to the experimental points corresponding to the operating conditions and bundles reported in Table (3.9). Each of these points is assumed to represent a steady state flux value. For the sake of convenience and on account of the different operating conditions and different bundles (different geometries), a parity chart was applied to consider the different experimental points during the comparison between the experimental and modeled flux results.

The modeled results presented in Fig(3.13a) were estimated by the contributions of the morphological properties of each membrane layer given in Table (3.2) estimated according to the "layer-by-layer" (LBL) approach as it was discussed in Chapter (2). The general trend of the experimental points showed an accepted agreement between the modeled and experimental water flux values except for few points that showed large deviations namely, points E, F and C. These deviations could be attributed to possible experimental errors. As a result, SGMD modeling using the morphological properties characterized by the "layer-by-layer" method was validated.

The confrontation between the modeled results using morphology characterized by the "layer-by-layer" (LBL) method and those following the concept of the "average membrane morphology" (AMM) method (commonly applied in literature [1,36,172]) is presented in Fig(3.13b). The corresponding experimental values are also shown.

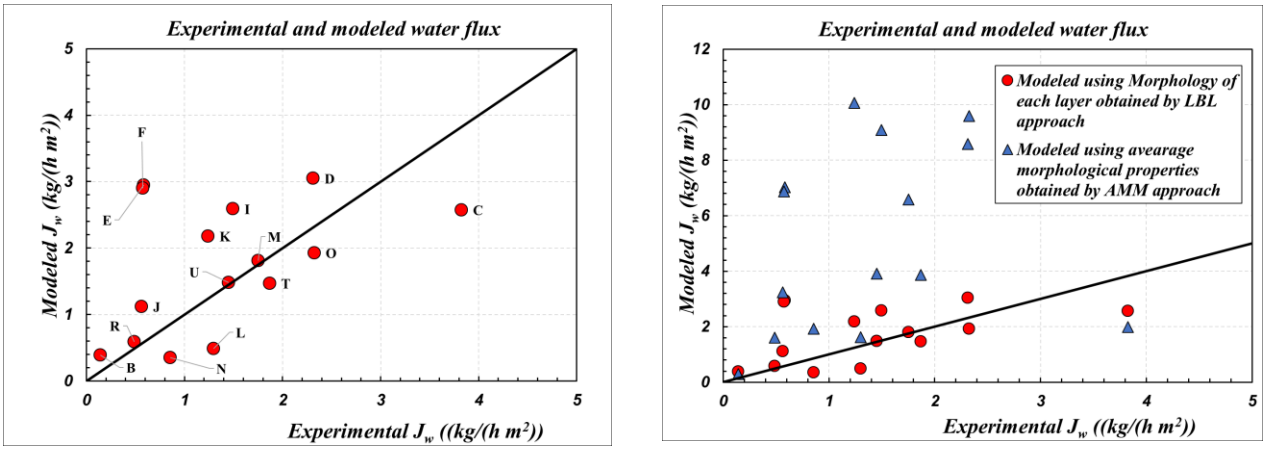

(a) *(b)*

Figure (3.13) *Parity chart for comparing SGMD experimental results with modeled results obtained by the : (a)"Layer-by-layer" method (b) "Layer-by-layer" and "Average membrane morphology" methods (The corresponding operating conditions of each point can be found in Table(3.9))*

The "AMM" approach in SGMD modeling method used the membrane average morphological properties given in Table (3.3). It is quite apparent that the experimental results favor the modeled results using the LBL approach over the modeled results using the AMM method. This could reveal the invalidity of the AMM approach in characterizing the morphological properties of the multi-layer membranes studied in this PhD thesis. Even through the morphological characterization by the AMM approach took place in many works in literature, its ability to estimate the important mass transfer properties showed a quite obvious inconvenience in the case of membranes composed of membrane layers possessing very different morphological properties.

3.4.3. SGMD Simulations

3.4.3.1.Effect of Operating Conditions

Owing to the agreement between the experimental flux values and those obtained by the axially discretized SGMD model following the LBL approach, this modeling approach was utilized in predicting the effect of the operating conditions on the water flux. This was done for the case of counter-current flow of the liquid feed (NaCl(aq.)) and the sweeping gas (dry air) considering the geometric parameters and morphological properties of the bundle B2758 which can be found in Tables (3.1) and (3.2) on using a module length of 20 cm. The corresponding modeled results are given in Fig (3.14). The fixed operating conditions corresponding to the results shown in Figures (3.14a – 3.14f) are reported in Table (3.10).

The effect of the liquid temperature on the water flux is shown in Fig (3.14a). At a given gas pressure, the flux increased exponentially with the liquid temperature. This was expected due to the exponential increase of the water vapor pressure with the liquid temperature. At a neglected water partial pressure in the shell side, increasing the temperature would result in an exponential increase in the mass transfer driving force during the SGMD operation.

The effect of the liquid velocity on the flux is shown in Fig (3.14b). Increasing the liquid velocity led to improvements in the flux. This could be attributed to the fact that increasing the turbulence in the liquid side could mitigate the negative effects of the concentration and polarization phenomena. However, increasing the liquid velocity above a certain value results in negligible improvements in the flux.

The effect of the salinity could be pinpointed in Fig (3.14b) and (3.14c). Increasing the salinity of the liquid feed corresponded to a reduction in the flux. This reduction is related to the reduced water activity on increasing the salt content in the liquid feed which could negatively affect the

vaporization at the liquid-membrane interface and consequently decreases the mass transfer driving force.

The effect of the gas interstitial velocity, pressure and temperature are shown in Fig (3.14d), (3.14e) and (3.14f) respectively. Rising the gas interstitial velocity enhanced the obtainable flux. However, this enhancement effect decreased as the gas velocity increased. In fact, as the velocity of the sweeping gas increases, the corresponding water partial pressure in the permeate side decreases. That is true until the gas flow rate is much greater than the transmembrane water flow rate where further increase in the gas flow rate will not significantly improve the driving force due to the absence of appreciable amount of water vapor in the permeate side.

The flux could be also improved by decreasing the gas pressure as shown in Fig (3.14e). This is due to the fact that decreasing the gas pressure facilitates the vaporization process and favors the equilibrium mole fraction of water in the gaseous state at the liquid/membrane interface according to Eq (3.5).

The negative effect of the relative humidity on the mass transfer driving force could also be indicated in Fig (3.14d) and (3.14e) since the relative humidity represented the vapor partial pressure of water in the permeate side. Finally, it can be indicated from Fig (3.14f) that the gas inlet temperature has a negligible effect on the flux. This demonstrates that the heat transfer resistance in the gas side could be negligible. It is worth noting that the effects of the operating conditions on the modeled flux go in agreement with the observations obtained in many works in literature dedicated to the experimental and/or modeling studies of SGMD [82,111,184,200,201].

Table (3.10) *The fixed operating conditions used in Figs (3.14a-3.14f)*

Figure	3.14a	3.14b	3.14c	3.14d	3.14e	3.14f
$T_{L\,in}$ *(°C)*	*	*	*	100	100	*
$P_{L\,in}$ *(bar)*	*	2	2	2	2	2
S_{in} *(g/kg)*	20	*	*	45	45	45
$v_{L\,in}$ *(m/s)*	0.5	*	0.5	0.5	0.5	0.5
$T_{G\,in}$ *(°C)*	45	45	45	45	45	*
$P_{G\,in}$ *(bar)*	*	1.7	1.7	1.7	*	1.7
Rel. humidity (%)	0	0	0	*	*	0
$v_{G\,in}$ *(m/s)*	1	1	1	*	1	1

* *variable condition indicated in the corresponding figure*

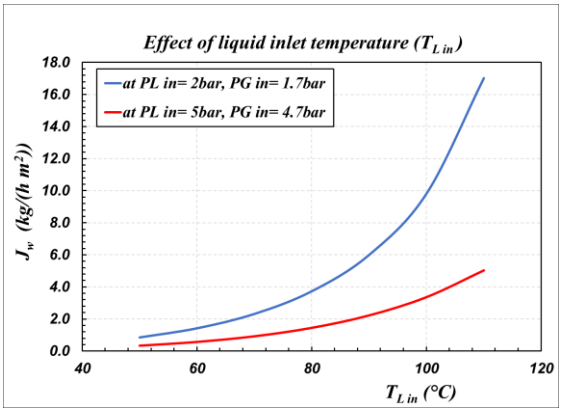

(a)

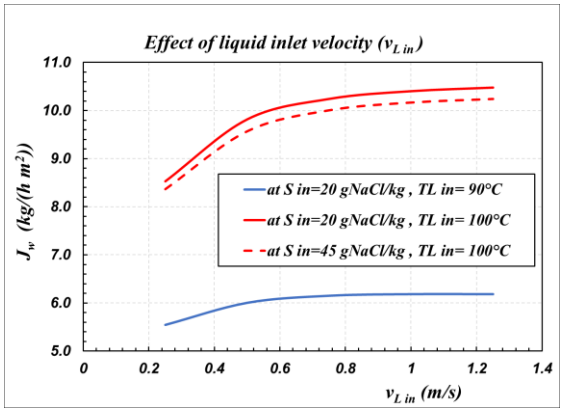

(b)

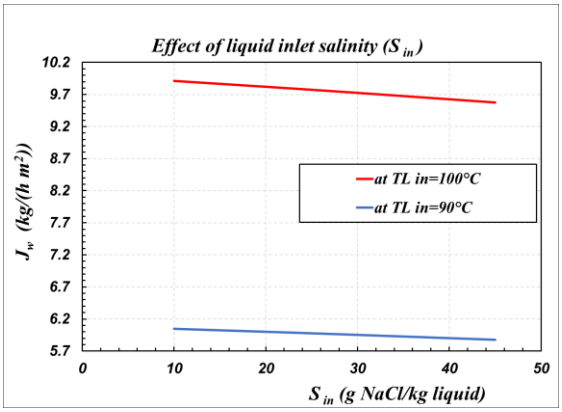

(c)

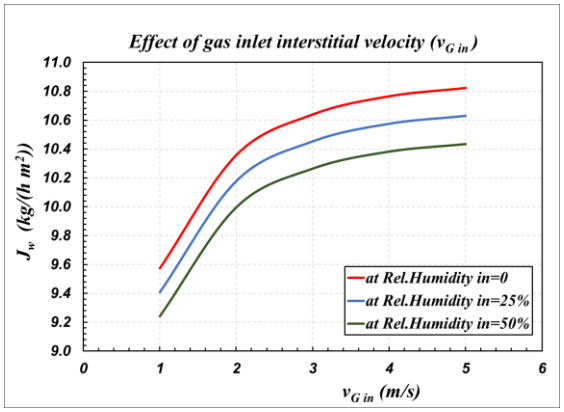

(d)

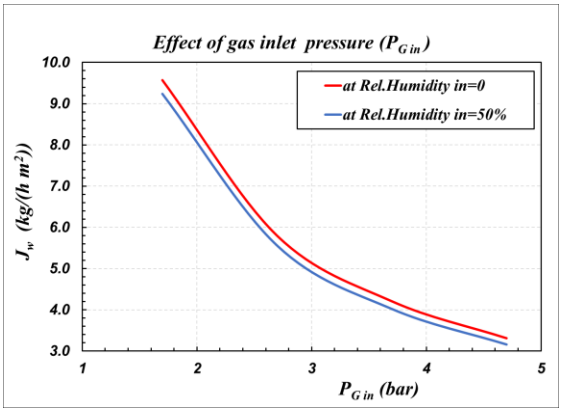

(e)

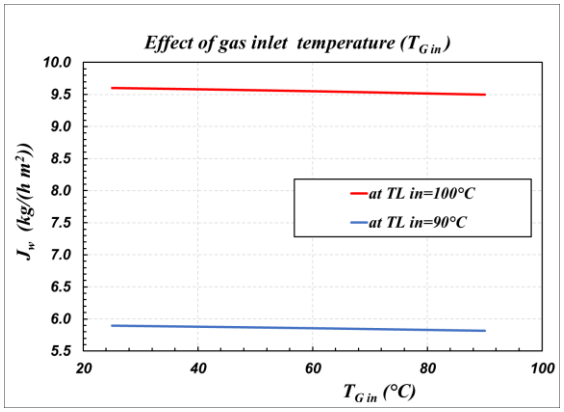

(f)

Figure (3.14) *The effect of the inlet operating conditions on the modeled flux in case of counter-current flow for the bundle B2758. The varied inlet operating conditions are: (a) Liquid temperature (b) Liquid velocity (c) Liquid salinity (d) Gas interstitial velocity (e) Gas pressure (f) Gas temperature (The fixed operating conditions in each figure are reported in Table(3.10))*

It is worth noting that the effects of the operating conditions on scale formation (inorganic fouling) were not investigated in the modeling study conducted in this PhD thesis. However, operating conditions like temperature, pH, concentration and velocity of the feed play an important role in the scaling degree in membrane distillation (MD) operations [1]. Seawater contains dissolved ions like Ca^{2+}, Mg^{2+}, CO_3^{2-}, SO_4^{2-} , etc. which could lead to the deposition of salts as $CaCO_3$, $CaSO_4$ and $Mg(OH)_2$ at certain operating conditions. The building up of scale on the membrane surface could lead to membrane fouling resulting in partial pore clogging and wetting [1, 99]. Consequently, a decline in the operation performance and resulting flux quantity and quality might be engendered especially in case of supersaturated solutions [1, 9]. Still, fouling in MD is considered less problematic than RO and UF due to the relatively large pore possessed by membranes used in MD operations [9]. In case of irreversible scaling, the flux and membrane performance could be restored by washing using demineralized water [1].

The effect of the temperature gradient on the scale formation of a certain salt depends on the nature of this salt [1]. In case of solutes having positive solubility/temperature coefficients, increasing the feed temperature promotes the solubility of such solutes as NaCl for example. On the contrary, in case of solutes possessing negative solubility/temperature coefficients, increasing the feed temperature could exacerbate scale formation like $CaCO_3$ and $CaSO_4$. Other solutes could experience opposite dependence of the solubility on the liquid temperature according to the operating temperature range as $NaSO_4$. Accordingly, in multi-effect distillation (MED), the typical maximum operating temperature in the first stage (effect) during seawater desalination does not exceed 120°C to avoid scale formation. For the same reason and application, the operating temperature does not exceed 110°C in case of multi-stage flash (MSF) operations [1]. Following this concept, the experimental and modeling studies performed in this PhD thesis regarded 110°C as the maximum feed temperature during SGMD operations for seawater desalination purposes aiming at avoiding both, pore wetting and scale formation. In addition to the effect of temperature on the solubility constant, the excessive rate of vaporization at relatively high operating temperatures could lead to an increase in the salt concentration in the liquid. In fact, this could result in supersaturation engendering crystallization and scale formation. Such phenomenon can be appreciable in case of high water flux and high initial salt content in feed [1, 9].

The scale formation could be mitigated by increasing the feed velocity, decreasing the pH values and using antiscalant compounds [1, 83]. However, low pH values can exacerbate corrosion rates in the process equipment. The high feed velocity in the membrane module reduces the concentration polarization in the feed side which mitigates the accumulation of solutes on the membrane surface [83]. Therefore, operating conditions and feed pretreatment procedures could be optimized to ensure a scale-free SGMD at relatively high temperatures. This matter would necessitate a further study which might constitute some restrictions on the applicable ranges of operating conditions.

3.4.3.2.Axial Profiles in The Module

The axially discretized SGMD model applying the "layer-by-layer" approach was used to investigate the axial profiles in case of the bundle B2758 having a length of 20 cm. This was done for NaCl (aq.) feed having an inlet temperature of 90°C, inlet velocity in the tube-side of 0.5 m/s, pressure of 1.5 bar and salinity of 40 g NaCl/kg liquid. The sweeping gas used for this case was dry air introduced at 30°C and 1.3 bar and flowing with an interstitial velocity of 3 m/s. The corresponding axial profiles are shown in Fig (3.15) and Fig (3.16) for the counter-current and co-current configurations respectively.

For the counter-current flow configuration, the axial profiles of the liquid and the gas stream are shown in Fig (3.15a). It is worth noting that the gas enters at z=0 and the liquid enters at z=0.2 m. It can be easily observed that the gradient of the gas temperature is much greater than the gradient of the liquid temperature. However, a slight drop in the liquid inlet temperature could be pinpointed such that the percentage reduction in the liquid temperature along the module was found to be around 1.8 %. As for the sweeping gas, the percentage increase in its temperature along the module was found to be around 128% increase. This can be attributed to the relatively high liquid mass flow rate when compared to that of the gas stream. This would result in a liquid heat capacity that is significantly higher than that of the sweeping gas stream.

The profiles of the NaCL salt mole fraction (X_s) in the liquid feed and the mole fraction of water vapor (y_{wG}) in the sweeping gas are given in Fig(3.15b) for the counter-current configuration. On one side, there was a slight increase in the water content in the permeate side due to the water transmembrane flow rate from the feed side such that the mole fraction of water vapor at the sweeping gas outlet was almost 0.07 mol/mol. On the other side, negligible change in the salt concentration in the liquid side was noticed. This could also be attributed to the large liquid mass flow rate when compared to that of the sweeping gas.

The water flux profile is shown in Fig (3.15c). It can be demonstrated that the water flux increases along the positive axial direction. In other words, the flux is enhanced from the gas inlet towards the gas outlet. However, this enhancement declines along the positive axial direction. Besides, the percentage increase in the flux along the module was found to be around 1.3 %. In fact, the profile of the flux is greatly affected by the profiles of the liquid temperature and the water concentration in the shell side. Along the positive axial direction, the liquid temperature slightly increases towards the liquid inlet where the maximum liquid temperature exists. As the liquid temperature increases, the vapor pressure of the liquid increases exponentially. This could lead to an improvement in the driving force across the membrane. This could explain the reason of the flux increase along the positive axial direction. However, along the positive axial direction, the water content in the shell-side increases. This could result in a reduction in the mass transfer driving force This could also explain the reason behind the declination in the enhancement effect of the liquid temperature on the obtained flux along the positive axial direction.

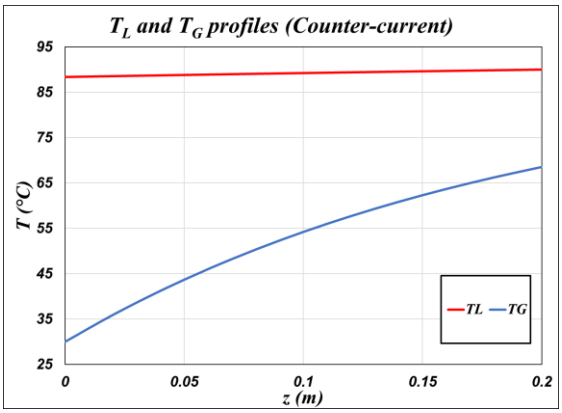

(a)

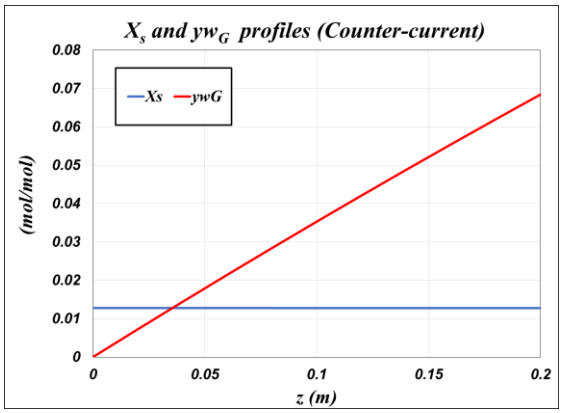

(b)

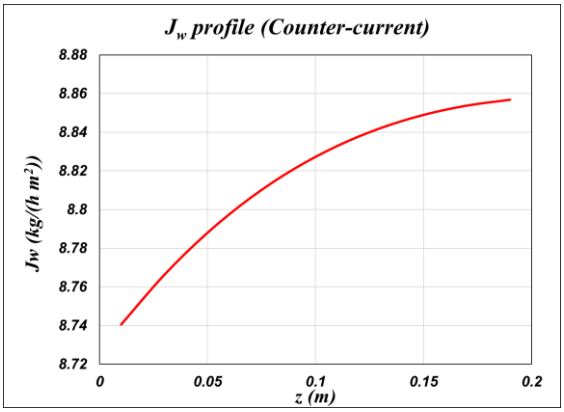

(c)

Figure (3.15) *SGMD modeled results in case of counter-current flow between NaCl(aq.) feed and dry air sweeping gas for the bundle B2758 showing profiles of: (a) Liquid and gas temperatures (b) Mole fractions of salt in liquid and water vapor in gas (c) water flux (at T_{Lin}=90°C , S_{in}=40gNaCl/kg , v_{Lin}=0.5m/s, T_{Gin}=30°C, P_{Gin}=1.3bar)*

In case of the co-current flow configuration, the profiles of the liquid and gas temperatures are shown in Fig (3.16a) while the profiles of the mole fraction of the NaCl salt in the liquid and the mole fraction of the water content in the sweeping gas are presented in Fig (3.16b). The same observations noted in case of the counter-current flow hold true for the co-current configuration. The gradients in the gas temperature and concentration are much greater than the corresponding values in the liquid due to the relatively high liquid mass flow rate with respect to that of the sweeping gas.

The water flux profile in case co-current configuration is shown in Fig (3.16c). It is quite apparent that the flux profile in case of counter-current flow (given by Fig (3.15c)) is very different than that of the co-current flow. The maximum flux is at the inlet of the gas and the liquid which corresponds to z=0 and then the flux decreases steadily along the axial direction of the module in

case of the co-current flow as it could be observed in Fig (3.16c). This is attributed to the fact that along the positive axial direction, the liquid temperature slightly decreases and the water content in the shell side increases. Both of these two phenomena reduce the mass driving force across the positive axial direction of the membrane. It is worth noting that at the same operating conditions, the modeled water fluxes were 8.8 and 9.9 kg/(h m^2) for the counter-current and the co-current configurations respectively. Although the flux resulting from the co-current configuration is higher than that obtained from the counter-current configuration, the fact that the driving force diminishes along the module favors the application of the counter-current configuration. At longer axial lengths, the counter-current flux would surpass that of the co-current configuration. Besides, on using modules in series inside SGMD vessels for large-scale applications, the driving force in co-current configuration will vanish at short vessel lengths requiring many unnecessary inter-stage operations.

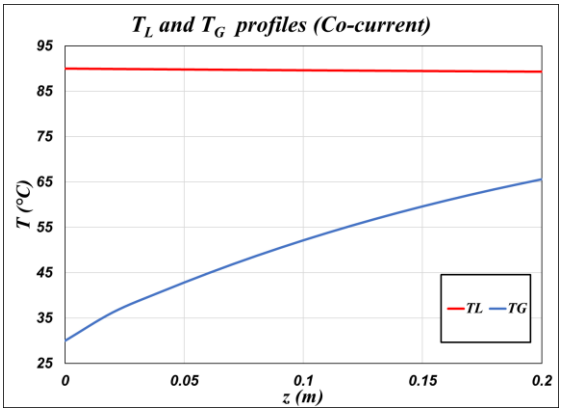

(a)

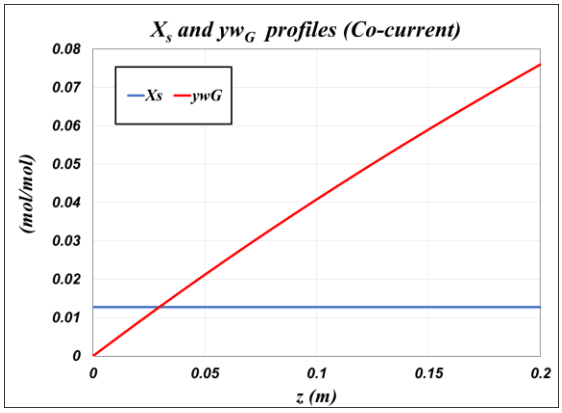

(b)

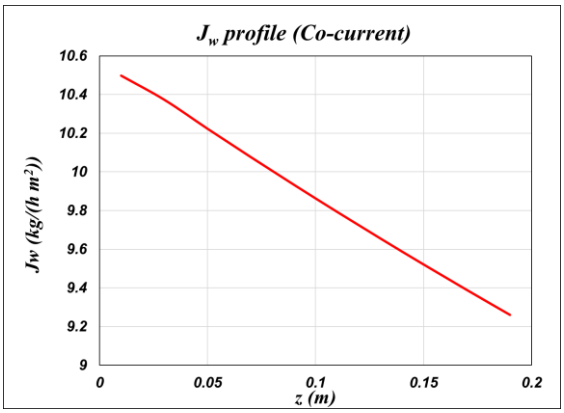

(c)

Figure (3.16) *SGMD modeled results in case of counter-current flow between NaCl(aq.) feed and dry air sweeping gas for the bundle B2758 showing profiles of: (a) Liquid and gas temperatures (b) Mole fractions of salt in liquid and water vapor in gas (c) water flux (at T_{Lin}=90°C , S_{in}=40gNaCl/kg , v_{Lin}=0.5m/s, T_{Gin}=30°C, P_{Gin}=1.3bar)*

3.4.3.3.Contributions of Knudsen and Molecular Diffusion Mechanisms

In order to evaluate the contributions of the molecular (ordinary) and Knudsen diffusion mechanisms in the membrane mass transfer, a comparison took place between modeled results considering both mechanisms and modeled results considering only the molecular diffusion. This is represented in Fig (3.17) for the bundle B2758 using the axially discretized SGMD model following the "layer-by-layer" (LBL) modeling approach. This was done for the cases reported in Table (3.11). The co-current flow configuration was modeled in case of NaCl (aq.) feed and dry air sweeping gas. It is worth noting that in case of neglecting the Knudsen diffusion and considering only the molecular diffusion, the equivalent diffusion coefficient becomes identical to the molecular diffusion coefficient.

Table (3.11) *The operating conditions of the cases used in Fig (3.17)*

Case	Basic	A	B	C	D
$T_{L\ in}$ *(℃)*	90	70	90		
$P_{L\ in}$ *(bar)*	2.5	2.5	3.5	2.5	
S_{in} *(g/kg)*	40				
$v_{L\ in}$ *(m/s)*	0.5				1.2
$T_{G\ in}$ *(℃)*	30				
$P_{G\ in}$ *(bar)*	2.3		3.3	2.3	
Rel. humidity (%)	0				
$v_{G\ in}$ *(m/s)*	1			3	1

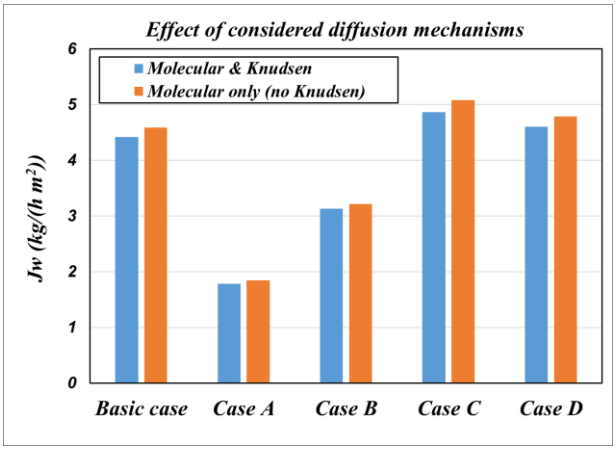

Figure (3.17) *SGMD modeled flux bundle B2758 at the co-current configurations for the cases considering molecular and Knudsen diffusion and the cases considering only the molecular diffusion. (The operating conditions of the cases are reported in Table (3.11))*

According to the results shown in Fig (3.17), at different operating conditions, the deviations between the modeled results considering the two mechanisms (molecular and Knudsen diffusion mechanisms) and the modeled results considering only the molecular diffusion mechanism were negligible with a percentage difference around 3%. This observation affirms that molecular diffusion controls the diffusion mechanism and that the Knudsen diffusion role could be neglected.

This was expected because typically, at operating gas pressure values above the atmospheric pressure, the Knudsen diffusion in the large pores of the membrane (especially the support layer) could play an insignificant role with respect to the molecular diffusion [136]. The different modeled cases illustrated that the flux could be improved by increasing the temperature, the gas velocity and the liquid velocity and by decreasing the gas pressure due to the reasons that have been already discussed in the section regarding the effect of the operating conditions.

3.5. Conclusions

Sweeping gas membrane distillation (SGMD) experimental and modeling studies were performed for the ceramic capillary bundles. Experimental results confirmed the ability of the modules to undergo SGMD operations at relatively high temperatures (up to 110°C) without significant problems like wetting, flooding, leakage and thermal shocks.

On one side, there was an acceptable agreement between the experimental results and the modeled results obtained by following the "layer-by-layer" (LBL) modeling approach by utilizing the morphological properties of each membrane layer. On the other side, modeling the SGMD using the "average membrane morphology" (AMM) approach by considering the membrane average morphological properties resulted in big deviations between the modeled and experimental water flux. Therefore, it was observed that treating the multi-layer membrane as a single membrane of average morphological properties (according to the AMM approach) was inconvenient for modeling and module investigation of the multilayer membranes studied in this thesis.

The axially discretized model was used in simulating SGMD cases. Results showed that the flux increased exponentially with the liquid temperature and was improved by decreasing the gas pressure and by increasing the liquid and gas velocities. Moreover, the flux was found to be almost independent of the value of the gas inlet temperature indicating that the gas thermal resistance was negligible. The negative effect of increasing the liquid inlet salinity or the gas inlet humidity was also confirmed and estimated.

According to the axial profiles in the module during SGMD, the gradients of the gas temperature and concentration were much higher than the corresponding values for the liquid stream in case of co-current and counter-current flow configurations. This was attributed to the relatively high mass flow rate of the liquid when compared to that of the gas. The flux profiles revealed that it is a decreasing function of the length of the module in case of co-current configuration. As for the counter-current configuration, the flux profile is affected by two phenomena opposing each other such that in one direction the mass transfer driving force is improved by the increase in liquid temperature while in the same direction, the driving force is reduced by the increase in water content in the permeate side. This would require optimization of the total SGMD unit length at given operating conditions. In fact, this will be discussed in Chapter (5).

Finally, modeling was used to compare the effect of the considered diffusion mechanisms on the obtained flux at different operating conditions. Results demonstrated that the molecular diffusion controlled the diffusion mechanism inside the membrane and that the Knudsen diffusion contribution is quite negligible.

List of Symbols

Latin Letters	
A	Area
$\tilde{C}_p$	Molar heat capacity at constant pressure
$\hat{C}_p$	Specific heat capacity at constant pressure
c	Total molar concentration
d	Diameter
d_p	Pore diameter
D_{Weq}	Equivalent diffusion coefficient of water
D_{WG}	Molecular diffusion coefficient of water in the gas
$D_{W,Kn}$	Knudsen diffusion coefficient of water
f	Friction factor
Gz	Graetz number
h	Convective heat transfer coefficient
J	Mass flux
k	Mass transfer coefficient
$k^{cond.}$	Thermal conductivity coefficient
L	Length
l^*	Characteristic length
$< \dot{m}''_w\|_{t_i} >$	Average molar flow rate of water permeating across the membrane at time t_i
m	Mass
M	Molecular weight
$\dot{n}$	Molar flow rate per fiber (tube)
n	Number of axially discretized units in the SGMD model
N'_w	Molar flow rate of water per unit length and per fiber (tube)
N_f	Number of fibers (tubes)
Nu	Nusselt number
P	Pressure
P^*	Vapor pressure
Pr	Prandtl number
Q'	Heat energy flow rate per unit length and per fiber (tube)
R_g	Universal gas constant

Re	Reynolds number
Sh	Sherwood number
Sc	Schmidt number
t	Time
T	Temperature
V	Velocity
$v_{0,G}$	Interstitial velocity of gas
v^*	Characteristic velocity
$\dot{V}$	Volumetric flow rate
x	Mole fraction in the liquid state
y	Mole fraction in the vapor state
Z	Axial direction
Greek Letters	
γ	Activity coefficient
δ	Thickness
ε	Porosity
ε_p	Packing factor of the module
η	Dynamic viscosity
λ	Latent heat of vaporization per mole
ρ	Density
τ	Tortuosity
Subscripts and Superscripts	
a	Air
eff	Effective
eq	Equivalent
G	Gas
Gm	Gas/membrane interface
Gb	Gas bulk
H	Heat transfer
IN	Inner or inlet
j	Layer j
L	Liquid
lm	Logarithmic mean
Lb	Liquid bulk
m	Membrane
M	Mass transfer
net	Net amount
OUT	Outer or outlet
S	NaCl salt

S	Shell
solid	Solid matrix in membrane
tube	Tube-side
w	Water

[This page intentionally left blank]

Chapter Four

Modeling Sweeping Gas Membrane Distillation of Ethanol Aqueous Solution

4.1.Introduction

Even though most of the studies in literature related to membrane distillation (MD) focus on the seawater desalination application, the removal of volatile organic compounds (VOCs) by MD can have a wide range of industrial applications. This could include biofuel processing [157,161–163], wastewater treatment [24,136] and pollution mitigation in surface and groundwater [139–141]. Ethanol is one of the commonly studied VOCs that can be separated from aqueous solutions by MD due to the possible applications in bioethanol dewatering [161], ethanol separation from fermentation broth [57] and in wastewater treatment [136]. Different MD configurations were studied for the (water/ethanol) separation like the vacuum membrane distillation (VMD) [24,57,202–204] , air gap membrane distillation (AGMD) [162] and sweeping gas membrane distillation (SGMD) [136,161]. Besides, the application of membrane contactors in ethanol extraction was studied by C. Gostoli et al. [205] utilizing glycerol extractant in the permeate side.

During the separation of VOCs present in aqueous solutions by MD, both water and the VOCs are capable of permeation across the membrane. The Maxwell-Stefan modeling approach is recommended for the description of the permeation of multi-component mixtures during MD operations [205–208] since it considers the interdependence of the fluxes of the involved permeating species. This approach is named after its developers who were the Scottish physicist J. C. Maxwell and the Austrian scientist J. Stefan [209]. The Maxwell-Stefan approach is considered as an extension to Fick's law for a multicomponent gas mixture [180]. In general, Fick's law is applicable for the description of diffusion in binary gases where there is only one independent flux, one independent diffusion coefficient and one independent concentration gradient [210]. This is not true in the case of multicomponent gases due to the involvement of more than two species in the gas mixture. The concentration gradients are correlated and need to be determined in order to describe the diffusion of each species [100,211]. In the multicomponent mixture, molecule-molecule collisions take place between all the involved species. According to the Maxwell-Stefan approach, for an ideal gas mixture, the number of collisions per unit volume and per unit time between molecules of two different species is directly proportional to the product of their concentrations and the difference between their velocities such that the flux of each species is affected by the exchanged momentum with the other species [209,212].

In theoretical studies, F. A. Banat et al. used the Maxwell-Stefan approach to investigate the use of the AGMD in breaking the formic acid/water and propionic/water azeotropes [206–208]where modeling was validated by experimental results [213,214]. In some cases, both the Fickian diffusion and the Maxwell-Stefan modeling were used and compared. The experimental results went in agreement with the Maxwell-Stefan modeled results more than those estimated by the simple Fickian diffusion.

In the current chapter, the employment of SGMD in (water/ethanol) separation using hydrophobic ceramic membranes was investigated using modeling studies. The model used in the simulation of the modules during SGMD of ethanol (aq.) followed the same concept as that used in the investigation of the modules during SGMD of NaCl (aq.) as it was discussed in Chapter (3). However, the case of ethanol (aq.) experiences more complications due to the permeating of both water and ethanol. The Maxwell-Stefan approach was followed in expressing the molecular diffusion of the water and ethanol molecules across the membrane putting into account the effect of the mutual interaction between the permeating species on the final resulting diffusion rate of each species. According to the modeling elaborations from Chapter (3), the molecular diffusion was found to be the controlling diffusive mechanism with insignificant role played by the Knudsen diffusion. Therefore, in the current chapter, the transmembrane mass transfer of water and ethanol during SGMD was assumed to take place by the molecular diffusion mechanism. The developed model considered the geometrical parameters and the morphological properties of the ceramic capillary bundle B2758 characterized and investigated in Chapters (2) and (3). The local model developed in the current chapter enabled the estimation of the mass flux of each species, the heat flux, the membrane interfacial temperatures and the radial concentration profile inside the membrane. The discretization of the module was employed in the estimation of the axial gradients of the operating conditions, mass transfer driving force of each species, the flux of each species in addition to the 2-D representation of the concentration of each species inside the membrane domain. This has resulted in a better demonstration of the axial and radial gradients of the mass transfer driving force for water and ethanol. The modeling results were also utilized in comparing the performance of the modules in case of co-current and counter-current flow manners.

4.2.Materials

As it has been already mentioned in Chapter (2), the capillary bundles studied in this PhD thesis were manufactured by the Fraunhofer Institute for Ceramic Technologies and Systems (IKTS, Hermsdorf, Germany). They were represented by hydrophobic ceramic multi-layer membranes such that the membrane is composed of four layers that possess different morphological properties. The developed model in the current chapter used the geometric parameters and morphological properties of the Bundles B2758. Details about the geometric parameters of bundle B2758 and the morphological properties of its layers can be found in Chapter (3). Details regarding the manufacturing process, the characterization steps and the hydrophobization protocols of the membranes were discussed in Chapter (2).

4.3.Modeling of Sweeping Gas Membrane Distillation of Ethanol (aq.) Solution

The SGMD of ethanol (aq.) in the characterized tubular bundles was modeled and simulated using a similar manner to that discussed in Chapter (3). The model was discretized in order to account for the gradients of the operating conditions. This was done along the axial direction (z-

direction) of the module. A MATLAB code was developed for the required computational execution. The following assumptions were considered in the developed model.

- Steady-state
- The liquid feed is allocated in the tube-side while the sweeping gas (Nitrogen) is allocated in the shell-side.
- No mass and heat losses to the surroundings (well-insulated and leakage-free system)
- The sweeping gas is insoluble in the liquid feed.
- The transmembrane mass transfer was due to the molecular diffusion described by the Maxwell-Stefan equations where the effect of the interactions between the permeating species was assumed to be only significant in the membrane domain.
- Ideal gas behavior of the sweeping gas
- The gas stream in the shell side flows parallelly to the tubes.
- The fibers are identical and uniformly packed in the shell ensuring uniform hydrodynamics.
- High homogeneity of each membrane layer.

4.3.1. Local Model

The mass transfer of the permeating species (water and ethanol) occurs over three consecutive steps which are:

1) Mass transfer across the liquid boundary layer
2) Diffusion across the membrane pores
3) Mass transfer across the gas boundary layer

The total molar flow is equal to the sum of the molar flow rates of water and ethanol according to Eq (4.1). The flow rates in this equation are per fiber having a unit length.

$$N'_{w} + N'_{et.} = N'_{TOT} \tag{4.1}$$

The subscripts (*TOT*), (*w*), (*et.*) refer to "total", "water" and "ethanol" respectively. According to the film theory [187], the total molar flow rate in a single fiber per unit length can be expressed by Eq (4.2) in the liquid boundary layer. Similarly, Eqs (4.3) and (4.4) express the mass transfer in the gas boundary layer.

$$N'_{TOT} = \frac{k_{et,L}\,\rho_L}{M_L} \ln\left(\frac{\psi_{et.} - x_{et,Lm}}{\psi_{et.} - x_{et,Lb}}\right) \pi d_{IN} \tag{4.2}$$

$$N'_{TOT} = \frac{k_{w,G}\,P_G}{R_g T_G} \ln\left(\frac{\psi_{w} - y_{w,Gb}}{\psi_{w} - y_{w,Gm}}\right) \pi d_{OUT} \tag{4.3}$$

$$N'_{TOT} = \frac{k_{et,G}\, P_G}{R_g T_G} \ln\left(\frac{\psi_{et.} - y_{et,Gb}}{\psi_{et.} - y_{et,GI}}\right) \pi d_{OUT} \tag{4.4}$$

where, ρ, M, P, T, R_g refer to density, molecular weight, pressure, temperature and universal gas constant respectively. The subscripts (*Lm*), (*Lb*), (*Gm*), (*Gb*) refer to the liquid/membrane interface, liquid bulk, gas/membrane interface and gas bulk respectively. $k_{et,L}, k_{et,G}, k_{w,G}$ represent the mass transfer coefficients of ethanol in the liquid, ethanol in the gas and water in the gas respectively. The area of mass transfer in each boundary layer was considered such that d_{In}, d_{OUT} refer to the inner and outer diameters of the membrane respectively. The mole fractions in liquid and vapor states are represented by x, y respectively. ψ represents the ratio between the molar flow rate of the permeating species with respect to the total molar flow rate. It is defined by Eq (4.5) and (4.6) for water and ethanol respectively. Obviously, Eq (4.7) can be used to explicitly calculate this ratio for one component by knowing that of the other.

$$\psi_w = \frac{N'_w}{N'_{TOT}} \tag{4.5}$$

$$\psi_{et.} = \frac{N'_{et.}}{N'_{TOT}} \tag{4.6}$$

$$\psi_w + \psi_{et.} = 1 \tag{4.7}$$

The vapor/liquid equilibrium taking place at the pore entrance at the liquid/membrane interface can be expressed by Eqs. (4.8) and (4.9) for water and ethanol respectively. It is worth noting that the activity coefficients were calculated by the NRTL model as applied by C. Gostoli et al. for the same components during ethanol extraction by membrane contactors [205].

$$y_{w,Lm}\ P_G = P^*_{w(T_{Lm})}\ \ \gamma_{w(T_{Lm},\, x_{w,Lm})}\ \ x_{w,Lm} \tag{4.8}$$

$$y_{et,Lm}\ P_G = P^*_{et(T_{Lm})}\ \ \gamma_{et\,(T_{Lm},\, x_{et,Lm})}\ \ x_{et,Lm} \tag{4.9}$$

where P^*, γ, T_{Lm} refer to the vapor pressure, activity coefficient and temperature at the liquid/membrane interface respectively.

For the ternary gas (water/ethanol/N_2) in the membrane pores, the mass transfer of water vapor and ethanol across the stagnant N_2 entrapped inside the pores was modeled according to the Maxwell-Stefan approach as expressed by Eqs. (4.10) and (4.11) [210] respectively while the radial gradient in the concentration of N_2 was estimated by Eq (4.12). The membrane interfacial concentrations were used as the boundary conditions.

$$\frac{-dy_w}{dr} = \left(\frac{N'_{TOT}}{2\pi r}\right)\left(\frac{\tau}{\varepsilon}\right)_j\left(\frac{R_g T_m}{P_G}\right)\sum_{\substack{q=1\\q\neq i}}^{3}\left(\frac{y_q\psi_w - y_w\psi_q}{D_{w,q}}\right) \tag{4.10}$$

$$\frac{-dy_{et.}}{dr} = \left(\frac{N'_{TOT}}{2\pi r}\right)\left(\frac{\tau}{\varepsilon}\right)_j\left(\frac{R_g T_m}{P_G}\right)\sum_{\substack{q=1\\q\neq i}}^{3}\left(\frac{y_q\psi_{et.} - y_{et.}\psi_q}{D_{et.,q}}\right) \tag{4.11}$$

$$\frac{dy_{N_2}}{dr} = \frac{-dy_w}{dr} + \frac{-dy_{et.}}{dr} \tag{4.12}$$

$$at\ r = R_{IN} \quad \Rightarrow \quad y_w = y_{w,Lm}\ ,\ y_{et.} = y_{et.,Lm}\ ,\ y_{N_2} = y_{N_2,Lm} = 1 - y_{w,Lm} - y_{et.,Lm}$$

$$at\ r = R_{OUT} \quad \Rightarrow \quad y_w = y_{w,Gm}\ ,\ y_{et.} = y_{et.,Gm}\ ,\ y_{N_2} = y_{N_2,Gm} = 1 - y_{w,Gm} - y_{et.,Gm}$$

r represents the radial direction which is the direction of the transmembrane flow. $(\tau/\varepsilon)_j$ refers to the tortuosity-porosity ratio of layer j. R_{IN} and R_{OUT} represent the inner and outer membrane radii respectively. T_m refers to the membrane temperature while $D_{w,q}$ represents and the molecular diffusion coefficient of water in a binary gaseous mixture composed of water and component (q). At a given axial position, radial discretization took place by dividing the thickness of the membrane into elements having a thickness of (Δr) each. The finite-difference numerical method was implemented to transform the differential equations (Eqs. (4.10-4.12)) into a system of nonlinear algebraic equations. It is worth noting that the radial discretization considered the variation in morphological properties according to the radial position inside the membrane pore since the four membrane layers possess different morphological properties. A scheme representing the radial discretization in the membrane domain is shown in Fig (4.1).

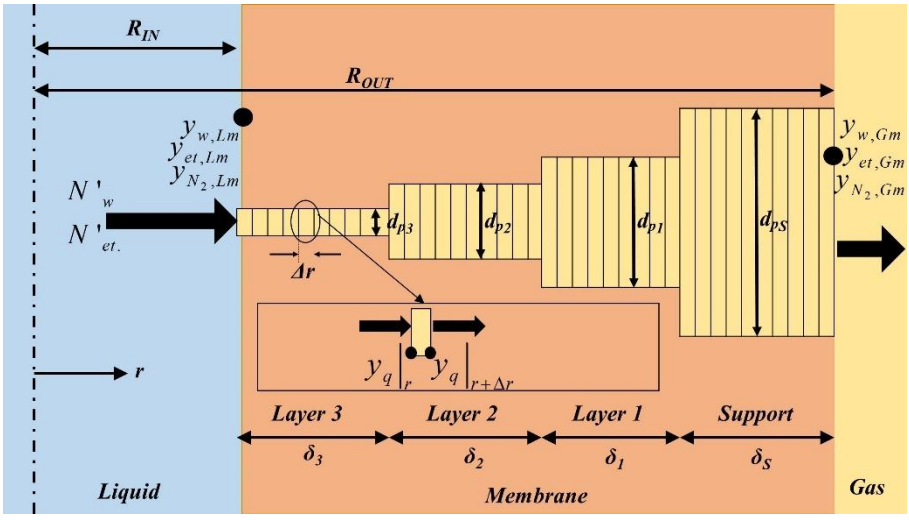

Figure (4.1) *Representation of the radial discretization of the mole fractions of water, ethanol and nitrogen in the multi-layer membrane for the local model at a given axial position*

In addition to mass transfer, heat transfer takes place during SGMD as well. This happens over the following steps.

1) Heat transfer through the thermal liquid boundary layer. The heat transfer rate per unit axial length for a single fiber across the liquid thermal boundary layer Q'_L can be estimated by Eq (4.13).
2) At the liquid/membrane interface, a fraction of the heat transferred from the liquid bulk is employed in vaporizing the permeating stream composed of water and ethanol while the remaining fraction represents the net heat energy Q'_{net}.
3) Thermal conduction through the membrane at neglected convective contribution. This is described by Fourier's law [188] according to Eq (4.14).
4) Heat transfer through the thermal gas boundary layer from the gas-membrane interface towards the gas bulk as expressed by Eq (4.15).

$$Q'_L = h_L \left(T_{Lb} - T_{Lm}\right) \pi d_{IN} \tag{4.13}$$

$$Q'_{net} = \frac{k_m^{cond.}\, 2\pi \left(T_{Lm} - T_{Gm}\right)}{\ln\left(d_{out} / d_{in}\right)} \tag{4.14}$$

$$Q'_{net} = h_G (T_{Gm} - T_{Gb}) \pi\, d_{out} \tag{4.15}$$

where, $k_m^{cond.}, h$ represent the thermal conductivity of the membrane and the convective heat transfer coefficient respectively. The heat balance at the liquid/membrane interface can be expressed by Eq (4.16).

$$Q'_L = \dot{N}'_w \lambda^w_{(T_{Lm})} + \dot{N}'_{et.} \lambda^{et}_{(T_{Lm})} + Q'_{net} \tag{4.16}$$

where, $\lambda^w_{(T_{Lm})}, \lambda^{et}_{(T_{Lm})}$ represent the latent heat of vaporization for water and ethanol respectively evaluated at the temperature of the liquid/membrane interface T_{Lm}. By simple algebraic operations, Eq (4.16) can be written in the form of Eq (4.17) to explicitly express the total molar flow rate per axial unit length in a single fiber.

$$N'_{TOT} = \frac{\left(h_L (T_{Lb} - T_{Lm}) \pi d_{in}\right) - Q'_{net}}{\psi_w \lambda^w_{(T_{Lm})} + \psi_{et.} \lambda^{et}_{(T_{Lm})}} \tag{4.17}$$

At a given axial position, the local model was used to obtain the mass and heat fluxes in addition to the membrane interfacial temperatures and the membrane concentration radial profile for water and ethanol. The local model was solved iteratively. The graphical representations of the solution strategy and the algorithm followed in the local model are shown in Fig (4.2) and (4.3) respectively.

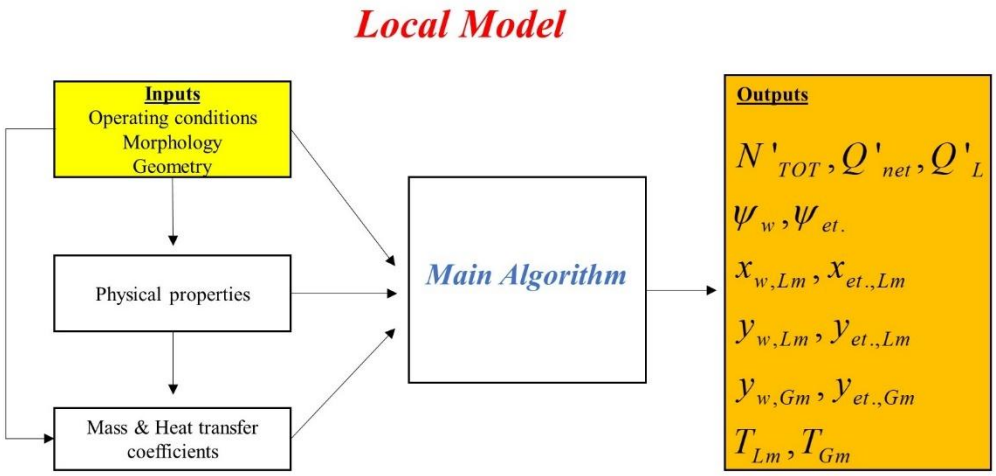

Figure (4.2) *The strategy of the solution of the SGMD local model (ethanol(aq.) feed)*

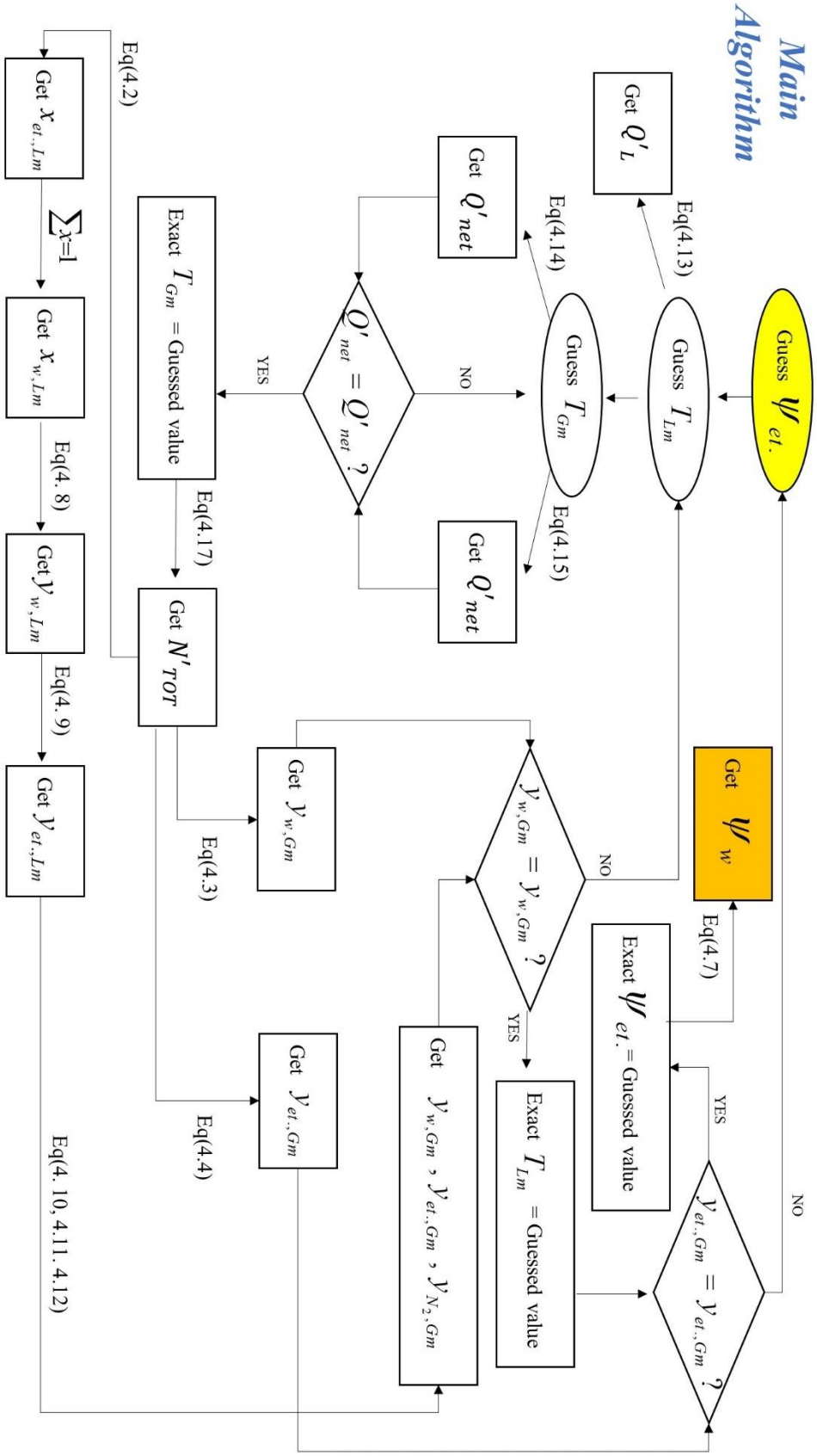

Figure (4.3) *The algorithm used in the solution of the SGMD local model (ethanol(aq.) feed)*

4.3.2. Modeling according to Plug Flow Concept

Similar to what has been mentioned in Chapter (3), the axial discretization took place by dividing the module into elements (units) connected in-series along the axial direction (z-direction) applying the plug flow model concept. Each element represents a control volume of constant physical properties for each of the two streams. The discretization schemes in case of co-current and counter-current flow manners can be illustrated by Figs (4.4) and (4.5) respectively.

Although the length of the studied bundle B2758 is 20 cm, longer separation lengths were simulated by the developed axially discretized SGMD model. In the industrial scale, the SGMD modules could be connected with each other in series and in parallel inside a vessel (SGMD vessel). The total axial separation length (L_{tot}) represents the length of the vessel which equals to the sum of the lengths of the modules connected in series after neglecting the length of the connections between the connected modules. Apparently, as the value of (L_{tot}) increases, the effect of the axial gradients of the operating conditions on the resulting fluxes also increase. In such cases, the local model would be considered inconvenient for accurate prediction of the fluxes. Therefore, the effect of (L_{tot}) on the overall separation performance was investigated by the axially discretized developed SGMD model. For a single fiber, the differential transfer equations in the axial direction describing the SGMD of ethanol (aq.) are given in Table (4.1) and (4.2) for the liquid feed and the sweeping gas respectively.

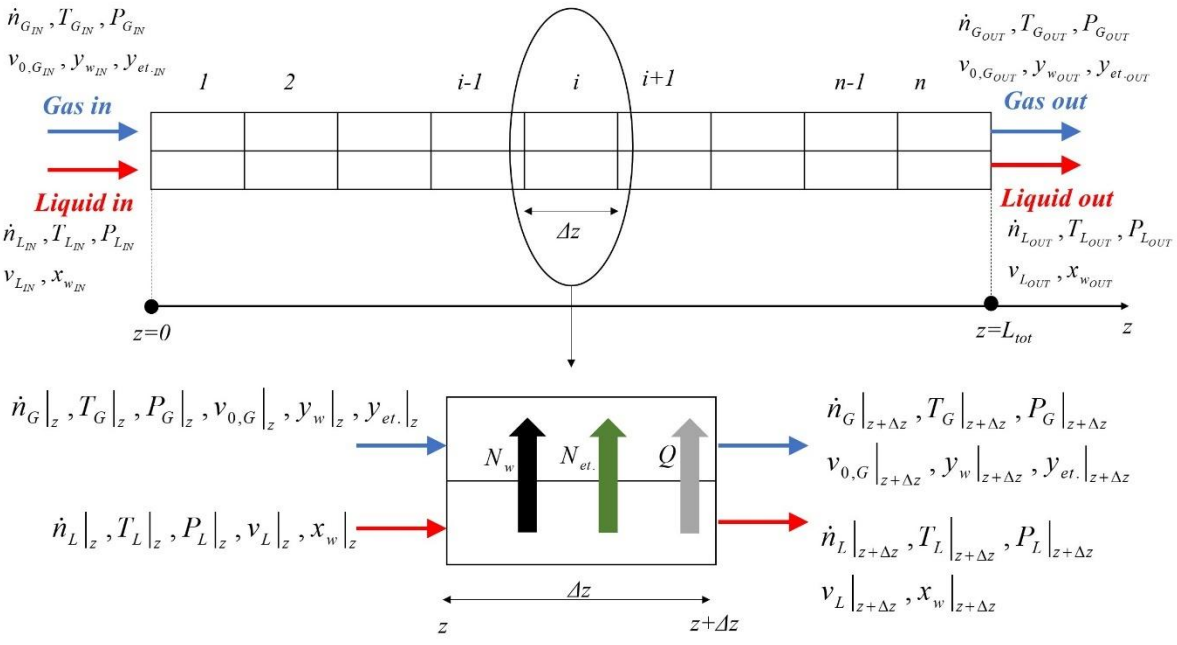

Figure (4.4) *Representation of the axial discretization of the module in case of co-current flow (ethanol(aq.) feed)*

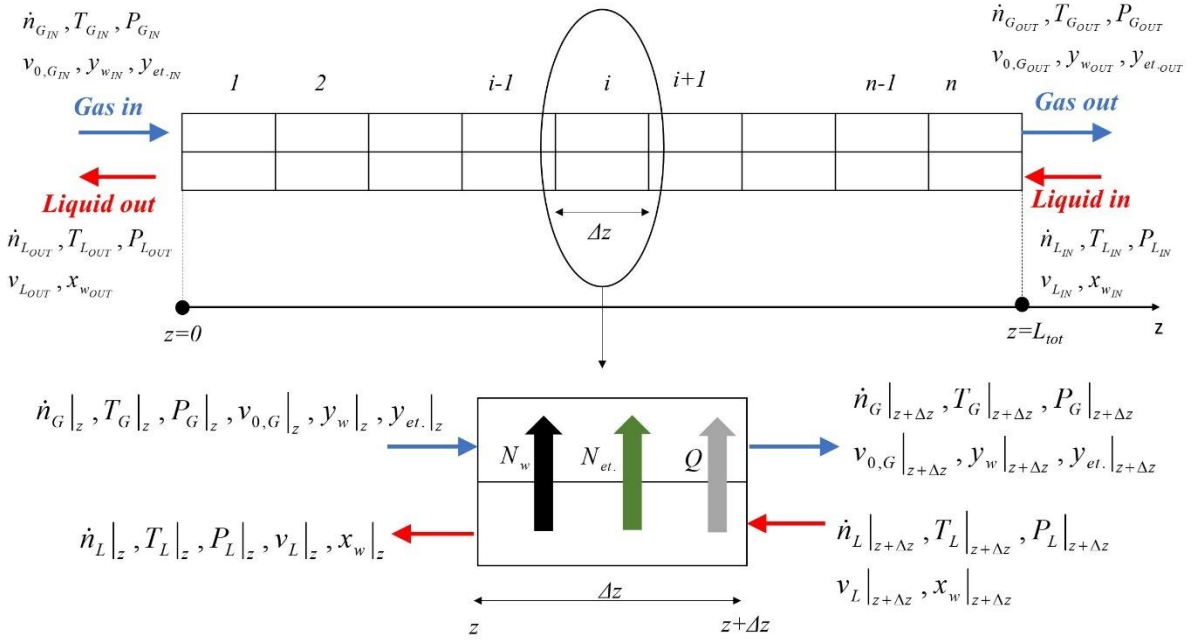

Figure (4.5) *Representation of the axial discretization of the module in case of counter-current flow (ethanol(aq.) feed)*

Table(4.1) *Governing axial differential transfer equations in the liquid feed*

Co-current	Counter-current	Comments	Eq.
$\frac{d\dot{n}_L}{dz} = -N'_{TOT}$	$\frac{d\dot{n}_L}{dz} = N'_{TOT}$	From total mass balance	(4.18)
$\frac{d\dot{n}_{w,L}}{dz} = -N'_{w}$	$\frac{d\dot{n}_{w,L}}{dz} = N'_{w}$	From water mass balance	(4.19)
$\frac{d\dot{n}_{et,L}}{dz} = -N'_{et.}$	$\frac{d\dot{n}_{et,L}}{dz} = N'_{et.}$	From ethanol mass balance	(4.20)
$\frac{dT_L}{dz} = \frac{-Q'_L}{\dot{n}_L M_L \hat{C}_{p,L}}$	$\frac{dT_L}{dz} = \frac{Q'_L}{\dot{n}_L M_L \hat{C}_{p,L}}$	From heat balance	(4.21)
$\frac{dv_L}{dz} = \frac{-4N'_{TOT}\left(M_w\psi_w + M_{et.}\psi_{et.}\right)}{\pi\, d_{IN}^2\ \rho_L}$	$\frac{dv_L}{dz} = \frac{4N'_{TOT}\left(M_w\psi_w + M_{et.}\psi_{et.}\right)}{\pi\, d_{IN}^2\ \rho_L}$	From continuity equation	(4.22)
$\frac{dP_L}{dz} = -4f\rho_L\frac{v_L^2}{2d_{IN}}$	$\frac{dP_L}{dz} = 4f\rho_L\frac{v_L^2}{2d_{IN}}$	Darcy–Weisbach equation[189]	(4.23)

Table(4.2) *Governing axial differential transfer equations in the sweeping gas*

Co-current or Counter-current	Comments	Eq.
$\frac{d\dot{n}_G}{dz}=\frac{d\dot{n}_{w,G}}{dz}+\frac{d\dot{n}_{et,G}}{dz}+\frac{d\dot{n}_{N_2,G}}{dz}$	From total mass balance	(4.24)
$\frac{d\dot{n}_{w,G}}{dz}=N'_{w}$	From water mass balance	(4.25)
$\frac{d\dot{n}_{et,G}}{dz}=N'_{et.}$	From ethanol mass balance	(4.26)
$\frac{d\dot{n}_{N_2,G}}{dz}=0$	From nitrogen mass balance	(4.27)
$\frac{dT_G}{dz}=\frac{Q'_{net}}{\dot{n}_G\tilde{C}_{P,G}}$	From heat balance	(4.28)
$\frac{d\rho_G}{\rho_G dz}=\frac{-dT_G}{T_G dz}+\frac{dP_G}{P_G dz}+\frac{\left(M_w-M_{N_2}\right)dy_w}{M_G dz}+\frac{\left(M_{et.}-M_{N_2}\right)dy_{et.}}{M_G dz}$	From ideal gas law	(4.29)
$\rho_G\left(\frac{dv_{0,G}}{dz}\right)+v_{0,G}\left(\frac{d\rho_G}{dz}\right)=\frac{4N'_{tot}\left(M_w\psi_w+M_{et.}\psi_{et.}\right)}{\pi\left(\frac{d_S^2}{N_f}-d_{OUT}^2\right)}$	From continuity equation	(4.30)
$\frac{dP_G}{dz}=\frac{8N_f\eta_G v_{0,G}}{d_S^2\left(\frac{1}{2}\left(\frac{\ln(\varepsilon_p)}{1-\varepsilon_p}+1+\frac{1-\varepsilon_p}{2}\right)\right)}$, $\varepsilon_p=N_{f,tot}\left(\frac{d_{OUT}}{d_S}\right)^2$	From equivalent annulus theorem [190]	(4.31)

$\dot{n}$ represents the molar flow rate per fiber while f,ε_p,η_G refer to the friction factor, the module packing factor and the gas viscosity respectively. $v_L,v_{0,G}$ represent the liquid velocity in the tube side and the gas interstitial velocity in the shell side respectively.

As it has been mentioned in Chapter (3) the expression of the sweeping gas pressure gradient was based on the equivalent annulus theorem introduced by C. Gostoli et al. [190] in case of laminar flow. In case of non-laminar flow, Eq (4.32) was used to estimate the gas pressure gradient.

$$\frac{dP_G}{dz}=-4\frac{f}{d_{eq}}\rho_G\frac{v_{0,G}^2}{2} \qquad (4.32)$$

Dirichlet boundary conditions were specified for the governing equations in the SGMD of ethanol (aq.) according to the inlet conditions of both streams. In case of co-current flow, the following boundary conditions were used.

$$at\ z=0:\quad \dot{n}_G=\dot{n}_{G,IN},\quad \dot{n}_{N_2}=\dot{n}_{G,IN},\quad T_G=T_{G,IN},\quad P_G=P_{G,IN}$$

$$v_{0,G}=v_{0,G,IN},\quad \rho_G=\rho_{G,IN},\quad y_w=0,\quad y_{et.}=0$$

$$at\ z=0:\quad \dot{n}_L=\dot{n}_{L,IN},\quad \dot{n}_w=x_{w,IN}\dot{n}_{L,IN},\quad \dot{n}_{et.}=x_{et.,IN}\dot{n}_{L,IN},\quad T_L=T_{L,IN},\quad P_L=P_{L,IN},\quad v_L=v_{L,IN}$$

In case of counter-current flow, the following boundary conditions were used.

$$at\ z=0:\quad \dot{n}_G=\dot{n}_{G,IN},\quad \dot{n}_{N_2}=\dot{n}_{G,IN},\quad T_G=T_{G,IN},\quad P_G=P_{G,IN}$$

$$v_{0,G}=v_{0,G,IN},\quad \rho_G=\rho_{G,IN},\quad y_w=0,\quad y_{et.}=0$$

$$at\ z=L_{tot}:\quad \dot{n}_L=\dot{n}_{L,IN},\quad \dot{n}_w=x_{w,IN}\dot{n}_{L,IN},\quad \dot{n}_{et.}=x_{et.,IN}\dot{n}_{L,IN},\quad T_L=T_{L,IN},\quad P_L=P_{L,IN},\quad v_L=v_{L,IN}$$

Eventually, the mass fluxes (based on the membrane inner area) of water J_w and ethanol J_{et} obtained from a SGMD vessel having a total length L_{tot} can be calculated by Eq (4.33) and (4.34) respectively.

$$J_w=\frac{1}{L_{tot}}\int_0^{L_{tot}} J_{w,z}\,dz \tag{4.33}$$

$$J_{et}=\frac{1}{L_{tot}}\int_0^{L_{tot}} J_{et,z}\,dz \tag{4.34}$$

Following the same approach discussed in Chapter (3), the finite-difference numerical method was employed to transform the governing axial differential equations into a system of nonlinear algebraic equations. MATLAB code was developed for the computational requirements. For n axially discretized units (elements) having a uniform axial thickness Δz , Eq(4.33) and (4.34) could be written in the form of Eq (4.35) and (4.36) respectively. Then, the total mass flux from the SGMD vessel can be simply calculated by Eq(4.37).

$$J_w=\frac{M_w}{n\,\pi d_{IN}}\sum_{i=1}^{n} N'_{w,i} \tag{4.35}$$

$$J_{et}=\frac{M_{et}}{n\,\pi d_{IN}}\sum_{i=1}^{n} N'_{et,i} \tag{4.36}$$

$$J_{TOT}=J_w+J_{et} \tag{4.37}$$

The algorithms implemented in the iterative solution of the axially discretized models are demonstrated in Figs (4.6) and (4.7) for the co-current and counter-current cases respectively.

4.3.3. Constitutive Equations

Constitutive equations were required for solving the model represented in the current chapter. These equations were used in the estimation of the mass and heat transfer coefficients in the liquid and gas boundary layers in addition to the prediction of the membrane thermal conductivity and the friction factor utilized in the estimation of the axial pressure gradients. The same constitutive equations and the same empirical correlations of Nusselt and Sherwood numbers applied in modeling the SGMD of NaCl (aq.) in Chapter (3) were applied in modeling the SGMD of ethanol (aq.) as well. However, there is no need to estimate the mass transfer coefficient of each species in the membrane for the case corresponding to the SGMD of ethanol (aq.) since the Maxwell-Stefan was adopted in describing the transmembrane mass transfer in this case.

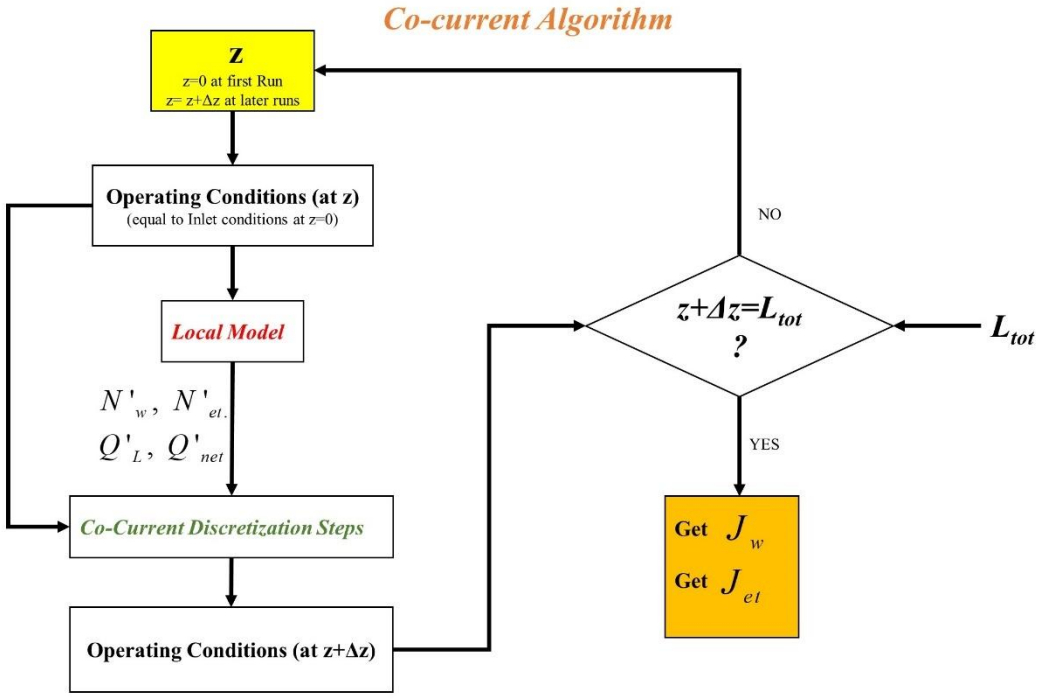

Figure (4.6) *Algorithm used in the solution of the axially discretized SGMD model for co-current flow (ethanol(aq.) feed)*

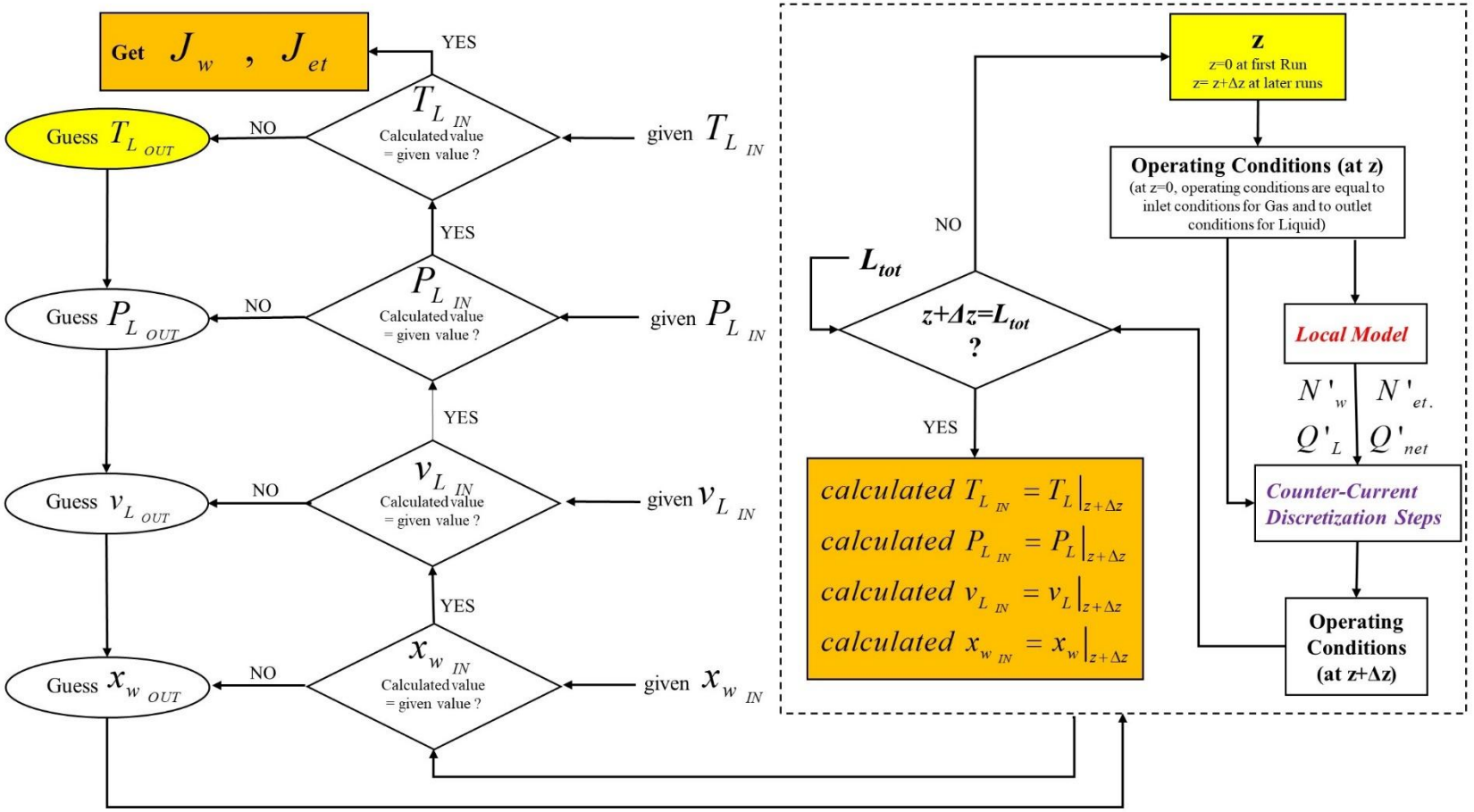

Figure (4.7) *The algorithm used in the solution of the axially discretized SGMD model in case of counter-current flow (ethanol(aq.) feed)*

4.4.Results and Discussion

The effect of the number of the axially discretized elements on the modeled water and ethanol fluxes is shown in Fig (4.8) in case of counter-current flow for the module B2758. This considers the case corresponding to a feed entering the SGMD module at temperature of 110 °C, velocity of 0.5 m/s, pressure of 3.3 bar and ethanol mass fraction $\omega_{et.}$ of 0.1 kg/kg in addition to dry sweeping gas that is introduced to the module at 25°C and 3 bar and flowing at an interstitial velocity of 3 m/s. As demonstrated by the results, for the module B2758 (having a length of 20 cm), the improvement effect of the number of discretization elements (units) on the accuracy of the obtained fluxes becomes relatively negligible at above 10 elements. In other words, the discretization can be accepted at a discretization length of 2 cm. Therefore, the following simulations will be modeled using a discretization length that is not larger than 2 cm

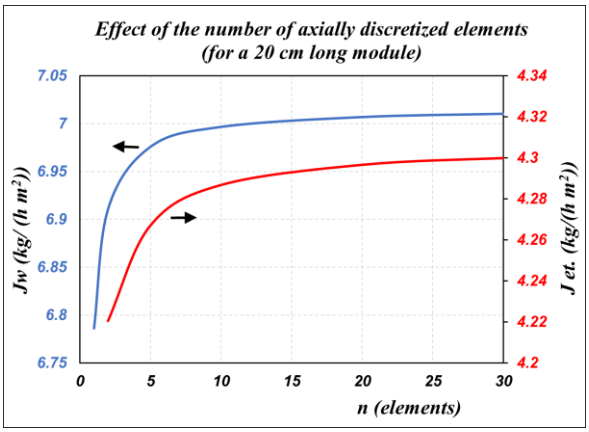

Figure (4.8) *Effect of the number of the axially discretized elements in module on modeled fluxes of water and ethanol at T_{Lin}=110°C , $\omega et._{in}$=0.1kg/kg , v_{Lin}=0.5m/s, v_{Gin}=3/s, T_{Gin}=25°C, P_{Gin}=3 bar, inlet gas rel.humidity=0%*

4.4.1. Effect of SGMD Operating Conditions for a Single Module

The effect of the operating conditions on the modeled fluxes of water and ethanol in case of counter-current flow were inspected for the bundle B2758 as illustrated in Fig (4.9). The used fixed operating conditions for the Figs (4.9a – 4.9f) are listed in Table (4.3). Fluxes were found to increase exponentially with the liquid inlet temperature (See Fig (4.9a)). In fact, this was expected due to the exponential dependence of the vapor pressure of each component on the liquid temperature. Therefore, in case of neglected vapor pressure of water and ethanol in the shell side, their corresponding mass transfer driving forces can be enhanced exponentially with the liquid temperature. Besides, elevating the liquid inlet temperature increases the obtainable ratio of ethanol

mass flux to water mass flux ($J_{et.}/J_w$). This could be attributed to the fact that higher temperatures favor the percentage removal of the highly volatile component (ethanol) with respect to the less volatile component (water).

Table (4.3) *The fixed operating conditions used in Figs (4.9a-4.9f)*

Figure	5.10a	5.10b	5.10c	5.10d	5.10e	5.10f
$T_{L\,in}$ (°C)	*	105	90	90	90	105
$P_{L\,in}$ (bar)	3.3	3.3	2.3	1.6	2.3	3.3
$v_{L\,in}$ (m/s)	0.5	*	0.5	0.5	0.5	0.5
$x_{et\,in}$ (kg ethanol/kg)	0.1	0.1	0.1	0.1	0.1	0.1
$T_{G\,in}$ (°C)	25	25	25	25	25	*
$P_{G\,in}$ (bar)	3	3	2	*	2	3
$v_{G\,in}$ (m/s)	3	3	*	3	3	3
Rel. humidity (%)	0	0	0	0	*	0

* *variable condition indicated in the corresponding figure*

In Fig (4.9b), the modeled fluxes increase with the liquid inlet velocity in the tube-side. This could be due to the mass transfer coefficient enhancement caused by the turbulence created at high velocity. The ratio ($J_{et.}/J_w$) was found to be augmented by increasing the liquid velocity tending to reach a steady value. This could be due to the low ethanol inlet mass fraction which is only 0.1 kg/kg. So, the reduction in the mass transfer boundary thickness due to the created turbulence could have a larger relative improvement on ethanol flux than on that of water. Eventually, the improvement effect at higher values of liquid velocity become neglected for both components making the ratio ($J_{et.}/J_w$) approach a steady value.

Fig (4.9c) shows that increasing the gas interstitial velocity could have a positive impact on the fluxes until the gas velocity reaches 2 m/s. Above this value, increasing the gas velocity might have a very neglected enhancing effect. Besides, the ratio ($J_{et.}/J_w$) declines on raising the gas velocity. In fact, the higher the gas velocity, the higher is the sweeping effect and the lower is the vapor pressure of the permeating components in the permeate-side. This in turns improves the corresponding mass transfer driving forces. This is true until a value of gas velocity that above which, further sweeping is not very practical as there is not much in the shell-side to be swept out of the module. In case of longer modules (longer than 20 cm), this limiting value might be higher than 2 m/s as more vapor of water and ethanol will be present in the permeate-side. Since water flux outnumbers that of ethanol, the increase in the sweeping gas velocity might reduce the relative content of water vapor more than ethanol in the permeate side increasing the driving force of water more than that of ethanol.

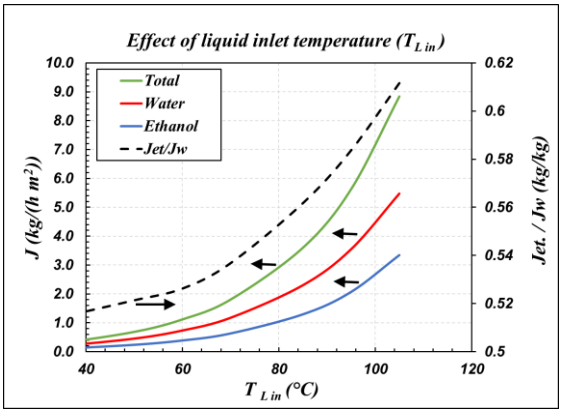

(a)

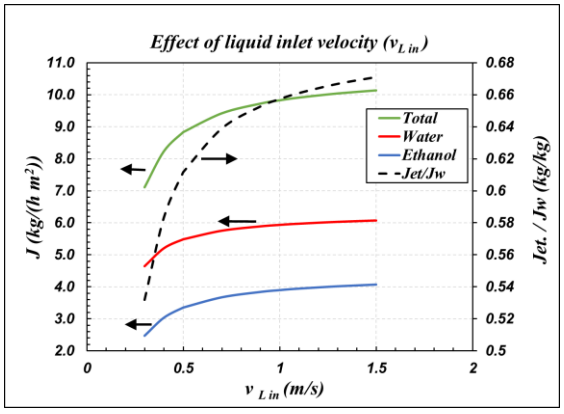

(b)

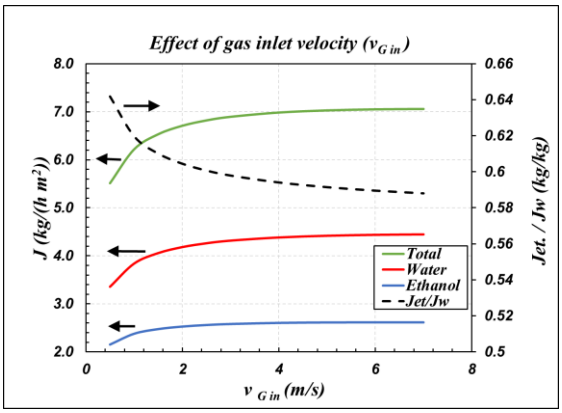

(c)

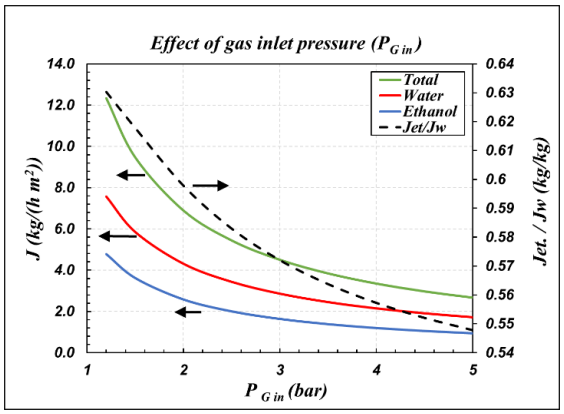

(d)

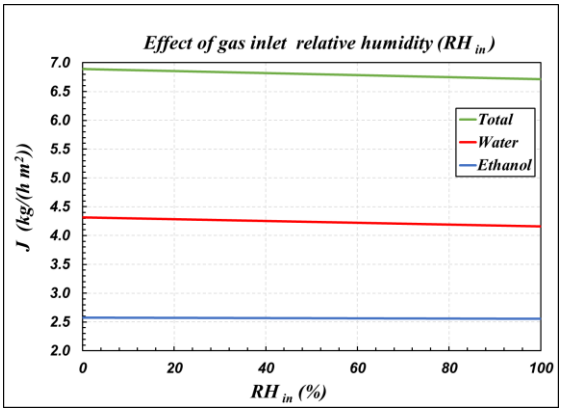

(e)

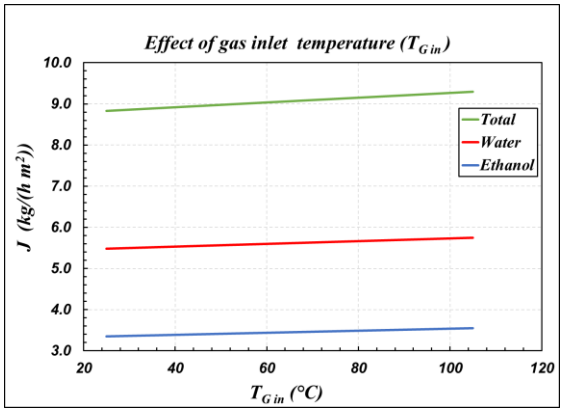

(f)

Figure (4.9) *The effect of the inlet operating conditions on the modeled flux in case of counter-current flow for the bundle B2758. The varied inlet operating conditions are: (a) Liquid temperature (b) Liquid velocity (c) Gas interstitial velocity (d) Gas pressure (e) Gas relative humidity (f) Gas temperature (The fixed operating conditions in each figure are reported in Table(4.3))*

Expectedly, the permeation rate rises as the inlet gas pressure declines (See Fig (4.9d)). In addition to that, the ratio ($J_{et.}/J_w$) is reduced on elevating the gas inlet pressure. As a matter of fact, the liquid/vapor equilibrium at the liquid/membrane interface is affected by the gas pressure. The low gas pressure favors the vaporization rate which results in a higher value of the mole fraction of the permeating component in the vapor state at the liquid/membrane interface. As a result, the mass transfer driving force increases. This effect is more apparent in the more volatile component (ethanol). That could be the reason for the decrease in the ratio ($J_{et.}/J_w$) on raising the inlet gas pressure.

The effect of the relative humidity (*RH*) at the gas inlet is given in Fig (4.9e). A slight decline in the water flux takes place on increasing the relative humidity while the ethanol flux remains almost unaffected. As the relative humidity increases in the permeate side, the permeation of water slightly decreases due to the drop in the driving force arising from increasing the partial pressure of water vapor in the permeate-side. Such effect is small in case of short modules (20 cm) that do not experience a great drop in the liquid side temperature resulting in almost fixed high vapor pressure of the permeating components in the feed-side.

Elevating the gas inlet temperature resulted in a very slight enhancement in the fluxes as shown in Fig (4.9f). This observation was also obtained in the case of SGMD with NaCl (aq.) feed as discussed in Chapter (3) indicating insignificant heat transfer resistance in the gas-side. However, this enhancement in fluxes could be due to the less amount of heat lost from the liquid side on using gases at elevated temperatures. This could correspond to higher energy available for vaporizing the permeating stream.

4.4.2. Simulation of Modules Connected in Series

As it has been mentioned, the total length (L_{tot}) refers to the total axial separation length in the modules connected in series inside an SGMD vessel. The considered modules also have the same geometric parameters and morphological properties of the bundle B2758 having a length of 20 cm. It is worth noting that the simulations did not consider the concentrated pressure drops in the connections between the modules.

4.4.2.1.Axial and Radial Profiles

In the current chapter, the axial profiles across the SGMD vessel are shown in Fig (4.10) and (4.12) for the co-current and counter-current cases respectively. Moreover, the two-dimensional profiles of the mole fractions inside the membrane are represented by Fig (4.11) and (4.13) for the co-current and counter-current flow configurations respectively. All the represented cases in Fig

(4.10-4.13) correspond to inlet liquid feed at 110 flowing at 0.5 m/s having ethanol mass fraction of 0.1 kg/kg and dry sweeping gas entering the shell-side with an interstitial velocity of 3 m/s at 25 °C and 3 bar in a SGMD vessel of L_{tot} that is 10 m. In case of co-current flow configuration, it can be demonstrated from Fig (4.10a) that the ethanol vapor mole fraction at the liquid/membrane interface and that at the gas/membrane interface approach each other as the liquid and gas streams flow in the positive axial direction. This leads to a decline in the mass transfer driving force along the positive axial direction of the SGMD vessel. The same observation was obtained for water according to Fig (4.10b). This could be due to the fact that, along the positive axial direction, the liquid temperature drops due to heat transferred from the liquid side to the gas side and due to heat used in the vaporization of the permeating molecules as illustrated by Fig (4.10c).

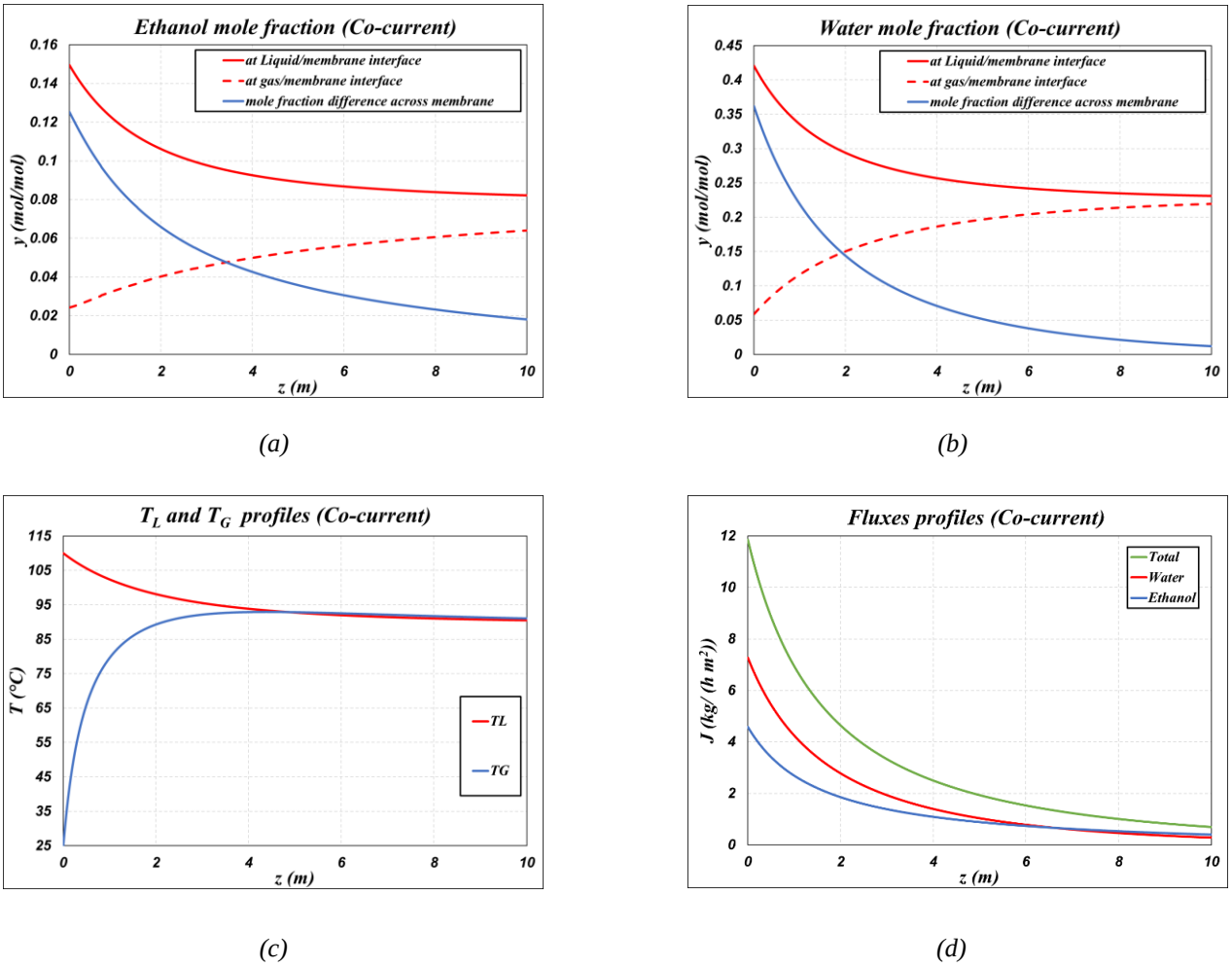

Figure (4.10) *Modeled axial profiles during SGMD of ethanol(aq.) in co-current flow for: (a)Ethanol mole fractions in membrane (b)Water mole fractions in membrane (c)Liquid and gas temperatures (d)Water, ethanol, and total mass fluxes (at T_{Lin}=110°C , $\omega et._{in}$=0.1kg/kg , v_{Lin}=0.5m/s, v_{Gin}=3/s, T_{Gin}=25°C, P_{Gin}=3 bar, inlet gas rel.humidity=0%, L_{tot}=10m)*

This decline in the liquid temperature causes a decrease in the vaporization at the liquid/membrane interface due to the decreased vapor pressure of water and ethanol. This in turn lowers their corresponding vapor molar fractions at the liquid/membrane interface. Besides, the permeation of water and ethanol augments their partial pressures in the permeate side along the direction of the flow of the liquid and gas streams. Consequently, the mass transfer driving force for both of water and ethanol diminishes as shown in Fig (4.10a) and (4.10b). In fact, this explains the negative effect of the total axial separation length on the water and ethanol fluxes as it is demonstrated by Fig (4.10d).

For an explicit visual illustration of Fig (4.10a) and (4.10b), the 2-D profiles of ethanol and water inside the membrane are represented by Fig (4.11a) and (4.11b) respectively. According to the contours of the mole fractions for both components, the color gradient in the radial (r) direction represents the mass transfer driving force that is at its maximum value at (z=0) which is the inlet of the gas and liquid streams. Then the driving force vanishes along the positive axial direction.

For the case corresponding to the counter-current flow, interesting profiles for the mass transfer driving forces of ethanol and water were obtained along the axial direction as shown in Fig (4.12a) and (4.12b) respectively. The vapor mole fractions for both components increase at both, the liquid/membrane interface and the gas/membrane interface along the positive axial direction. The driving force for ethanol was found to be a non-steady increasing function of the positive axial direction while the driving force for water was found to have a parabolic function reaching a minimum value in at almost half of the total axial separation length. In case of water, this could be explained by the two opposing phenomena taking place. The first phenomenon is the increase in the liquid temperature and so the water vapor pressure along the positive axial direction towards the liquid inlet (see (Fig (4.12c)). The second phenomenon is the increase in the water partial pressure inside the gas along the axial direction due to the permeated water molecules. The first phenomenon enhances the driving force while the second negatively affects the driving force along the axial direction. The same is true for ethanol but since its flux is much less than that of water, the second phenomenon is less effective than the first for ethanol leading to an increase of the driving force of ethanol in the direction of the gas flow.

(a)

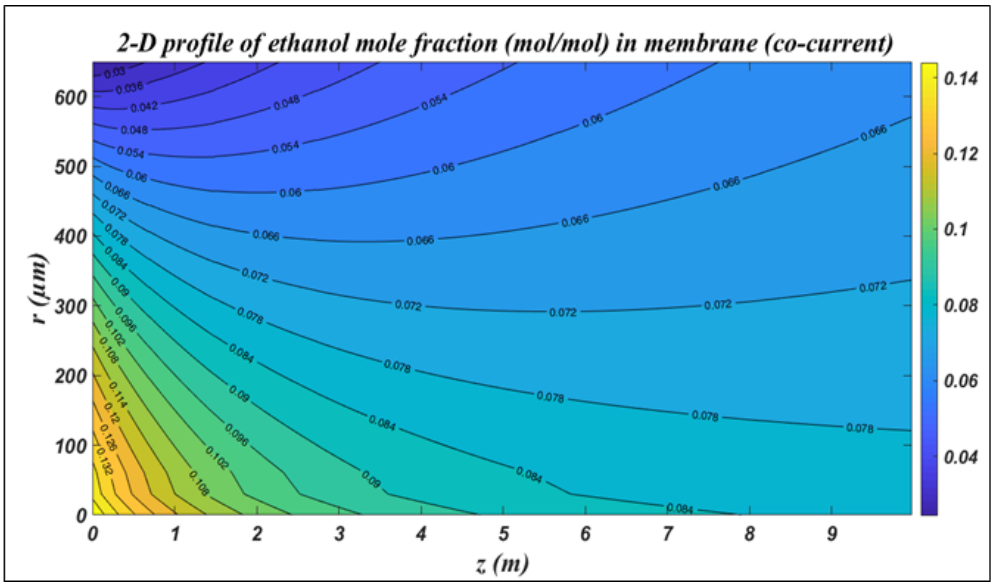

(b)

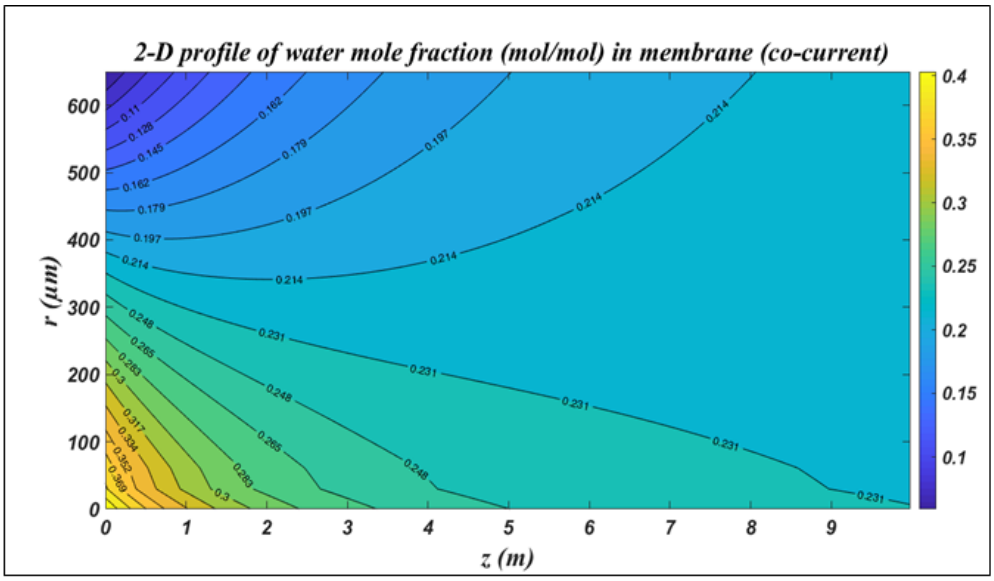

Figure (4.11) *Modeled 2-D profiles during SGMD of ethanol(aq.) in co-current flow for: (a)Ethanol mole fractions in membrane (b)Water mole fractions in membrane (at T_{Lin}=110℃ , $\omega et._{in}$=0.1kg/kg , v_{Lin}=0.5m/s, v_{Gin}=3/s, T_{Gin}=25℃, P_{Gin}=3 bar, inlet gas rel.humidity=0%, L_{tot}=10m)*

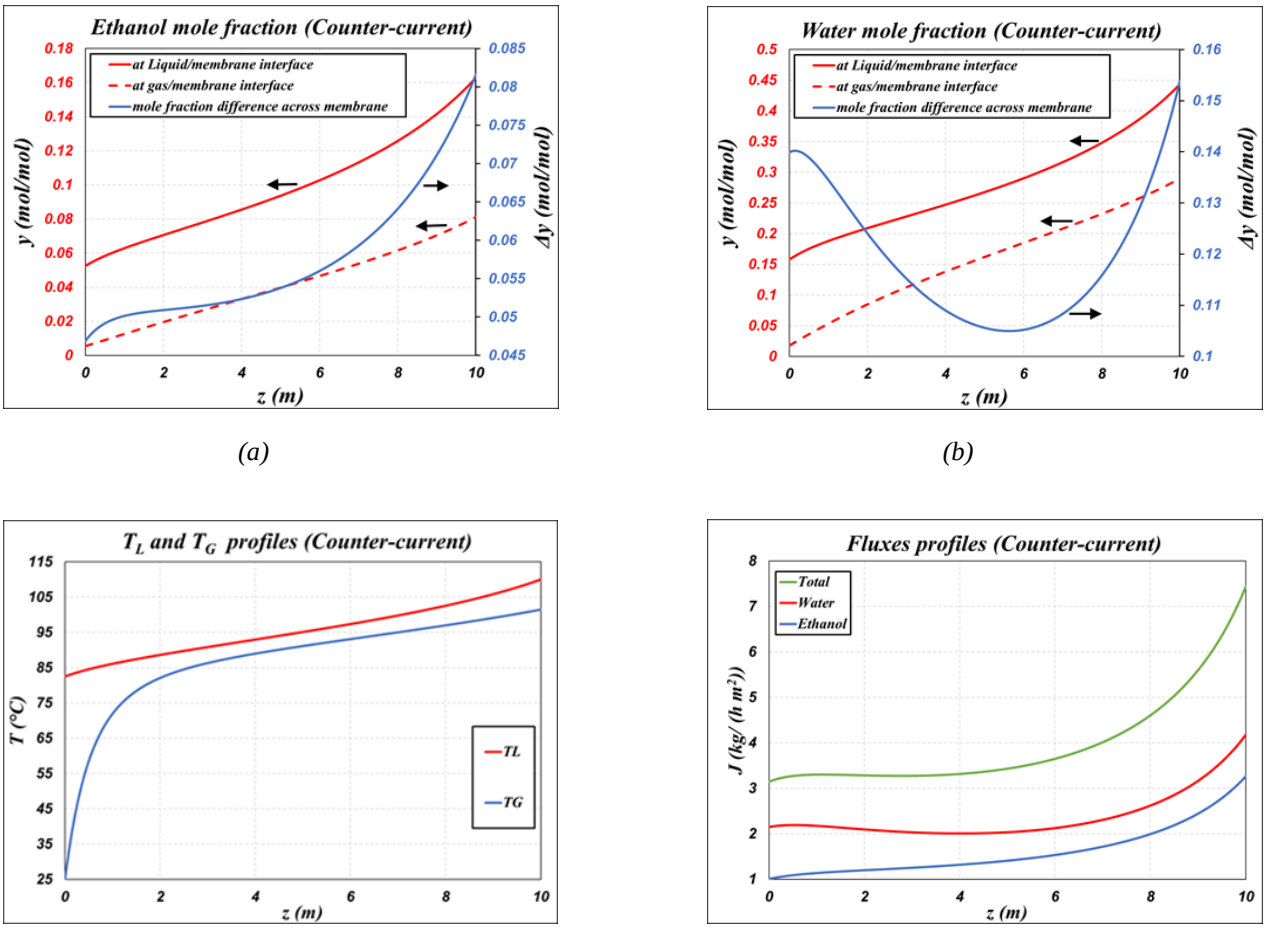

Figure (4.12) *Modeled axial profiles during SGMD of ethanol(aq.) in counter-current flow for: (a)Ethanol mole fractions in membrane (b)Water mole fractions in membrane (c)Liquid and gas temperatures (d)Water, ethanol, and total mass fluxes (at T_{Lin}=110°C , $\omega et._{in}$=0.1kg/kg , v_{Lin}=0.5m/s, v_{Gin}=3/s, T_{Gin}=25°C, P_{Gin}=3 bar, inlet gas rel.humidity=0%, L_{tot}=10m)*

This explains the resulting profiles of the fluxes of both components given in Fig (4.12d) such that water flux reaches a minimum value at almost half of the axial separation length while ethanol flux is always increasing along the axial positive direction. The 2-D representations of the mole fractions of ethanol and water are shown in Fig (4.13a) and (4.13b) respectively manifesting the difference between the driving forces encountered for water and ethanol according to the reasons that have been already discussed.

(a)

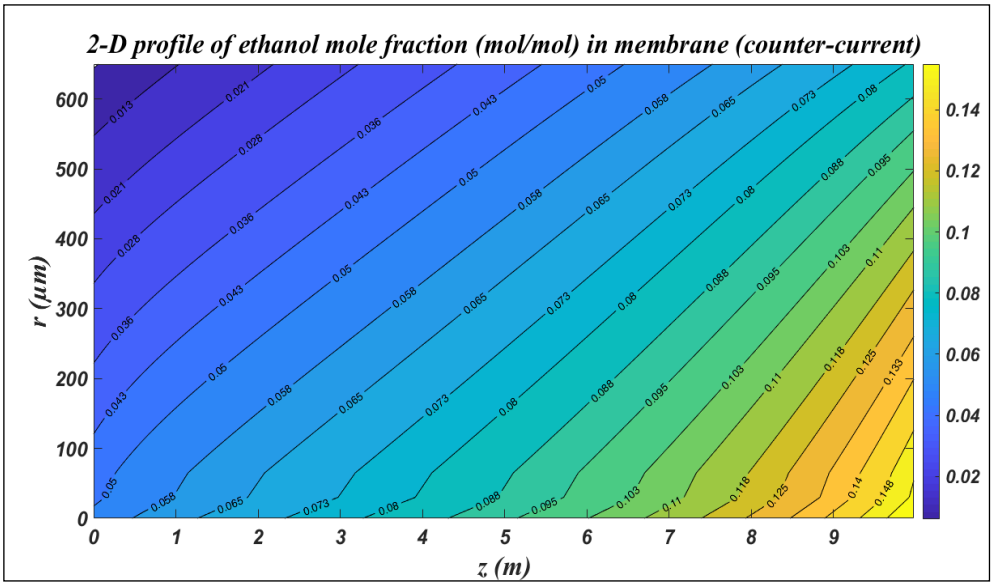

(b)

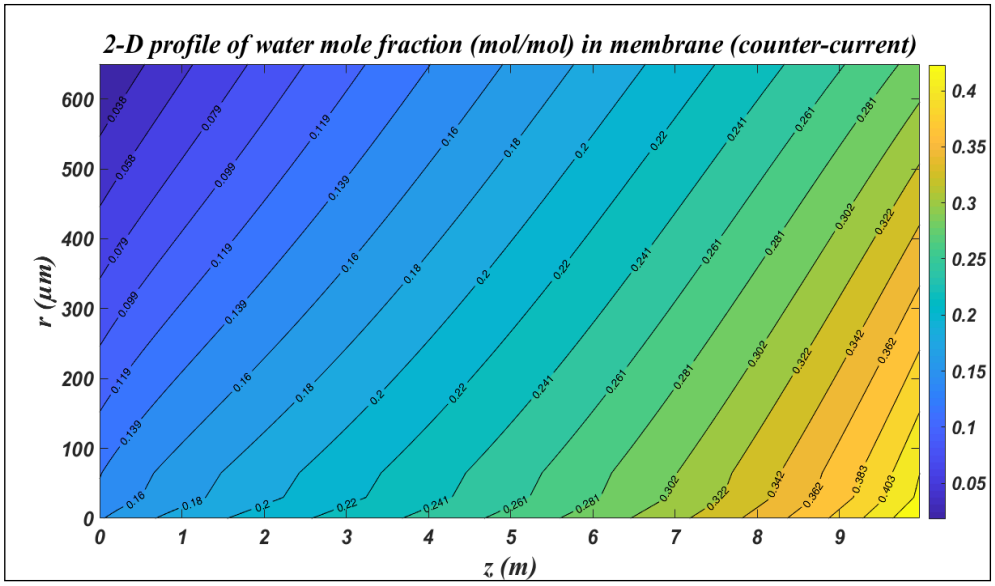

Figure (4.13) *Modeled 2-D profiles during SGMD of ethanol(aq.) in counter-current flow for: (a)Ethanol mole fractions in membrane (b)Water mole fractions in membrane (at T_{Lin}=110℃ , $\omega et._{in}$=0.1kg/kg , v_{Lin}=0.5m/s, v_{Gin}=3/s, T_{Gin}=25℃, P_{Gin}=3 bar, inlet gas rel.humidity=0%, L_{tot}=10m)*

4.4.2.2.Effect of SGMD Vessel Total Length and Liquid Inlet Temperature

The coupled effect of the inlet liquid temperature and the total SGMD vessel length was investigated as shown in Fig (4.14) for the SGMD of ethanol (aq.) feed using dry N_2 as the sweeping gas in a counter-current flow configuration.

(a)

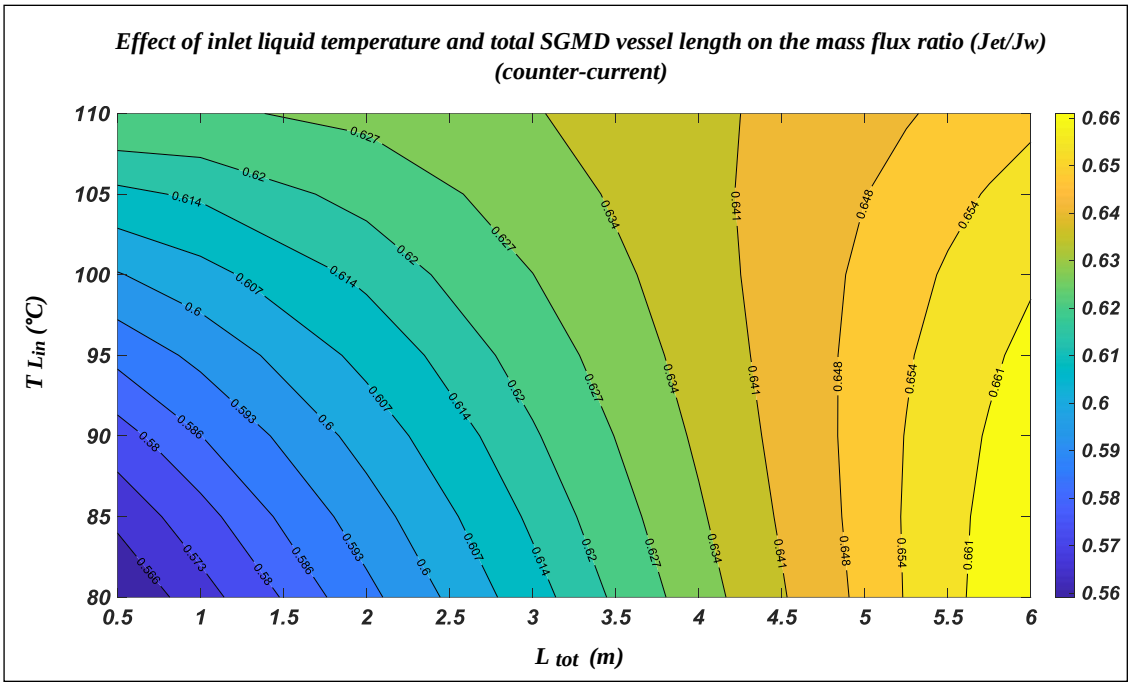

(b)

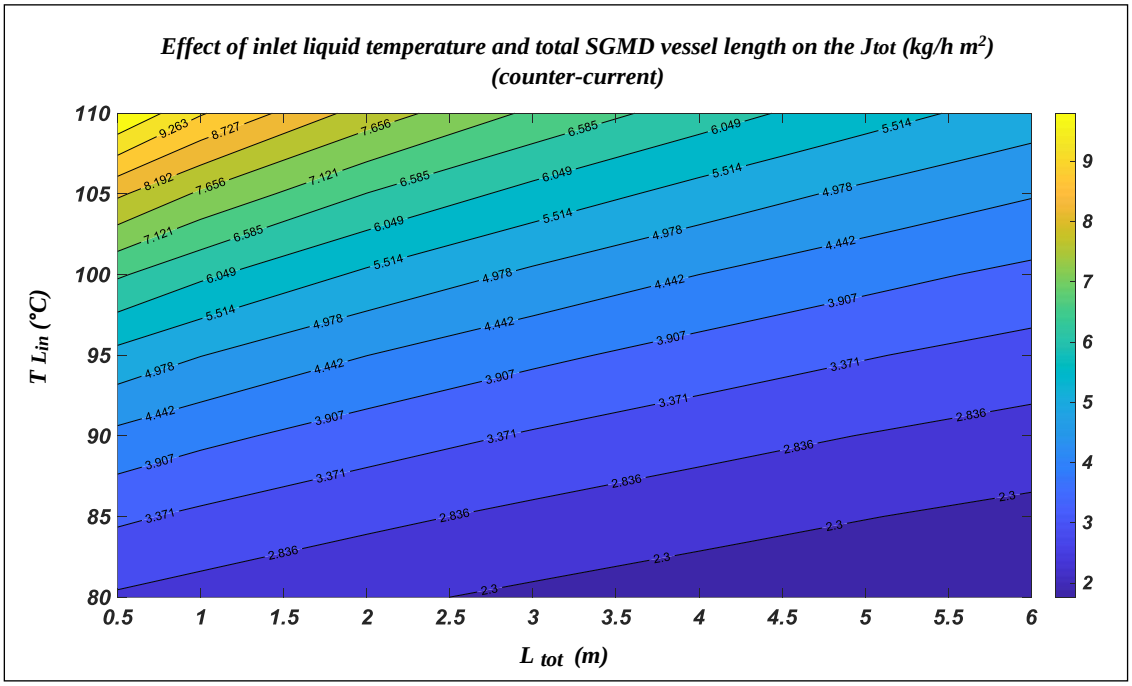

Figure (4.14) *Results of SWGM modeling of ethanol (aq.) in counter-current flow configuration showing the coupled effect of the inlet liquid temperature and the total axial separation length (SGMD vessel length) on: (a) The ratio (ethanol mass flux/water mass flux) (b)Total mass flux ($\omega et._{in}$=0.1kg/kg , v_{Lin}=0.5m/s, T_{Gin}=25°C, P_{Gin}=3 bar, inlet gas rel.humidity=0%)*

Fig (4.14) corresponds to inlet liquid feed flowing at 0.5 m/s having ethanol mass fraction of 0.1 kg/kg and dry sweeping gas entering the shell-side with an interstitial velocity of 3 m/s at 25 °C and 3 bar. It can be observed form Fig (4.14a) that on increasing the liquid temperature and the total length of the SGMD vessel (L_{tot}), the ratio ($J_{et.}/J_w$) increases until reaching a total length around 4.6 m. Interestingly, above this total length value, increasing the temperature leads to a decline in the ratio ($J_{et.}/J_w$). This could be attributed to the fact that ethanol represents the more volatile component, so the percentage increase of its flux is favored more than that of water by elevating the temperature. Besides, according to Fig (4.14a) and Fig (4.14b), it was found that water end ethanol experience different behaviors of the mass transfer driving force with respect to the positive axial separation distance. This is due to their different permeation rates and different volatility. As the total length of the vessel length increases, the average liquid temperature is expected to be lower due to the vaporization of more permeating components and greater conduction losses. Therefore, the effect of the high liquid temperature on favoring ethanol flux over that of water decreases. So, it can be concluded from Fig (4.14a) that in case the maximum ($J_{et.}/J_w$) is desired, the liquid inlet temperature and total SGMD vessel length could be optimized at given operating conditions. According to Fig (4.14b), elevating the liquid inlet temperature and/or decreasing the total length of the SGMD vessel enhances the total flux. The positive effect of the liquid inlet temperature is related to the vapor pressure of the permeating components as it has been already discussed. On increasing the total SGMD vessel length, the average liquid temperature decreases and the content of water and ethanol in the shell side increase. This could lead to a decline in the mass transfer driving forces of both components.

4.5.Conclusions

The investigation of employing SGMD in (water/ethanol) separation using hydrophobic ceramic membranes took place by the aid of modeling studies. This aimed at understanding the effect of the operating conditions and total separation length on the driving forces of mass transfer for water and ethanol. The Maxwell-Stefan approach was applied in describing the mass transfer inside the membrane pore. This was utilized in obtaining the radial concentration profile inside the membrane for the axial local model. Axial discretization of the model was carried out to consider longer axial separation lengths (SGMD vessel total lengths).

Modeling results showed that the liquid temperature and gas pressure could have significant effects on the fluxes and the ratio between the mass fluxes of the permeating species ($J_{et.}/J_w$). Raising the liquid temperature and/or decreasing the pressure enhanced the total flux and augmented the ratio ($J_{et.}/J_w$). Increasing the gas and liquid velocity values also increased the flux to certain limits. As for the gas temperature, its role was considered insignificant.

The case of an SGMD vessel having a total length of 10 m was considered for the co-current and counter-current flow configurations. For the co-current flow, the fluxes of water and ethanol declined along the direction of the liquid and gas flow due to the diminishing driving force arising from the decrease in liquid temperature and the increase in water and ethanol content in the permeate-side. This was not true in case of counter-current flow configuration such that ethanol driving force increased unsteadily in the direction of the gas flow while water driving force reached a minimum value at the middle of the module. This was explained by the opposing phenomena taking place in the counter-current flow configuration. One phenomenon is related to the increase in liquid temperature along the gas flow direction while the second phenomenon was related to the increase in water content in the shell side in the same direction. Both phenomena affect the driving forces oppositely with varying magnitudes along the module axial length.

By modeling the coupled effect of the inlet liquid temperature and the total length of the SGMD vessel for the counter-current flow configuration, the total flux was found to decrease by increasing the vessel total length. However, the liquid inlet temperature and the total vessel length could be optimized for maximizing the ratio (J_{et}/J_w). This could be interesting for process development for the related applications.

List of Symbols

Latin Letters	
$\hat{C}_p$	Molar heat capacity at constant pressure
$\tilde{C}_p$	Specific heat capacity at constant pressure
d	Diameter
$D_{w,q}$	Binary diffusion coefficient for water and component q
f	Friction factor
h	Convective heat transfer coefficient
J	Mass flux
k	Mass transfer coefficient
$k_m^{cond.}$	Thermal conductivity coefficient
L_{tot}	Total length
M	Molecular weight
n	Number of the axially discretized units in the SGMD model
$\dot{n}$	Molar flow rate per fiber (tube)
N'	Molar flow rate per unit length and per fiber (tube)
$N_{f,tot}$	Total number of fibers (tubes)
P	Pressure
p^*	Vapor pressure
Q'	Heat energy flow rate per unit length and per fiber (tube)
r	Radial direction
R	Radius
R_g	Universal gas constant
T	Temperature
v	Velocity
$v_{0,G}$	Interstitial gas velocity
x	Mole fraction in the liquid state
y	Mole fraction in the vapor state
z	Axial direction
Greek Letters	
γ	Activity coefficient
ε	Porosity
ε_p	Packing factor of the module

η	Dynamic viscosity
λ	Latent heat of vaporization per mole
ρ	Density
τ	Tortuosity
ψ	Fraction of molar flux
Subscripts and Superscripts	
eq	Equivalent
$et.$	Ethanol
G	Gas
Gb	Gas bulk
Gm	Gas/membrane interface
IN	Inner or inlet
IN	Liquid
Lm	Liquid membrane
Lb	Liquid bulk
net	Net amount
N_2	Nitrogen gas
OUT	Outer or outlet
S	Shell
TOT	Total
W	Water

[This page intentionally left blank]

Chapter Five

Process Development for Seawater Desalination using Sweeping Gas Membrane Distillation

5.1.Introduction

Membrane distillation is often viewed as an auspicious technology for seawater desalination [215]. In fact, the investigation of membrane distillation (MD) processes for seawater desalination constitutes a paramount contribution of the works found in literature regarding membrane distillation applications [123]. This is due to the fact that on being compared to conventional industrial desalination methods as the reverse osmosis (RO), MD can offer higher salt rejection, less feed pretreatment requirements and possible savings in the energy demands in case waste heat sources are available [23,81]. In addition to that, MD can be used as a subsequent separation unit downstream of the RO since MD can handle relatively higher salt concentrations in the feed [67,69]. According to E. El-zanati et al. [65], the application of vacuum membrane distillation (VMD) after RO improved the water productivity and decreased the required cost when compared to RO stand-alone systems. Similarly, according to the economic analysis by Y. J. Choi et al. [68,216], MD-RO hybrid systems could offer less water production cost (WPC) than MD stand-alone systems and can be competitive to RO stand-alone systems in case of the availability of low-cost steam.

The industrial breakthrough of MD has not been yet accomplished due to a lack of sufficient economic and process design studies. Such studies are required to manifest the level of competency of MD with other conventional industrial separation methods [66]. In the majority of the works found in literature regarding MD, the discussion is limited to membrane characterization and module performance investigation based on laboratory-scale and pilot-scale studies. However, the discussions related to scaling up and process development are rarely addressed. In fact, the development and optimization of the MD process for a given application is the key to a better comprehension of the industrial applicability of membrane distillation and its competency level with the other conventional separation methods. The comparison between the separation methods can be in terms of the water production cost (WPC). Typically, the WPC by RO is below 1 $\$/m^3$ for large-scale separation units and below 3 $\$/m^3$ for small-scale units [1].

Details about many cost items involved in the MD desalination processes are quite ambiguous due to the absence of sufficient information about energy analysis and cost estimation. This resulted in contradicting opinions among authors about the obtainable water production cost (WPC) ranging from 0.3 to 130 $\$/m^3$ on using MD for water desalination [1]. However, there is a common conclusion regarding the considerable reduction in the WPC in case cheap heat resources are employed [64,68,69]. The problem of high energy demands in MD process could be mitigated by the use of solar energy and heat recovery systems. F. Banat et al. [63] investigated the economics of compact and large solar-powered MD for water desalination. The WPC obtained in this work ranged from 12 to 42 $\$/m^3$. However, according to G. Zaragoza et al. [69], MD stand-alone systems powered by solar energy could face challenges in competing with photovoltaic reverse osmosis (PV-RO) desalination systems but can be useful in MD-RO hybrid systems. Similarly, based on the process optimization and economic analysis performed by S. E. Moore at el. [183], the WPC for a solar-powered sweeping gap membrane distillation (SGMD) water desalination process was estimated to be 85 $\$/m^3$ making this suggested process incapable of competing with the

conventional water desalination methods. In fact, very few studies of solar-driven MD plants were performed in literature [217].

Heat recovery in DCMD for water desalination was investigated by S. Al-Obaidani et al. [64] such that a low WPC of 1.3 \$/m^3 was claimed to be achievable for low feed temperatures. Besides, the coupling of another process to membrane distillation could present energy savings as it was proposed by J. Wang et al. [218] where the water desalination process by DCMD was coupled with a recirculating cooling water system. Results suggested a possible reduction in pure water production cost by DCMD. In an attempt to reduce the energy requirements of MD processes, multi-effect membrane distillation (MEMD) was investigated by B. L. Pangarkar [70] for water treatment. Although this application is different from water desalination, the concept of using 4 stages of AGMD was suggested in this work for mitigating the energy requirements with an estimated cost of 4.7 \$ for every m^3 of treated water. Regarding the utilization of AGMD in desalination processes, M. J. P. Bappy et al. [71] proposed a hybrid low-cost freshwater production system. In this system, energy recovery was suggested by employing wind, solar and geothermal power plants for feed pumping requirements and by employing solar energy for feed heating. Still, the absence of the detailed information required for process development and optimization is considered one of the main stumbling blocks facing the implementation of membrane distillation for water desalination in a commercial scale [1].

The process development and optimization of water desalination by sweeping gas membrane distillation (SGMD) will be the scope of the current chapter using the same hydrophobic ceramic membrane (bundle B2758) studied in Chapters (2-4). The same developed SGMD model in Chapter (3) was applied in the current chapter for simulating the SGMD unit included in the overall desalination process. The model considered the role of each membrane layer on the obtained flux. The aim of the current chapter is to study the possibility of incorporating SGMD unit in water desalination on an industrial scale. This would facilitate the preliminary quantification of process demands and clarify the corresponding challenges. Besides, it would be beneficial in the prediction of the industrial applicability of the studied hydrophobic ceramic membranes for water desalination purposes. The presented simulated results were based on a preliminary design of the involved equipment and non-rigorous cost estimation for a hypothetical water desalination plant. In general, the design and development of MD plants should take place before rigorous economic analysis for comparison with the conventional separation methods. Further intensive theoretical and experimental research works are essential to ensure accurate scale-up procedures [1].

The approach followed in the current chapter was based on a hypothetical water desalination plant. Preliminary design calculations were performed in order to have an estimation of the properties of the main steams and the sizing of the main equipment involved in the overall desalination process. Several case studies of different operating conditions and SGMD vessel lengths were simulated. The SGMD constraints were defined and were not violated for each of the simulated cases. Accordingly, the accepted range of operating conditions was defined for each case. Eventually, the optimization procedures took place with the aim of minimizing the water product cost (WPC) for a specified flow rate of the obtained freshwater.

5.2.Proposed Hypothetical Process

5.2.1. Process Description

A simple single-pass hypothetical seawater desalination process including SGMD as the separation unit is proposed. The aim of this process is to produce fresh water at a rate of 5000 kg/h. Seawater was simulated by using an aqueous solution of NaCl having a salinity of 40g/L at ambient conditions. Air was used as the sweeping gas. The liquid feed and the sweeping gas in the SGMD unit represented the tube-side and shell-side streams respectively flowing in a counter-current manner. The flowsheet of the proposed process is given in Fig (5.1). The feed to the overall process is stream (L_1). Pump (*P-1)* is used to raise the pressure of the stream (L_1) towards the desired pressure of stream (L_{in}) which is the inlet liquid stream to the SGMD vessel. The liquid pressure drop in the intermediate equipment was considered. The preheating of the overall process liquid feed stream takes place in the heat exchangers (*HX-3)*and (*HX-1)* respectively making use of the SGMD gas outlet and liquid outlet streams respectively. Then, the final heating step to make the liquid stream reach the desired SGMD liquid operating temperature takes place in (*HX-2)* using hot steam. The condenser (*HX-3*) is also used to cool the outlet gas stream from the SGMD (G_{out}) and condense the water vapor that permeated during SGMD. This results in a two-phase stream (G_1) where the liquid/gas separation takes place inside the separator *S-1* at 40°C. The uncondensed gas is recycled back to the SGMD vessel at the desired inlet gas pressure by means of the compressor (*C-1)*.

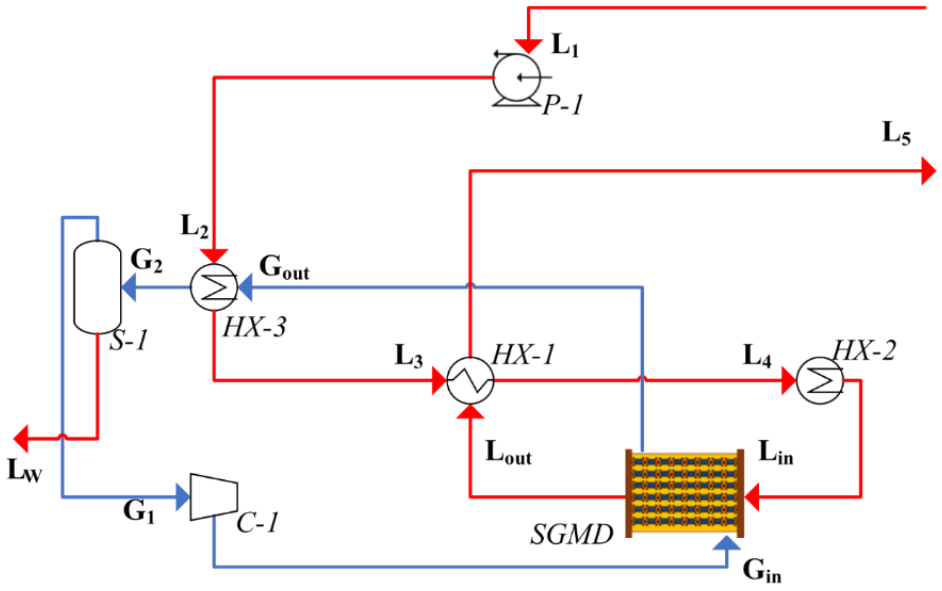

Figure (5.1) *Flowsheet showing the main involved equipment in the proposed process using SGMD separation unit for water desalination (Single-pass configuration)*

The SGMD unit and the liquid/gas separator (*S-1*) represent the mass transfer units in the process such that the SGMD is used to extract fresh water from the liquid feed by the sweeping gas then the separator recovers this freshwater from the wet sweeping gas in a steady continuous manner. Regarding the SGMD unit, it is represented by a vessel containing membrane modules connected in series and parallel according to the array specified by the proposed design. The expected scheme related to the arrangement of the SGMD modules in the vessel is shown in Fig (5.2). The morphological properties of each membrane layer, the inner and outer tube diameters and the packing factor were used according to the values of the bundle (B2758). Details about its morphological and geometric parameters can be found in Chapter (2). The module length used in the current chapter was 20 cm.

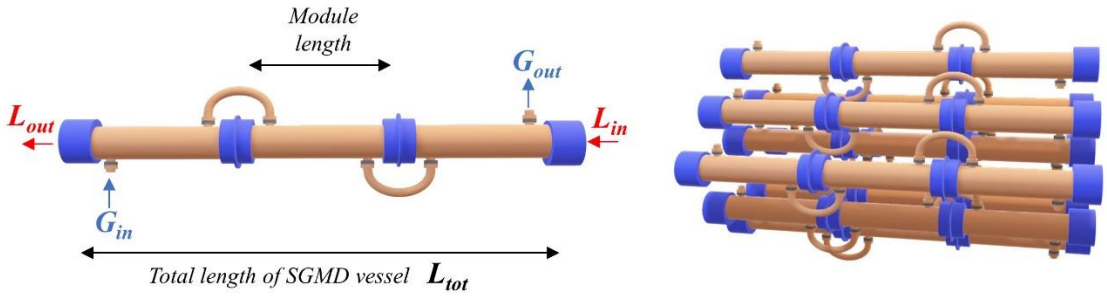

Figure (5.2) *Scheme of: (a)Modules connected in series (b)Modules connected in series and parallel according to the expected array in the SGMD vessel (in case of 3 modules in series as an example)*

5.2.2. Process Constraints

Before starting the process development and optimization procedures, it is important to identify the accepted operating ranges of the conditions and modules array in the SGMD unit. This would avoid the consideration of non-applicable cases. The limitations in the operating ranges are dictated mainly to prevent some undesired phenomena like pore wetting, feed boiling, and condensation of water in the sweeping gas and intrusion of the gas into the feed-side (bubbling).

As it has been discussed in Chapter (1), pore wetting could be detrimental to SGMD operations as it can lead to precipitation of salts inside the pores and decreased salt rejection. In worse cases, excessive pore wetting can lead to flooding which marks the failure of the separation process. However, the pore wetting can be avoided as long as the transmembrane pressure difference (P_L–P_G) is kept below the liquid entry pressure $LEP_{(T_L)}$ at the given liquid temperature [1,4] According to the experimental works by F. Varela-Corredor et al. [8,80] performed on the same ceramic membranes studied in this PhD thesis, the *LEP* value was found to be a decreasing function of the liquid temperature due to the variation in the surface energy and corresponding hydrophobicity with temperature. Accordingly, the liquid temperature at which the *LEP* value is

equal to zero was defined as the "wetting temperature" *(T_{wet})* [80]. At this temperature, the membrane cannot be longer considered hydrophobic such that pore wetting and flooding are guaranteed to occur. On experimental investigation of several hydrophobic ceramic membranes of different geometrical parameters and morphological properties, the wetting temperature values fell within a very narrow temperature range (between 120 and 130 °C) [80] as shown in Fig (5.3a). Therefore, in order to prevent simulation of case studies that can suffer from pore wetting, it is crucial to operate at a transmembrane temperature below the *LEP* value and at a liquid temperature below the wetting temperature. The mentioned experimental *LEP* results at different liquid temperatures using pure water for the bundle (B2758) enabled the estimation of the *LEP* in (bar) as a function of liquid temperature T_L in (°C) according to a fitted equation.

Although it is desired to operate at a transmembrane pressure difference that is below the *LEP* value in order to avoid pore wetting, a negative transmembrane pressure difference could lead to gas bubbling [80]. This happens due to the intrusion of gas bubbles from the pore towards the feed-side. The gas flow, in this case, is driven by the pressure difference across the membrane. Such a phenomenon is fatal to the SGMD separation process since the mass transfer takes place in the undesired direction. It is worth noting that the wetting problem becomes critical at the gas outlet while the bubbling problem becomes critical towards the liquid outlet. This is attributed to the counter-current flow manner and the pressure drops along the axial direction of the module. For illustration, the expected axial profiles of the $LEP_{(T_L)}$ and the transmembrane pressure difference (P_L–P_G) in the SGMD unit are shown in Fig (5.3b). The *LEP* profile can be determined by the liquid temperature profile. In case of counter-current flow, the gas enters the SGMD vessel at ($z=0$) and moves in the positive axial direction ($+z$) towards its outlet at ($z=L_{tot}$) while the liquid moves in the negative axial direction ($-z$). The operating conditions are specified for each inlet stream ensuring the absence of bubbling and wetting. A safety margin accounting for the possible pressure drop of each stream is considered. Therefore, the gas pressure reaches its lowest value at its outlet engendering high risk of wetting at this position. Similarly, the liquid pressure reaches its lowest value at its outlet ($z=0$) where the maximum approach between the liquid and gas pressure values occur. Excess liquid pressure drops could result in a zero or even a negative transmembrane pressure difference at the liquid outlet causing bubbling at this region. The velocity of each stream plays an important role in its resulting pressure gradient. For the given values of liquid velocity and gas interstitial velocity, the pressured drop in each stream is mainly affected by the total length of the SGMD vessel (L_{tot}). Therefore, at given operating conditions, the maximum allowable total length should be the total SGMD vessel length that prevents the occurrence of bubbling and wetting.

Other problems related to the operating conditions of the streams is due to the possible undesired phase changes, namely liquid boiling in the feed-side and water condensation in the permeate-side. Liquid boiling is undesired as it can lead to vibrations inducing stress on connections and joints, cavitation in case of used pumps and can lead to negative effects on the mass transfer due to the

possible destabilization of the liquid/vapor interface that should be immobilized in the ideal cases at the pore entrance.

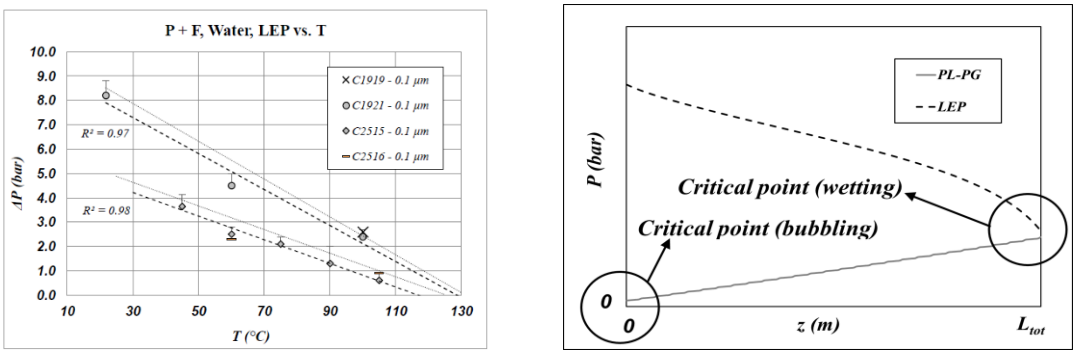

(a) *(b)*

Figure (5.3) *Representation of the possible SGMD process constraints due to : (a) Pore wetting in case of operating temperature above the wetting temperature* [80] *(b) Bubbling at gas inlet (z=0) and pore wetting at liquid inlet (z=L_{tot}) in case of counter-current flow*

Liquid boiling can be avoided by operating at a liquid pressure P_L above the saturation pressure at the given liquid temperature $P^{sat}_{(T_L)}$. Similarly, condensation of the permeated vapor molecules in the gas present in the shell-side is undesired due to the possible accumulation of liquid in the shell-side. Ensuring that the water partial pressure P^G_W is below its saturation pressure at the gas temperature $P^{sat}_{(T_G)}$ in the shell side would avoid the condensation of the water vapor molecules carried by the sweeping gas

Both the liquid saturation pressure and the *LEP* values at the liquid inlet are dependent on its temperature. Therefore, to avoid boiling, the assigned value of the liquid pressure P_{Lin} should be set to be above its saturation pressure. Then, the gas inlet pressure is assigned to achieve a transmembrane pressure difference that prevents wetting at the inlet and a safety margin should be used to account for the expected pressure drop in the gas across the module in order to avoid wetting at the gas outlet. This safety margin puts into account the velocity values of each stream and the total SGMD vessel length. Therefore, at given velocity values of the gas and liquid streams, the maximum total SGMD vessel length L_{tot} is implicitly determined by the inlet liquid temperature. Regarding the problem of water condensation in the sweeping gas, it is less critical than those of the bubbling and the wetting. The sweeping gas is almost dry at its entrance into the SGMD unit.

In the positive axial direction, the water partial pressure increases in the sweeping gas due to the permeated water across the membrane. However, the gas temperature also increases in the positive axial direction due to the heat transferred from the feed-side raising the water saturation pressure which mitigates the risk of water condensation in the permeate-side. Therefore, the axial profiles of the water partial pressure and saturation pressure in the gas-side need to be checked for each simulated study case to ensure the absence of water condensation. Modeling studies usually do not consider condensation in the permeate side. However, V. Karanikola et al. [82] considered it during SGMD modeling for water desalination using hollow fiber membranes.

5.3.Process Development

5.3.1. Preliminary Process Design

Typical preliminary design equations [219–221] and simple mass and energy balances were used for the approximate equipment sizing and the prediction of the properties of each process stream involved in the flowsheet shown in Fig (5.1). The following assumptions were adopted in the performed calculations.

- Steady-state
- No heat losses and no leakages
- Ideal gas behavior
- The steam enters the preheater (*HX-2*) as a saturated vapor and exits as a saturated liquid.
- 100 % salt rejection by the SGMD.
- Neglected pressure drop in the separator
- The pressure drops take place in the main process equipment only.
- The pressure drop values of the liquid and gas streams were assumed to be 0.25-0.35 and 0.035 bar respectively in the single heat exchanger equipment [220].
- Concentrated pressure drop due to the connection between two modules in series as shown in Fig(5.2) correspond to 3 velocity heads for the liquid (expansion at outlet nozzle and contraction at inlet nozzle) and to 3.5 velocity heads for the gas (expansion at outlet nozzle, 180° bend and contraction at inlet nozzle) [222].
- The overall heat transfer coefficients for the heat exchangers (*HX-1*), (*HX-2*) and (*HX-3*) were assumed to be 120, 1100, 850 W/m^2K respectively. This was based on the nature and conditions of the process streams involved in each heat exchanger [220] .
- Centrifugal rotary equipment having an efficiency of 85%
- Shell-tube heat exchangers
- Single-stage gas compression
- Gas temperature rise takes place due to isentropic compression
- Vertical liquid/gas separator

In addition to the defined morphology and geometric parameters of the used module (B2758), the properties of the streams entering the SGMD vessel were used as inputs to the axially discretized SGMD model discussed in Chapter (3). The model was employed in estimating the properties of the streams exiting from the SGMD vessel, the obtained water flux and the heat exchanged between the gas and liquid streams. The main mass balance and simple preliminary design equations of the SGMD vessel are given by the set of Eqs. (5.1-5.4).

$$\dot{m}_{Gout} - \dot{m}_{Gin} = \dot{m}_{Lin} - \dot{m}_{Lout} = J_W A_{tot} \quad ; A_{tot} = N_{f,tot}\, \pi\, d_{IN}\, L_{tot} \tag{5.1}$$

$$N_{f,tot} = \frac{4\,\dot{m}_{Lin}}{\pi\, \rho_{Lin}\, v_{Lin}\, d_{IN}^2} \tag{5.2}$$

$$v_{Gin} = \frac{\dot{m}_{Gin}}{\rho_{Gin}\, S_{t,tot}} \tag{5.3}$$

$$S_{t,tot} = \frac{\pi}{4} N_{f,tot}\, d_{OUT}^2 \left(\frac{1}{\varepsilon_p} - 1 \right) \tag{5.4}$$

where A_{tot} and $N_{f,tot}$ refer to the total area and total number of fibers for all the modules in the SGMD vessel. Eq (5.4) resulted from the definitions of the packing factor ε_p given by Eq (5.5) and the total available cross-sectional area $S_{t,tot}$ given by Eq(5.6) which represents the area in the shell-side available for a gas stream entering the SGMD vessel with an interstitial velocity v_{Gin}.

$$\varepsilon_p = N_{f,tot} \left(\frac{d_{OUT}}{d_S} \right)^2 \tag{5.5}$$

$$S_{t,tot} = \frac{\pi}{4} \left(d_S^2 - N_{f,tot}\, d_{OUT}^2 \right) \tag{5.6}$$

The intensive properties of the inlet streams of the SGMD are used to estimate the resulting water flux by the SGMD model. On using the assigned value of the extensive property of stream (L_w) represented by its mass flow rate, it is possible to calculate the total required membrane area from Eq(5.7). Apparently, the overall process mass balance can be expressed by Eq (5.8). It is worth noting that the humidity of stream (G_1) is very low such that it depends on the separator operating temperature and pressure according to Eq (5.9).

$$\dot{m}_{Lw} = J_W A_{tot} \tag{5.7}$$

$$\dot{m}_{Lw} = \dot{m}_{L1} - \dot{m}_{L5} \tag{5.8}$$

$$y_{w,G1} = \frac{P_{w\ (T_{G2})}^{sat}}{P_{G1}} \tag{5.9}$$

5.3.2. Assigned Design Quantities

In addition to the design equations and the SGMD model, some design quantities related to parameters of equipment and operating conditions of streams were predefined for the process. These quantities were assigned according to the typical values used in industrial processes. Some of these values were assigned with the aim of having a zero degree of freedom in the system of equations combining the design calculations and the SGMD model. For example, the temperature approach between two streams in a heat exchanger, the steam operating pressure, the separator temperature and other quantities were assigned for this aim. Other values were assumed in order to simplify equipment sizing procedures. This saved detailed rigorous design procedures required for each piece of equipment. The main assigned design quantities and parameters are listed as follows.

- The overall process production is 5000 kg/h pure water with 100% salt rejection. Apparently, this is represented by stream (L_w).
- The overall process fresh feed (L_1) is provided at ambient conditions of 30°C and 1 atm.
- The liquid/gas separator temperature operates at 40°C.
- In the heat exchanger (*HX-1*), the temperature approach between streams (L_4) and (L_{out}) was used as 20 °C.
- Steam pressure of 2 bar was used in the preheater (*HX-2*)
- Liquid hold-up time in the separator is 10 min.
- The inlet liquid velocity in the lumen-side of the SGMD module is 0.4 m/s.

The assigned value of the liquid inlet velocity was based on the accepted range of liquid velocity in the tube-side of the shell-tube heat exchangers. Increasing the velocity has a positive effect on the overall mass transfer due to the reduction in the concentration polarization phenomena in the liquid boundary layer. However, it was shown by modeling results in Chapter (3) that the enhancement effect of increasing the liquid velocity on the flux was not very significant. Besides, increasing the liquid velocity could exacerbate the liquid pressure drop making bubbling more critical and could reduce the process productivity.

5.3.3. Cost Estimation

Typically, the cost of the desalination process is affected by the plant location and capacity, feed pretreatment requirements, energy demands, plant lifetime and depreciation extent [63]. However, a non-rigorous cost estimation took place for the proposed hypothetical plant in the current chapter. This aimed at evaluating the role of the operating conditions and design parameters on the economics of the process. The total annual cost (*TAC*) in ($/year) was calculated by summing the annual capital cost *CC* and operating cost *OC* according to Eq (5.10).

$$TAC = CC + OC \tag{5.10}$$

5.3.3.1.Capital Cost

In general, the capital cost should cover the purchasing equipment cost, auxiliary equipment, land and charges of installation [63]. In the cost estimation followed for the proposed hypothetical plant, only the purchasing and installation costs of the main equipment were considered assuming neglected auxiliary equipment cost. The set of the main assumptions adopted during the estimation of the capital cost of the hypothetical plant are as follows.

- The capital cost considers only the bare module cost of the main equipment (SGMD vessel, feed pump, gas compressor, liquid/gas separator and heat transfer equipment) where stainless steel is the material of construction.
- The specific cost of the ceramic module is 100 \$/m^2 [223].
- The production lifetime of the plant is 20 years.
- The percentage of the working days in the year is 90%. The remaining days are for periodic maintenance and replacements.
- The chemical engineering plant cost index (CEPCI) used is 567.6 corresponding to that of the year 2017 [224].
- The required funds will be borrowed at the expense of annual interest payments [2]. The assumed interest rate (i) is 5 %.

The equipment bare module cost (CBM) considers all the direct and indirect expenses related to the purchasing and installation of the equipment. The direct costs are due to the equipment and required labor and materials while the indirect costs are due to the shipment, management and overhead expenses (accounting, insurance, taxes …etc.). The bare module cost for the year 2001 was calculated according to Eq (5.11) [225] .

$$CBM_{2001} = C_P^o \left(B_1 + B_2 \, F_M \, F_P \right) \tag{5.11}$$

The equipment basic purchased cost C_P^o represents the purchased cost of equipment that is made of carbon steel and operates at 1 atm regardless of the equipment configuration. Therefore, the pressure correction factor F_P , material correction factor F_M and equipment configuration factors B_1, B_2 are included in Eq (5.11). The equipment basic purchased cost is predicted according to an equipment sizing parameter Ω as expressed by Eq (5.12). As the size of the equipment increases, its cost increases but its specific cost decreases [225]. Required power, area and volume were used as the sizing parameters for the rotary equipment, the heat exchangers and the liquid/gas separator respectively. The values of the equipment parameters (K_1, K_2 and K_3) are dependent on the equipment type. The values of all the used parameters and correction factors during the capital cost estimation can be found in Appendix B.

$$\log_{10}\left(C_P^o\right) = K_1 + K_2 \log_{10}(\Omega) + K_3 \left(\log_{10}(\Omega)\right)^2 \tag{5.12}$$

The effect of inflation on the equipment cost was accounted for in Eq (5.13). The CEPCI for the year 2001 is 582 [225]. It is worth noting that the SGMD bare module cost in 2017 was predicted directly from the assumed membrane specific cost. Finally, the annual capital cost (*CC*) resulting from the annual interest payments of all the borrowed equipment is calculated by Eq (5.14).

$$CBM_{2017} = CBM_{2001}\left(\frac{CEPCI_{2017}}{CEPCI_{2001}}\right) \tag{5.13}$$

$$CC = A_F\left(\sum_{All\ equipment} CBM_{2017}\right) \tag{5.14}$$

A_F represents the amortization factor calculated according to the years of the project lifetime (n) and the annual interest rate (i) according to Eq (5.15) [63].

$$A_F = \frac{i(1+i)^n}{(1+i)^n - 1} \tag{5.15}$$

5.3.3.2.Operating Cost

The operating cost considered the cost of electricity and steam. In fact, many studies in literature concluded that the main problem facing the development and application of membrane distillation in an industrial scale is the large amount of energy required in heating the liquid feed to the desired temperature. Steam was chosen to be the heating utility for the proposed desalination process. In literature, large ranges of the specific cost of steam were applied ranging from 3 to 24 €/ton [66]. The steam cost can be affected by many factors like the type of boiler used in steam generation, the used fuel and the steam circuit design in addition to many other factors. An average value of 10 €/ton was applied by R. Schwantes et al. [66] in the steam cost estimation for desalination processes involving air gap membrane distillation (AGMD) or vacuum membrane distillation (VMD). The estimation of the operating cost for the proposed hypothetical process in the current chapter was based on the following assumptions.

- Utility costs were due to the steam used in the feed preheater and the electric power required by the rotary equipment.
- The cost of the required electricity was calculated by the method recommended by G. D. Ulrich and P. T. Vasudevan [226] employing natural gas at the cost of 3.794 $/GJ in the utility cost estimation [227].
- The steam cost was assumed to be 10 $/ton based on the value applied by R. Schwantes et al. [66].
- Operation and periodic maintenance costs (OMC) were taken as 20% of the cost of all the main equipment.
- Periodic membrane replacement cost (RC) was taken as 20% of the SGMD unit cost.

According to the method of G. D. Ulrich and P. T. Vasudevan [226], the specific cost of the utility can be calculated from Eq (5.16).

$$C_{SU} = a\,(CEPCI) + b\,C_f \tag{5.16}$$

C_{SU} represents the utility specific cost. Its unit is ($/ kWh) in case of electric energy cost estimation. The parameters (*a*) and (*b*) are estimated according to the utility type. Their values and estimation are given in Appendix (B). The fuel cost in the utility estimation is represented by C_f in ($/GJ).

5.3.4. Process Development Approach

The assigned design quantities were fixed for all of the simulated cases used in the first optimization step. This is in addition to the fixed values of liquid velocity (0.5 m/s) and salinity (40 g NaCl/L). For each case, the process constraints and limits were checked in order to avoid their violation. The set of the optimized quantities (T_{Lin}, P_{Lin}, P_{Gin}, T_{Gin}, v_{Gin}, L_{tot}) changed from one simulated case to the other aiming at minimizing the attainable water production cost (WPC). The computation of the design calculations and the SGMD modeling equations was performed in an iterative manner using MATLAB. Both the assigned design quantities and the optimized quantities were employed as inputs.

The following steps were implemented.

1) A temperature value of the liquid entering the SGMD T_{Lin} was assigned.
2) The liquid saturation pressure at the liquid inlet to the SGMD $\left(P^{sat}_{(T_{Lin})}\right)$ was calculated.
3) A pressure value of the liquid entering the SGMD P_{Lin} was assigned such that it should be above the value of $\left(P^{sat}_{(T_{Lin})}\right)$ to avoid feed boiling.
4) The liquid entry pressure at the liquid inlet to the SGMD $\left(LEP_{(T_{Lin})}\right)$ was calculated as a function of the corresponding liquid temperature.
5) A pressure value of the gas entering the module P_{Gin} was assigned (with considering potential gas pressure drop along the SGMD vessel) such that the transmembrane pressure difference calculated at inlet conditions ($P_{Lin} - P_{Gin}$) should be less than the estimated liquid entry pressure $\left(LEP_{(T_{Lin})}\right)$.
6) The gas inlet temperature to the SGMD vessel T_{Gin} was estimated from the compression ratio in the compressor. This was based on a guessed value of the gas pressure drop in the main equipment including the SGMD vessel. The validity of the guessed value was confirmed by the iterative solution.

7) For the defined values of (T_{Lin}, P_{Lin}, P_{Gin}, T_{Gin}) and by using the SGMD axially discretized (plug flow) model described in Chapter (3) and the preliminary design calculations described in the current chapter , the maximum allowable value of v_{Gin} was obtained at a given L_{tot} and the maximum allowable value of L_{tot} was obtained at a given v_{Gin}. The maximum interstitial velocity of the inlet gas to the SGMD $(v_{Gin})_{max}$ is the value that above which gas pressure drop becomes exacerbated to the extent of inducing wetting at the gas outlet of the SGMD vessel. The maximum SGMD vessel length $(L_{tot})_{max}$ represents the value that above which liquid pressure drop is high enough for bubbling to take place at the liquid outlet of the SGMD. This has been discussed with more details in section (5.2.2).

8) For the simulated cases at which feed boiling, wetting and bubbling were considered absent, the condensate presence is in the shell-side was checked by comparing the axial profiles of the partial pressure and the vapor pressure of water in the permeate-side.

9) For the simulated cases at which condensation in shell, feed boiling, wetting and bubbling were believed to be absent, the cost estimation took place.

10) Steps (2 to 9) were repeated for different assigned values of T_{Lin} to simulate different cases.

11) For the case of the optimized conditions (T_{Lin}, P_{Lin}, P_{Gin}, v_{Gin}, L_{tot}) corresponding to the lowest water production cost (WPC), further optimization was implemented regarding process assigned values as temperature approaches and pressure of steam used in addition to and flow sheet modifications.

The main calculated values for each simulated case included the following.

- Total required membrane area, total number of fibers and the obtainable water flux in the SGMD vessel
- Areas and heating duties of the heat exchangers
- Required amount of steam in the preheater
- Required power of the rotary equipment
- Volume of separator
- Properties of the main process streams (flow rate, concentration, temperature, pressure and liquid/gas ratio).
- Estimated water production cost

5.4.Results and Discussion

5.4.1. Effect of Main Operating Conditions and SGMD Vessel Length

Aiming at investigating the role of the gas velocity in the obtained flux and water production cost (WPC), cases were simulated at different values of the interstitial velocity of the gas inlet to the SGMD vessel v_{Gin}. This is shown in Fig (5.4) for cases corresponding to liquid entering the SGMD vessel at 1.5 bar, flowing with a velocity of 0.5 m/s and having 40g NaCl/L and sweeping gas inlet stream at 1.3 bar in an SGMD vessel that is 1m long. As it is illustrated by the figure, at a given inlet liquid temperature, the flux increases by raising the gas interstitial velocity. However, this improvement becomes less significant as the gas interstitial velocity increases such that the percentage increase in water flux on raising the value of v_{Gin} from 3 to 4 m/s is less appreciable than that occurring on raising the value of v_{Gin} from 1 to 2 m/s. The effect of the interstitial gas velocity on the flux was apparent on the corresponding obtained WPC.

At given operating conditions, the WPC was reduced by raising the gas velocity. Similar to what has been mentioned regarding the water flux, this reduction in WPC declines at high values of the gas interstitial velocity. It can be also noted from Fig (5.4) that at given operating conditions, there is an exponential increase of the water flux and an exponential decrease of the WPC with the SGMD liquid inlet temperature. Besides, the effect of v_{Gin} becomes negligible at high liquid inlet temperatures. The effects of the gas velocity and the liquid temperature on the water flux during SGMD have been discussed in Chapter (3) such that increasing the velocity of the sweeping gas could reduce the water vapor content in the shell-side (permeate-side) causing a reduction in the water partial pressure in the sweeping gas. This could augment the mass transfer driving force across the membrane leading to an enhancement in the obtainable water flux. However, at high gas velocities, the water content becomes negligible in the shell-side, so a further increase in the gas velocity would not be very effective in raising the water flux.

The exponential increase in the water flux with the SGMD liquid inlet temperature was expected due to the exponential dependence of the vapor pressure of water on the liquid temperature. At relatively small water content in the permeate-side, increasing the liquid temperature could result in an exponential rise in the mass transfer driving force. In case of short SGMD vessels where the axial distance is not sufficient for building up appreciable amounts of water vapor molecules in the shell-side, increasing the liquid temperature could lead to a vapor pressure at the liquid-membrane interface that is much higher than the water partial pressure at the membrane-gas interface. Therefore, the reduction in the water partial pressure on increasing the gas velocity could lead to insignificant improvements on the flux in case of relatively high liquid temperatures.

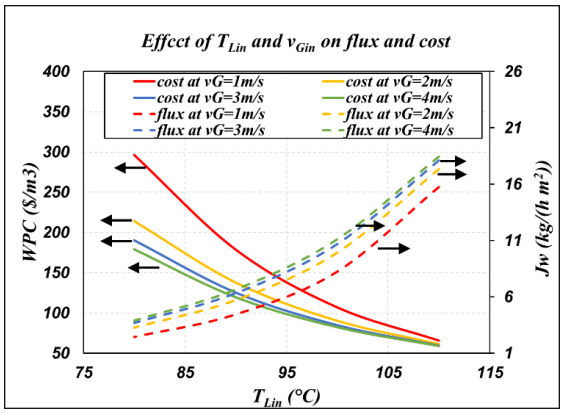

Figure (5.4) *Effect of SGMD inlet gas interstitial velocity and inlet liquid temperature on the flux and WPC at S_{in}=40gNaCl/kg , v_{Lin}=0.5m/s, P_{Lin}=1.5bar, P_{Gin}=1.3bar*

The positive effect of increasing the flux on reducing the water production cost could be pinpointed in Fig (5.4) whether this increase in flux is due to the rise in liquid temperature and/or gas interstitial velocity. In fact, increasing the flux decreases the required membrane area and the required fresh feed flow rate which leads to savings in membrane capital cost and heating requirements of the feed. This would result in savings in the corresponding WPC.

Following the concepts discussed in the process development approach, the key design parameters that could be optimized are mainly the liquid inlet temperature, the inlet gas interstitial velocity and the total length of the SGMD. According to the results of Fig (5.4), the optimum gas velocity was taken as 3 m/s since a further increase in the gas velocity could result in exacerbating the wetting problem at the gas outlet without significant improvement on the water flux. Regarding the liquid inlet temperature $\left(T_{Lin}\right)$ and the total length of the SGMD $\left(L_{tot}\right)$, their effects on the important design requirements and cost items are shown in Fig (5.5) for the cases corresponding to liquid inlet stream at 1.5 bar, flowing with a velocity of 0.5 m/s and a salinity of 40g NaCl/L and sweeping gas inlet stream flowing with an interstitial velocity of 3 m/s at 1.3 bar.

It can be indicated from Fig (5.5a) that at given operating conditions increasing the total length of the SGMD vessel negatively affects the obtainable water flux. In addition to that, the improvement in flux arising from elevating the liquid temperature becomes more significant for short SGMD vessels. This could be due to the decrease in the average liquid temperature and the increase in the average water content in the permeate side taking place on increasing the SGMD length. This could cause a decrease in the average mass transfer driving force. In case of short SGMD vessels, the negative effect of the water partial pressure in the permeate side on the flux is less significant which manifests the positive impact of liquid temperature elevation on the obtainable water flux.

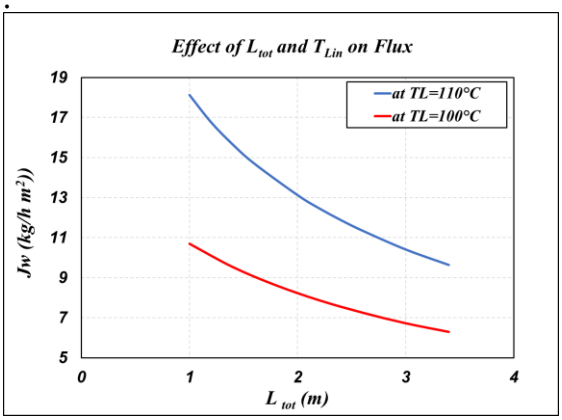

(a)

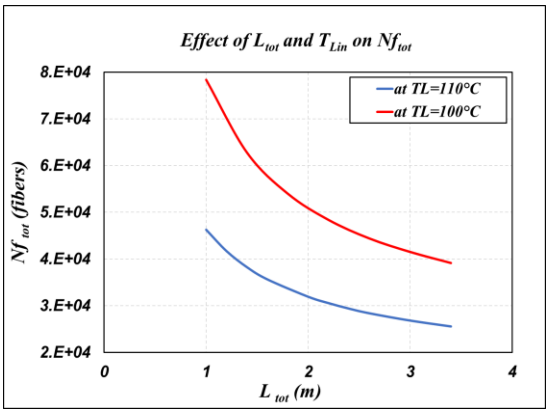

(b)

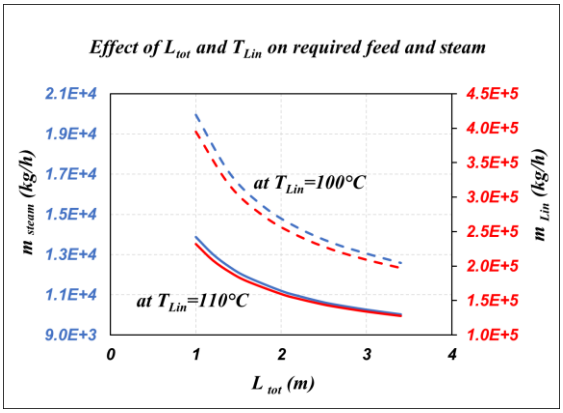

(c)

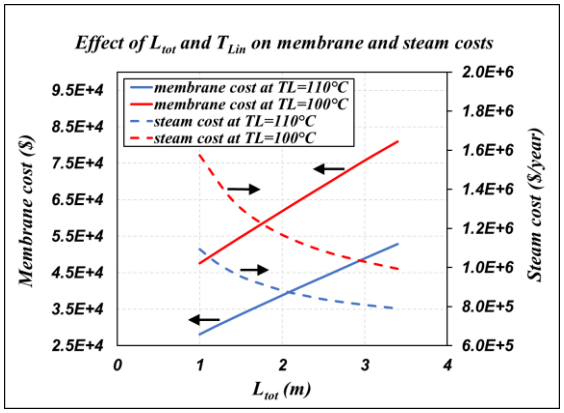

(d)

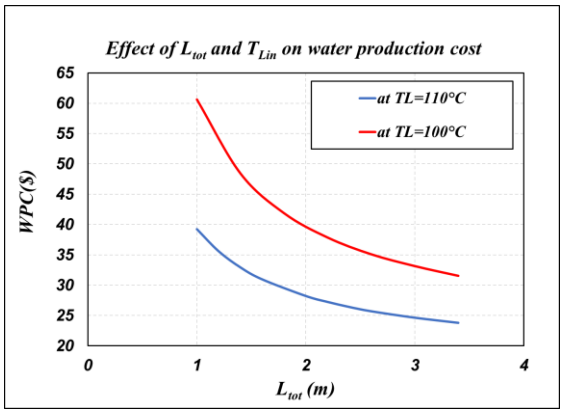

(e)

Figure (5.5) *Effect of SGMD vessel length and inlet liquid temperature on: (a)Flux (b)Total number of fibers (c)Required feed and steam (d)Membrane and steam costs (e)WPC at* S_{in}*=40gNaCl/kg ,* v_{Lin}*=0.5m/s,* P_{Lin}*=1.5bar,* v_{Gin}*=3m/s,* P_{Gin}*=1.3bar*

Obviously, the decline in flux resulting from elongating the SGMD vessel could increase the required total membrane area which exacerbated the fixed costs. However, the required total number of fibers is determined by both, the flux and the total SGMD vessel length according to Eq(5.1). Therefore, the resultant effect of the total length of the SGMD vessel on the total required number of fibers was inspected as shown in Fig (5.5b). It can be demonstrated that increasing the total SGMD vessel length enabled savings in the required number of fibers. This could be explained by Eq(5.1) such that a given percentage increase in the total SGMD vessel length resulted in a less percentage decrease in the water flux. Also, at a given total SGMD vessel length, increasing the liquid temperature led to a reduction in the required number of fibers. This is due to the corresponding improved flux corresponding to less required total membrane area

On investigating the effect of the total length of the SGMD vessel L_{tot} and the liquid inlet temperature T_{Lin} on the required flow rates of the fresh feed and the heating steam, Fig (5.5c) was obtained. Increasing both, T_{Lin} and L_{tot} could decrease the required feed and steam flow rates. In fact, the flow rate of the fresh feed could be determined by the required total number of fibers according to Eq(5.2). The former affects the process heating requirements expressed by the steam flow rate. This is due to the fact that the required heating duty in the preheater is determined by the required elevation in the heating capacity of the liquid entering the preheater towards the desired SGMD inlet liquid temperature. This also indicates that even though raising the liquid feed temperature could be expected to increase the required heating duty in the preheater, the savings in the feed flow rate due to the improved flux resulting from raising the feed temperature offers fewer energy requirements.

The effects of T_{Lin} and L_{tot} on the bare module membrane cost in ($) and the annual steam cost are explicitly shown in Fig (5.5d). As it has been already mentioned, increasing T_{Lin} or decreasing L_{tot} could enhance the flux and cause savings in the required membrane area. This corresponds to decreased membrane module cost. Moreover, the savings in steam requirements on increasing T_{Lin} and L_{tot} could offer less steam annual cost as it is shown in Fig (5.5d).

The explicit role of T_{Lin} and L_{tot} on the final water production cost (WPC) is illustrated in Fig (5.5e). It was found that increasing T_{Lin} and L_{tot} could result in large savings in the total WPC. By coupling this observation to those obtained from Fig (5.5d), it could be revealed that the steam is the controlling cost item in the SGMD process as it was expected. Besides, the positive effect of increasing the total SGMD vessel length on decreasing the steam requirements and WPC declines as L_{tot} increases as indicated in Fig (5.5d) and (5.5e). This could indicate that the ratio of the percentage increase in L_{tot} to the percentage decrease in the corresponding flux declines on increasing L_{tot}.

5.4.2. Optimizing SGMD Inlet Liquid Temperature

According to the findings of Fig (5.5), it is desired to operate at the maximum possible SGMD inlet liquid temperature T_{Lin} and the maximum allowable total SGMD vessel length L_{tot} in order to minimize the water production cost (WPC). The maximum allowable T_{Lin} should be below the wetting temperature (120°C) in order to avoid wetting and flooding as it has been already discussed. At a given T_{Lin} and operating conditions, the maximum allowable L_{tot} could represent the axial length of the SGMD vessel that above which bubbling is highly probable to occur at the sweeping gas inlet to the SGMD. This is due to the fact that increasing the total axial length could exacerbate the liquid pressure drop. Owing to the importance of the roles of both T_{Lin} and L_{tot} on the cost savings, the relation between both was investigated as shown in Fig (5.6).

According to the described process development approach, T_{Lin} affects the assigned values of the gas inlet pressure and the liquid inlet pressure to the SGMD vessel in order to avoid feed boiling and wetting phenomena. Also, the assigned value of the inlet gas temperature to the SGMD is affected as discussed in the process development approach. This applies to the cases simulated in Fig (5.6). However, the simulated cases correspond to feed entering the SGMD vessel at a velocity of 0.5 m/s with a salinity of 40 g/L and sweeping gas introduced to the SGMD vessel at an interstitial velocity of 3 m/s.

Results of the different simulated cases shown in Fig (5.6) manifested the effect of T_{Lin} on the maximum allowable L_{tot} as well. On elevating the value of the operating T_{Lin} the corresponding value of the maximum allowable T_{Lin} declines. This could be explained as follows. At given inlet gas and inlet liquid velocity values, as the value of T_{Lin} increases, the corresponding liquid entry pressure $LEP_{(T_{Lin})}$ decreases. This necessitates the assignment of close values of the pressures of the gas and liquid streams entering the SGMD vessel in order to avoid wetting at the gas outlet. The fact that the operating transmembrane pressure difference is small in such cases could make the bubbling problem more critical at the liquid outlet. This requires the application of shorter SGMD vessels in order to avoid excessive liquid pressure drops in order to avoid the risk of bubbling at the liquid outlet.

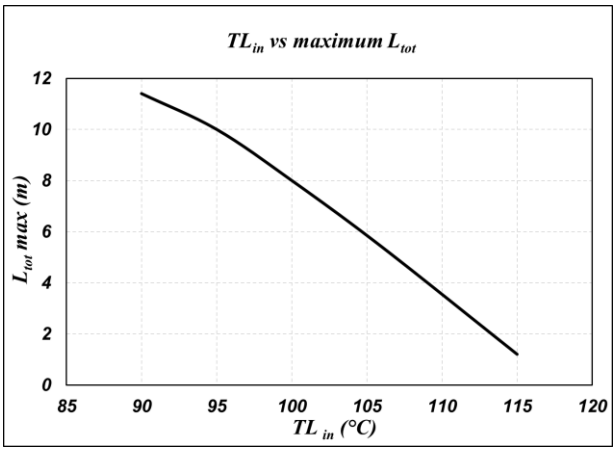

Figure (5.6) *Effect of SGMD inlet liquid temperature on maximum allowable SGMD vessel length at S_{in}=40gNaCl/kg , v_{Lin}=0.5m/s ,v_{Gin}=3m/s*

It can be implied that at given inlet liquid and gas velocity values, the SGMD liquid inlet temperature T_{Lin} has either a direct or an indirect effect on the assigned values of the liquid inlet pressure P_{Lin}, the gas inlet pressure P_{Gin} and temperature T_{Gin} and the maximum allowable SGMD vessel length $(L_{tot})_{max}$. Therefore, T_{Lin} represents the key operating condition that needs to be optimized. The optimization of the liquid inlet temperature to the SGMD vessel was performed according to the minimum water production cost (WPC) as shown in Fig (5.7). This corresponded to the simulated cases shown in Fig (5.6).

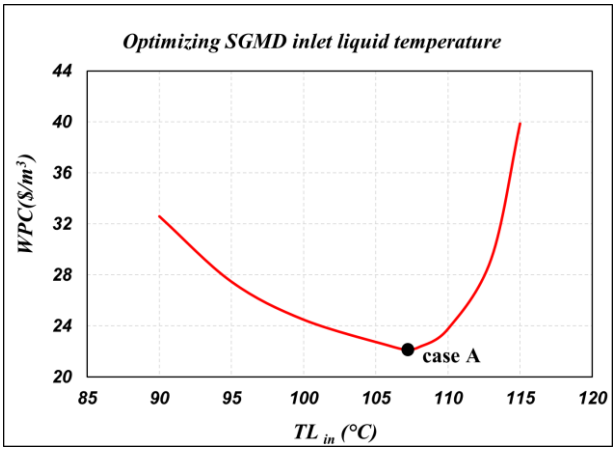

Figure (5.7) *Optimization of the SGMD inlet liquid temperature at S_{in}=40gNaCl/kg , v_{Lin}=0.5m/s ,v_{Gin}=3m/s*

On increasing the value T_{Lin}, two phenomena having opposite effects on the WPC take place. The first phenomenon is the enhancement in flux causing savings in the required flow rates of the fresh feed and steam as shown in Fig (5.5c). This leads to savings in the WPC (at a given value of

the total SGMD vessel length) as shown in Fig (5.5e). The second phenomenon is represented by the augmented limitation in the SGMD vessel length on increasing T_{Lin}. This leads to reduced maximum allowable SGMD vessel length $(L_{tot})_{max}$. This in turn negatively affects the possible savings in the WPC because increasing the total SGMD vessel length at a given T_{Lin} could lead to savings in the required steam and WPC according to Fig (5.5c) and (5.5e) respectively. The resultant of these two phenomena could explain the behavior observed in Fig (5.7) such that the optimum T_{Lin} was found to be 117°C corresponding to $(L_{tot})_{max}$ of 5.4 meters. This is referred to as the "optimized case A" having a WPC cost of 22.16 \$/m^3 of obtained freshwater. Details about the properties of the liquid and gas streams involved in the "optimized case A" are listed in Tables (5.1) and (5.2) respectively while the comparison between its cost items is presented in Fig (5.8). It can be demonstrated that the steam cost represents the controlling cost item. The capital cost comes in second place with an insignificant contribution of the required electricity and other cost items on the required total annual cost.

Table (5.1) *Properties of liquid streams for the optimized case A (by referring to Fig (5.1))*

Stream	L_1	L_2	L_3	L_4	L_{in}	L_{out}	L_5	L_w
$\dot{m}$ [kg/h]	1.18E+5	1.18E+5	1.18E+5	1.18E+5	1.18E+5	1.13E+5	1.13E+5	5.00E+3
T [°C]	30	30	58	62	107	82	77	40

Table (5.2) *Properties of gas streams for the optimized case A (by referring to Fig (5.1))*

Stream	G_1	G_{in}	G_{out}	G_2
$\dot{m}$ [kg/h]	4.61E+3	4.61E+3	9.61E+3	9.61E+3
T [°C]	40	45	102	40

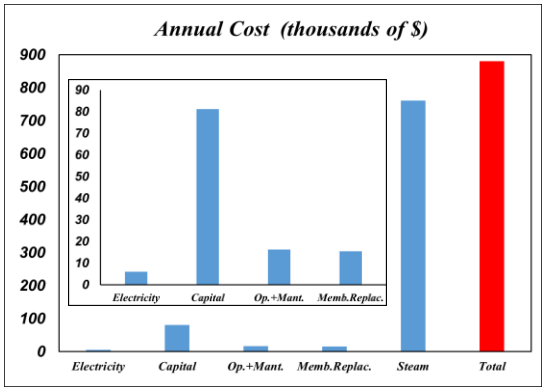

Figure (5.8) *Cost contributions for the optimized case A*

5.4.3. Further Optimization

5.4.3.1.Assigned Process Parameters

Further optimization could be related to modifications in the assigned process parameters aiming at mitigating the steam requirements. Following this concept, "optimized case A" was investigated for further optimization based on the assigned value of the temperature approach in the heat exchanger *HX-1* (See Fig (5.1)). This temperature approach represents the temperature difference between streams L_4 and L_{out} . This represents a critical process design parameter as it affects the temperature of the liquid entering the preheater *HX-2* which could affect the steam requirements. The optimization of this temperature approach is presented in Fig (5.9a). It can be indicated that decreasing the temperature approach reduced the steam cost but increased the fixed charges (due to the larger area required for the heat exchanger *HX-1*) such that the optimum temperature approach was found to be 12℃ corresponding to WPC of 20.94 \$/m^3 of freshwater produced. This is referred to as "optimized case B".

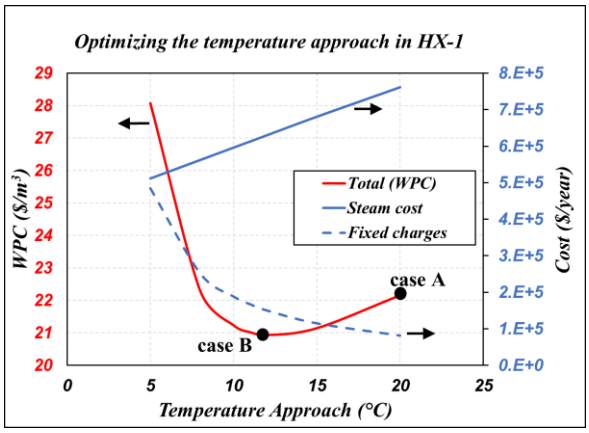

Figure (5.9) *Optimization of the temperature approach in heat exchanger HX-1 for streams L_4 and L_{out} (by referring to Fig (5.1))*

Another process design parameter affecting the steam requirements is represented by the pressure of the steam P_{Steam} used in the preheater *HX-2*. In fact, the steam pressure determines the operating steam temperature which in turn affects the corresponding heat of steam condensation and the temperature approach in the preheater. Therefore, the "optimized case B" underwent further optimization regarding the pressure of the steam used in the preheater. The results of this optimization process are shown in Fig (5.10). It can be observed from the figure that on reducing the steam pressure, the steam cost slightly decreases while the fixed charges increase. This could be due to the fact that high steam pressure value corresponds to high-temperature approach in the preheater requiring less area of heat transfer which reduces the fixed charges. However, increasing the steam pressure augments the operating steam temperature. This corresponds to lower water latent heat increasing the required steam flow and decreasing the gained output ratio (GOR) (kg produced freshwater/kg used steam).

The optimized case in Fig (5.10) was found to be at a steam pressure of 1.85 bar. This is referred to as "optimized case C" which corresponds to a WPC cost of 20.92 \$/m^3 of freshwater product. Obviously, optimizing the steam pressure resulted in a negligible reduction in the cost from case B to case C.

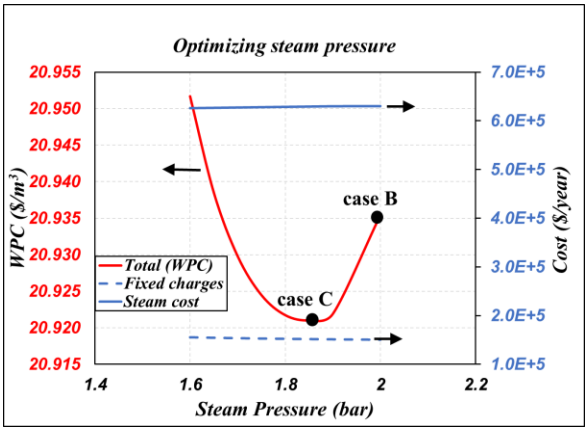

Figure (5.10) *Optimization of pressure of the steam used in the preheater HX-2 (by referring to Fig (5.1))*

5.4.3.2.Applying The "Feed and Bleed Configuration"

According to the results of the optimized cases A, B and C belonging to the flow sheet of the "single-pass" proposed in Fig (5.1), steam represents the main contributing factor of the resulting high water production cost (WPC). Besides, low water productivity was obtained. This is could be clarified by the aid of Table (5.1) and by considering the stream entering the overall process (L_1) and those exiting the overall process (L_5 and L_w). The flow rate of the stream (L_1) is much greater than that of the freshwater product stream (L_w). Consequently, low process productivity was attained. Besides, the flow rate of stream (L_5) was significantly greater than (L_w) such that stream (L_5) exits from the overall process with a much higher temperature than that of the stream entering the overall process (L_1). In fact, this unused high thermal energy (heating capacity) of stream (L_5) negatively affects the process thermal efficiency. This could explain the relatively high steam requirements and WPC in case of the "single pass" flow sheet proposed in Fig (5.1).

Accordingly, an alternative flow sheet was suggested for further optimization regarding the water production cost (WPC). The suggested alternative flow sheet is shown in Fig (5.11). This flow sheet employs the "feed and bleed" configuration in order to increase the overall process productivity and decrease the energy required for heating the feed to the SGMD vessel. This was approached by recycling a large portion of the liquid outlet of the SGMD vessel back to join the fresh feed.

By referring to Fig (5.11), on using a high recycle ratio (RR) such that the flow rate of the recycled stream (L_{rec}) represents 99% of that of the stream (L_{out}), the following outcomes could be expected.

- A very small flow rate of the hot stream (L_5) exiting the overall process when compared to the freshwater product stream (L_w). This could mitigate the unused thermal energy in the process which could increase the corresponding process thermal efficiency.
- Less flow rate of the process fresh feed stream (L_1) could be required due to being combined with the stream recycled from the SGMD vessel. This could greatly improve the process productivity.
- The high thermal energy of the recycled stream due to its high flow rate and temperature, when compared to the heated fresh feed stream (L_3), could offer savings in the required duty and steam in the preheater *HX-3*. This could in turns decrease the resulting steam cost.

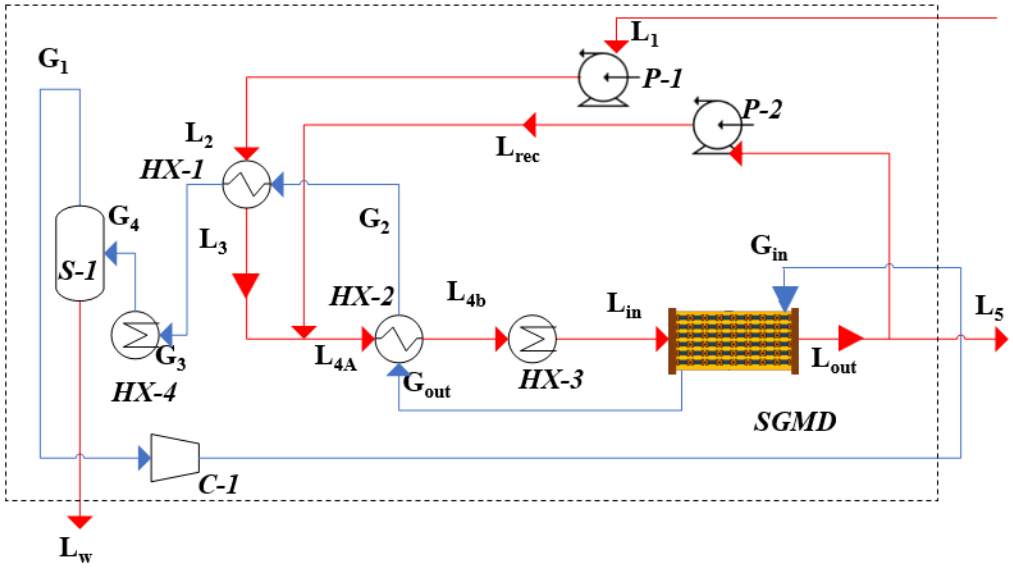

Figure (5.11) *Alternative Flowsheet using "feed and bleed" configuration*

The same concepts of the preliminary design calculations discussed in the current chapter for the "single pass" configuration shown in Fig(5.1) were adopted in the "feed and bleed" configuration represented by Fig (5.11) after considering the different involved streams and equipment. Moreover, extra heat transfer equipment was utilized in the "feed and bleed" configuration aiming at maximizing the heat recovery while the condenser *HX-4* employed cooling water. In fact, the cooling water was added to the electricity and steam during the operating cost estimation and was calculated according to the method of G. D. Ulrich and P. T. Vasudevan [226]. The specific cost of the cooling water ($/m^3) was predicted by Eq (5.16) where the estimation of

the corresponding parameters (*a* and *b*) used in this equation can be found in Appendix (B). The assigned values of the required process parameters in the "feed and bleed" configuration followed the same approach of the single-stage process after considering the updates in the flow sheet. Moreover, the cooling water was assumed to enter the condenser *HX-4* and exit with a 10 °C. The simulation of the "feed and bleed" process took place at the same SGMD inlet operating conditions and assigned values of the "optimized case C" that was employed for the "single pass" configuration.

Results showed that the "feed and bleed" configuration managed to reduce the steam cost reaching a value of 11.14 $ per every 1 m^3 of produced fresh water. However, there was an extra cost due to the high flow rate of the cooling water required for cooling the gas towards the separator *S-1* temperature and for condensing the water amount that permeated during the SGMD separation step. The cooling water utility cost reached 14.64 $/$m^3$ of distilled water. Therefore, the cost of steam and cooling water only in the "feed and bleed" configuration was around 25.8 $/$m^3$ of distilled water. This was higher than the total water production cost (WPC) for each of the "optimized cases A, B and C" (using single-pass) calculated after considering both their capital and operating costs. Details about the liquid streams, gas streams and equipment resulting from simulation of the "feed and bleed" configuration can be found in Tables (5.3), (5.4) and (5.5) respectively.

Even though the "single pass" configuration shown in Fig (5.1), used higher steam requirements, it offered savings in the cooling requirements of the sweeping gas before its entrance to the separator due to the high cooling capacity of the fresh feed entering the overall process with a flow rate that is much greater than the fresh feed entering the process suggested by the "feed and bleed" configuration in Fig (5.11). This could explain the very close duties of the heat exchangers HX-3 and HX-4 in case of the "feed and bleed" configuration given in Table (5.5). At the same SGMD inlet operating conditions, this finding favored the flow sheet configuration of the "single pass" and the corresponding "optimized case C" since the optimization is based on the WPC.

However, the process productivity (m^3 distilled water/m^3 fresh feed) was much higher in the "feed and bleed" case. In fact, the "optimized case C" corresponded to very low process productivity (4.24%) while at the same SGMD inlet operating conditions, the "feed and bleed" configuration managed to reach process productivity of 84.75%. Therefore, the "feed and bleed" can be favored from the point of view of process productivity.

Table (5.3) *Properties of liquid streams for "Feed and bleed" configuration (by referring to Fig (5.11))*

Stream	L_1	L_2	L_3	L_{4A}	L_{4B}	L_{in}	L_{out}	L_5	L_{rec}	L_w
$\dot{m}$ [kg/h]	5.90E+3	5.90E+3	5.90E+3	1.18E+5	1.18E+5	1.18E+5	1.13E+05	9.00E+2	1.12E+5	5.00E+3
T [°C]	30	30	36	80	81	107	82	82	82	40

Table (5.4) *Properties of gas streams for "Feed and bleed" configuration (by referring to Fig (5.11))*

Stream	G_1	G_{in}	G_{out}	G_2	G_3	G_4
$\dot{m}$ [kg/h]	4.61E+3	4.61E+3	9.61E+3	9.61E+3	9.61E+3	9.61E+3
T [°C]	40	45	101	61	52	40

Table (5.5) *Heat Exchange Requirements for "Feed and bleed" configuration (by referring to Fig (5.11))*

Equipment	Quantity	Value
HX-1	Q [Watt]	3.99E+4
HX-2		1.70E+05
HX-3 (Heater)	Q [Watt]	3.42E+06
	Steam Flow [kg/h]	5568
	Steam Cost [$/m^3 distilled water]	11.14
HX-4 (Condenser)	Q [Watt]	3.39E+06
	Cooling water Flow [kg/h]	174882
	Cooling water Cost [$/m^3 distilled water]	14.64

5.4.4. Optimized Case

The following remarks are based on the "single-pass" flow sheet presented by Fig (5.1). According to the simulated cases, the optimum SGMD inlet gas interstitial velocity was found to be around 3 m/s while the optimum SGMD liquid inlet temperature T_{Lin} was found to be 107 ℃ with a total SGMD vessel length L_{tot} of 5.4 m. This represented the maximum allowable total length corresponding to the applied T_{Lin} .On further optimization, " the optimized case C" employing the single pass configuration (flow sheet of Fig (5.1)) was found to be the case corresponding to the least water production cost (WPC) among all the simulated cases. The optimized temperature approach in the heat exchanger HX-1 and optimized steam pressure used in the preheater HX-2 were found to be 12℃ and 1.85 bar for the "optimized case C" which corresponds to a WPC of

20.92 \$/m^3 of distilled water. Details about the properties of the liquid and gas streams of the "optimized case C" are given in Tables (5.6) and (5.7) respectively.

Table (5.6) *Properties of liquid streams for the optimized case C (by referring to Fig (5.1))*

Stream	L_1	L_2	L_3	L_4	L_{in}	L_{out}	L_5	L_w
$\dot{m}$ [kg/h]	1.19E+5	1.19E+5	1.19E+5	1.19E+5	1.19E+5	1.14E+5	1.14E+5	5.00E+3
$\dot{N}$ [mol/h]	6.40E+6	6.40E+6	6.40E+6	6.40E+6	6.40E+6	6.12E+6	6.12E+6	2.77E+5
T [°C]	30.0	30.0	57.4	69.9	107.0	81.9	68.9	40.0
P [bar]	1.01	2.52	2.18	1.84	1.50	1.26	1.01	1.17
x_s [mol/mol]	0.0128	0.0128	0.0128	0.0128	0.0128	0.0133	0.0133	0.0

Table (5.7) *Properties of gas streams for the optimized case C (by referring to Fig (5.1))*

Stream	G_1	G_{in}	G_{out}	G_2
$\dot{m}$ [kg/h]	4.64E+3	4.64E+3	9.64E+3	9.64E+3
$\dot{N}$ [mol/h]	1.69E+5	1.69E+5	4.47E+5	4.47E+5
T [°C]	40.0	44.8	101.4	40.0
P [bar]	1.17	1.23	1.20	1.17
y_w [mol/mol]	0.06	0.06	0.65	0.06

The axial profiles of the flux, the temperatures and concentrations in the liquid and gas streams in addition to the checks of the wetting, bubbling and water condensation in shell-side are all shown in Fig (5.12) for the "optimized case C". The axial profiles shown in Fig (5.12a), (5.12b) and (5.12c) were expected according to the modeling results shown and discussed in detail in Chapter (3). The axial profiles of the liquid entry pressure and the transmembrane pressure difference are shown in Fig (5.12d). This figure manifests the importance of ensuring the absence of wetting at the SGMD gas outlet (SGMD liquid inlet) and the absence of bubbling at the SGMD gas inlet (SGMD liquid outlet). According to this figure, the "optimized case C" could avoid wetting and bubbling in case of very minor process disturbances. Similarly, Fig (5.12e) represents the check of the absence of water condensation in the shell side (permeate-side). Although the water content and water partial pressure increase in the positive axial direction according to Fig (5.12b), the water saturation temperature also increases in the same direction due to the rise in the gas temperature according to Fig (5.12a). Therefore, the final observation drawn from Fig (5.12e) is that water condensation in the shell side could be considered absent for the "optimized case C". Details about the most important design parameters and cost items for the "optimized case C" can be found in Table (5.8)

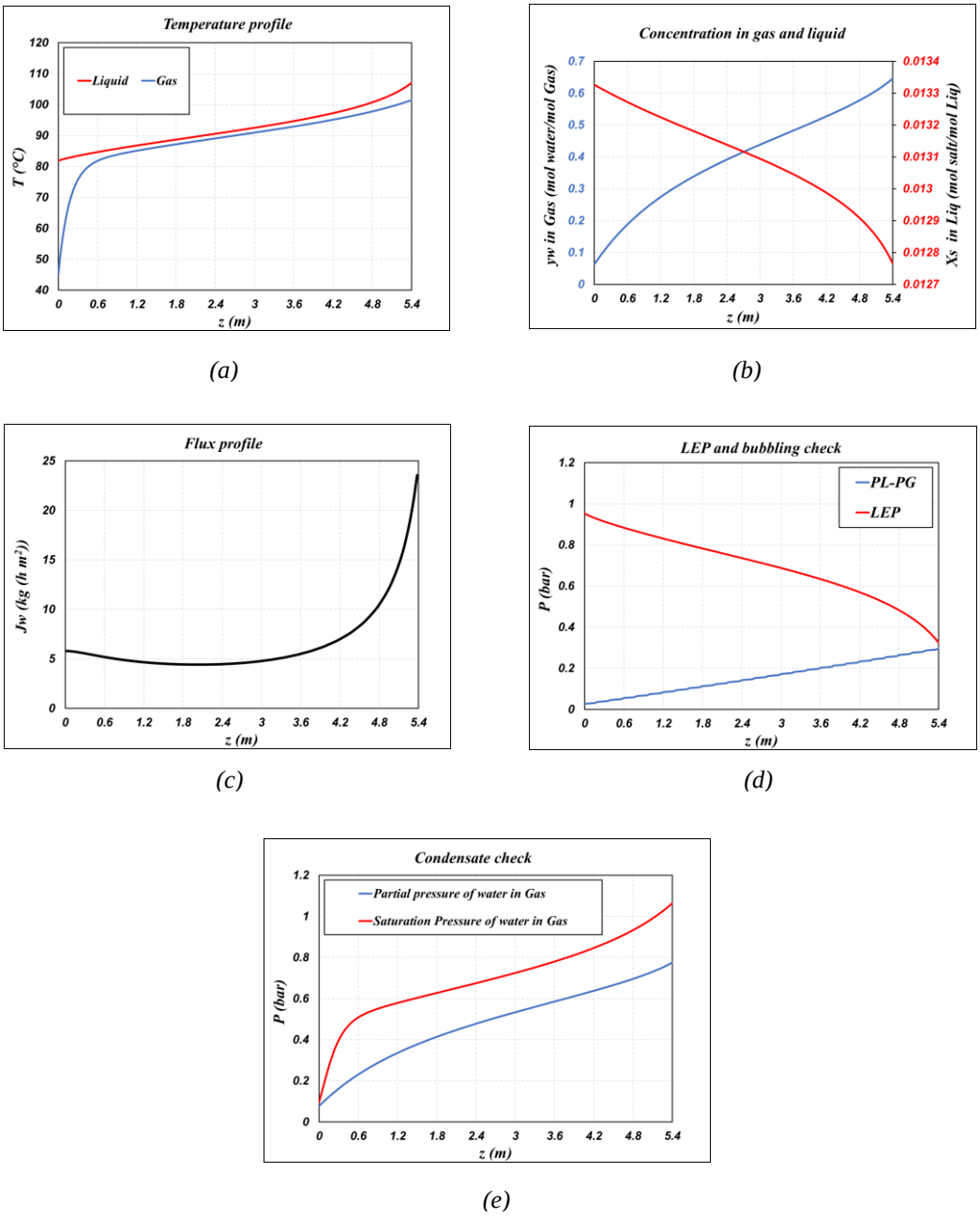

Figure (5.12) *Axial profiles in the SGMD vessel for the optimized case C of: (a)Liquid and gas temperatures (b)Mole fraction of salt in liquid and of water vapor in gas (c)Flux (d)LEP and transmembrane pressure difference (e)Partial pressure and saturation pressure of water in the gas*

The value of the water production cost (WPC) of the "optimized case C" employing the studied hydrophobic ceramic multi-layer membranes was considered relatively high. This was attributed to the large energy demands of the SGMD process expressed by high steam cost. However, this value (20.92 $/m^3) was considered much lower than the value estimated by S. E. Moore at el. [183], where according to their cost estimation, the WPC for a solar-powered SGMD water desalination process

was found to be 85 $/m^3. Possible improvements could be related to enhancements in the thermal efficiency of the process or to advancement in the membrane manufacturing phase to offer higher fluxes.

One of the possible ways to minimize the energy costs of the "optimized case C" is the employment of solar energy membrane distillation units. This approach was followed by F. Banat et al. [63] where the economic analysis of a solar-powered air gap membrane distillation (AGMD) for water desalination took place. For a 20-year plant lifetime, the WPC for compact plants reached was estimated to be 18 $/m^3 [63]. Even though this value is still higher than that obtained by RO, the use of photovoltaic solar panels could result in an appreciable percentage reduction in the WPC of desalination processes utilizing MD.

Table (5.8) *Important design parameters and results for the optimized case C*

SGMD vessel	Flux [kg/(h m^2)]	6.56
	Total number of fibers [fibers]	23646
	Total membrane area [m^2]	762
	Total vessel length [m]	5.4
	Number of modules in series (20 cm long each) [modules]	27
	Number of modules in parallel (60 fibers per module) [modules]	394
Other equipment	Area of *HX-1* [m^2]	1162
	Area of *HX-2* [m^2]	178
	Area of condenser [m^2]	184
	Power of pump [W]	5693
	Power of compressor [W]	634
	Volume of separator [m^3]	1.9
Steam requirements	Steam flow rate [kg/h]	7967
	Pressure of steam [bar]	1.85
Cost	Cost of steam [$/y]	629116
	Cost of fixed charges [$/y]	151469
	Water production cost (WPC) [$/m^3]	20.92

Another approach of maximizing the SGMD desalination process heat efficiency is by using a waste heat source. This could be achieved by making use of the thermal energy of a stream exiting from a separate process in heating the fresh stream entering the SGMD desalination process. This could lead to appreciable savings in the required steam. According to the economic analysis of U. K. Kesieme et al. [67], the application of waste heat source in heating the fresh feed to the MD processes was believed to offer savings of the steam cost up to 90%. In fact, this is one of the

advantages of MD over RO because the latter is electrically driven so the application of the waste heat source will be more practical in energy savings related to MD processes. By applying this concept and using 10% of the steam cost, the final expected WPC cost on employing waste heat source could reach 6.7 $/m^3 for the desalination process proposed in the current chapter. This WPC value is deemed to be very interesting as it reveals the promising competency of MD to RO in compact plants where the WPC by RO could reach values up to 3 $/m^3 [1]. Besides, the application of the proposed SGMD desalination process for high salinity solutions can be employed in the further treatment of the retentate streams form the RO leading to an increase in the overall process productivity and reduction in the WPC [65,67,69].

Finally, further optimization of the membrane thermophysical properties and morphological parameters could play an important role in the further possible enhancement in the obtainable flux. This could be translated into higher productivity and/or fewer energy requirements.

5.5.Conclusion

Process development and optimization took place for a water desalination process employing sweeping gas membrane distillation (SGMD) that uses the studied hydrophobic ceramic multi-layer membrane modules. Results were based on comparing different simulated cases that do not violate the constraints of the SGMD process. These constraints affected the accepted ranges of the operating conditions and the total SGMD vessel length for the simulated cases. The process development was based on a hypothetical single pass SGMD desalination process with assigned process parameters. Preliminary design equations were coupled with the axially discretized SGMD model in order to simulate cases of different operating conditions and SGMD vessel length. Non-rigorous cost estimation was then applied to compare the water production cost (WPC) of each case. Optimization was based on the lowest attainable WPC.

The optimum gas interstitial velocity was found to be around 3 m/s. Further increase in the gas velocity does not offer appreciable improvement in the flux and could exacerbate the gas-side pressured drop which could engender higher wetting risk. At given velocity values of the liquid and gas streams in the SGMD vessel, maximizing the SGMD liquid inlet temperature and the total length of the SGMD vessel was found to minimize the required amount of feed flow rate and heating steam. This revealed the importance of using the maximum allowable liquid temperature and SGMD vessel length. However, the increase in the liquid temperature at the inlet of the SGMD resulted in a decrease in the maximum allowable total SGMD vessel length. This was due to the combined effect of the liquid inlet temperature and the total length on the criticality of the wetting risk at the gas outlet and the bubbling problem at the liquid outlet. In addition to the total SGMD vessel length, other important operating conditions were affected either directly or indirectly by the SGMD inlet liquid temperature like the inlet gas pressure and temperature and the inlet liquid pressure. As a result, the key operating parameter was considered to be the temperature of the liquid

entering the SGMD vessel. Its optimized value was found to be 107°C corresponding to an SGMD vessel having a total length of 5.4m.

On comparing the cost items involved in the process, the total cost was mainly determined by the steam cost due to the high thermal energy required for heating the SGMD liquid feed. Aiming at reducing the steam requirements, further optimization was implemented regarding the steam pressure and the temperature approach in the heat exchanger used prior to the final heating of the feed by steam. This resulted in possible energy savings. An alternative process flow sheet using the "feed and bleed" configuration was proposed. Results showed that the "feed and bleed" configuration could offer less steam demand than the "single pass" process configuration. However, the "single pass" configuration could offer savings in the cooling requirements needed for cooling the wet sweeping gas and condensing the water molecules that permeated across the membrane during the SGMD. The final comparison between the two configurations favored the "single pass" process in terms of water production cost and favored the "feed and bleed" configuration in terms of the process productivity.

In the absence of a waste heat source, the WPC of the optimized case of the proposed hypothetical process was found to be 20.92 $\$/m^3$. However, on making use of waste heat source, appreciable savings in steam could be attained where in case of 90% savings in steam cost, the optimized case of the proposed desalination process using SGMD could reach WPC of 6.7 $\$/m^3$. On being compared to WPC of RO process, this value could show possible future competency of SGMD, especially for the compact process. Besides, the application of the proposed SGMD process for high salinity solutions could be useful for treating the retentate streams of the RO process. This could improve the productivity and the energy savings of the overall desalination process.

List of Symbols

Latin Letters	
A_{tot}	Total membrane area
A_F	Amortization factor
C_P^o	Purchased cost of equipment (at basic conditions)
C_{SU}	Specific utility cost
C_f	Fuel cost
CC	Annual capital cost
CBM	Bare module cost
$CEPCI$	Chemical engineering plant cost index
d	Diameter
F_M	Correction factor of equipment material
F_P	Correction factor of equipment operating pressure
i	Interest rate
J_W	Water mass flux
L_{tot}	Total length of the sweeping gas membrane distillation vessel
LEP	Liquid entry pressure
$\dot{m}$	Mass flow rate
n	Number of years
$N_{f,tot}$	Total number of fibers (tubes)
$\dot{N}$	Molar flow rate
OC	Annual operating cost
P	Pressure
P^{sat}	Saturation pressure
P_W^G	Partial pressure of water in the gas
Q	Heating duty
$S_{t,tot}$	Actual shell area available for gas flow
T	Temperature
T_{wet}	Critical wetting temperature
TAC	Total annual cost
v	velocity

WPC	Water production cost
x	Mole fraction in the liquid state
y	Mole fraction in the vapor state
Z	Axial direction
Greek Letters	
ε_p	Packing factor of the module
ρ	Density
Ω	Equipment sizing parameter
Subscripts and Superscripts	
G	Gas
in	Inlet to the sweeping gas membrane distillation
IN	Inner
L	Liquid
out	Outlet from the sweeping gas membrane distillation
OUT	Outer
S	NaCl salt
sat	saturated
S	Shell
tot	Total
w	Water

[This page intentionally left blank]

Chapter Six

Conclusions

In this PhD thesis, the process development and optimization of proposed hypothetical seawater desalination were implemented. This process employed sweeping gas membrane distillation (SGMD). The membranes used were tubular hydrophobic multi-layer membranes. Before process development, the characterization of some membrane morphological properties and the investigation of the module performance during SGMD were carried out.

The membranes are composed of four layers possessing different morphological properties. "Layer 3" represented the hydrophobic layer that is to be in contact with the liquid feed during SGMD operations. The pore diameter and the porosity-tortuosity ratio of this layer were either unknown or unconfirmed by the manufacturer. In this PhD thesis, the characterization of these properties took place by coupling single gas permeation experimental tests with modeling for both coated (hydrophobized) and uncoated (unhydrophobized) membranes. The estimated morphological properties were based on two modeling approaches which were referred to as the "layer-by-layer" (LBL) method and as the "average membrane morphology" (AMM) method. The former considered the unique contribution of the morphological properties of each single membrane layer on the overall membrane mass transfer resistance while the latter viewed the membrane as a single layer and considered the average morphological properties of the entire membrane. For both approaches, the dusty gas model (DGM) was adopted in the description of the transmembrane mass transfer during gas permeation arising from the Knudsen and viscous flow mechanisms.

According to the experimental and modeling results, "Layer 3" represented the controlling resistance during gas permeation. This was attributed to its relatively small pores when compared to the other membrane layers. Comparing the results of the coated and uncoated membranes allowed the evaluation of the negative effect of the hydrophobization on the membrane permeance. This was related to the possible alteration in the morphological properties resulting from carbonization and hydrophobization procedures that had taken place for the coated membranes.

The transmembrane mass transfer resistance during SGMD was modeled on considering the membrane morphological properties predicted from the "layer-by-layer" (LBL) approach and on considering those obtained by the "average membrane morphology" (AMM) approach. This was performed for the simple case corresponding to the permeation of water vapor across air-filled pores during SGMD. The model put into account the contributions of the Knudsen and molecular diffusion mechanisms. Results showed that the membrane mass transfer resistance was underestimated in the case of using the characterized average membrane morphological properties according to the AMM approach. Besides, on using the morphological properties of each membrane layer during SGMD modeling, the support layer was found to be the controlling mass transfer resistance due to its relatively large thickness when compared to the other membrane layers. Therefore, the transmembrane mass transfer resistance during SGMD could be mitigated by

reducing the support thickness. However, this could negatively affect the membrane mechanical strength.

The performance of the hydrophobic membrane modules during SGMD operations was investigated by experimental and modeling studies for NaCl (aq.) feed. The results of the lab-scale experiments showed that the modules were capable of undergoing SGMD at liquid temperatures up to 110°C. The performance of the modules was satisfactory since water flux was achievable without possible problems as flooding, thermal shocks and leakages. The experimental flux values went in agreement with the modeled results obtained on considering the morphological properties of each membrane layer. On the contrary, the experimental flux values were much less than those predicted by the model considering the membrane average morphological properties. This manifested the inconvenience of using the "average membrane morphology" (AMM) approach in the morphological characterization of the studied membranes.

The developed SGMD model was utilized in estimating the effect of the operating conditions and the flow patterns on the water flux. Results showed that the most significant operating conditions affecting the flux were the liquid feed temperature and the sweeping gas pressure. The flux was found to increase exponentially on elevating the liquid temperature. Enhancements of the flux could be attained by reducing the gas pressure and increasing the liquid and gas velocities. However, increasing the liquid velocity could negatively influence the SGMD productivity. In addition to that, the enhancement in flux by raising the gas velocity diminishes as the gas velocity increases. The effect of the gas temperature on the flux was found to be negligible. The model allowed the evaluation of the negative effect of the salinity on the flux due to the corresponding reduction in water activity. Besides, modeling results demonstrated that the molecular diffusion was the controlling flow mechanism while the contribution of Knudsen diffusion was considered negligible. The relatively large pore size of the support layer (the controlling resistance during SGMD) could be the reason for the predominance of the molecular diffusion at the studied operating conditions.

The developed SGMD model allowed the simulation of the axial profiles of the operating conditions, the driving forces and the water flux inside the module in case of co-current and counter-current flow manners. The axial gradients of the sweeping gas temperature and concentration were found to be much greater than those corresponding to the liquid feed. This was ascribed to the relatively high flow rate of the liquid when compared to that of the sweeping gas. In case of co-current flow, the mass transfer driving force and the flux decreased along the flow direction of the liquid and gas. This was expected due to the reduction in the liquid temperature and the rise of the sweeping gas humidity along this direction. A different observation was obtained in case of the counter-current flow such that the flux reached a minimum value at the middle of the module length. This was attributed to the occurrence of two phenomena in the same direction but with opposite impacts on the mass transfer driving force. The first is the decline in the liquid temperature in the

direction of the liquid flow. In the same direction, the second phenomenon takes place which is the decrease in the water content in the permeate side. Apparently, the first phenomenon negatively affects the driving force while the second phenomenon enhances it. This could play an important role in optimizing the liquid temperature and the total length of the SGMD unit vessel. Moreover, by comparing the effect of the number of the discretized units on the accuracy of the estimated flux, it was found that the flux predicted by the local model for a 20 cm long module could be accepted.

The performance of the ceramic membrane modules in SGMD of ethanol (aq.) feed was evaluated using modeling studies. The Maxwell-Stefan approach was adopted in modeling the transmembrane mass transfer of water and ethanol. The simulated length was not limited to the length of a single module. Instead, longer separation lengths were simulated. Results showed that increasing the liquid inlet temperature and/or reducing the sweeping gas pressure could enhance the ethanol selectivity. This can be explained by the relatively high volatility of ethanol when compared to that of water. The driving force of water reached a minimum value at the middle of the module in case of counter-current flow due to the same reasons that have been mentioned for the case of NaCl (aq.). However, the driving force of ethanol, in this case, decreased unsteadily in the direction of the liquid flow. This observation indicates that the effect of the liquid temperature gradient and the effect of the gradient of the ethanol concentration in the permeate-side were never balanced for ethanol unlike the case of water. Accordingly, the liquid temperature, gas pressure and SGMD vessel length could be optimized for maximizing the ethanol selectivity.

The developed SGMD model for NaCl (aq.) feed was implemented in simulating an SGMD separation unit in a hypothetical seawater desalination process. A "single pass" configuration was proposed for the SGMD unit employing the counter-current flow configuration. The same ceramic membrane modules that had been characterized and investigated were utilized in the simulated SGMD unit. Preliminary design and non-rigorous cost estimation were carried out for the required process development and optimization procedures. The optimization was based on minimizing the obtainable water production cost (WPC). The optimum interstitial gas velocity in the SGMD unit was found to be 3 m/s. For the studied range of the SGMD vessel total length, further increase in the gas velocity above 3m/s could engender wetting due to exacerbated gas pressure drop without significant enhancement effect on the water flux. For an assigned value of the flow rate of the produced fresh water by the hypothetical plant, maximizing the SGMD inlet liquid temperature and the total SGMD unit vessel were found to minimize the required feed flow rate, the required heating requirements and so, the required WPC. However, on increasing the SGMD liquid inlet temperature, the maximum allowable SGMD vessel length decreases. This was the result of the criticality of the pore wetting at the liquid inlet and of the bubbling problem at the gas inlet. In addition to that, at given velocity values of the liquid and gas streams in the SGMD, the temperature of the liquid entering the SGMD unit had either a direct or indirect impact on the other inlet operating conditions of the SGMD unit. Therefore, the SGMD inlet liquid temperature was considered as the key operating quantity. Its optimized value was found to be 107°C. This corresponded to an SGMD unit vessel having a total length of 5.4 m. The heating steam was found

to be the determinant cost item. Therefore, further optimization took place aiming at reducing the steam requirements. The optimized quantities were the used steam pressure and the temperature approach in the heat exchanger used prior to the SGMD feed preheater. The reduction in the WPC on optimizing these two quantities was attained. However, this reduction was not very significant. Therefore, the "feed and bleed" process configuration was tried instead of the proposed "single pass" hypothetical process at the same optimized conditions. The "feed and bleed" configuration decreased the steam requirements and cost due to the improved water productivity and lower required feed flow rate. However, this was at the expense of requiring a high cooling water flow rate in order to cool down the sweeping gas exiting from the SGMD separation unit and to condense the permeated water vapor molecules in the sweeping gas. On one side, the estimated cost of steam and cooling water requirements in case of the "feed and bleed" configuration was found to be 25.8 $\$/m^3$ of distilled water while the process productivity achieved was 84.75%. On the other side, on considering the operating and fixed costs, the WPC of the "single pass" case was estimated to be 20.9 $\$/m^3$. However, the corresponding process recovery was very low (4.24%). Therefore, the "single pass" configuration could be favored in terms of WPC while the "feed and bleed" could be favored in terms of process productivity.

Eventually, the WPC of the optimized case of the proposed hypothetical desalination process is deemed to be much higher than the corresponding value achieved on using reverse osmosis. Therefore, the competency of SGMD with reverse osmosis could be improved by applying solar energy or by using a waste heat source. This could result in appreciable savings in the steam requirements. Besides, optimization of the membrane morphological properties could play an important role in maximizing the water flux at given operating conditions. This could improve the process productivity and reduce the WPC. Last but not least, the proposed hypothetical desalination unit employing SGMD could be applied to treat the retentate of reverse osmosis since membrane distillation can handle feed streams with relatively large salinity. According to the economic analysis of some works in literature, this can correspond to a WPC that is lower than that achieved by reverse osmosis stand-alone systems. This would require further research and studies to ensure accurate scale-up procedures.

[This page intentionally left blank]

References

[1] M. Khayet, T. Matsuura, Membrane Distillation Principles and Applications, 2011. doi:10.1016/B978-0-444-53126-1.10016-8.

[2] W. Eykamp, Handbook of industrial membrane technology, J. Memb. Sci. 53 (1990) 301–302. doi:10.1016/0376-7388(90)80022-e.

[3] K. Scott, Handbook of industrial membranes, 1995. doi:10.1016/0958-2118(95)90218-x.

[4] E. Drioli, A.Criscuoli, E.Curcio, Membrane Contactors: Fundamentals, Applications and Potentialities, 1st ed., Elsevier, 2006.

[5] K.Li, Ceramic Membranes for Separation and Reaction, 1st ed., Wiley, 2007.

[6] J. Zhang, Theoretical and experimental investigation of membrane distillation, Thesis. (2011) 228. http://core.kmi.open.ac.uk/download/pdf/10834615.pdf.

[7] P. Wang, T.S. Chung, Recent advances in membrane distillation processes: Membrane development, configuration design and application exploring, J. Memb. Sci. 474 (2015) 39–56. doi:10.1016/j.memsci.2014.09.016.

[8] F. Varela-Corredor, S. Bandini, Advances in water breakthrough measurement at high temperature in macroporous hydrophobic ceramic/polymeric membranes, J. Memb. Sci. 565 (2018) 72–84. doi:10.1016/j.memsci.2018.08.005.

[9] K. W. Lawson, D.R. Lloyd, Review: Membrane Distillation, J. Memb. Sci. (1997) 1–25.

[10] P.K. Weyl, Recovery of Demineralized Water form Saline Waters, 3340186, 1967.

[11] B.R. Bodell, Distillation of Saline Water Using Silicone Rubber Membrane, 1968.

[12] D. Y. Cheng, S. J. Weirsma, Composite membrane for membrane Distillation System, 4316772, 1982.

[13] D.W.Gore. W. L. Gore, R. W. Gore, Desalination Device and Process, 4545862, 1985.

[14] M.E. Findley, Vaporization through porous membranes, Ind. Eng. Chem. Process Des. Dev. 6 (1967) 226–230. doi:10.1021/i260022a013.

[15] E. Drioli, A. Ali, F. Macedonio, Membrane distillation: Recent developments and perspectives, Desalination. 356 (2015) 56–84. doi:10.1016/j.desal.2014.10.028.

[16] M.A. Izquierdo-Gil, M.C. García-Payo, C. Fernández-Pineda, Air gap membrane distillation of sucrose aqueous solutions, J. Memb. Sci. 155 (1999) 291–307. doi:10.1016/S0376-7388(98)00323-8.

[17] V.D. Alves, I.M. Coelhoso, Orange juice concentration by osmotic evaporation and membrane distillation: A comparative study, J. Food Eng. 74 (2006) 125–133. doi:10.1016/j.jfoodeng.2005.02.019.

[18] V.A. Bui, L.T.T. Vu, M.H. Nguyen, Modelling the simultaneous heat and mass transfer of direct contact membrane distillation in hollow fibre modules, J. Memb. Sci. 353 (2010) 85–93. doi:10.1016/j.memsci.2010.02.034.

[19] Y.R. Chen, L.H. Chen, C.H. Chen, C.C. Ko, A. Huang, C.L. Li, C.J. Chuang, K.L. Tung, Hydrophobic alumina hollow fiber membranes for sucrose concentration by vacuum membrane distillation, J. Memb. Sci. 555 (2018) 250–257. doi:10.1016/j.memsci.2018.03.048.

[20] W.U. Rehman, A. Muhammad, Q.A. Khan, M. Younas, M. Rezakazemi, Pomegranate juice concentration using osmotic distillation with membrane contactor, Sep. Purif. Technol. 224 (2019) 481–489. doi:10.1016/j.seppur.2019.05.055.

[21] C.F. Couto, M. Amaral, L.C. Lange, L.V. de S. Santos, Effect of humic acid concentration on pharmaceutically active compounds (PhACs) rejection by direct contact membrane

distillation (DCMD), Sep. Purif. Technol. 212 (2019) 920–928. doi:10.1016/j.seppur.2018.12.012.
[22] F. Jia, J. Li, J. Wang, Recovery of boric acid from the simulated radioactive wastewater by vacuum membrane distillation crystallization, Ann. Nucl. Energy. 110 (2017) 1148–1155. doi:10.1016/j.anucene.2017.07.024.
[23] M.M.A. Shirazi, A. Kargari, M. Tabatabaei, A.F. Ismail, T. Matsuura, Concentration of glycerol from dilute glycerol wastewater using sweeping gas membrane distillation, Chem. Eng. Process. Process Intensif. 78 (2014) 58–66. doi:10.1016/j.cep.2014.02.002.
[24] S. Bandini, A. Saavedra, G.C. Sarti, Vacuum Membrane Distillation: Experiments and Modeling, AIChE J. 43 (1997) 398–408. doi:10.1002/aic.690430213.
[25] F. Banat, S. Al-Asheh, M. Qtaishat, Treatment of waters colored with methylene blue dye by vacuum membrane distillation, Desalination. 174 (2005) 87–96. doi:10.1016/j.desal.2004.09.004.
[26] N.P. Khumalo, L.N. Nthunya, E. De Canck, S. Derese, A.R. Verliefde, A.T. Kuvarega, B.B. Mamba, S.D. Mhlanga, D.S. Dlamini, Congo red dye removal by direct membrane distillation using PVDF/PTFE membrane, Sep. Purif. Technol. 211 (2019) 578–586. doi:10.1016/j.seppur.2018.10.039.
[27] I. E. Noor, J. Coenen, A. Martin, O. Dahl, M. Åslin, Experimental investigation and techno-economic analysis of tetramethylammonium hydroxide removal from wastewater in nano-electronics manufacturing via membrane distillation, J. Memb. Sci. 579 (2019) 283–293. doi:10.1016/j.memsci.2019.02.067.
[28] L.Z. Zhang, S.M. Huang, J.H. Chi, L.X. Pei, Conjugate heat and mass transfer in a hollow fiber membrane module for liquid desiccant air dehumidification: A free surface model approach, Int. J. Heat Mass Transf. 55 (2012) 3789–3799. doi:10.1016/j.ijheatmasstransfer.2012.03.034.
[29] M.M. Rafique, P. Gandhidasan, H.M.S. Bahaidarah, Liquid desiccant materials and dehumidifiers - A review, Renew. Sustain. Energy Rev. 56 (2016) 179–195. doi:10.1016/j.rser.2015.11.061.
[30] R. Lefers, N.M.S. Bettahalli, N. Fedoroff, S.P. Nunes, T.O. Leiknes, Vacuum membrane distillation of liquid desiccants utilizing hollow fiber membranes, Sep. Purif. Technol. 199 (2018) 57–63. doi:10.1016/j.seppur.2018.01.042.
[31] J. Zhou, X. Zhang, W. Su, B. Sun, Performance analysis of vacuum membrane distillation regenerator in liquid desiccant air conditioning system, Int. J. Refrig. 102 (2019) 112–121. doi:10.1016/j.ijrefrig.2019.03.017.
[32] A.S. Rattner, A.K. Nagavarapu, S. Garimella, T.F. Fuller, Modeling of a flat plate membrane-distillation system for liquid desiccant regeneration in air-conditioning applications, Int. J. Heat Mass Transf. 54 (2011) 3650–3660. doi:10.1016/j.ijheatmasstransfer.2011.02.064.
[33] C.C. Ko, A. Ali, E. Drioli, K.L. Tung, C.H. Chen, Y.R. Chen, F. Macedonio, Performance of ceramic membrane in vacuum membrane distillation and in vacuum membrane crystallization, Desalination. 440 (2018) 48–58. doi:10.1016/j.desal.2018.03.011.
[34] C.Y. Huang, C.C. Ko, L.H. Chen, C.T. Huang, K.L. Tung, Y.C. Liao, A simple coating method to prepare superhydrophobic layers on ceramic alumina for vacuum membrane distillation, Sep. Purif. Technol. 198 (2018) 79–86. doi:10.1016/j.seppur.2016.12.037.
[35] Y. Fan, S. Chen, H. Zhao, Y. Liu, Distillation membrane constructed by TiO2nanofiber followed by fluorination for excellent water desalination performance, Desalination. 405

(2017) 51–58. doi:10.1016/j.desal.2016.11.028.
[36] S. Koonaphapdeelert, K. Li, Preparation and characterization of hydrophobic ceramic hollow fibre membrane, J. Memb. Sci. 291 (2007) 70–76. doi:10.1016/j.memsci.2006.12.039.
[37] C. Ren, H. Fang, J. Gu, L. Winnubst, C. Chen, Preparation and characterization of hydrophobic alumina planar membranes for water desalination, J. Eur. Ceram. Soc. 35 (2015) 723–730. doi:10.1016/j.jeurceramsoc.2014.07.012.
[38] J. Gu, C. Ren, X. Zong, C. Chen, L. Winnubst, Preparation of alumina membranes comprising a thin separation layer and a support with straight open pores for water desalination, Ceram. Int. 42 (2016) 12427–12434. doi:10.1016/j.ceramint.2016.04.183.
[39] R. Das, K. Sondhi, S. Majumdar, S. Sarkar, Development of hydrophobic clay–alumina based capillary membrane for desalination of brine by membrane distillation, J. Asian Ceram. Soc. 4 (2016) 243–251. doi:10.1016/j.jascer.2016.04.004.
[40] J. Kujawa, S. Cerneaux, W. Kujawski, Investigation of the stability of metal oxide powders and ceramic membranes grafted by perfluoroalkylsilanes, Colloids Surfaces A Physicochem. Eng. Asp. 443 (2014) 109–117. doi:10.1016/j.colsurfa.2013.10.059.
[41] H.J. Hwang, K. He, S. Gray, J. Zhang, I.S. Moon, Direct contact membrane distillation (DCMD): Experimental study on the commercial PTFE membrane and modeling, J. Memb. Sci. 371 (2011) 90–98. doi:10.1016/j.memsci.2011.01.020.
[42] S.R. Krajewski, W. Kujawski, M. Bukowska, C. Picard, A. Larbot, Application of fluoroalkylsilanes (FAS) grafted ceramic membranes in membrane distillation process of NaCl solutions, J. Memb. Sci. 281 (2006) 253–259. doi:10.1016/j.memsci.2006.03.039.
[43] P. Jacob, S. Laborie, C. Cabassud, Visualizing and evaluating wetting in membrane distillation: New methodology and indicators based on Detection of Dissolved Tracer Intrusion (DDTI), Desalination. 443 (2018) 307–322. doi:10.1016/j.desal.2018.06.006.
[44] S.K. Hubadillah, Z.S. Tai, M.H.D. Othman, Z. Harun, M.R. Jamalludin, M.A. Rahman, J. Jaafar, A.F. Ismail, Hydrophobic ceramic membrane for membrane distillation: A mini review on preparation, characterization, and applications, Sep. Purif. Technol. 217 (2019) 71–84. doi:10.1016/j.seppur.2019.02.014.
[45] A. Carrero-Parreño, V.C. Onishi, R. Ruiz-Femenia, R. Salcedo-Díaz, J.A. Caballero, J.A. Reyes-Labarta, Optimization of multistage membrane distillation system for treating shale gas produced water, Desalination. 460 (2019) 15–27. doi:10.1016/j.desal.2019.03.002.
[46] M. Weyd, H. Richter, P. Puhlfürß, I. Voigt, C. Hamel, A. Seidel-Morgenstern, Transport of binary water-ethanol mixtures through a multilayer hydrophobic zeolite membrane, J. Memb. Sci. 307 (2008) 239–248. doi:10.1016/j.memsci.2007.09.032.
[47] M.K. Fawzy, F. Varela-Corredor, S. Bandini, On the Morphological Characterization Procedures of Multilayer Hydrophobic Ceramic Membranes for Membrane Distillation Operations, Membranes (Basel). 9 (2019) 125. doi:10.3390/membranes9100125.
[48] C.M. Guijt, G.W. Meindersma, T. Reith, A.B. De Haan, Air gap membrane distillation: 1. Modelling and mass transport properties for hollow fibre membranes, Sep. Purif. Technol. 43 (2005) 233–244. doi:10.1016/j.seppur.2004.09.015.
[49] C.M. Guijt, G.W. Meindersma, T. Reith, A.B. De Haan, Air gap membrane distillation: 2. Model validation and hollow fibre module performance analysis, Sep. Purif. Technol. 43 (2005) 245–255. doi:10.1016/j.seppur.2004.09.016.
[50] C.M. Guijt, G.W. Meindersma, T. Reith, A.B. De Haan, Method for experimental determination of the gas transport properties of highly porous fibre membranes: A first step

before predictive modelling of a membrane distillation process, Desalination. 147 (2002) 127–132. doi:10.1016/S0011-9164(02)00598-2.
[51] F. Gao, X.C. Chen, G. Yu, C. Asumana, Compressible gases transport through porous membrane: A modified dusty gas model, J. Memb. Sci. 379 (2011) 200–206. doi:10.1016/j.memsci.2011.05.064.
[52] S. Chung, C.D. Seo, H. Lee, J.H. Choi, J. Chung, Design strategy for networking membrane module and heat exchanger for direct contact membrane distillation process in seawater desalination, Desalination. 349 (2014) 126–135. doi:10.1016/j.desal.2014.07.001.
[53] M. Ramezanianpour, M. Sivakumar, An analytical flux decline model for membrane distillation, Desalination. 345 (2014) 1–12. doi:10.1016/j.desal.2014.04.006.
[54] D.J. Park, E. Norouzi, C. Park, Experimentally-validated computational simulation of direct contact membrane distillation performance, Int. J. Heat Mass Transf. 129 (2019) 1031–1042. doi:10.1016/j.ijheatmasstransfer.2018.10.035.
[55] Y.M. Manawi, M. Khraisheh, A.K. Fard, F. Benyahia, S. Adham, Effect of operational parameters on distillate flux in direct contact membrane distillation (DCMD): Comparison between experimental and model predicted performance, Desalination. 336 (2014) 110–120. doi:10.1016/j.desal.2014.01.003.
[56] A.R. Kurdian, M. Bahreini, G.H. Montazeri, S. Sadeghi, Modeling of direct contact membrane distillation process: Flux prediction of sodium sulfate and sodium chloride solutions, Desalination. 323 (2013) 75–82. doi:10.1016/j.desal.2013.05.002.
[57] J.Y. Shi, Z.P. Zhao, C.Y. Zhu, Studies on simulation and experiments of ethanol-water mixture separation by VMD using a PTFE flat membrane module, Sep. Purif. Technol. 123 (2014) 53–63. doi:10.1016/j.seppur.2013.12.015.
[58] A.S. Alsaadi, L. Francis, G.L. Amy, N. Ghaffour, Experimental and theoretical analyses of temperature polarization effect in vacuum membrane distillation, J. Memb. Sci. 471 (2014) 138–148. doi:10.1016/j.memsci.2014.08.005.
[59] F. Shao, C. Hao, L. Ni, Y. Zhang, R. Du, J. Meng, Z. Liu, C. Xiao, Experimental and theoretical research on N-methyl-2-pyrrolidone concentration by vacuum membrane distillation using polypropylene hollow fiber membrane, J. Memb. Sci. 452 (2014) 157–164. doi:10.1016/j.memsci.2013.09.041.
[60] S. Soukane, M.W. Naceur, L. Francis, A. Alsaadi, N. Ghaffour, Effect of feed flow pattern on the distribution of permeate fluxes in desalination by direct contact membrane distillation, Desalination. 418 (2017) 43–59. doi:10.1016/j.desal.2017.05.028.
[61] M.E. Leitch, G. V. Lowry, M.S. Mauter, Characterizing convective heat transfer coefficients in membrane distillation cassettes, J. Memb. Sci. 538 (2017) 108–121. doi:10.1016/j.memsci.2017.05.028.
[62] A.M. Karam, T.M. Laleg-Kirati, Electrical equivalent thermal network for direct contact membrane distillation modeling and analysis, J. Process Control. 47 (2016) 87–97. doi:10.1016/j.jprocont.2016.08.001.
[63] F. Banat, N. Jwaied, Economic evaluation of desalination by small-scale autonomous solar-powered membrane distillation units, Desalination. 220 (2008) 566–573. doi:10.1016/j.desal.2007.01.057.
[64] S. Al-Obaidani, E. Curcio, F. Macedonio, G. Di Profio, H. Al-Hinai, E. Drioli, Potential of membrane distillation in seawater desalination: Thermal efficiency, sensitivity study and cost estimation, J. Memb. Sci. 323 (2008) 85–98. doi:10.1016/j.memsci.2008.06.006.
[65] E. El-Zanati, K.M. El-Khatib, Integrated membrane -based desalination system,

Desalination. 205 (2007) 15–25. doi:10.1016/j.desal.2006.03.548.
[66] R. Schwantes, K. Chavan, D. Winter, C. Felsmann, J. Pfafferott, Techno-economic comparison of membrane distillation and MVC in a zero liquid discharge application, Desalination. 428 (2018) 50–68. doi:10.1016/j.desal.2017.11.026.
[67] U.K. Kesieme, N. Milne, H. Aral, C.Y. Cheng, M. Duke, Economic analysis of desalination technologies in the context of carbon pricing, and opportunities for membrane distillation, Desalination. 323 (2013) 66–74. doi:10.1016/j.desal.2013.03.033.
[68] Y. Choi, S.H. Kim, S. Lee, Comparison of performance and economics of reverse osmosis, membrane distillation, and pressure retarded osmosis hybrid systems, Desalin. Water Treat. 77 (2017) 19–29. doi:10.5004/dwt.2017.20660.
[69] G. Zaragoza, J.A. Andrés-Mañas, A. Ruiz-Aguirre, Commercial scale membrane distillation for solar desalination, Npj Clean Water. 1 (2018) 1–6. doi:10.1038/s41545-018-0020-z.
[70] B.L. Pangarkar, S.K. Deshmukh, M. V. Guddad, Economic assessment of multi-effect membrane distillation (MEMD) for water treatment, Int. J. Eng. Res. Technol. 10 (2017) 253–257.
[71] M.J. Perves Bappy, R. Bahar, T.F. Ariff, Low energy and low cost freshwater production by membrane distillation, Proc. Int. Conf. Ind. Eng. Oper. Manag. 8-10 March (2016) 1799–1804.
[72] M. Khayet, M.P. Godino, J.I. Mengual, Theoretical and experimental studies on desalination using the sweeping gas membrane distillation method, Desalination. 157 (2003) 297–305. doi:10.1016/S0011-9164(03)00409-0.
[73] C.A. Rivier, M.C. García-Payo, I.W. Marison, U. Von Stockar, Separation of binary mixtures by thermostatic sweeping gas membrane distillation - I. Theory and simulations, J. Memb. Sci. 201 (2002) 1–16. doi:10.1016/S0376-7388(01)00648-2.
[74] A.G.F. G. Guan, X. Yang, R. Wang, R. Field, Evaluation of Hollow Fiber-based Direct Contact and Vacuum Membrane Distillation Systems using Aspen Process Simulation, J. Memb. Sci. (2014) 127–139.
[75] M. Essalhi, M. Khayet, Application of a porous composite hydrophobic/hydrophilic membrane in desalination by air gap and liquid gap membrane distillation: A comparative study, Sep. Purif. Technol. 133 (2014) 176–186. doi:10.1016/j.seppur.2014.07.006.
[76] M.C. García-Payo, C.A. Rivier, I.W. Marison, U. Von Stockar, Separation of binary mixtures by thermostatic sweeping gas membrane distillation II. Experimental results with aqueous formic acid solutions, J. Memb. Sci. 198 (2002) 197–210. doi:10.1016/S0376-7388(01)00649-4.
[77] L. García-Fernández, B. Wang, M.C. García-Payo, K. Li, M. Khayet, Morphological design of alumina hollow fiber membranes for desalination by air gap membrane distillation, Desalination. 420 (2017) 226–240. doi:10.1016/j.desal.2017.07.021.
[78] C.C. Ko, C.H. Chen, Y.R. Chen, Y.H. Wu, S.C. Lu, F.C. Hu, C.L. Li, K.L. Tung, Increasing the performance of vacuum membrane distillation using micro-structured hydrophobic aluminum hollow fiber membranes, Appl. Sci. 7 (2017). doi:10.3390/app7040357.
[79] J.W. Zhang, H. Fang, J.W. Wang, L.Y. Hao, X. Xu, C.S. Chen, Preparation and characterization of silicon nitride hollow fiber membranes for seawater desalination, J. Memb. Sci. 450 (2014) 197–206. doi:10.1016/j.memsci.2013.08.042.
[80] F. Varela-Corredor, Membrane Contactors for High Temperature Applications, [PhD

dissertation thesis], Alma Mater Studiorum Università di Bologna, Dottorato di ricerca in Ingegneria chimica dell'ambiente e della sicurezza, 28 Ciclo.(2016) doi: 10.6092/unib, (n.d.).
[81] A. Alkhudhiri, N. Darwish, N. Hilal, Membrane distillation: A comprehensive review, Desalination. 287 (2012) 2–18. doi:10.1016/j.desal.2011.08.027.
[82] V. Karanikola, A.F. Corral, H. Jiang, A. Eduardo Sáez, W.P. Ela, R.G. Arnold, Sweeping gas membrane distillation: Numerical simulation of mass and heat transfer in a hollow fiber membrane module, J. Memb. Sci. 483 (2015) 15–24. doi:10.1016/j.memsci.2015.02.010.
[83] M.R. Choudhury, N. Anwar, D. Jassby, M.S. Rahaman, Fouling and wetting in the membrane distillation driven wastewater reclamation process – A review, Adv. Colloid Interface Sci. 269 (2019) 370–399. doi:10.1016/j.cis.2019.04.008.
[84] J. Zhang, J. De Li, M. Duke, M. Hoang, Z. Xie, A. Groth, C. Tun, S. Gray, Modelling of vacuum membrane distillation, J. Memb. Sci. 434 (2013) 1–9. doi:10.1016/j.memsci.2013.01.048.
[85] K.Y. Wang, T.S. Chung, M. Gryta, Hydrophobic PVDF hollow fiber membranes with narrow pore size distribution and ultra-thin skin for the fresh water production through membrane distillation, Chem. Eng. Sci. 63 (2008) 2587–2594. doi:10.1016/j.ces.2008.02.020.
[86] J. Li, W. Zhou, S. Fan, Z. Xiao, Y. Liu, J. Liu, B. Qiu, Y. Wang, Bioethanol production in vacuum membrane distillation bioreactor by permeate fractional condensation and mechanical vapor compression with polytetrafluoroethylene (PTFE) membrane, Bioresour. Technol. 268 (2018) 708–714. doi:10.1016/j.biortech.2018.08.055.
[87] C. Picard, A. Larbot, E. Tronel-Peyroz, R. Berjoan, Characterisation of hydrophilic ceramic membranes modified by fluoroalkylsilanes into hydrophobic membranes, Solid State Sci. 6 (2004) 605–612. doi:10.1016/j.solidstatesciences.2004.03.017.
[88] C. Gostoli, G. C. Sarti, S. Matulli, Low Temperature Distillation through Hydrophobic Membranes, Sep. Sci. Technol. (1987) 855–872.
[89] J.W. Zhang, H. Fang, L.Y. Hao, X. Xu, C.S. Chen, Preparation of silicon nitride hollow fibre membrane for desalination, Mater. Lett. 68 (2012) 457–459. doi:10.1016/j.matlet.2011.11.041.
[90] S.K. Hubadillah, M.H.D. Othman, T. Matsuura, M.A. Rahman, J. Jaafar, A.F. Ismail, S.Z.M. Amin, Green silica-based ceramic hollow fiber membrane for seawater desalination via direct contact membrane distillation, Sep. Purif. Technol. 205 (2018) 22–31. doi:10.1016/j.seppur.2018.04.089.
[91] Y. Yang, Q. Liu, H. Wang, F. Ding, G. Jin, C. Li, H. Meng, Superhydrophobic modification of ceramic membranes for vacuum membrane distillation, Chinese J. Chem. Eng. 25 (2017) 1395–1401. doi:10.1016/j.cjche.2017.05.003.
[92] M.Y. Yang, J.W. Wang, L. Li, B. Bin Dong, X. Xin, S. Agathopoulos, Fabrication of low thermal conductivity yttrium silicate ceramic flat membrane for membrane distillation, J. Eur. Ceram. Soc. 39 (2019) 442–448. doi:10.1016/j.jeurceramsoc.2018.09.028.
[93] J.W. Wang, L. Li, J.W. Zhang, X. Xu, C.S. Chen, β-Sialon ceramic hollow fiber membranes with high strength and low thermal conductivity for membrane distillation, J. Eur. Ceram. Soc. 36 (2016) 59–65. doi:10.1016/j.jeurceramsoc.2015.09.027.
[94] H. Fang, J.F. Gao, H.T. Wang, C.S. Chen, Hydrophobic porous alumina hollow fiber for water desalination via membrane distillation process, J. Memb. Sci. 403–404 (2012) 41–46. doi:10.1016/j.memsci.2012.02.011.

[95] A. Larbot, L. Gazagnes, S. Krajewski, M. Bukowska,W.Kujausky, Water desalination using ceramic membrane distillation, Water Desalin. Using Ceram. Membr. Distill. 168 (2004) 367–372.
[96] S. Cerneaux, I. Struzyńska, W.M. Kujawski, M. Persin, A. Larbot, Comparison of various membrane distillation methods for desalination using hydrophobic ceramic membranes, J. Memb. Sci. 337 (2009) 55–60. doi:10.1016/j.memsci.2009.03.025.
[97] A. Luo, N. Lior, Critical review of membrane distillation performance criteria, Desalin. Water Treat. 57 (2016) 20093–20140. doi:10.1080/19443994.2016.1152637.
[98] M. Khayet, Membranes and theoretical modeling of membrane distillation: A review, Adv. Colloid Interface Sci. 164 (2011) 56–88. doi:10.1016/j.cis.2010.09.005.
[99] A. Zarebska, Á.C. Amor, K. Ciurkot, H. Karring, O. Thygesen, T.P. Andersen, M.B. Hägg, K.V. Christensen, B. Norddahl, Fouling mitigation in membrane distillation processes during ammonia stripping from pig manure, J. Memb. Sci. 484 (2015) 119–132. doi:10.1016/j.memsci.2015.03.010.
[100] C. K. Ho, S. W. Webb, Gas Transport in Porous Media, Springer, 2006.
[101] I. Hitsov, T. Maere, K. De Sitter, C. Dotremont, I. Nopens, Modelling approaches in membrane distillation: A critical review, Sep. Purif. Technol. 142 (2015) 48–64. doi:10.1016/j.seppur.2014.12.026.
[102] E.A. Mason, Malinauskas, Mason E.A., Gas transport in porous media. Dusty-gas model, 1983.pdf, (1983).
[103] H.A. Jakobsen, Chemical Reactor Modeling: Multiphase Reactive Flows, 2nd ed., Springer, 2014.
[104] A. Basile, F. Dalena, Methanol: Science and Engineering, 1st ed., Elsevier, 2017.
[105] A. Seidel-Morgenstern, Membrane Reactors: Distributing Reactants to Improve Selectivity and Yield, 1st ed., 2010.
[106] A.S. Kim, A two-interface transport model with pore-size distribution for predicting the performance of direct contact membrane distillation (DCMD), J. Memb. Sci. 428 (2013) 410–424. doi:10.1016/j.memsci.2012.10.054.
[107] A.S. Kim, H.S. Lee, D.S. Moon, H.J. Kim, Self-adjusting, combined diffusion in direct contact and vacuum membrane distillation, J. Memb. Sci. 543 (2017) 255–268. doi:10.1016/j.memsci.2017.08.059.
[108] A.S. Kim, Cylindrical cell model for direct contact membrane distillation (DCMD) of densely packed hollow fibers, J. Memb. Sci. 455 (2014) 168–186. doi:10.1016/j.memsci.2013.12.067.
[109] S. Khaisri, D. deMontigny, P. Tontiwachwuthikul, R. Jiraratananon, CO2 stripping from monoethanolamine using a membrane contactor, J. Memb. Sci. 376 (2011) 110–118. doi:10.1016/j.memsci.2011.04.005.
[110] T. Liu, L. Lei, J. Gu, Y. Wang, L. Winnubst, C. Chen, C. Ye, F. Chen, Enhanced water desalination performance through hierarchically-structured ceramic membranes, J. Eur. Ceram. Soc. 37 (2017) 2431–2438. doi:10.1016/j.jeurceramsoc.2017.02.001.
[111] F. Anisi, K.M. Thomas, H.J.M. Kramer, Membrane-assisted crystallization: Membrane characterization, modelling and experiments, Chem. Eng. Sci. 158 (2017) 277–286. doi:10.1016/j.ces.2016.10.036.
[112] D. U. Lawal, A. E. Khalifa, Flux Prediction in Direct Contact Membrane Distillation, Int. J. Mater. Mech. Manuf. 2 (2014) 302–308. doi:10.7763/ijmmm.2014.v2.147.
[113] S. Lin, N.Y. Yip, M. Elimelech, Direct contact membrane distillation with heat recovery:

Thermodynamic insights from module scale modeling, J. Memb. Sci. 453 (2014) 498–515. doi:10.1016/j.memsci.2013.11.016.
[114] D. González, J. Amigo, F. Suárez, Membrane distillation: Perspectives for sustainable and improved desalination, Renew. Sustain. Energy Rev. 80 (2017) 238–259. doi:10.1016/j.rser.2017.05.078.
[115] A. Hagedorn, G. Fieg, D. Winter, J. Koschikowski, T. Mann, Methodical design and operation of membrane distillation plants for desalination, Chem. Eng. Res. Des. 125 (2017) 265–281. doi:10.1016/j.cherd.2017.07.024.
[116] Q.F. Alsalhy, S.S. Ibrahim, F.A. Hashim, Experimental and theoretical investigation of air gap membrane distillation process for water desalination, Chem. Eng. Res. Des. 130 (2018) 95–108. doi:10.1016/j.cherd.2017.12.013.
[117] M.R.S. Kebria, A. Rahimpour, G. Bakeri, R. Abedini, Experimental and theoretical investigation of thin ZIF-8/chitosan coated layer on air gap membrane distillation performance of PVDF membrane, Desalination. 450 (2019) 21–32. doi:10.1016/j.desal.2018.10.023.
[118] H. Zhang, B. Li, D. Sun, X. Miao, Y. Gu, SiO 2 -PDMS-PVDF hollow fiber membrane with high flux for vacuum membrane distillation, Desalination. 429 (2018) 33–43. doi:10.1016/j.desal.2017.12.004.
[119] K. Charfi, M. Khayet, M.J. Safi, Numerical simulation and experimental studies on heat and mass transfer using sweeping gas membrane distillation, Desalination. 259 (2010) 84–96. doi:10.1016/j.desal.2010.04.028.
[120] M. Khayet, C. Cojocaru, A. Baroudi, Modeling and optimization of sweeping gas membrane distillation, Desalination. 287 (2012) 159–166. doi:10.1016/j.desal.2011.04.070.
[121] A.M. Karam, A.S. Alsaadi, N. Ghaffour, T.M. Laleg-Kirati, Analysis of direct contact membrane distillation based on a lumped-parameter dynamic predictive model, Desalination. 402 (2017) 50–61. doi:10.1016/j.desal.2016.09.002.
[122] G. Rao, S.R. Hiibel, A.E. Childress, Simplified flux prediction in direct-contact membrane distillation using a membrane structural parameter, Desalination. 351 (2014) 151–162. doi:10.1016/j.desal.2014.07.006.
[123] Ó. Andrjesdóttir, C.L. Ong, M. Nabavi, S. Paredes, A.S.G. Khalil, B. Michel, D. Poulikakos, An experimentally optimized model for heat and mass transfer in direct contact membrane distillation, Int. J. Heat Mass Transf. 66 (2013) 855–867. doi:10.1016/j.ijheatmasstransfer.2013.07.051.
[124] H.Y. Wu, R. Wang, R.W. Field, Direct contact membrane distillation: An experimental and analytical investigation of the effect of membrane thickness upon transmembrane flux, J. Memb. Sci. 470 (2014) 257–265. doi:10.1016/j.memsci.2014.06.002.
[125] A. Criscuoli, M.C. Carnevale, E. Drioli, Modeling the performance of flat and capillary membrane modules in vacuum membrane distillation, J. Memb. Sci. 447 (2013) 369–375. doi:10.1016/j.memsci.2013.07.044.
[126] Y. Zhang, Y. Peng, S. Ji, S. Wang, Numerical simulation of 3D hollow-fiber vacuum membrane distillation by computational fluid dynamics, Chem. Eng. Sci. 152 (2016) 172–185. doi:10.1016/j.ces.2016.05.040.
[127] A.C. Sun, W. Kosar, Y. Zhang, X. Feng, Vacuum membrane distillation for desalination of water using hollow fiber membranes, J. Memb. Sci. 455 (2014) 131–142. doi:10.1016/j.memsci.2013.12.055.
[128] A.S. Alsaadi, N. Ghaffour, J.D. Li, S. Gray, L. Francis, H. Maab, G.L. Amy, Modeling of

air-gap membrane distillation process: A theoretical and experimental study, J. Memb. Sci. 445 (2013) 53–65. doi:10.1016/j.memsci.2013.05.049.
[129] M. Khemakhem, S. Khemakhem, R. Ben Amar, Emulsion separation using hydrophobic grafted ceramic membranes by, Colloids Surfaces A Physicochem. Eng. Asp. 436 (2013) 402–407. doi:10.1016/j.colsurfa.2013.05.073.
[130] Z.D. Hendren, J. Brant, M.R. Wiesner, Surface modification of nanostructured ceramic membranes for direct contact membrane distillation, J. Memb. Sci. 331 (2009) 1–10. doi:10.1016/j.memsci.2008.11.038.
[131] S.K. Hubadillah, M.H.D. Othman, A.F. Ismail, M.A. Rahman, J. Jaafar, A low cost hydrophobic kaolin hollow fiber membrane (h-KHFM) for arsenic removal from aqueous solution via direct contact membrane distillation, Sep. Purif. Technol. (2019) 31–39. doi:10.1016/j.seppur.2018.04.025.
[132] L. Li, J.W. Wang, H. Zhong, L.Y. Hao, H. Abadikhah, X. Xu, C.S. Chen, S. Agathopoulos, Novel A-Si 3 N 4 planar nanowire superhydrophobic membrane prepared through in-situ nitridation of silicon for membrane distillation, J. Memb. Sci. 543 (2017) 98–105. doi:10.1016/j.memsci.2017.08.049.
[133] S. Khemakhem, R. Ben Amar, Modification of Tunisian clay membrane surface by silane grafting: Application for desalination with Air Gap Membrane Distillation process, Colloids Surfaces A Physicochem. Eng. Asp. 387 (2011) 79–85. doi:10.1016/j.colsurfa.2011.07.033.
[134] L. Li, H. Abadikhah, J.W. Wang, X. Xu, S. Agathopoulos, One-step synthesis of flower-like Si2N2O nanowires on the surface of porous SiO2 ceramic membranes for membrane distillation, Mater. Lett. 232 (2018) 74–77. doi:10.1016/j.matlet.2018.08.043.
[135] X. Chen, X. Gao, K. Fu, M. Qiu, F. Xiong, D. Ding, Z. Cui, Z. Wang, Y. Fan, E. Drioli, Tubular hydrophobic ceramic membrane with asymmetric structure for water desalination via vacuum membrane distillation process, Desalination. 443 (2018) 212–220. doi:10.1016/j.desal.2018.05.027.
[136] C. Boi, S. Bandini, G.C. Sarti, Pollutants removal from wastewaters through membrane distillation, Desalination. 183 (2005) 383–394. doi:10.1016/j.desal.2005.03.041.
[137] W. Kujawski, J. Kujawa, E. Wierzbowska, S. Cerneaux, M. Bryjak, J. Kujawski, Influence of hydrophobization conditions and ceramic membranes pore size on their properties in vacuum membrane distillation of water-organic solvent mixtures, J. Memb. Sci. 499 (2016) 442–451. doi:10.1016/j.memsci.2015.10.067.
[138] J. Kujawa, S. Cerneaux, W. Kujawski, Highly hydrophobic ceramic membranes applied to the removal of volatile organic compounds in pervaporation, Chem. Eng. J. 260 (2015) 43–54. doi:10.1016/j.cej.2014.08.092.
[139] B. Wu, X. Tan, K. Li, W.K. Teo, Removal of 1,1,1-trichloroethane from water using a polyvinylidene fluoride hollow fiber membrane module: Vacuum membrane distillation operation, Sep. Purif. Technol. 52 (2006) 301–309. doi:10.1016/j.seppur.2006.05.013.
[140] N. Couffin, C. Cabassud, V. Lahoussine-Turcaud, A new process to remove halogenated VOCs for drinking water production: vacuum membrane distillation, Desalination. 117 (1998) 233–245. doi:10.1016/S0011-9164(98)00103-9.
[141] A.M. Urtiaga, E.D. Gorri, G. Ruiz, I. Ortiz, Parallelism and differences of pervaporation and vacuum membrane distillation in the removal of VOCs from aqueous streams, Sep. Purif. Technol. 22–23 (2001) 327–337. doi:10.1016/S1383-5866(00)00116-7.
[142] Q. He, T. Tu, S. Yan, X. Yang, M. Duke, Y. Zhang, S. Zhao, Relating water vapor transfer

to ammonia recovery from biogas slurry by vacuum membrane distillation, Sep. Purif. Technol. 191 (2018) 182–191. doi:10.1016/j.seppur.2017.09.030.
[143] E.U. Khan, A.R. Martin, Water purification of arsenic-contaminated drinking water via air gap membrane distillation (AGMD), Period. Polytech. Mech. Eng. 58 (2014) 47–53. doi:10.3311/PPme.7422.
[144] M. Khayet, Treatment of radioactive wastewater solutions by direct contact membrane distillation using surface modified membranes, Desalination. 321 (2013) 60–66. doi:10.1016/j.desal.2013.02.023.
[145] F. Jia, J. Wang, Separation of cesium ions from aqueous solution by vacuum membrane distillation process, Prog. Nucl. Energy. 98 (2017) 293–300. doi:10.1016/j.pnucene.2017.04.008.
[146] F. Jia, J. Li, J. Wang, Y. Sun, Removal of strontium ions from simulated radioactive wastewater by vacuum membrane distillation, Ann. Nucl. Energy. 103 (2017) 363–368. doi:10.1016/j.anucene.2017.02.003.
[147] E.U. Khan, Å. Nordberg, Thermal integration of membrane distillation in an anaerobic digestion biogas plant – A techno-economic assessment, Appl. Energy. 239 (2019) 1163–1174. doi:10.1016/j.apenergy.2019.02.023.
[148] E.U. Khan, Å. Nordberg, Membrane distillation process for concentration of nutrients and water recovery from digestate reject water, Sep. Purif. Technol. 206 (2018) 90–98. doi:10.1016/j.seppur.2018.05.058.
[149] D. Amaya-Vías, L. Tataru, B. Herce-Sesa, J.A. López-López, J.A. López-Ramírez, Metals removal from acid mine drainage (Tinto River, SW Spain) by water gap and air gap membrane distillation, J. Memb. Sci. 582 (2019) 20–29. doi:10.1016/j.memsci.2019.03.081.
[150] C. Cojocaru, M. Khayet, Sweeping gas membrane distillation of sucrose aqueous solutions: Response surface modeling and optimization, Sep. Purif. Technol. 81 (2011) 12–24. doi:10.1016/j.seppur.2011.06.031.
[151] C.A. Quist-Jensen, F. Macedonio, C. Conidi, A. Cassano, S. Aljlil, O.A. Alharbi, E. Drioli, Direct contact membrane distillation for the concentration of clarified orange juice, J. Food Eng. 187 (2016) 37–43. doi:10.1016/j.jfoodeng.2016.04.021.
[152] R. Bagger-Jørgensen, A.S. Meyer, M. Pinelo, C. Varming, G. Jonsson, Recovery of volatile fruit juice aroma compounds by membrane technology: Sweeping gas versus vacuum membrane distillation, Innov. Food Sci. Emerg. Technol. 12 (2011) 388–397. doi:10.1016/j.ifset.2011.02.005.
[153] S. Bandini, G.C. Sarti, Concentration of must through vacuum membrane distillation, Desalination. 149 (2002) 253–259. doi:10.1016/S0011-9164(02)00776-2.
[154] S. Al-Asheh, F. Banat, M. Qtaishat, M.Y. El-Khateeb, Concentration of sucrose solutions via vacuum membrane distillation, Desalination. 195 (2006) 60–68. doi:10.1016/j.desal.2005.10.036.
[155] C. Zambra, J. Romero, L. Pino, A. Saavedra, J. Sanchez, Concentration of cranberry juice by osmotic distillation process, J. Food Eng. 144 (2014) 58–65. doi:10.1016/j.jfoodeng.2014.07.009.
[156] E. Yilmaz, P.O. Bagci, Production of phytotherapeutics from broccoli juice by integrated membrane processes, Food Chem. 242 (2018) 264–271. doi:10.1016/j.foodchem.2017.09.056.
[157] L. Terki, W. Kujawski, J. Kujawa, M. Kurzawa, A. Filipiak-Szok, E. Chrzanowska, S.

Khaled, K. Madani, Implementation of osmotic membrane distillation with various hydrophobic porous membranes for concentration of sugars solutions and preservation of the quality of cactus pear juice, J. Food Eng. 230 (2018) 28–38. doi:10.1016/j.jfoodeng.2018.02.023.
[158] P. Onsekizoglu, K. Savas Bahceci, J. Acar, The use of factorial design for modeling membrane distillation, J. Memb. Sci. 349 (2010) 225–230. doi:10.1016/j.memsci.2009.11.049.
[159] P. Onsekizoglu, Membrane Distillation: Principle, Advances, Limitations and Future Prospects in Food Industry, Distill. - Adv. from Model. to Appl. (2012). doi:10.5772/37625.
[160] A. Khalid, M. Aslam, M.A. Qyyum, A. Faisal, A.L. Khan, F. Ahmed, M. Lee, J. Kim, N. Jang, I.S. Chang, A.A. Bazmi, M. Yasin, Membrane separation processes for dehydration of bioethanol from fermentation broths: Recent developments, challenges, and prospects, Renew. Sustain. Energy Rev. 105 (2019) 427–443. doi:10.1016/j.rser.2019.02.002.
[161] M.M.A. Shirazi, A. Kargari, M. Tabatabaei, Sweeping Gas Membrane Distillation (SGMD) as an Alternative for Integration of Bioethanol Processing: Study on a Commercial Membrane and Operating Parameters, Chem. Eng. Commun. 202 (2015) 457–466. doi:10.1080/00986445.2013.848805.
[162] P. Loulergue, B. Balannec, L. Fouchard-Le Graët, A. Cabrol, W. Sayed, H. Djelal, A. Amrane, A. Szymczyk, Air-gap membrane distillation for the separation of bioethanol from algal-based fermentation broth, Sep. Purif. Technol. 213 (2019) 255–263. doi:10.1016/j.seppur.2018.12.047.
[163] A. Kujawska, J.K. Kujawski, M. Bryjak, M. Cichosz, W. Kujawski, Removal of volatile organic compounds from aqueous solutions applying thermally driven membrane processes. 2. Air gap membrane distillation, J. Memb. Sci. 499 (2016) 245–256. doi:10.1016/j.memsci.2015.10.047.
[164] C.A. Quist-Jensen, F. Macedonio, D. Horbez, E. Drioli, Reclamation of sodium sulfate from industrial wastewater by using membrane distillation and membrane crystallization, Desalination. 401 (2017) 112–119. doi:10.1016/j.desal.2016.05.007.
[165] J. Kim, J. Kim, S. Hong, Recovery of water and minerals from shale gas produced water by membrane distillation crystallization, Water Res. 129 (2018) 447–459. doi:10.1016/j.watres.2017.11.017.
[166] S. Koonaphapdeelert, Z. Wu, K. Li, Carbon dioxide stripping in ceramic hollow fibre membrane contactors, Chem. Eng. Sci. 64 (2009) 1–8. doi:10.1016/j.ces.2008.09.010.
[167] F.A. Qusay, S.S. Ibrahim, S.R. Khaleel, Performance of vacuum poly(propylene) membrane distillation (VMD) for saline water desalination, Chem. Eng. Process. Process Intensif. 120 (2017) 68–80. doi:10.1016/j.cep.2017.06.011.
[168] M.B. Jensen, K.V. Christensen, R. Andrésen, L.F. Søtoft, B. Norddahl, A model of direct contact membrane distillation for black currant juice, J. Food Eng. 107 (2011) 405–414. doi:10.1016/j.jfoodeng.2011.06.014.
[169] Z. Xie, T. Duong, M. Hoang, C. Nguyen, B. Bolto, Ammonia removal by sweep gas membrane distillation, Water Res. 43 (2009) 1693–1699. doi:10.1016/j.watres.2008.12.052.
[170] A. Rom, W. Wukovits, F. Anton, Development of a vacuum membrane distillation unit operation: From experimental data to a simulation model, Chem. Eng. Process. Process Intensif. 86 (2014) 90–95. doi:10.1016/j.cep.2014.09.006.

[171] X. Yang, M. Duke, J. Zhang, J. De Li, Modeling of heat and mass transfer in vacuum membrane distillation for ammonia separation, Sep. Purif. Technol. 224 (2019) 121–131. doi:10.1016/j.seppur.2019.05.004.
[172] J. Kong, K. Li, An improved gas permeation method for characterising and predicting the performance of microporous asymmetric hollow fibre membranes used in gas absorption, J. Memb. Sci. 182 (2001) 271–281.
[173] C.C.Wei, K. Li, Preparation and Characterization of a Robust and Hydrophobic Ceramic Membrane via an Improved Surface Grafting Technique, Ind. Eng. Chem. Res. 48 (2009) 3446–3452.
[174] H.Richter, I.Voigt, G.Fisher, P.Puhlfuerss, Preparation of zeolite membranes on the inner surface of ceramic tubes and capillaries, Sep. Purif. Technol. 32 (2003) 133–138.
[175] I. Voigt, G. Fischer, P. Puhlfürß, M. Schleifenheimer, M. Stahn, TiO2-NF-membranes on capillary supports, Sep. Purif. Technol. 32 (2003) 87–91. doi:10.1016/S1383-5866(03)00064-9.
[176] H.Richter, I.Voigt, S. Kaemnitz, J.Gruetzner, D.Martin, Carbon membrane, process for the manufacture of carbon membranes and use thereof, US Patent n. US2016/0175767 A1,Fraunhofer and MUW Screentec Filter, 2016.
[177] S. Zeidler, P. Puhlfürß, U. Kätzel, I. Voigt, Preparation and characterization of new low MWCO ceramic nanofiltration membranes for organic solvents, J. Memb. Sci. 470 (2014) 421–430. doi:10.1016/j.memsci.2014.07.051.
[178] A. Pashkova, R. Dittmeyer, N. Kaltenborn, H. Richter, Experimental study of porous tubular catalytic membranes for direct synthesis of hydrogen peroxide, Chem. Eng. J. 165 (2010) 924–933. doi:10.1016/j.cej.2010.10.011.
[179] I.Voigt, G. Dudziak, T.Hoyer, P.Puhlfuerss, A.Nickel, Membrana ceramica de nanofiltracao para a utilizacao em solvents organicos e processo para a sua preparacao, PT 1603663 E, Fraunhofer (DE), 2004.
[180] R. B. Bird, W. E. Stewart, E. N. Lightfoot, Transport Phenomena, 2nd ed., John Wiley & Sons, 2002.
[181] D. S. Scott, F. A. L. Dullien, Diffusion of ideal Gases in Capillaries and Porous Solids, A.I.Ch.E. J. 8 (1962) 113–117.
[182] D. S. Scott, F. A. L. Dullien, The flow of Rarefied Gases, A.I.Ch.E. J. 8 (1962) 293–297.
[183] S.E. Moore, S.D. Mirchandani, V. Karanikola, T.M. Nenoff, R.G. Arnold, A. Eduardo Sáez, Process modeling for economic optimization of a solar driven sweeping gas membrane distillation desalination system, Desalination. 437 (2018) 108–120. doi:10.1016/j.desal.2018.03.005.
[184] A. Aboulkasem, M. Hassan, A. Ibrahim, S. El-Shamarka, Numerical Study of Transfer Processes in Sweeping Gas Membrane Water Distillation, Int. Conf. Appl. Mech. Mech. Eng. 17 (2016) 1–18. doi:10.21608/amme.2016.35275.
[185] P. Boutikos, E.S. Mohamed, E. Mathioulakis, V. Belessiotis, A theoretical approach of a vacuum multi-effect membrane distillation system, Desalination. 422 (2017) 25–41. doi:10.1016/j.desal.2017.08.007.
[186] A. Luo, N. Lior, Study of advancement to higher temperature membrane distillation, Desalination. 419 (2017) 88–100. doi:10.1016/j.desal.2017.05.020.
[187] C.D. Grant, Chemical Engineering Vol. 1—Fluid Flow, Heat Transfer and Mass Transfer, Chem. Eng. Sci. 47 (1992) 513–514. doi:10.1016/0009-2509(92)80052-e.
[188] F.P. Incropera, D.P. Dewitt, T.L. Bergman, A.S. Lavine, Fundamentals of Heat and Mass

Transfer, 6th ed., John Wiley & Sons, 2006.
[189] G.O. Brown, The History of the Darcy-Weisbach Equation for Pipe Flow Resistance, Proc. Environ. Water Resour. Hist. 38 (2003) 10.1061/40650.
[190] C. Gostoli, A. Gatta, Mass transfer in a hollow fiber dialyzer, J. Memb. Sci. 6 (1980) 133–148.
[191] V. Soni, J. Abildskov, G. Jonsson, R. Gani, A general model for membrane-based separation processes, Comput. Chem. Eng. 33 (2009) 644–659. doi:10.1016/j.compchemeng.2008.08.004.
[192] T.H. Chilton, A.P. Colburn, Ind. Eng. Chem., 26 (1934) 1183, (n.d.).
[193] P.K. Sarma, P.S. Kishore, T. Subrahmanyam, V.D. Rao, A novel method to determine laminar convective heat transfer in the entry region of a tube, Int. J. Therm. Sci. 43 (2004) 555–559.
[194] C. Gostoli, Recovery of Biosynthetic Products Using Membrane Contactors, Mass Transf. - Adv. Asp. (2011) 619–644.
[195] D. Liu, L. Yu, Single-Phase Thermal Transport of Nanofluids in a Mini channel, J. Heat Transf. 133 (2010) 031009–11.
[196] D.A. Donohue, Heat Transfer and Pressure Drop in Heat Exchangers, Lummus Company,New York. (1949) 2499–2511.
[197] J.G. Knudsen, D.L. Katz, Fluid Dynamics and Heat Transfer Part II, 1st ed., , McGRAW-Hill Inc., 1958.
[198] B.Short, Heat transfer and pressure drop in heat exchangers, Univ.Texas Pub. 4324. (1943) 1–5.
[199] E.Heinrich, R.Stuckle, Ver.deut.Ing Mitt.Forsch, Gebiete Ingegnieurw.,h. 271. (1925).
[200] M. Khayet, P. Godino, J.I. Mengual, Theory and experiments on sweeping gas membrane distillation, J. Memb. Sci. 165 (2000) 261–272. doi:10.1016/S0376-7388(99)00236-7.
[201] M. Khayet, P. Godino, J.I. Mengual, Nature of flow on sweeping gas membrane distillation, J. Memb. Sci. 170 (2000) 243–255. doi:10.1016/S0376-7388(99)00369-5.
[202] M.A. Izquierdo-Gil, G. Jonsson, Factors affecting flux and ethanol separation performance in vacuum membrane distillation (VMD), J. Memb. Sci. 214 (2003) 113–130. doi:10.1016/S0376-7388(02)00540-9.
[203] N. Diban, O.C. Voinea, A. Urtiaga, I. Ortiz, Vacuum membrane distillation of the main pear aroma compound: Experimental study and mass transfer modeling, J. Memb. Sci. 326 (2009) 64–75. doi:10.1016/j.memsci.2008.09.024.
[204] S. Bandini, G.C. Sarti, Heat and mass transport resistances in vacuum membrane distillation per drop, AIChE J. 45 (1999) 1422–1433. doi:10.1002/aic.690450707.
[205] C. Gostoli, S. Bandini, Gas membrane extraction of ethanol by glycols: Experiments and modelling, J. Memb. Sci. 98 (1995) 1–12. doi:10.1016/0376-7388(94)00155-R.
[206] F.A. Banat, F. Abu Al-Rub, R. Jumah, M. Shannag, On the effect of inert gases in breaking the formic acid-water azeotrope by gas-gap membrane distillation, Chem. Eng. J. 73 (1999) 37–42. doi:10.1016/S1385-8947(99)00014-5.
[207] F.A. Banat, F. Abu Al-Rub, R. Jumah, M. Al-Shannag, Application of Stefan-Maxwell approach to azeotropic separation by membrane distillation, Chem. Eng. J. 73 (1999) 71–75. doi:10.1016/S1385-8947(99)00016-9.
[208] F.A. Banat, F.A. Al-Rub, R. Jumah, M. Shannag, Theoretical investigation of membrane distillation role in breaking the formic acid-water azeotropic point: Comparison between Fickian and Stefan-Maxwell-based models, Int. Commun. Heat Mass Transf. 26 (1999)

879–888. doi:10.1016/S0735-1933(99)00076-7.
[209] R. Taylor, R. Krishna, MULTICOMPONENT MASS TRANSFER, 1st ed., Wiley-Interscience, 1993.
[210] R. Krishna, J.A. Wesselingh, Review article number 50: The Maxwell-Stefan approach to mass tranfer, Chem. Eng. Sci. 52 (1997) 861–911. doi:10.1016/S0009-2509(96)00458-7.
[211] L. Boudin, B. Grec, F. Salvarani, A mathematical and numerical analysis of the maxwell-stefan diffusion equations, Discret. Contin. Dyn. Syst. - Ser. B. 17 (2012) 1427–1440. doi:10.3934/dcdsb.2012.17.1427.
[212] E. Leonardi, C. Angeli, On the maxwell - Stefan approach to diffusion: A general resolution in the transient regime for one-dimensional systems, J. Phys. Chem. B. 114 (2010) 151–164. doi:10.1021/jp900760c.
[213] C. Rivier, U. Stoekar, Poster presented at the EUROMEMBRANE 95, Bath, UK, in: 1997.
[214] H. Udriot, A. Araque, U. Von Stockar, Azeotropic mixtures may be broken by membrane distillation, Chem. Eng. J. Biochem. Eng. J. 54 (1994) 87–93.
[215] D.L.M. Mendez, C. Castel, C. Lemaitre, E. Favre, Improved performances of vacuum membrane distillation for desalination applications: Materials vs process engineering potentialities, Desalination. 452 (2019) 208–218. doi:10.1016/j.desal.2018.11.012.
[216] Y.J. Choi, S. Lee, J. Koo, S.. Kim, Evaluation of economic feasibility of reverse osmosis and membrane distillation hybrid system for desalination, Desalin. Water Treat. 57 (2016) 1–12.
[217] M.R. Qtaishat, F. Banat, Desalination by solar powered membrane distillation systems, Desalination. 308 (2013) 186–197. doi:10.1016/j.desal.2012.01.021.
[218] J. Wang, B. Fan, Z. Luan, D. Qu, X. Peng, D. Hou, Integration of direct contact membrane distillation and recirculating cooling water system for pure water production, J. Clean. Prod. 16 (2008) 1847–1855. doi:10.1016/j.jclepro.2007.12.004.
[219] R.K. Sinnott, Coulson and Richardson's Chemical Engineering Design VOL 6, 4th ed., Butterworth-Heinemann, 2005.
[220] H. Silla, Chemical Process Engineering: Design And Economics, 2003. doi:10.1201/9780203912454.
[221] G. Towler, R. Sinnott, Chemical Engineering Design:Principles,Practice and Economics of Plant and Process Design, 2nd ed., Elsevier, 2012.
[222] D. Cengel, A. Yunus, J.M. Cimbala, Fluid Mechanics Fundamentals and Applications, 3rd ed., McGraw-Hill Education, 2013.
[223] Ceramic Membranes for Water and Wastewater Treatment, 2015. https://www.bluetechresearch.com/reports/ceramic-membranes-water-wastewater-treatment/.
[224] S. Jenkins, CEPCI Updates: January 2018 (prelim.) and December 2017 (final), 2018. https://www.chemengonline.com/cepci-updates-january-2018-prelim-and-december-2017-final/.
[225] R. Turton, R.C. Bailie, W.B. Whiting, J.A. Shaeiwitz, D. Bhattacharyya, Analysis, Synthesis and Design of Chemical Processes, 4th ed., Prentice Hall, 2012.
[226] G.D. Ulrich, P.T. Vasudevan, How to estimate utility costs, Chem. Eng. 113 (2006) 66–69.
[227] T. Wang, Global industrial prices for natural gas by select country 2018, 2019. https://www.statista.com/statistics/253047/natural-gas-prices-in-selected-countries/.
[228] R. Robinson, R.H. Stokes, Electrolyte Solutions, 2nd ed., Dover Publications Inc., 2012.
[229] M.H. Sharqawy, J.H. Lienhard V, S.M. Zubair, Thermophysical properties of seawater: A

review of existing correlations and data, Desalin. Water Treat. 16 (2010) 354–380. doi:10.5004/dwt.2010.1079.
[230] E.L. CUSSLER, Multicomponent Mass Transfer, 1976. doi:10.1016/b978-0-444-41326-0.50014-9.
[231] B.E. Poling, J.M. Prausnitz, J.P. O'Connell, The Properties of Gases and Liquids, 5th ed., McGraw-Hill Education, 2000.
[232] D.W. Green, R.H. Perry, Perry's Chemical Engineers' Handbook, 8th ed., McGraw-Hill Education, 2007.
[233] J.F. Shackelford, W. Alexander, CRC Materials Science and Engineering Handbook, 3rd ed., CRC Press, 2000.
[234] H. Chamani, T. Matsuura, D. Rana, C.Q. Lan, Modeling of pore wetting in vacuum membrane distillation, J. Memb. Sci. 572 (2019) 332–342. doi:10.1016/j.memsci.2018.11.018.

Appendix A: Estimation of Thermophysical Properties

Table of coefficients used in the following equations for the estimation of the thermophysical properties during modeling of SGMD of NaCl(aq.)

a_0	*1*	a_1	*-0.55493*	a_2	*-0.64871*	a_3	*-3.11496*
b_0	*1.541*	b_1	*1.998E-2*	b_2	*-9.52E-5*	c_0	*7.9747*
c_1	*-7.561 E-2*	c_2	*4.724E-4*	d_0	*4.2844E-5*	d_1	*0.157*
d_2	*64.993*	d_3	*-91.296*	e_0	*9.999E+2*	e_1	*2.034E-2*
e_2	*-6.162E-3*	e_3	*2.261E-5*	e_4	*-4.657E-8*	e_5	*8.02E+2*
e_6	*-2.001*	e_7	*1.677E-2*	e_8	*-3.06E-5*	e_9	*-1.613E-5*
f_0	*5.328*	f_1	*-9.76E-2*	f_2	*4.04E-4*	f_3	*-6.913E-3*
f_4	*7.351E-4*	f_5	*-3.15E-6*	f_6	*9.6E-6*	f_7	*-1.927E-6*
f_8	*8.23E-9*	f_9	*2.5E-9*	f_{10}	*1.666E-9*	f_{11}	*-7.125E-12*
g_0	*240*	g_1	*0.0002*	g_2	*0.434*	g_3	*2.3*
g_4	*343.5*	g_5	*0.037*	g_6	*1*	g_7	*647*
g_8	*0.03*	h_0	*6.968E-9*	h_1	*1.443*	p_0	*6.5592E-7*
p_1	*0.6081*	p_2	*54.714*	p_3	*1.7096E-8*	p_4	*1.1146*
q_0	*0.29105E+5*	q_1	*0.086149E+5*	q_2	*1.7016E+3*	q_3	*0.0010347E+5*
q_4	*909.79*	q_5	*0.33363E+5*	q_6	*0.2679E+5*	q_7	*2.6105E+3*
q_8	*0.08896E-5*	q_9	*1169*	u_0	*0.00033143*	u_1	*0.7722*
u_2	*16.323*	u_3	*373.72*	u_4	*6.2041E-6*	u_5	*1.3973*
z_0	*9.25489.9*	z_1	*-3.1821E-2*	z_2	*6.5998E-5*	z_3	*-6.15515E-8*
z_4	*2.14725E-11*						

$[S]$: *g salt / kg solution* $[\omega_s]$: *kg salt / kg solution*

<u>Liquid Feed (NaCl (aq.))</u>

Water activity [228]

$$a_w = a_0 + a_1\omega_s + a_2\omega_s^2 + a_3\omega_s^3$$

Viscosity [229]

$$\eta_L = \left(1+\left(b_0+b_1T+b_2T^2\right)\omega_s+\left(c_0+c_1T+c_2T^2\right)\omega_s^2\right)\times\left(d_0+\left(\left(d_1\times\left(T+d_2\right)^2\right)+d_3\right)^{-1}\right) \quad ,[T]:{}^oC,[\eta]:Pa.s$$

Diffusion Coefficient [230,231]

$$D_{s,L} = D_{s,L25}\times\left(\frac{T+273.15}{298.15}\right)\times\left(\frac{\eta_{L25}}{\eta_L}\right)$$

$$D_{s,L25} = 1.607\times10^{-9}\,m^2/s \qquad [T]:{}^oC, \quad [\eta]:Pa.s, \quad [D]:m^2/s$$

Density [229]

$$\rho_L = e_0+e_1T+e_2T^2+e_3T^3+e_4T^4+e_5\omega_s+e_6\omega_sT+e_7\omega_sT^2+e_8\omega_sT^3+e_9\omega_s^2T^2 \qquad ,[T]:{}^oC, \quad [\rho]:kg/m^3$$

Specific Heat Capacity [229]

$$Cp_L = \left(\left(f_0+f_1S+f_2S^2\right)+\left(f_3+f_4S+f_5S^2\right)T+\left(f_6+f_7S+f_8S^2\right)T^2+\left(f_9+f_{10}S+f_{11}S^2\right)T^3\right)\times1000$$

$$[T]:K, \quad [Cp]:J/(kg.K)$$

Thermal Conductivity [229]

$$k_L^{cond.} = \frac{10^{\sigma}}{1000}, \sigma = \log_{10}\left(g_0+g_1S\right)+g_2\left(g_3-\left(\frac{g_4+g_5S}{T}\right)\right)\left(g_6-\left(\frac{T}{g_7+g_8S}\right)\right)^{1/3} ,[T]:K, \quad [k_L^{cond.}]:\frac{W}{m.K}$$

<u>Sweeping Gas</u>

Diffusion Coefficient

$$D_{wv,N_2} = \frac{h_0\ T^{h_1}}{P} \qquad ,[T]:K, \quad [P]:bar, \quad [D]:m^2/s$$

Viscosity [231,232]

$$\eta_G = \frac{y_{N_2}\eta_{N_2}}{y_{N_2} + \left(y_w \Phi_{N_2,w}\right)} + \frac{y_w \eta_{wv}}{y_w + \left(y_{N_2} \times \left(\Phi_{N_2,w} \times \left(\frac{\eta_{wv}}{\eta_{N_2}}\right) \times \left(\frac{M_{N_2}}{M_w}\right)\right)\right)}$$

$$\Phi_{N_2,w} = \left(1 + \left(\left(\frac{\eta_{N_2}}{\eta_{wv}}\right)^{0.5} \times \left(\frac{M_w}{M_{N_2}}\right)^{0.25}\right)\right)^2 \times \left(8 \times \left(1 + \left(\frac{M_{N_2}}{M_w}\right)\right)\right)^{-0.5}$$

$$\eta_{N_2} = \frac{p_0 \times T^{\,p_1}}{1 + \frac{p_2}{T}} \quad , \quad \eta_{wv} = p_3 \times T^{\,p_4} \qquad [T]: K, \quad [\eta]: Pa.s$$

Specific Heat Capacity [232]

$$Cp_G = \omega_{wv} Cp_{wv} + \omega_{N_2} Cp_{N_2} \qquad ,[T]: K, \quad [M]: kg/mol, \quad [Cp]: J/(kg.K)$$

$$Cp_{N_2} = \frac{q_0 + \left(q_1 \times \left(\frac{q_2}{T}\right)^2 \times \left(\sinh\left(\frac{q_2}{T}\right)\right)^{-2}\right) + \left(q_3 \times \left(\frac{q_4}{T}\right)^2 \times \left(\sinh\left(\frac{q_4}{T}\right)\right)^{-2}\right)}{1000 M_{N_2}}$$

$$Cp_{wv} = \frac{q_5 + \left(q_6 \times \left(\frac{q_7}{T}\right)^2 \times \left(\sinh\left(\frac{q_7}{T}\right)\right)^{-2}\right) + \left(q_8 \times \left(\frac{q_9}{T}\right)^2 \times \left(\sinh\left(\frac{q_9}{T}\right)\right)^{-2}\right)}{1000 M_w}$$

Thermal Conductivity [231,232]

$$k_G^{cond.} = \frac{y_{N_2} k_{N_2}^{cond.}}{y_{N_2} + \left(y_w \Psi_{N_2,w}\right)} + \frac{y_w k_{wv}^{cond.}}{y_w + \left(y_{N_2} \times \left(\Psi_{N_2,w} \times \left(\frac{k_{wv}^{cond.}}{k_{N_2}^{cond.}}\right) \times \left(\frac{M_{N_2}}{M_w}\right)\right)\right)}$$

$$\Psi_{N_2,w} = \left(1 + \left(\left(\frac{k_{N_2}^{cond.}}{k_{wv}^{cond.}}\right)^{0.5} \times \left(\frac{M_w}{M_{N_2}}\right)^{0.25}\right)\right)^2 \times \left(8 \times \left(1 + \left(\frac{M_{N_2}}{M_w}\right)\right)\right)^{-0.5}$$

$$k_{N_2}^{cond.} = \frac{u_0 T^{\,u_1}}{1 + \frac{u_2}{T} + \frac{u_3}{T^2}} \quad , \quad k_{wv}^{cond.} = u_4 T^{\,u_5} \qquad ,[T]: K, \quad [k^{cond.}]: W/(m.K)$$

Solid Titania Thermal Conductivity [233]

$$k_{solid}^{cond.} = z_0 + z_1 T + z_2 T^2 + z_3 T^3 + z_4 T^4 \qquad ,[T]: {}^{o}C, \quad [k_{solid}^{cond.}]: W/(m.K)$$

SGMD of Ethanol (aq.)

Regression equations were employed according to results obtained from the software PRO/II (Schneider Electric SimSci) by applying mixing rules and NRTL activity coefficient model for the following ethanol mass fraction and liquid temperature ranges.

$$0 < \omega_{et.} \le 0.1\, g/g \qquad 50 < T < 110°C$$

Water Activity Coefficient

$$\gamma_w = a + b \cdot T + c \cdot T^2 + d \cdot T^3 + e \cdot \omega_{et.} + f \cdot \omega_{et.}^2 + g \cdot \omega_{et.}^3 + h \cdot T \cdot \omega_{et.}$$

a	*b*	*c*	*d*
0.9997	$8.9105 \cdot 10^{-6}$	$-1.1364 \cdot 10^{-7}$	$5.0505 \cdot 10^{-10}$
e	*f*	*g*	*h*
$6.0882 \cdot 10^{-3}$	*0.3609*	*0.5911*	$-4.7403 \cdot 10^{-5}$

Ethanol Activity Coefficient

$$\gamma_{et.} = a + b \cdot T + c \cdot T^2 + d \cdot T^3 + e \cdot \omega_{et.} + f \cdot \omega_{et.}^2 + g \cdot \omega_{et.}^3 + h \cdot T \cdot \omega_{et.}$$

a	*b*	*c*	*d*
4.9279	$5.299 \cdot 10^{-3}$	$-3.2713 \cdot 10^{-5}$	$7.222 \cdot 10^{-8}$
e	*f*	*g*	*h*
- 11.228	*10.322*	*- 4.6176*	$5.7208 \cdot 10^{-3}$

Density of The Solution

$$\rho_L = a + b \cdot T + c \cdot T^2 + d \cdot T^3 + e \cdot \omega_{et.} + f \cdot \omega_{et.}^2 + g \cdot \omega_{et.}^3 + h \cdot T \cdot \omega_{et.} \qquad [kg/m^3]$$

a	*b*	*c*	*d*
1002.725	*- 0.2154*	$-2.2189 \cdot 10^{-3}$	$9.6869 \cdot 10^{-7}$
e	*f*	*g*	*h*
- 253.2834	*101.0396*	*- 30.8869*	*- 0.7429*

Specific Heat Capacity of The Solution at Constant Pressure

$$\hat{C}p_L = a + b \cdot T + c \cdot T^2 + d \cdot T^3 + e \cdot \omega_{et.} + f \cdot \omega_{et.}^2 + g \cdot \omega_{et.}^3 + h \cdot T \cdot \omega_{et.} \qquad [J/(kg \cdot K)]$$

a	*b*	*c*	*d*
4195.9806	*- 0.774*	*- 7.5217·10^{-3}*	*2.2257·10^{-5}*
e	*f*	*g*	*h*
- 2041.9943	*- 0.3913*	*2.4041*	*11.1619*

Thermal Conductivity of The Solution

$$k_L^{cond.} = a + b \cdot T + c \cdot T^2 + d \cdot T^3 + e \cdot \omega_{et.} + f \cdot \omega_{et.}^2 + g \cdot \omega_{et.}^3 + h \cdot T \cdot \omega_{et.} \qquad [W/(m \cdot K)]$$

a	*b*	*c*	*d*
0.6061	*1.0763·10^{-3}*	*- 4.952·10^{-6}*	*8.3169·10^{-9}*
e	*f*	*g*	*h*
- 4.8986	*45.6191*	*- 171.2281*	*- 8.1164·10^{-3}*

Viscosity of The Solution

$$\eta_L = a + b \cdot T + c \cdot T^2 + d \cdot T^3 + e \cdot \omega_{et.} + f \cdot \omega_{et.}^2 + g \cdot \omega_{et.}^3 + h \cdot T \cdot \omega_{et.} \qquad [Pa \cdot s]$$

a	*b*	*c*	*d*
1.3026·10^{-3}	*- 2.2707·10^{-5}*	*1.7634·10^{-7}*	*5.1583·10^{-10}*
e	*f*	*g*	*h*
9.1295·10^{-5}	*1.9022·10^{-5}*	*1.3859·10^{-5}*	*- 7.66·10^{-7}*

Latent heat of Vaporization of Ethanol [232]

$$\lambda_{et.}^{vap.} = a(1 - T_r)^{b + cT_r + dT_r^2 + e \cdot T_r^3} \qquad [J/kmol], \qquad T_r = \frac{T}{T_C}$$

a	*b*	*c*	*d*
5.5789·10^{-7}	*0.31245*	*0*	*0*

Water Vapor Pressure [231]

$$P_w^* = 10^{a-\frac{b}{c+T}} \qquad [bar], \qquad T \text{ in } °C$$

a	b	c
5.11564	1687.537	230.17

Ethanol Vapor Pressure [232]

$$P_{et.}^* = \exp\left(a + b/T + c \cdot \ln(T) + d \cdot T^e\right) \qquad [Pa], \qquad T \text{ in } K$$

a	b	c	d	e
73.304	- 7122.3	- 7.1424	$2.8853 \cdot 10^{-6}$	2

Specific Heat Capacity at Constant Temperature of Ethanol (Vapor State) [232]

$$\hat{C}p_{et,G} = a + b \cdot T + c \cdot T^2 + d \cdot T^3 + e \cdot T^4 \qquad [J/(kmol \cdot K)], \qquad T \text{ in } K$$

a	b	c	d	e
32585	87.4	8.125	0.05	0

Thermal Conductivity of Ethanol (Vapor State) [232]

$$k_{et,G}^{cond.} = \frac{a \cdot T^b}{1 + c/T + d/T^2} \qquad [W/(m \cdot K)], \qquad T \text{ in } K$$

a	b	c	d
- 0.010109	0.6475	- 7332	- 268000

Viscosity of Ethanol (Vapor State) [232]

$$\eta_{et.,G} = \frac{a \cdot T^b}{1 + c/T + d/T^2} \qquad [Pa \cdot s], \qquad T \text{ in } K$$

a	b	c	d
$1.0613 \cdot 10^{-7}$	0.8066	52.7	0

Appendix B: Cost Estimation Coefficients

Equipment Cost [225]

$$CBM_{2001} = C_P^o \left(B_1 + B_2 \, F_M \, F_P \right)$$

Equipment	B_1	B_2	F_M	F_P
Compressor	0	1	5.8	1
Pump	1.89	1.35	2.3	1
Heat exchanger	1.63	1.66	2.8	1
Separator	2.25	1.82	3.2	1

$$\log_{10}\left(C_P^o\right) = K_1 + K_2 \log_{10}(\Omega) + K_3 \left(\log_{10}(\Omega)\right)^2$$

Equipment	Ω	K_1	K_2	K_3
Compressor	Power (kW)	2.2897	1.3604	-0.10127
Pump	Power (kW)	3.3892	0.0536	0.1538
Heat exchanger	Area (m^2)	4.1884	-0.2503	0.1974
Separator	Volume (m^3)	3.4974	0.4485	0.1074

Utility Cost [226]

$$C_{SU} = a\,(CEPCI) + b\,C_f$$

Utility	C_{SU}	a	b
Electricity	\$/kWh	1.4×10^{-4}	0.011
Cooling water	\$/m^3	$0.0001 + \frac{3}{q \times 10^5}$	0.003

q: Flowrate of cooling water in m^3/s

Appendix C: Modeling Pore Wetting during Vacuum Membrane Distillation (VMD)

The work presented in this Appendix took place during the research period at the LISBP laboratory of the The Institut National des Sciences Appliquées de Toulouse (INSA) in Toulouse in France under the supervision of Professor Corinne Cabassud. This took place during the period 20/02/2019 – 20/05/2019.

Objectives:

The main objective is to develop modeling equations aiming at simulating the performance of vacuum membrane distillation (VMD) in case of pore wetting and predicting the mass flux at given operating conditions resulting in a certain pore wetting ratio.

Followed Approach:

1) Literature survey
   Literature survey concerning modeling of pore wetting, capillary rise in nanopores and mass transfer in porous wicks.

2) Simple sensitivity analysis
   This aimed at checking the effect of the wetting ratio on the modeled flux. In this case, the same typical VMD modeling equations were implemented in addition to changing the Knudsen permeance according to the wetting ratio. This was based on the MATLAB code already used by Jean-Pierre at the INSA.

3) Local modeling of pore wetting in VMD
   A new MATLAB code was written in order to model the pore wetting phenomenon in VMD. This was based on the model that had been developed by H.Chamani and T.Matsuura [234]. They compared their modeled flux to experimental results from another work for sodium chloride solution and the deviation was accepted. The model was based on the following assumptions.

- Mass transfer inside the unwetted portion of the pore is described by Knudsen diffusion.
- Liquid flow inside the wetted portion of the pore is described by Hagen-Poiseuille flow (validity range can be determined according to L/d).
- Only water vapor passes from feed to permeate side (No salt permeates).
- Steady state.
- Neglected heat conduction in the membrane solid portion.

- Inside the wetted portion of the pore, the velocity and physical properties of the liquid are constant and are evaluated at the mean values of temperature and composition. (The other possibility is the discretization inside the pore)
- In case of wetting, water vaporization occurs inside the pore at the liquid/vapor interface.
- Flat membranes of homogeneous surfaces and uniform morphology

The following equations and results regard a proposed modeling of the pore wetting during vacuum membrane distillation (VMD). The simple case of pure water feed was considered. This was based on the model that had been developed by H.Chamani et. al [234]. The first experimental work in literature visualizing the degree of wetting was performed by C. Cabassud et.al. [43]

Model Inputs

Flat PVDF membrane

Morphological properties

$d_p = 0.22 \mu m$ $\varepsilon = 0.751$ $CA = 117°$

$\delta_m = 114.4 \mu m$ $K_{M,20} = 3.07 \times 10^{-6} \text{s.mol}^{1/2}.\text{m}^{-1}.\text{kg}^{-1/2}$

Geometric parameters

$Length = 87.6mm$ $Width = 47.5mm$ $Depth = 0.5mm$

Operating conditions

Feed side: $P_F = 1.8bar$ $T_{Lb} = 40 - 45°C$ $v_L = 1.77 m.s^{-1}$ $x_{w,Lb} = 1$

Permeate side: $P_p = 40 - 60mbar$

Local Model

$$T^* = T_{LI} - \left(\frac{\dot{N}_{w,Pore}\ \Delta\tilde{H}_{wv\left(T^*\right)}}{\hat{C}_{P_L}\rho_L v_z \pi r_p^2} \right)\left(1 - e^{\left(\frac{-v_z \delta_l}{\alpha_L} \right)} \right)$$

$$v_z = \left(\frac{r_p^2}{8\mu_L\ \delta_L} \right)\left(P_F - P^*_{w(T^*)} + \frac{\beta 2\gamma \cos\varphi}{r_p} \right)$$

$$\dot{N}_{w,Pore} = \frac{2r_p^3}{3\left(\delta_m - \delta_L\right)} \sqrt{\frac{8\pi}{RTM_w}} \left(P^*_{w(T^*)} - P_p \right)$$

$$\dot{N}_{w,Pore} = \frac{\rho_L}{M_L} v_z\ \pi r_p^2 \quad , \quad w_p = \delta_L \Big/ \delta_m$$

$$h_L \left(T_{Lb} - T_{LI} \right) W = \dot{N}'_{w_{memb}} \Delta\tilde{H}_{wv\left(T^*\right)}$$

$$\frac{\dot{N}'_{w_{memb}}}{\dot{N}_{w,Pore}} = \left(\frac{\varepsilon}{\tau} \right)\left(\frac{W}{\pi r_p^2} \right)$$

$\hat{C}_{P_L}$: *liquid specific heat capacity* $(J/(kg.K))$ h_L : *liquid heat transfer coefficient* $(W/(m^2K))$

α_L : *thermal difusivity of liquid in pore* (m^2/s) β : *pore geometrical factor* $(-)$ ε : *porosity* $(-)$

$\Delta\tilde{H}_{wv\left(T^*\right)}$: *molar latent heat of vaporization* (J/mol) $\dot{N}_{w,Pore}$: *molar flow rate across one pore* (mol/s)

$\dot{N}'_{w_{memb}}$: *molar flow rate across membrane of unit length* $(mol/(s.m))$ P_F : *feed pressure* (Pa)

$P^*_{w(T^*)}$: *water vapor pressure* (Pa) P_p : *permeate pressure* (Pa) r_p : *pore radius* (m)

T_{Lb} : *temperature at liquid bulk* (K) T_{LI} : *temperature at liquid / membrane interface* (K)

T^* : *temperature at liquid / vapor interface* (K) v_z : *velocity of liquid inside pore* (m/s)

W : *width of membrane* (m) Δl : *unit length of membrane* (m) φ : *contact angle* $(°)$

δ_m : *membrane thickness* (m) δ_l : *length of liquid portion in pore* (m) τ : *tortuosity* $(-)$

μ_L : *liquid viscosity* $(Pa.s)$ γ_w : *water activity coefficient* $(-)$

γ : *surface tension of water at the liquid / vapor interface* (J/m^2)

Results

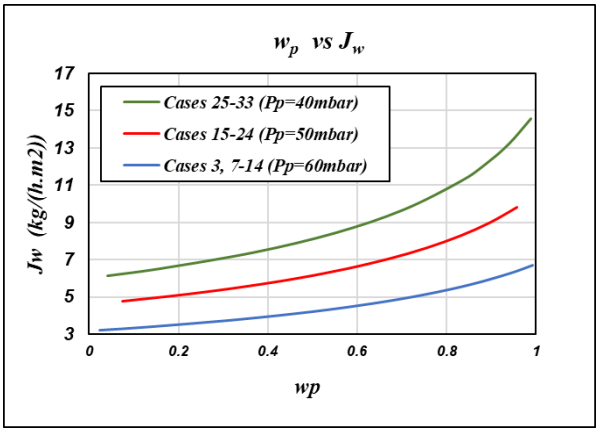

(a)

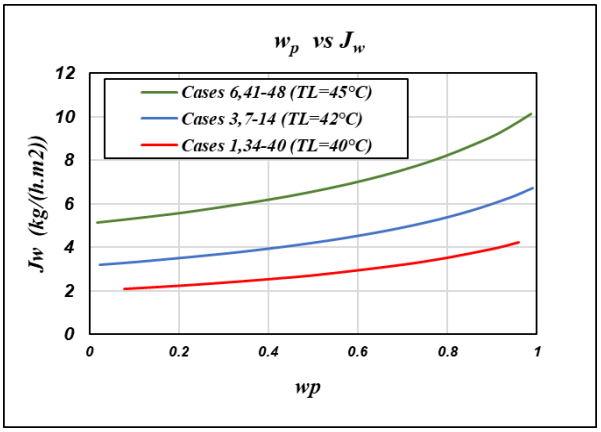

(b)

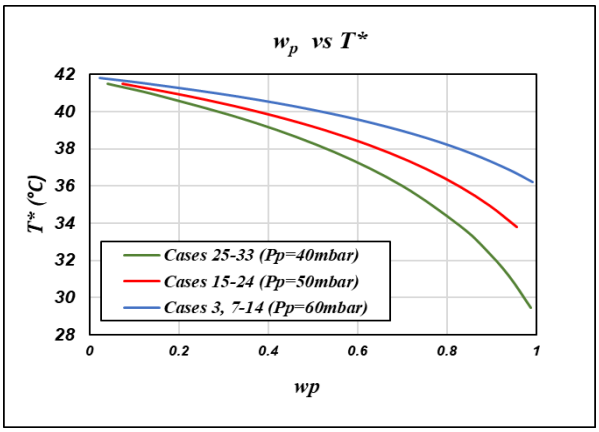

(c)

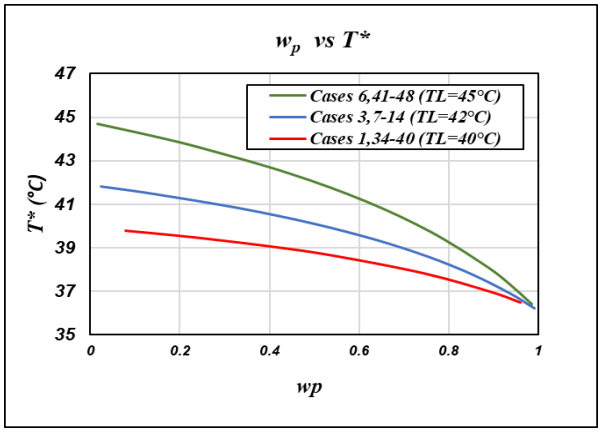

(d)

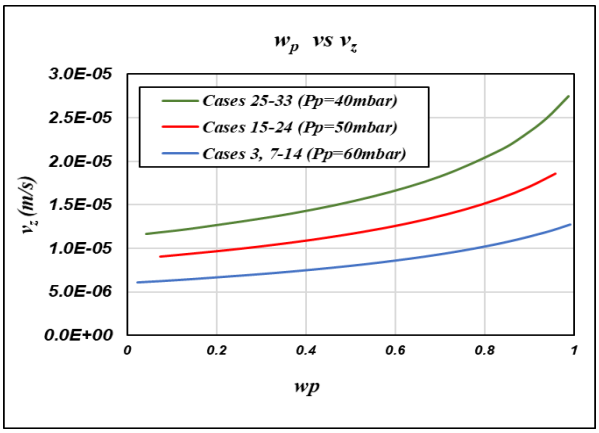

(e)

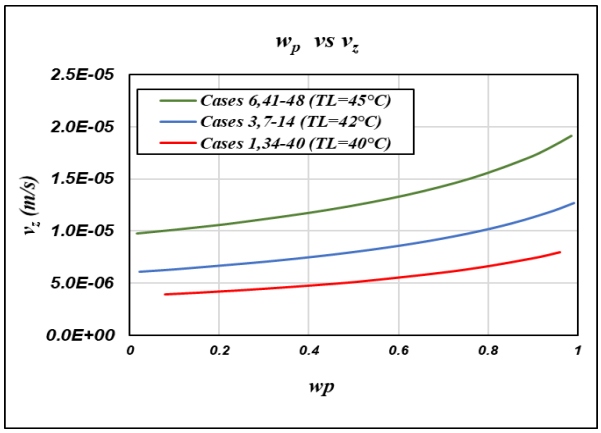

(f)

Comments:

- Modeling results demonstrated the effect of the pore wetting ratio on the resulting flux which becomes more significant at high values of pore wetting ratio.
- Modeling of pore wetting in case of VMD of pure water showed the large dependence of the results on the geometric factor and pore size of the pores.
- The attempt to model pore wetting in case of NaCl (aq.) using the same concept of the pure water was not possible due to inconsistency problems. Therefore, different approach needs to be followed.
- The works in literature about modeling of pore wetting during membrane distillation are extremely scarce due to the complexity of this phenomenon.
- Suggestions for possible further studies:
    - Improving the modeling equations for pore wetting in case of pure water by trying different approaches of modeling. One of which is not using the same value of pore size in all the modeling equations.
    - Trying to develop the model for pore wetting in case of NaCl (aq.) and not just the simple case of pure water.
    - Comparing the modeled results to the experimental values in terms of flux and wetting ratio in order to assign the suitable fitting parameter and validate the model.

Appendix D: The Sweeping Gas Membrane Distillation Bench-scale Equipment

The bench-scale equipment that was used in the SGMD experimental studies presented in Chapter (3) was built by Dr. Felipe Vareala-Corredor [80] at the University of Bologna. The following pictures refer to the bench- scale SGMD equipment.